FACHBEREICH C - MATHEMATIK UND NATURWISSENSCHAFTEN
FACHGRUPPE PHYSIK

Identification of bottom-quarks in searches for new heavy resonances decaying into boosted top-quarks with the ATLAS detector and a development of an improved *b*-tagging algorithm

Dominik Duda

30th May 2016

1st referee: Prof. Dr. Peter Mättig (Bergische Universität Wuppertal, Fachbereich C)
2nd referee: Dr. Frank Filthaut (Radboud University Nijmegen, Faculty of Science)
3rd referee: Prof. Dr. Tobias Golling (Université de Genève, Section de physique)

Abstract

This thesis describes the performance of the common ATLAS b-tagging algorithms in the context of the dense environments that can be found in the decay of boosted top quarks into jets and addresses the problems related to such conditions. The results of these studies lead to the development of two new multivariate-analysis-based b-tagging algorithms called MVb and MVbCharm. The training of these new b-tagging algorithms is modified with respect to that of the current tools to take the conditions of boosted topologies better into account. Their performance is significantly improved relative to the standard algorithms for high p_{T} b-jets and jets contained in dense environments.

These new developed b-tagging algorithms are calibrated with a new approach using reconstructed $t\bar{t}$ candidate events that have one charged lepton, missing transverse momentum, and at least four jets in the final state. Expanding on previous b-tagging calibration studies, the b-tagging efficiencies are measured not only as a function of the transverse momentum or the pseudorapidity of the jets, but also as a function of quantities that are sensitive to close-by jet activity. The results measured in data are in good agreement with the predictions from simulation.

Furthermore, it is shown how a connection between the topology of reconstructed $t\bar{t}$ candidate decays and the b-tagged jets contained in the studied events can be exploited to improve the sensitivity to search for new heavy particles decaying into top-quark pairs by classifying the selected $t\bar{t}$ candidate events into several categories. The expected exclusion limits on the cross section times branching ratio for the production of hypothetical new heavy particles decaying into top-quark pairs are significantly improved using this new event classification scheme.

Die Dissertation kann wie folgt zitiert werden:

urn:nbn:de:hbz:468-20160530-114431-6
[http://nbn-resolving.de/urn/resolver.pl?urn=urn%3Anbn%3Ade%3Ahbz%3A468-20160530-114431-6]

Contents

Chapter 1

Introduction

Elementary particle physics aims to describe the production, interaction and decays of natures' smallest constituents, the fundamental (or elementary) particles. A theoretical description of these processes is given by the so-called Standard Model of particle physics. This model is one of the most extensively tested theories in physics. Its validity is currently probed in phase space regions that were never accessible before using the high energetic particle collisions provided by the Large Hadron Collider [1], which is located at the European Organisation for Nuclear Research (CERN). This particle accelerator is the largest single machine ever constructed by mankind.

From all the so far discovered elementary particles, the top-quark is the heaviest. Its large mass of 173.34 GeV is unexplained and suggests that the top-quark may play a special role in nature, as it occurs in many beyond the Standard Model predictions. Several of these theories anticipate the existence of heavy particles that decay predominantly into top-quark pairs. Favoured benchmark models in the search for these high mass resonances are topcolour-assisted technicolour [2] or Randall-Sundrum warped extra-dimensions [3], which predict particles such as a leptophobic Z', a bulk Kaluza-Klein gluon or a bulk Randall-Sundrum spin-2 graviton. Further theories that predict particles that might predominantly decay into top-quarks are supersymmetric extensions of the Standard Model [4, 5] or scenarios including further Higgs bosons [6].

Searches for such new particles have been already performed by the experiments of the TEVATRON collider located at the Fermi National Accelerator Laboratory as well as by the two largest LHC experiments, ATLAS and CMS. Meanwhile, the exclusion limits on some of these models extend already up to TeV mass scales. Thus the ongoing searches for new heavy particles decaying into top-quark pairs focus more strongly on events that contain high-p_{T} top-quarks. The decay products of a boosted top-quark (or any other highly boosted particle) can be strongly collimated and their signatures in the detector system might even have a significant overlap. In such a case the standard reconstruction techniques might fail to resolve the decay products of the top-quarks individually and dedicated algorithms are needed in order to recover the loss of sensitivity.

The identification of bottom-quark decays, called b-tagging, is an important tool for the selection and reconstruction of top-quarks in order to suppress most of the relevant background processes. Boosted particle decays are a particularly challenging environment, as the performance of the currently used b-tagging algorithms are strongly reduced under these conditions. Thus dedicated b-tagging algorithms are required that are more stable inside dense jet environments in order to recover for the effects that are connected to the performance degradation.

The outline of this thesis is the following: Chapter 2 summarises the relevant aspects of the Standard Model of particle physics, including its particle content and the fundamental interactions, and highlights the main properties of the top-quark. In Chapter 3 an overview of the experimental setup, including the LHC as well as the ATLAS detector and all its subsystems, is given. In addition, it is discussed how the detector is used to identify the various types of parti-

cles that are produced via the high energetic pp collisions provided by the LHC. The concept of b-tagging and the main b-tagging algorithms used in the analyses of the ATLAS collaboration are introduced in Chapter 4, while the various selection and reconstruction techniques that are currently used in the search for heavy resonances decaying into top-quark pairs are explained in Chapter 5.

Chapter 6 describes extensively the performance of the common ATLAS b-tagging algorithms in the context of dense environments as they can be found in the decay of boosted top-quarks. In addition, the development of a new set of multivariate analysis based b-tagging algorithms are presented as well. The training of these new b-taggers is modified with respect to that of the current tools to take the conditions of boosted topologies better into account. Their performance is compared in great detail to that of the current default b-tagging algorithm of the ATLAS collaboration. A significant part of these studies are published in the ATLAS note [7].

New developments within the ATLAS collaboration strive for the usage of jets clustered only from reconstructed particle tracks [8] for the purpose of b-tagging. Chapter 7 gives a short motivation for a possible application of this track jet based b-tagging to the top-quark sector.

A new method for the calibration of b-tagging algorithms is presented in Chapter 8. In contrast to previous b-tagging calibration studies, the b-tagging efficiencies are measured not only as a function of the transverse momentum or the pseudorapidity of the b-jet candidates, but also for the first time as function of quantities that are sensitive to close-by jet activity. A large fraction of these studies are published via an additional ATLAS note [9].

Finally Chapter 9 discusses how a connection between the topology of the reconstructed $t\bar{t}$ candidate decays and the b-tagged jets contained in the studied events can be exploited to improve the sensitivity to search for new heavy particles decaying into top-quark pairs.

Chapter 2

The top-quark and its role in the Standard Model of particle physics

The Standard Model (SM) of particle physics describes the elementary constituents of nature, and the fundamental forces with which those particles interact with each other. Developed in the 1960s and 1970s, the SM has meanwhile become one of the most extensively tested theories in physics. It is in a good agreement with the experimental findings in the fields of atomic, nuclear and sub-nuclear physics accomplished over the years and it made several precise predictions for a wide variety of phenomena. However, the Standard Model of particle physics is not a complete theory, as it does not include a description of gravitational interactions on quantum level nor does it explain the large difference in the mass scale of the elementary particles or the huge asymmetry between matter and antimatter existent in the universe. Thus the Standard Model has to be extended in order to give answers to these and further open questions.

Many theoretical efforts predict beyond the Standard Model (BSM) effects to occur at the TeV scale such that they are accessible to the current particle physics experiments. Due to its large mass, the top-quark, one of the SM particles, plays an important role in many of these new physics scenarios. Several of them predict the existence of so far unrecognised heavy particles that decay predominantly into top-quark pairs. Examples for such models can be found in the References [2, 3, 6].

2.1 Short summary of the Standard Model of particle physics

The mathematical description of the Standard Model of particle physics is based on a relativistic quantum field theory, which assigns a dynamical quantum field to each elementary particle. All known non-gravitational interactions between these particles are derived from one general principle, the requirement of local gauge invariance and renormalisability. The dynamics and kinematics of the quantum fields and their interactions are described by a Lagrangian, which is invariant under local $\mathrm{SU}(3) \otimes \mathrm{SU}(2) \otimes \mathrm{U}(1)$ gauge symmetry transformations [10].

The main purpose of the Standard Model of particle physics is to specify and classify all known elementary particles and to describe the fundamental interactions between them.

2.1.1 Particle content

Depending on their spin, the elementary particles are divided into two different categories called fermions and bosons. While fermions have a half-integer spin and build up matter, bosons have an integer spin and mediate the fundamental interactions between the elementary particles. Fermions are further subdivided into two different subgroups, leptons and quarks. They obey the Fermi-Dirac statistics as well as the Pauli exclusion principle, which forbids two fermionic particles to have identical quantum numbers. Both, leptons ℓ and quarks q are grouped into

three generations, whereas all known matter is built up only by the particles from the first generation leptons (the electron e and electron neutrino ν_e) and quarks (up u and down d). Quarks and leptons of the second and third generation can be produced in high energetic particle interactions, but due to their higher mass they decay subsequently into particles from the first generation. These are respectively the charm (c), strange (s), top (t), and bottom (b) quarks and in the leptonic sector the muon μ, muon neutrino ν_μ, tau τ and tau neutrino ν_τ. In addition, each of these particles has an associated anti-particle, which has the same mass but opposite colour and electrical charge.

Interactions between these fermions are described by the Standard Model via the exchange of gauge bosons. In this sense electromagnetism is mediated by the photon γ, while weak and strong interactions are described by the exchange of a $W^{\pm}$- or Z-boson and a gluon, respectively. The particle content of the SM is completed by the recently discovered Higgs-boson H, which is connected to the process of electroweak symmetry breaking and the generation of particle masses [11]. Having a spin of 0, the Higgs-boson is the only scalar elementary particle described by the SM.

Some properties of the SM particle spectrum, which include their electric charge and their mass, are presented in Figure 2.1. A detailed overview of all properties of the SM particles can be found in Reference [12]. The up-type quarks (u, c, t) have an electric charge of $+2/3$ (in units of the elementary charge e), while the down-type quarks (d, s, b) and the charged leptons (e, μ, τ) have $-1/3$ e and -1 e, respectively. Neutrinos have a very low mass compared to the other fermions, neither an electric nor a colour charge and interact only via the weak interaction.

Except of the W^+- and the W^--boson all other gauge bosons are electrically neutral. The masses of the SM particles range from zero (for the photon and gluon) to 173.34 GeV [13], which is the current world average mass value of the top-quark.

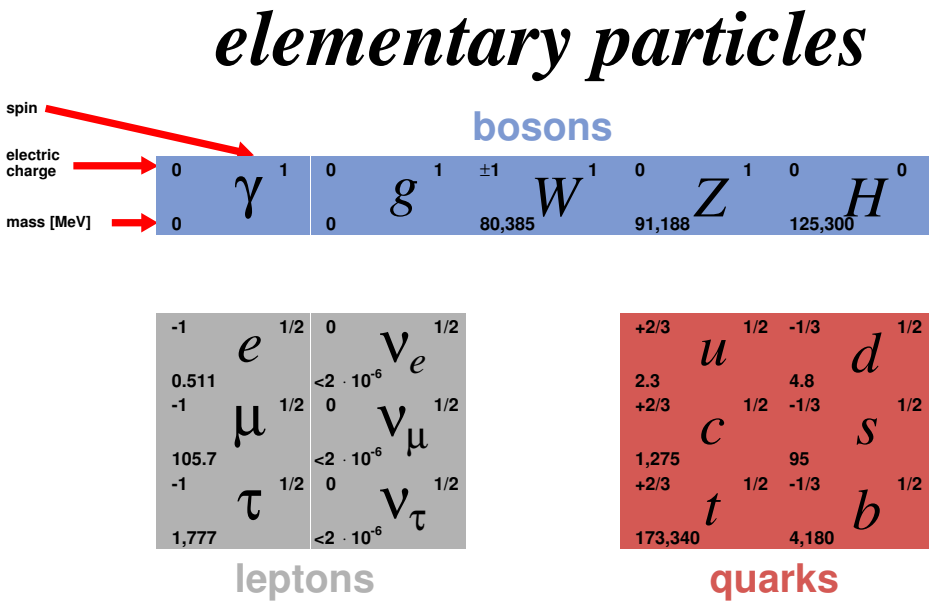

Figure 2.1: Elementary particles described by the SM displayed together with a subset of their properties including the spin, the electric charge (in units of the elementary charge) and the mass (in MeV) [12].

2.1.2 Fundamental interactions

As far as we know, there are four fundamental interactions observable in nature: Strong, electromagnetic, weak and gravitational. While the first three of these interactions are described by quantum field theories included in the Standard Model, a completely satisfactory quantum theory of gravity does not yet exist. However, as gravity is 43 order of magnitudes weaker than the strong interaction, it is assumed to be negligible for elementary particle physics below the so-called Planck scale ($\sim 10^{19}$ GeV). In order to participate in a certain type of interaction an elementary particle has to carry the corresponding charge.

Electromagnetic interaction

Quantum electrodynamics (QED) is a relativistic quantum field theory based on the abelian symmetry group U(1) and it is used to describe interactions between electrically charged particles. The photon is the corresponding gauge boson of the QED. It is massless and couples to electrical charge but as it is not charged itself, photon self-interaction does not occur in the Standard Model. Due to the fact that the photon is massless, the electromagnetic force extends to an infinite range.

Strong interaction

The strong interaction is mathematically described by the Quantum Chromodynamic (QCD), which is based on a non-abelian SU(3) gauge symmetry. It is mediated by a massless particle called gluon that couples to all particles carrying the strong charge (colour charge). According to the prediction of the Standard Model of particle physics these are the quarks and antiquarks and the gluon itself, as it has a colour charge as well. Quarks can have one of three possible colour states, while the anti-quarks have one of the corresponding anti-colours. Gluons have both a colour and an anti-colour. The interaction between a quark and a gluon rotates the colour state of the quark within the SU(3) space.

In any given process involving the strong interaction between two colour-charged particles, their effective coupling strength is given by

$$\alpha_S(Q^2) = \frac{12\pi}{(33 - 2n_f)\ln\left(Q^2/\Lambda^2\right)} \,. \tag{2.1}$$

Here n_f is the number of quark flavours that are relevant at the considered energy scale Q^2 and Λ refers to the energy scale at which the strong coupling can not be described by the perturbation theory anymore. This means that processes with energy scales below that value have to be described by empirical models. Its value is on the order of 200 MeV.

The dependence between the strong coupling constant and the energy scale of a process leads to quasi-free quarks at small distances (high energies), which is commonly referred to as asymptotic freedom [14]. At large distances the strong force increases and the quarks get constrained to form almost immediately colourless bound states containing either a quark-antiquark pair, called mesons, or three quarks (three antiquarks), called baryons. This characteristic is referred to as confinement.

Due to the confinement, quarks that are produced in particle interactions underly a process called hadronisation: If the distance between two quarks reaches approximately 10^{-15} m, the resulting potential energy becomes large enough to create additional quark-antiquark pairs from the vacuum that form collimated colour-neutral particle showers together with the initial quarks. These particle showers are referred to as jets.

Weak interaction

The weak interaction is the mechanism responsible for the nuclear β decay of subatomic particles and it plays an important role in nuclear fission. Weak interactions are either mediated by the emission or absorption of a $W^{\pm}$-boson (charged currents) or by a Z-boson (neutral currents). Typical for weak particle decays are relatively long lifetimes, which are related to the high mass of the $W^{\pm}$- and Z-boson. As the weak coupling is proportional to the inverse boson mass $1/m_W^2$, it is several order of magnitudes smaller than the couplings of the electromagnetic and strong interactions.

In general, all fermions participate in the weak interactions with the exception that the charged currents couple only to left-handed particles and right-handed antiparticles. Thus interactions involving the exchange of a $W^{\pm}$-boson violate the parity symmetry, the invariance under point reflection. In order to describe the weak interactions a $\mathrm{SU}(2)_L$ symmetry group is used, which requires the left-handed fermions (right-handed antifermions) to be classified into doublets and the right-handed fermions (left-handed antifermions) into singlets. Charged currents can provide a transition (flavour change) within each of these doublets

$$\begin{pmatrix} \nu_e \\ e^- \end{pmatrix}, \begin{pmatrix} \nu_\mu \\ \mu^- \end{pmatrix}, \begin{pmatrix} \nu_\tau \\ \tau^- \end{pmatrix}, \begin{pmatrix} u \\ d' \end{pmatrix}, \begin{pmatrix} c \\ s' \end{pmatrix}, \begin{pmatrix} t \\ b' \end{pmatrix}$$

where d', s' and b' denote the flavour eigenstates of the down-type quarks which differ from the mass eigenstates d, s, and b that are produced via the strong or the electromagnetic interaction. The transformation of the mass and flavour eigenstates into each other is described by a unitary 3×3 matrix M_{CKM}, the Cabibbo-Kobayashi-Maskawa (CKM) matrix [15, 16]:

$$\begin{pmatrix} d' \\ s' \\ b' \end{pmatrix} = \underbrace{\begin{pmatrix} V_{ud} & V_{us} & V_{ub} \\ V_{cd} & V_{cs} & V_{cb} \\ V_{td} & V_{ts} & V_{tb} \end{pmatrix}}_{M_{CKM}} \cdot \begin{pmatrix} d \\ s \\ b \end{pmatrix} \tag{2.2}$$

The flavour eigenstates d', s' and b' are therefore linear combinations of the physical quarks d, s and b, which means that the CKM matrix describes a mixing of the three mass eigenstates. Each of the nine (complex) matrix elements quantifies the weak coupling strength (transition probability) between a pair of two quarks. The magnitudes of the various elements (and all other properties of M_{CKM}) have to be determined from measurements, as they are free parameters in the theory [17]:

$$|V_{ij}| = \begin{pmatrix} 0.9743 & 0.2253 & 0.0035 \\ 0.2252 & 0.9735 & 0.0410 \\ 0.0086 & 0.0403 & 0.9992 \end{pmatrix}$$

Due to the fact that the off-diagonal elements of the CKM matrix are not equal to zero, also cross-generational transitions can be provided by the exchange of a weak charged boson. However, as the size of this elements are relatively small, these processes are strongly suppressed compared to the transition between two quarks of the same generation.

Similar to the mixing of the flavour eigenstates of down-type quarks, also a mixing in the leptonic sector is observed e.g. in the oscillation of neutrino flavours [18]. This mixing is described by the so-called Pontecorvo-Maki-Nakagawa-Sakata (PMNS) matrix.

2.1.3 Electroweak symmetry breaking

On the first glance, the weak and electromagnetic interactions appear to be very dissimilar due to the large-scale difference of their coupling strength. Still Sheldon Lee Glashow, Steven Weinberg and Abdus Salam independently discovered in the 1960s that the electromagnetic and weak interactions between elementary particles can be described by a combined gauge field theory invariant under transformations of a local $\mathrm{SU}(2)_L \otimes \mathrm{U}(1)_Y$ symmetry group [19]. Thus these two interactions can be understood as two different aspects of the same process. According to the unification of both theories four massless gauge fields were introduced to fully describe electroweak processes, where the three gauge fields W_1, W_2 and W_3 correspond to the $\mathrm{SU}(2)_L$, while one field, denoted as B^0, is associated to the $\mathrm{U}(1)_Y$ group. However, as weak interactions are mediated by massive particles, the gauge fields of the $\mathrm{SU}(2)_L$ group can not be identical with the fields corresponding to the $W^\pm$ or the Z-boson. Hence the $\mathrm{SU}(2)_L \otimes \mathrm{U}(1)_Y$ symmetry used to formulate this theory has to be broken by a mechanism that acquires mass to the particles exchanged in weak interactions but not to the photon mediating electromagnetic interactions. In the year 1964 Peter Higgs and Franois Englert & Robert Brout developed independently a formalism, later referred to as Brout-Englert-Higgs-mechanism that is capable of solving this problem. The formalism is based on the introduction of an additional scalar field with non-vanishing vacuum expectation value $v \approx 246$ GeV. Due to the existence of this so-called Higgs-field, the $\mathrm{SU}(2)_L \otimes \mathrm{U}(1)_Y$ symmetry is spontaneously broken down into a SU(2) and a U(1), which are associated with the weak and the electromagnetic interactions, respectively. The spontaneous symmetry breaking also causes the W_1, W_2, W_3 and B^0 fields to be merged into the well-known W^+, W^-, Z and γ fields via:

$$W^\pm = \frac{1}{\sqrt{2}} \left(W_1 \mp i W_2\right)$$

$$\begin{pmatrix} \gamma \\ Z \end{pmatrix} = \begin{pmatrix} \cos\theta_W & \sin\theta_W \\ -\sin\theta_W & \cos\theta_W \end{pmatrix} \cdot \begin{pmatrix} B^0 \\ W_3 \end{pmatrix},$$

where θ_W denotes the weak mixing angle, which is determined using experimental data to be approximately 28.74° [20]. Beside the generation of the $W^\pm$- and Z-boson masses, the spontaneous symmetry breaking is also expected to be responsible for the fermion mass terms as the fermion fields couple via the so-called Yukawa interaction to the Higgs-field. The particle masses are free parameters in this theory, which are specified by their coupling strength to this field.

Furthermore this mechanism leads to an additional massive elementary particle, the famous Higgs-boson, whose discovery was finally announced on the 4th July 2012 [21,22]. This particle has a spin of zero, a mass of $m_H \approx 125$ GeV and does not carry an electric nor a colour charge.

2.2 Top-quarks

The existence of the top-quark was predicted by the Standard Model of particle physics as the weak-isospin partner of the bottom-quark shortly after this was discovered in the year 1977. Still it took another 18 years until the top-quark was directly observed by the CDF [23] and D0 [24] collaborations in the $p\bar{p}$ collisions at a centre-of-mass energy of $\sqrt{s} = 1.8$ TeV [25] that were provided by the TEVATRON accelerator ring. With a world average mass of 173.34 GeV, the top-quark is the most massive of all known elementary particles. Due to its high mass the

lifetime of the top-quark is predicted to be $0.5 \cdot 10^{-24}$ s, which is shorter than the hadronisation scale. This means that it decays even before top-flavoured hadrons can be formed. Thus it is the only quark which occurs as a free state in nature passing its spin information directly on to its decay products. Therefore, it provides an unique opportunity to measure certain parameters contained in the Standard Model. Due to its unexplained large mass (which is in the same order of magnitude than the vacuum expectation value of the Higgs-field) it is expected that the top-quark has a significant connection to the process of electroweak symmetry breaking. In addition, the top-quark plays an important role in many beyond the Standard Model predictions.

In the following a short overview about the production and decay modes of the top-quark will be given. Details on the measurements of the various properties like the production cross-section, the electrical charge or the mass are presented in [26–30] and will not be discussed further in this thesis. However, Figure 2.2 displays results on recent measurements of the $t\bar{t}$ production cross section and the top quark mass. In general, an excellent agreement between the measured quantities and their theoretical predictions was found. A more complete review on top-quark physics in hadron collisions is given in References [31, 32].

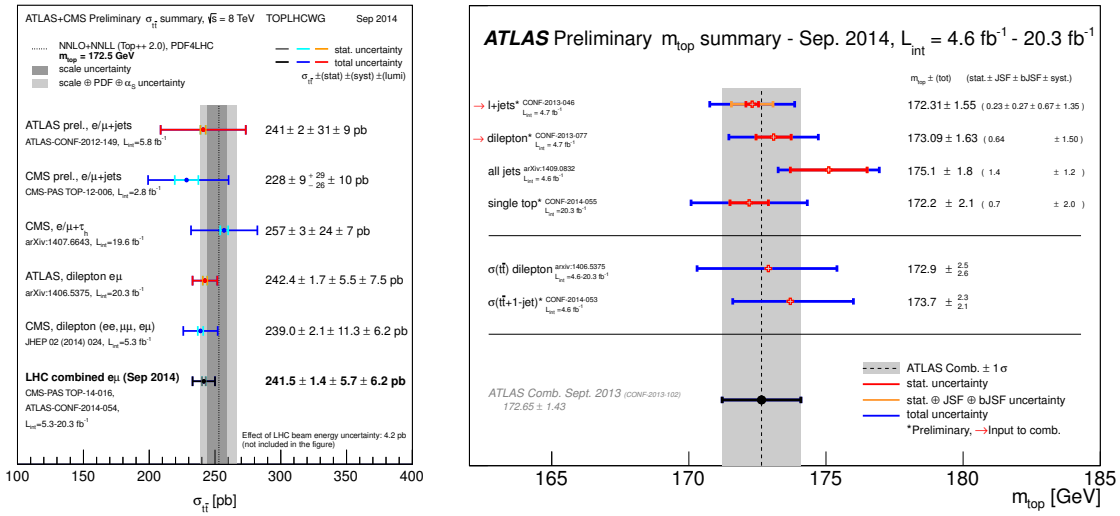

(a) Summary of various $t\bar{t}$ production cross section measurements

(b) Summary of various top-quark mass measurements

Figure 2.2: Summary of recent measurements of the $t\bar{t}$ production cross section at 8 TeV (a) and the top-quark mass (b). The measured production cross section is compared to recent QCD calculations. The results of the mass measurement are compared to the 2013 Tevatron and LHC combinations. More information on these measurements can be found via the References stated in these plots.

2.2.1 Top-quark production mechanism

The production of top-quarks in high energetic pp collisions at the LHC occurs either via the strong or electroweak interaction. While the strong interaction creates top-quarks only in pairs the electroweak interaction produces single top-quarks in association with a bottom-quark, a light-flavoured quark or a W-boson. Exemplary Feynman diagrams corresponding to various single and top-quark pair production modes are displayed in Figure 2.3. The diagrams in Figures 2.3 (a) to (c) show the top-quark pair production via gluon fusion at leading order (LO),

while Figures 2.3 (d), (e) represent the LO production due to quark-antiquark annihilation and the next-to-leading order (NLO) $t\bar{t}$ production via qg scattering. Examples of the single top-quark production in the s- and t- channel as well as in association with a W-boson are shown in Figures 2.3 (f), (g) and (h), respectively.

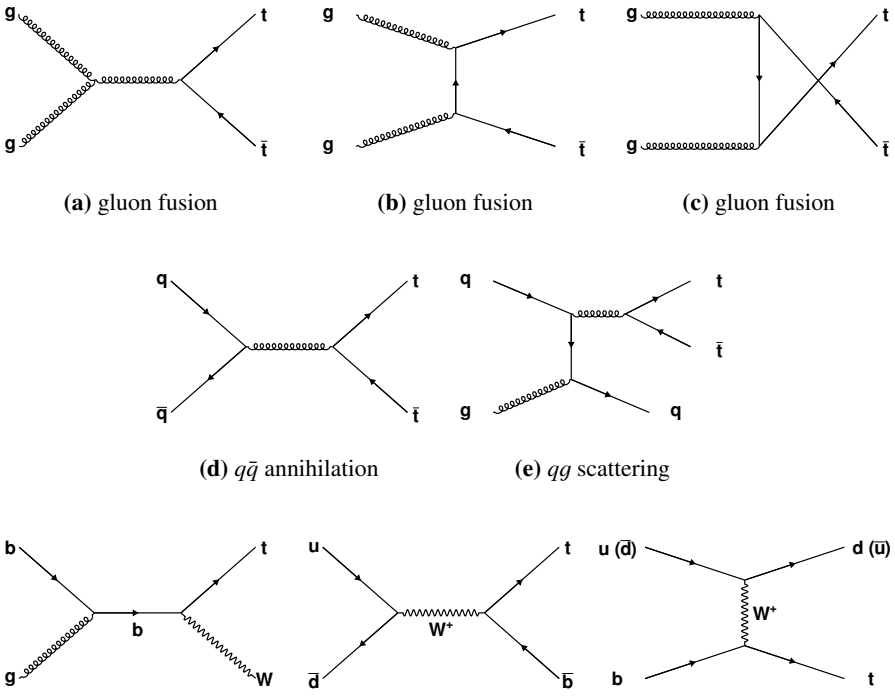

(a) gluon fusion **(b)** gluon fusion **(c)** gluon fusion

(d) $q\bar{q}$ annihilation **(e)** qg scattering

(f) associated Wt-channel production **(g)** s-channel **(h)** t-channel

Figure 2.3: Examples for Feynman diagrams of the leading order top-quark pair production due to gluon-fusion (a-c) and quark-antiquark-annihilation (d). In addition, examples for the next-to-leading order production of top-quark pairs via qg scattering (e) and the s-, t- and Wt-channel production of single top-quarks are presented as well.

The mathematical description of the top-quark pair production is based on perturbative QCD calculations, in which the hard scattering process between the two colliding protons is assumed to be an interaction of their constituents called partons (quarks and gluons). These partons carry a broad distributed fraction x of the longitudinal momentum of their parent hadrons, where the probability density to observe a parton of the flavour i inside a hadron A carrying the longitudinal momentum fraction x_i is given at a fixed energy scale μ^2 by the so-called parton distribution function (PDF) $f_i^A(x_i, \mu^2)$.

The total production cross-section for top-quark pairs in the collision of the two hadrons A and B can be therefore simply computed at any centre-of-mass energy $\sqrt{s}$ by evaluating the gg, $q\bar{q}$, qg and $\bar{q}g$ production modes individually and summing their contributions:

$$\sigma^{AB\to t\bar{t}}(\sqrt{s}) = \sum_{i,j=q,\bar{q},g} \int dx_i dy_j f_i^A(x_i,\mu^2) f_j^B(x_j,\mu^2) \hat{\sigma}^{ij\to t\bar{t}}(\hat{s},\mu^2) \tag{2.3}$$

Here $\hat{s} = x_i x_j s$ denotes the squared effective centre-of-mass energy of the interacting partons, which has to be at least twice the top-quark mass m_t, in order to produce top-quark pairs. At those $\hat{s}$ values the $t\bar{t}$ production is strongly dominated by gluon-gluon fusion, while the quark-antiquark annihilation becomes more important for larger values of the effective centre-of-mass energy. The distribution of the momentum densities for gluon, u, $\bar{u}$, d, $\bar{d}$ and b quarks contained in a proton are shown as a function of their longitudinal momentum fraction x in Figure 2.4. Presented is the parametrisation of the CT10 PDF [33] set at $\mu = 350$ GeV, which corresponds to the approximate $t\bar{t}$ production threshold.

The $t\bar{t}$ production cross-section using a top-quark mass of 172.5 GeV is calculated with the HATHOR software framework [34] at next-to-next-to-leading order (NNLO) accuracy in QCD calculations including also resummation of next-to-next-to-leading logarithmic (NNLL) soft gluon bremsstrahlung [35]. For a centre-of-mass energy of 8 TeV, these calculations lead to a value of 253^{+13}_{-15} pb [28]. A precise knowledge of this quantity is not only important for testing the Standard Model, but it is also needed to probe for new physics, as for example a resonant production of top-quark pairs would lead to an enhancement of the total production cross-section.

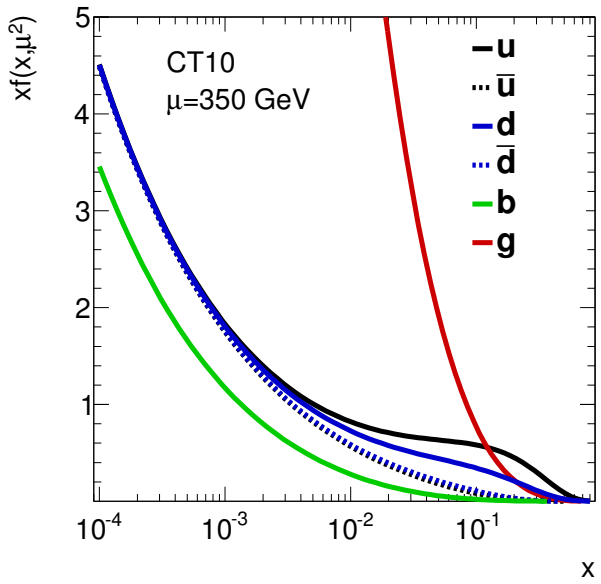

Figure 2.4: Momentum densities of the gluon and the u, $\bar{u}$, d, $\bar{d}$ and b quarks in the proton as a function of their longitudinal momentum fraction x with respect to the proton. Shown is the CT10 parametrisation [33] at the approximate $t\bar{t}$ production threshold $\mu = 350$ GeV.

2.2.2 Resonant top-quark pair production

As the top-quark is the heaviest of all known elementary particles, it is assumed to play an important role in many beyond the Standard Model theories. Several of such Standard Model extensions predict the existence of new heavy gauge bosons that predominantly decay to top-quark pairs. These additional, resonant and non-QCD based production modes can lead to peaks in the invariant $t\bar{t}$ mass spectrum, if the width of the new resonance is narrow enough. Examples for possible BSM theories that predict new heavy particles decaying into top-quark pairs are topcolour models [2], extra dimensions [3] and Two-Higgs-Doublet models (2HDMs)

[6], which are briefly summarised in the following section, while the potential to search for the resulting $t\bar{t}$ resonances is discussed extensively in Reference [36]. More technical details about the simulation (including the choice of the relevant parameters) of these BSM signals are given in Section 5.3.1.

Topcolour

Several theories connect directly the top-quark and its large mass with the dynamics of electroweak symmetry breaking (EWSB). Examples are the so-called topcolour models [37], which introduce a new strong gauge coupling, a $t\bar{t}$ condensate and explain in addition the scale of the top-quark mass. These models require a minimal extension of the SM such that strong interactions are described e.g. by a $SU(3)_1 \otimes SU(3)_2$ symmetry group, which is dynamically broken down to the well know $SU(3)_c$ of the QCD at a scale $\sim$ 1 TeV.

One of the possible topcolour scenarios (Model IV of [38]) causes a heavy Z' boson that couples preferable to quarks from the third generation, while it has no significant coupling to leptons. Thus it is referred to as leptophobic or topophyllic. The predicted Z' production cross-section of such a model is large enough to be discovered by the LHC experiments for resonance masses extending to several TeV[1].

Extra dimension

One approach to formulate gravity as a consistent quantum field theory and therefore include it into the Standard Model of particle physics is by introducing additional spatial dimensions, each being compactified at a well-defined energy scale. Within these extra dimensions, the gravitational interactions mediated by a Spin-2 particle, the graviton, could be as important as the SM interactions. The advantage of such models is that they incorporate a Grand Unification of all couplings, introduce dark matter candidates and give a solution to the so-called hierarchy problem, the large scale difference between the strength of weak and gravitational interactions [39].

Lisa Randall and Raman Sundrum suggested a model with one warped extra dimension detectable at the TeV scale. Scenarios of this model, in which the SM fields are allowed to propagate into the extra dimension, predict the existence of so-called Kaluza-Klein (KK) excitations for each SM particle [3]. The most promising candidate for (KK) excitations that might be observable at the LHC is the KK gluon, as KK fermions can only be produced in pairs and have therefore smaller production rates. Also the (KK) graviton, a colourless spin-2 resonance, itself could be experimental accessible [40].

Two-Higgs-Doublet models

The Higgs sector in the SM has been chosen such that it is as simple as possible. But indeed there is no theoretical restriction to the number of Higgs fields involved in the process of electroweak symmetry breaking and generation of particle masses. One of the most simplest extensions is provided by the so-called Two-Higgs-Doublet models [6], which introduce a second Higgs doublet into the Brout-Englert-Higgs-mechanism.

Such an extension could also be motivated by the fact that it provides a source for CP violation of sufficient size that would explain the baryon asymmetry of the universe [41]. Another

[1] Models in which the couplings of the Z' are analogous to that of the SM Z-boson are much more likely to be observed in the di-muon mass spectrum. Thus scenarios providing a significant branching ratio for decays into leptons are typically not considered in the search for $t\bar{t}$ resonances.

consequence of the 2HDMs is the existence of further scalar (CP-even) and pseudoscalar (CP-odd) Higgs-bosons. In total, two electrically charged scalars $H^{\pm}$, two neutral scalars h and H and one pseudoscalar A would emerge from the process of electroweak symmetry breaking.

While the light scalar h could be identified with the particle that was discovered in 2012 at a mass of 125.3 GeV, the mass of the second neutral scalar could extend to the TeV scale. Assuming the couplings of this heavy Higgs-boson to be SM-like, decays into top-quark pairs could have a significant branching ratio. Beside the masses of the five Higgs-bosons, such models have further free parameters of which in particular

$$\tan\beta = \frac{v_2}{v_1} \,, \tag{2.4}$$

where v_1 and v_2 are the vacuum expectation values corresponding to the two Higgs doublets and the angle α, which characterises the mixing between the two CP-even neutral scalars, are of great importance. These two parameters control the coupling strength between the Higgs-bosons and the SM particles and thus also the corresponding production cross-sections and branching ratios. In particular, the case $\cos(\beta - \alpha) = 0$, in which the lighter CP-even scalar h has the same couplings as the Higgs-boson of the Standard Model, is of great interest.

2.2.3 Top-quark decay

Top-quarks decay via the weak interaction into a W-boson and a down-type quark. The predominant decay channel is $t \to bW$ as the decays $t \to sW$ and $t \to dW$ are strongly suppressed by the size of their CKM matrix elements. The predicted branching ratios for these three decay modes are approximately 99.89%, 0.1% and 0.01% respectively.

Given the fact that the top-quark almost exclusively decays to a bottom-quark and a W-boson, a further classification depending on the decay mode of the associated W-boson is meaningful. The W-bosons can decay into a lepton pair from all three generations or into a quark pair from the first two generations, with three possible colour states each. As the sum of masses of the third generation quarks exceed the W-boson mass, the decay $W \to t\bar{b}$ is strongly suppressed. Due to the fermion universality in electroweak interactions, the W-boson decay occurs in lowest order in $1/3$ of the time into a lepton neutrino pair and in $2/3$ of the time into a pair of quarks. Thus the decay of a top-quark pair can be subdivided into three different channels: The all-hadronic channel ($t\bar{t} \to W^+bW^-\bar{b} \to q\bar{q}bq'\bar{q}'\bar{b}$), in which both W-bosons decay into quarks. This channel is the dominant decay mode (45.7%), but suffers from a large background contamination due to the production of QCD mutijet events. A slightly lower branching ratio (43.8%) and a significant lower background rate is associated to the single-lepton channel ($t\bar{t} \to W^+bW^-\bar{b} \to \ell\bar{\nu}_l bq\bar{q}\bar{b} + \bar{\ell}\nu_l bq\bar{q}\bar{b}$), while the dilepton channel ($t\bar{t} \to W^+bW^-\bar{b} \to \ell\bar{\nu}_\ell b\bar{\ell}\nu_\ell\bar{b}$) has the lowest expected background contamination but also the lowest branching ratio (10.5%). The branching ratios stated above take not yet into account that τ-leptons themself can either decay into a leptonic or hadronic final state, such that top-quarks for example decaying via the chain $t \to Wb \to \tau\bar{\nu}_\tau b \to q\bar{q}\bar{\nu}_\tau b$ will (in the following studies) be considered as hadronic as well.

Chapter 3

Experimental setup

The studies presented in this thesis are based on measurements of ATLAS (**A** **T**orodial **L**HC **A**pparatu**S**) [42], which is one of the two major multi-purpose particle detectors at the Large Hadron Collider (LHC) that records data from high energetic proton-proton collisions. These interactions take place at centre-of-mass energies never reached before by any of the previous collider experiments. Therefore, they provide the opportunity to test the Standard Model of particle physics at new energy regimes and enable the search for new heavy particles. Its greatest success so far was the discovery of the Higgs-boson in the year 2012 [21, 43].

The following Section summarises the experimental setups of the LHC and in particular of the ATLAS detector used in the data taking periods during 2012. This overview is needed in order to better discuss the results presented in Chapters 6, 7, 8 and 9, respectively. A more detailed presentation of the LHC and its experiments can be found in References [1, 44].

3.1 The Large Hadron Collider

The LHC is the most recent section in the accelerator complex of the European Organisation for Nuclear Research (CERN) located near Geneva, Switzerland. It was constructed between 2003 and 2008 into the tunnel of the former Large Electron Positron (LEP) ring accelerator, which lies between 45 m and 170 m below the surface on a plane with an inclination of 1.4%. Two separated 26.7 km long rings are used to accelerate two proton (or heavy ion) beams, containing up to $3 \cdot 10^{11}$ particles, in opposite direction and bring them to collision at four different interaction points.

The LHC is designed to collide either proton beams with centre-of-mass energies up to 14 TeV or heavy ions (Pb) with energies up to 2.8 TeV per nucleon. Before the particle beams are injected into the LHC rings, they are pre-accelerated by former accelerator facilities. The first stage of acceleration is done by a linear accelerator (LINAC), which brings the proton beams to an energy of 50 MeV. The following stages include the Booster, the Proton Synchrotron (PS) and the Super Proton Synchrotron (SPS), which accelerate the beams to 1.4 GeV, 25 GeV and 450 GeV, respectively.

The acceleration of the injected particle beams in the LHC is realised by using a 400 MHz superconducting niobium sputtered cavity system, which is designed to operate at a temperature of 4.5 K and a voltage of 16 MV.

In order to keep the particle beams on the nominal track, the LHC is equipped with high-field superconducting NbTi dipole, quadrupole and higher-order magnets that are operated in superfluid helium at a temperature of 1.9 K. Using a current of approximately 1200 A, these magnets provide field strengths up to 8.33 T. In total, 1232 dipole magnets with a length of 15 m each are used at the LHC to bend the particle beams around the arcs of the ring, while 392 quadrupole magnets with a length between 5 m and 7 m are used to focus them.

Beside the centre-of-mass energy $\sqrt{s}$ a further quantity, called luminosity L, is of great importance to characterise the performance of a particle accelerator. Assuming the beams collided by the accelerator to have a Gaussian shape in space, the machine luminosity is defined as

$$L = \frac{N_\mathrm{b} n_1 n_2 f_\mathrm{rev} \gamma_\mathrm{r}}{4\pi\varepsilon_\mathrm{n}\beta^*} F \ , \tag{3.1}$$

where n_1 and n_2 are the number of particles within the two colliding beams, while f_rev the revolution frequency, γ_r the relativistic gamma factor, ε_n the normalised transverse beam emittance, β^* the beta function at the collision point and F a geometric luminosity reduction factor, which depends on the beam crossing angle at the interaction point [1]. The machine luminosity of an accelerator is directly connected to the number of events of a certain process type generated in the provided particle collisions:

$$N = \mathcal{L} \cdot \sigma_\mathrm{process} \ , \tag{3.2}$$

in which σ_process is the production cross-section of the process under study, while $\mathcal{L} = \int L dt$ is the luminosity provided by the accelerator over a certain period of time. The LHC has four large experiments. The multipurpose detectors, ATLAS and CMS [45], aim both for a peak luminosity of about $10^{34}\,\mathrm{cm}^{-2}\,\mathrm{s}^{-1}$ during the pp collisions, while LHCb [46] aims for a luminosity of $10^{32} cm^{-2}\,\mathrm{s}^{-1}$. A dedicated heavy ion experiment, ALICE [47], aims at a peak luminosity of $10^{27}\,\mathrm{cm}^{-2}\,\mathrm{s}^{-1}$ for the nominal operation with lead-lead collisions. The high beam intensities required to reach luminosities up to $10^{34}\,\mathrm{cm}^{-2}\,\mathrm{s}^{-1}$ excludes the use of anti-particle beams and thus also the use of a common vacuum and magnet system for both circulating beams, as it was realised in the Tevatron accelerator complex. Therefore the LHC was designed to have separated magnetic fields and vacuum chambers in both rings, in order to store and accelerate the two counter-rotating proton beams. Figure 3.1 visualises the positions of these four experiments relative to the accelerator complex and to each other.
While the ATLAS and CMS detectors are designed to explore a broad spectrum of TeV scale physics processes that are predicted to occur in the pp interactions, the two experiments ALICE and LHCb are more dedicated devices. LHCb is optimised to investigate rare B-Meson decays in order to search for new physics appearing in the B sector and to explore the process of CP-violation extensively. The ALICE experiment is specialised to study the quark-gluon plasma resulting from the high energetic heavy ion collisions provided by the LHC in order to gain a better understanding of certain key aspects of Quantum Chromodynamics, such as the colour confinement. Beside these major detectors, three smaller experiments MoEDAL [50], TOTEM [51] and LHCf [52] are placed at the LHC as well. The prime motivation of MoEDAL is to directly search for magnetic monopoles, the dyon and other highly ionising stable (or pseudo-stable) massive particles produced in the pp collisions at the LHC. While TOTEM is dedicated to precisely measure the proton-proton interaction cross-section, LHCf is aimed to study the forward production of neutral particles at extremely low angles.

3.1.1 Operation of the LHC

Originally it was planned to operate the LHC in its first years at a centre-of-mass energy of 10 TeV, but due to a severe incident, which occurred on the 19th of September 2008 [53], the first collisions had to be postponed and the beam energy was reduced. On the 30th of March 2010, pp collisions were finally initiated at a centre-of-mass energy of 7 TeV for the first time and therefore the LHC experiments were able to start their research programs. The operation with two proton beams in 2010 was continued until the 4th of November. During this period the

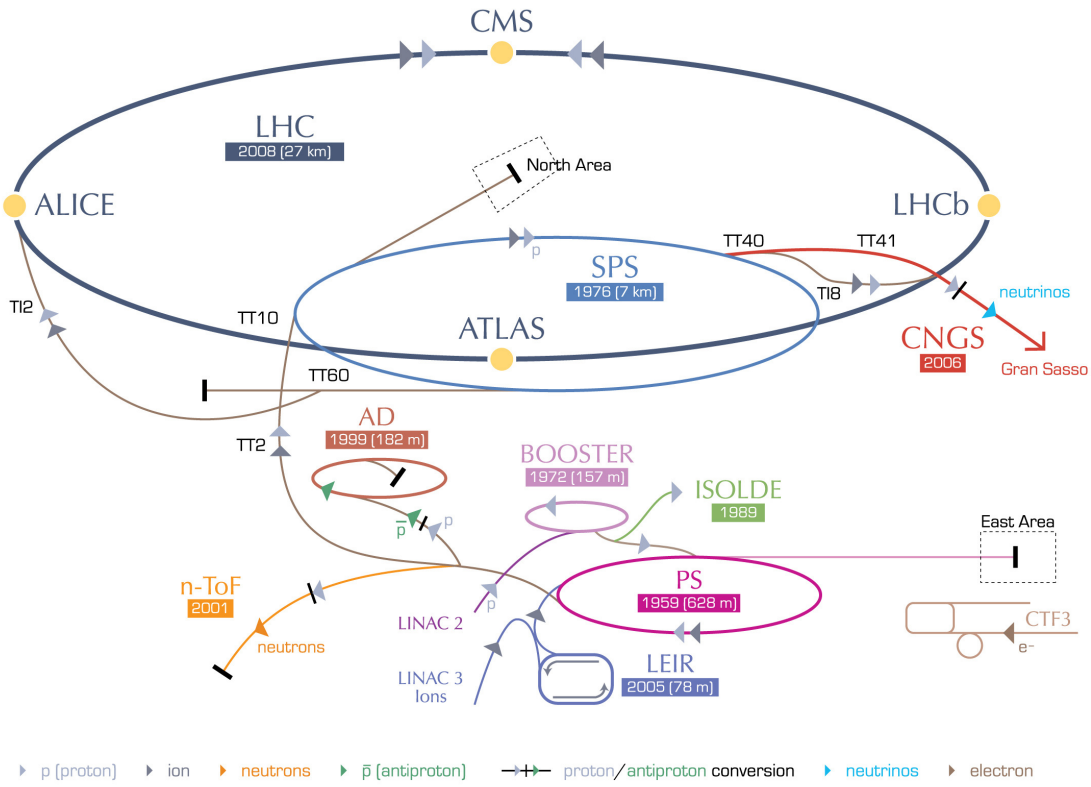

Figure 3.1: Schematic view of the CERN accelerator complex including the LHC and its pre-accelerator infrastructure as well as further accelerators (e.g. ISOLDE [48]) used for a variety of different collider experiments [49].

ATLAS detector recorded an integrated luminosity [54] of $45.0 \pm 1.5\,\text{pb}^{-1}$. After a short period of 29 days with lead-lead collisions, the LHC was shut down again for the 2011 run preparations. In the 2011 run, the LHC provided again pp collisions with a centre-of-mass energy of 7 TeV but with a substantially increased machine luminosity. Thus ATLAS was able to collect data corresponding to an integrated luminosity of $5.3 \pm 0.2\,\text{fb}^{-1}$ (see Figure 3.2 (a)) for the period between the 13th of March and the 30th of October. The 2011 run of the LHC was completed again by a short period of lead-lead collisions followed by the winter shutdown, during which the machine was prepared to provide an increase of the beam energy from $\sqrt{s} = 3.5$ TeV to $\sqrt{s} = 4$ TeV. First collisions with stable proton beams at a centre-of-mass energy of $\sqrt{s} = 8$ TeV were delivered to the experiments at the 5th of April 2012. The operation with this setup lasted until the 17th of December 2012. During this period, the ATLAS detector recorded in total an integrated luminosity of $21.7 \pm 0.6\,\text{fb}^{-1}$ (see Figure 3.2 (b)). The so-called Run I of the LHC was concluded with collisions between protons and lead ions occurring in the period of time between the 20th of January and the 11th of February 2013. Currently the whole accelerator facility is in preparation for the next round of pp collisions, which is supposed to start again in June 2015 at a centre-of-mass energy of $\sqrt{s} = 13$ TeV and a substantially increased machine luminosity.

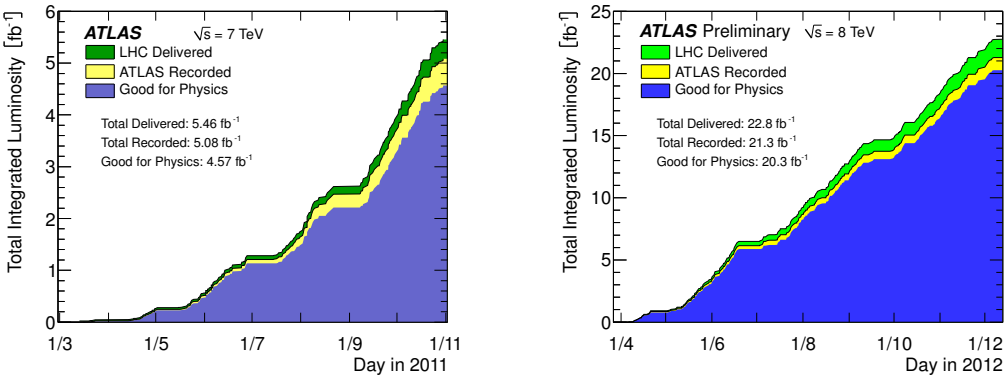

(a) Cumulative integrated luminosity (2011)

(b) Cumulative integrated luminosity (2012)

Figure 3.2: Cumulative integrated luminosity delivered by the LHC (in green) and recorded by the ATLAS detector (in yellow) during the operation with stable proton beams as a function of time. The corresponding centre-of-mass energy of the 2011 (a) and 2012 (b) runs of the LHC were 7 TeV and 8 TeV, respectively. In addition, also the cumulative luminosity is shown as a function of time that correspond to the case that all ATLAS sub-detectors were fully operational (in blue). This dataset is referred to as "Good for Physics".

3.2 The ATLAS experiment

The ATLAS detector [42] has a cylindrical forward-backward symmetric geometry and a close to 4π coverage of the solid-angle. It has a length of 46 m, a diameter of 25 m and weighs about 7000 t. Close to the interaction region (at the center of the detector) the Inner Detector is located, which has the purpose to measure the momenta of all charged particles. This sub-detector is embedded in a barrel shaped solenoid magnet that provides a field strength of up to 2 T. Energies of electromagnetic and hadronic particle showers are measured with the so-called Liquid-Argon (LAr) and Tile calorimeters, which surround the solenoid. The outermost part of the detector is formed by the Muon Spectrometer (MS), which is located within the large superconducting air-core coils of a toroid magnet. The overall layout of the ATLAS detector is displayed schematically in Figure 3.3. Approximately 3000 physicists from more than 177 universities and laboratories distributed over 38 countries worldwide collaborate to operate the ATLAS detector and to analyse the data collected with it.

3.2.1 Coordinate system

In the right-handed ATLAS-coordinate system the z-axis is defined parallel to the beam pipe, while the positive x- and y-axis pointing to the center of the LHC and upwards respectively. The origin is at the nominal interaction point in the center of the detector. A space point within this system is described using spherical coordinates. Thus Φ is the azimuthal angle in the x-y-plane, whereas θ denotes the polar angle between the z-axis and a particle trajectory. Both angles are measured in the range $[-\pi, +\pi]$ and increase clockwise. The pseudorapidity, defined as

$$\eta = -\ln\left[\tan\left(\frac{\theta}{2}\right)\right] , \tag{3.3}$$

is used in the following instead of θ. Transverse momentum and energy are defined in the x-y-plane as $p_{\mathrm{T}} = p \cdot \sin\theta$ and $E_{\mathrm{T}} = E \cdot \sin\theta$, respectively. The angular separation ΔR between the two objects i and j, reconstructed in the detector, is defined as

$$\Delta R = \sqrt{\Delta\eta_{ij}^2 + \Delta\phi_{ij}^2} \,. \tag{3.4}$$

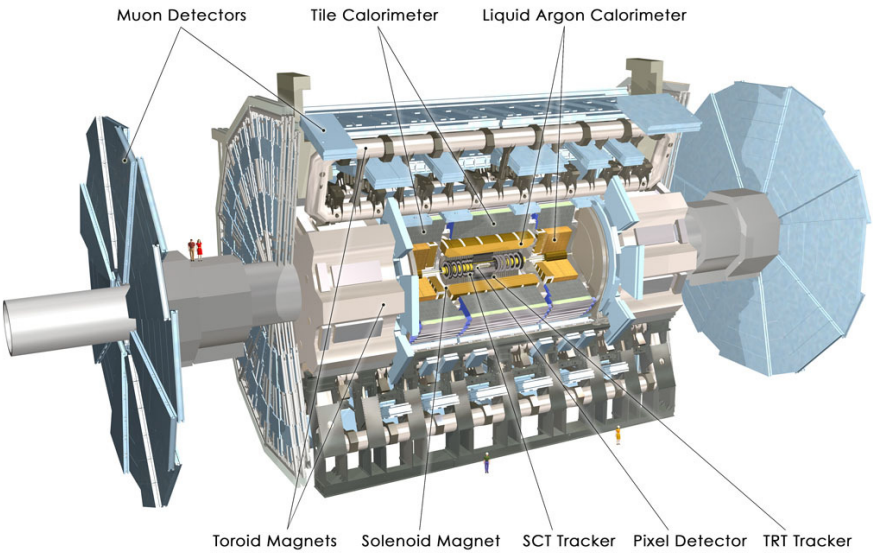

Figure 3.3: Computer generated image of the whole ATLAS detector showing and labelling the several subdetector components. [55]. | ATLAS Experiment © 2014 CERN

3.2.2 Inner Detector

The Inner Detector (ID) of the ATLAS experiment is a high granularity tracking device consisting of three different types of independent but complementary subdetectors, which are dedicated to perform measurements that allow to trace the trajectories of charged particles (called tracks), determine precisely their momenta and locate the approximate decay position of heavy and unstable particles (called secondary vertices). Each of these subdetectors provide a number of space points that correspond to the interaction of a charged particle with the detector material. These so-called hits along the particle flight path are used for the purpose of track reconstruction.

The innermost of the three detector components, the Pixel Detector, is based on silicon semiconductor pixel sensors of the size $50 \times 400\,\mu\mathrm{m}^2$ (in R-ϕ $\times z$), which are arranged on three concentric cylinders around the beam axis in the barrel region and on three disks perpendicular to the beam axis in the end-caps. With this layout intrinsic accuracies of up to $10\,\mu$m in R-ϕ and $115\,\mu$m in the z direction are obtained. This high resolution is in particular important for the identification of b-hadrons. Next to the Pixel Detector, the Semiconductor Tracker (SCT) is installed, which comprises four cylindrical double-layers of silicon based microstrip sensors around the beam axis and nine layers in each of the end-caps. These double-layered sensors consist of two 6.4 cm long strips that are shifted by an angle of 40 mrad to each other, in order to measure both the R-ϕ and z direction of a charged particle crossing the Inner Detector. The corresponding intrinsic accuracy is $17\,\mu$m and $580\,\mu$m in the R-ϕ and z direction, respectively.

The Transition Radiation Tracker (TRT) is the most outer part of the Inner Detector. It is built from straw tube detectors (proportional counters) filled with a gas mixture of 70% Xe, 27% CO_2 and 3% O_2 with 5-10 mbar over-pressure. The straws are arranged parallel to the beam axis in the barrel region and radially in the end-caps. Each tube has a diameter of 4 mm, a length of 144 cm (in the barrel) or 37 cm (in the end-caps) and contains a 31 μm diameter tungsten anode wire operated with a high voltage of about 1530 V in order to measure the drift time of electrons resulting from the ionisation of the gas mixture. Measurements of the TRT provide spatial information in R-ϕ with an accuracy of 130 μm.

In addition to its contribution to the track reconstruction, the TRT is also used to identify electrons. For this purpose the straw tube walls consist of several thin layers made from different materials. If charged particles pass the borders of these walls characteristic radiation (called transition radiation) is emitted, depending on the relativistic γ factor of the particle. Thus electrons can be distinguished from pions of the same momentum due to their smaller mass.

Figure 3.4 demonstrates the arrangement of the various Inner Detector components in the barrel region of the ATLAS detector and their distance from the beam axis. Both the Pixel Detector and the SCT provide a full coverage up to a pseudorapidity of $|\eta| < 2.5$, while the TRT enhances the momentum resolution and the electron identification in the region $|\eta| < 2.0$. The ID is surrounded by a superconducting solenoid magnet that provides an axial field with a strength up to 2 T. Thus charged particles passing the Inner Detector are deflected, which allows for the measurement of their momenta due to the curvature of the resulting track. The design goal of the Inner Detector in terms of track momentum resolution is

$$\frac{\sigma_{p_\mathrm{T}}}{p_\mathrm{T}} = 0,05\% \cdot p_\mathrm{T} \oplus 1\% \ ,$$

where $\oplus$ denotes an addition in quadrature.

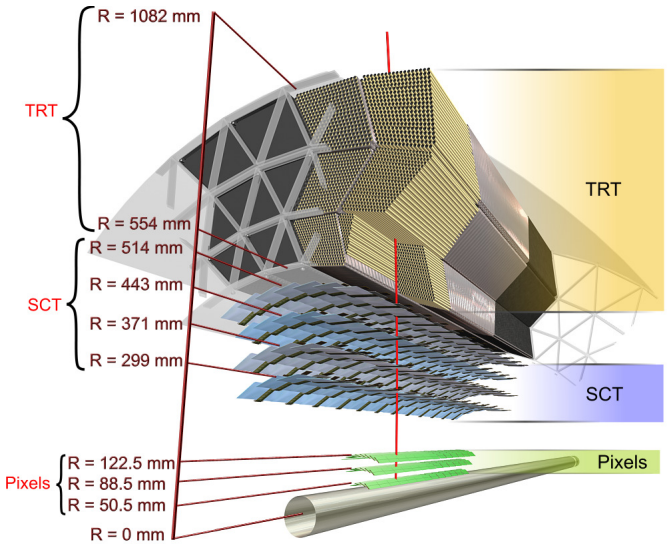

Figure 3.4: A schematic illustration of the sensors and structural elements alignment in the barrel region of the Inner Detector of the ATLAS experiment including the beryllium beam-pipe, the three cylindrical silicon-pixel layers, the four cylindrical double layers of the silicon-microstrip sensors (SCT) and the 72 straw tube layers of the Transition Radiation Tracker [56]. | ATLAS Experiment © 2014 CERN

3.2.3 Calorimeter system

The calorimeter system of the ATLAS detector serves the purpose of measuring the total energy of electrons, photons, and hadrons produced in the particle collisions that are provided by the LHC. Over a pseudorapidity range of $|\eta| < 4.9$, different calorimeter types are used to satisfy the widely varying requirements of the studied physics processes and the expected radiation environments being present in the various η regions. The fine granularity of the electromagnetic calorimeter, in the η region matched to the Inner Detector, is adapted to measure the energies of electrons and photons with high precision, while the coarser granularity of the rest of the calorimeter is sufficient to satisfy the demands of jet reconstruction [42]. Furthermore the calorimeter system operates as a shielding for the Muon Spectrometer by providing good containment of electromagnetic and hadronic particle showers in order to minimise punch-throughs by particles other than muons into the muon system.

The EM calorimeter provides a radiation lengths larger than 22 X_0 in the barrel region and larger than 24 X_0 in the end-caps, while the interaction lengths in the hadronic calorimeter is approximately 9.7 λ in the barrel and 10 λ in the end-caps. Both the radiation length and the interaction length are matter specific quantities. While X_0 defines the mean distance over which the energy of an electron is reduced by bremsstrahlung to $1/e$ of its initial value, λ describes similarly the energy loss of hadrons in matter due to nuclear interactions.

The so-called sampling technique is used for all the electromagnetic and the hadronic calorimeter components, which means that the absorber, the part that induces the particle showers, and the active material, the part that measures the deposited energies, alternate. Figure 3.5 presents a schematic view of the whole ATLAS calorimeter system. The EM calorimeter is based on the use of liquid argon as the active material including accordion-shaped electrodes and lead as the absorber. Due to the accordion geometry a complete and homogeneous coverage of the azimuthal angle Φ is provided.

In the barrel region the calorimeter consists of two identical half-barrels in the range $|\eta| < 1.475$, which are separated by a 4 mm small gap at $z = 0$. The end-cap calorimeters are mechanically divided into two coaxial wheels that cover the regions $1.375 < |\eta| < 2.5$ and $2.5 < |\eta| < 3.2$, respectively. Each calorimeter component consists of several layers of varying depth and granularity. The EM calorimeter of the ATLAS detector is designed to provide energy measurements with an approximate resolution of

$$\frac{\sigma_E}{E} = \frac{10\%}{\sqrt{E}} \oplus 0.7\% \ .$$

As the regions between the barrel and end-cap calorimeters ($1.37 < |\eta| < 1.52$) contain services and cables for the Inner Detector and the barrel EM calorimeter, the energy resolution is substantially degrade in this pseudorapidity range of the detector, even though special scintillators are used to partially recover the energy loss in the inactive material.

The hadronic calorimeter system includes three different subdetectors. In the most central part, directly outside the EM calorimeter envelope, is the tile calorimeter consisting of a barrel in the region $|\eta| < 1.0$ and of two identical extended barrels in $0.8 < |\eta| < 1.7$. These components use steel as the absorber and scintillating plastic plates (tiles) as the active material, which are read out by photomultiplier tubes. The tile calorimeter has in total a segmentation of three layers with a granularity of $\Delta\eta \times \Delta\phi = 0.1 \times 0.1$ in the first two layers and 0.2×0.1 in the last. Larger pseudorapidities are covered by the Hadronic End-Cap Calorimeter (HEC), which is directly located behind the end-caps of the electromagnetic calorimeter in the range $1.5 < |\eta| < 3.2$, and the Forward Calorimeter (FCal), which is placed in the region $3.1 < |\eta| < 4.9$. Both calorimeter

types use liquid argon as the active material, while the used absorbers are different. The design goal for energy measurements with the hadronic tile and forward calorimeters are

$$\frac{\sigma_E}{E} = \frac{50\%}{\sqrt{E}} \oplus 3\% \quad \text{and} \quad \frac{\sigma_E}{E} = \frac{100\%}{\sqrt{E}} \oplus 10\% \,,$$

respectively. Detailed information about the main parameters of the calorimeter system such as the granularity as a function of η or the number of readout channels can be found in Reference [42], while information about the performance of the several calorimeter components can be found in [44, 57].

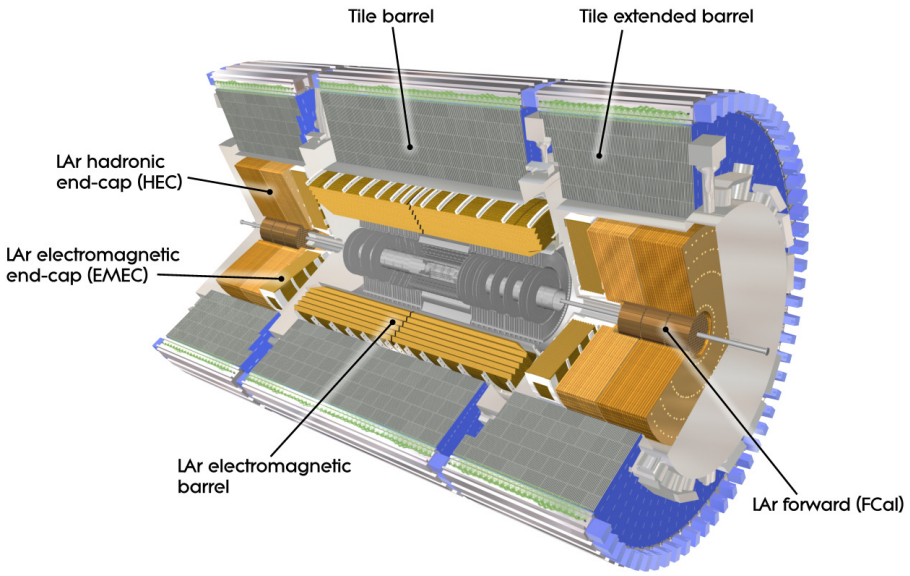

Figure 3.5: Cut-away view of the whole ATLAS calorimeter system [42]. | ATLAS Experiment © 2014 CERN

3.2.4 Muon Spectrometer

As muons are minimum ionising particles, they usually pass the whole calorimeter system without depositing a substantially fraction of their kinetic energy in the detector material. Thus a precise measurement of the muon kinematics is not possible using the electromagnetic or hadronic calorimeter. For this purpose the outermost part of the ATLAS detector is equipped with a variety of gaseous detectors, in which the reconstruction of muons and the measurement of their properties is based on the deflection of a candidate track in the magnetic field provided by the large superconducting air-core toroid magnets that surround the Muon Spectrometer [42]. The field strengths provided for this purpose reach 0.5 T in the barrel region and 1 T in the end-caps.

The muon system is instrumented with four different detector technologies, which serve either the purpose of high precision tracking or triggering. For the measurement of the track coordinates in the bending plane of the magnetic field both Monitored Drift Tubes (MDT) and Cathode Strip Chambers (CSC) are used, while trigger information is provided by Resistive Plate Chambers (RPC) and Thin Gap Chambers (TGC), as they provide an excellent time resolution of 1.5 ns and 4 ns, respectively.

Each MDT has a diameter of approximately 30 mm and is operated with a mixture of 93% Ar and 7% CO_2 gas at 3 bar. Electrons that result from the ionisation of this gas mixture are collected at a central gold-plated tungsten-rhenium wire using a potential of 3080 V. With this approach an average spatial resolutions of 80 μm per tube is reached, while the maximum drift time is of the order of 700 ns. Single tubes are combined in layers of three to eight (depending on the corresponding pseudorapidity region) in order to form MDT chambers which are mounted in three cylindrically layers around the beam axis and also in three layers as planes perpendicular to the beam. The MDT chambers provide a full coverage of the range $|\eta| < 2.7$, with the exception of a small gap in the center of the detector at $|\eta| \approx 0$ to allow for services to the solenoid magnet, the calorimeters and the Inner Detector. Also, the innermost layer in the forward region ($2.0 < |\eta| < 2.7$) is not covered by MDT chambers, but instead with Cathode Strip Chambers due to their higher rate capability and time resolution. These components are multiwire proportional chambers that provide a simultaneous measurement of both track coordinates with a spatial resolution of 40μ m in the bending plane and about 5 mm in the transverse plane. Similar to the drift tubes a mixture of 80% Ar and 20% CO_2 gas is used for the operation of the CSCs.

The Muon Spectrometer is complemented by Resistive Plate Chambers in the barrel region ($|\eta| < 1.05$) and Thin Gap Chambers in the end-caps ($1.05 < |\eta| < 2.4$). These components are used to obtain both a reliable identification of the beam-crossing and a measurement of the candidate tracks' azimuthal angle ϕ, which is the coordinate in the direction perpendicular to the bending plane. The RPCs are gaseous detectors, made of phenolic-melaminic plastic laminate, that contain parallel plates as electrodes. An electric field of 4.9 kV/mm between the plates, which are arranged with distances of 2 mm to each other, allow the forming of avalanches along the trajectory of an ionising particle towards the anode. The readout of the signal is realised by a capacitive coupling to metallic strips, which are installed on the outer faces of the resistive plates. The gas contained in this chambers are a mixture of 94.7% $C_2H_2F_4$, 5.0% Iso $- C_4H_{10}$ and 0.3% SF_6. The TGCs are multi-wire proportional chambers, in which the wire-to-cathode distance of 1.4 mm is smaller than the wire-to-wire distance of 1.8 mm and a mixture of CO_2 and C_5H_{12} gas is used for their operation. For muons with a transverse momentum of 1 TeV the measurements of the spectrometer are expected to provide a momentum resolution of

$$\frac{\sigma_{p_T}}{p_T} = 10\% \, . \tag{3.5}$$

3.2.5 Forward detectors

Beside the previously described subdetectors, ATLAS includes also a system of three smaller detectors in the very forward region. Two of these serve the purpose of determining the luminosity delivered by the LHC, while the third system is needed in order to measure the centrality of heavy-ion collisions. At a distance of ±17 m to the interaction point lies the LUCID (LUminosity measurement using Cerenkov Integrating Detector) detector, which is the main online instantaneous luminosity monitoring device of ATLAS. It consists of an array of twenty aluminium tubes filled with C_4F_{10} gas at a constant pressure of $1.2 - 1.4$ bar. Particles passing these tubes produce Cherenkov light, which is detected by photomultipliers. The resulting signal amplitudes are used to extrapolate to the number of particles per tube.

The second system is the Zero-Degree Calorimeter (ZDC), which is located at a distance of ±140 m relative to the interaction point. Its primary goal is to detect the number of very forward neutrons stemming from heavy-ion collisions as this quantity is strongly correlated with the centrality of such a collision.

The outermost component of the forward detector system is placed at a distance of ±240 m and aims to determine the absolute luminosity provided by the LHC, as it measures elastically scattered protons at very small angles based on scintillating-fibre trackers housed inside Roman pots. The corresponding detector is referred to as ALFA (Absolute Luminosity For ATLAS).

3.2.6 Magnet system and magnetic field

The alignment of the whole magnet system of the ATLAS detector is displayed schematically in Figure 3.6. It consists of one solenoid and three toroids (one barrel and two end-caps) and provides a field that covers a volume of approximately $12,000\,\mathrm{m}^3$ (defined as the region in which the field strength exceeds a value of 50 mT). The solenoid is aligned to the beam axis and provides an axial magnetic field with a strength of 2 T for the Inner Detector. Its axial length is 5.8 m, while its inner and outer diameters are 2.46 m and 2.56 m, respectively. In total the toroid magnet contains 24 coils, which produce a toroidal magnetic field of approximately 0.5 T for the muon detectors located in the barrel region and approximately 1 T for those in the end-caps.

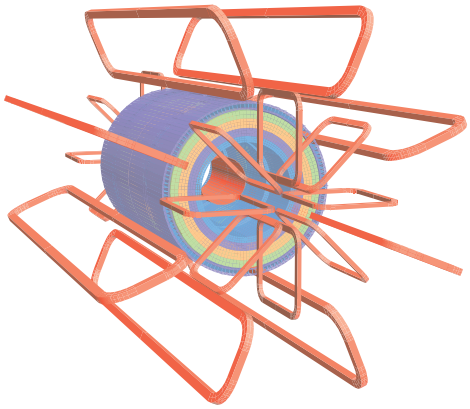

Figure 3.6: Schematic view of the geometry of the ATLAS magnet system showing the solenoid magnet and the eight coils of each the barrel and end-cap toroids. The solenoid winding is contained inside the calorimeter volume. For the sake of visibility the forward shielding disk is not displayed [42]. The whole magnet system is based on $NbTi/Cu$ conductors. | ATLAS Experiment © 2014 CERN

3.2.7 Trigger and data acquisition system

At the design luminosity of $10^{34}\,\mathrm{cm}^{-2}\,\mathrm{s}^{-1}$ the ATLAS detector systems have to face event rates of the order of 1 GHz, which exceed the maximum read-out rate of the full detector information (about 1 MHz). At the same time the production cross-section for processes containing heavy particles such as vector bosons, the top-quark, the Higgs-boson or also new particles are orders of magnitude smaller than for example soft QCD processes. Thus the collision data has to be filtered for potentially interesting events. For this purpose the ATLAS detector exploits a three-level trigger system in order to reduce the data to a manageable amount. Each trigger level refines the decisions made by the previous step and applies further quality requirements and selections criteria to the provided information. The first stage, the Level-1 (L1) trigger, is implemented in the hardware and uses a subset of detector components with reduced-granularity information to search for high-p_{T} objects such as muons, electrons, photons, jets, tau-leptons decaying into hadrons or in general for a large sum of transverse energy.

The geographical coordinates in η and ϕ of a possible candidate are associated to a so-called Region-of-Interest (RoI), which is then used to seed the Level-2 (L2) trigger. This trigger stage uses then the full granularity and precision of the detector systems corresponding to these regions. In the last trigger stage the so-called Event Filter (EF) processes the L2 output data with more sophisticated reconstruction techniques which are similar to the tools used in the ATLAS offline software. The event processing time in this step is of the order of several seconds, while the previous stages have to handle the available information in 2.5 μs (L1) and 40 ms (L2), respectively. Finally the EF decides whether an event is written to tape or not.

3.2.8 Event generation

The simulation of high energetic pp collisions, the resulting particles and the according detector response is essential to compare theoretical predictions to the measured data.

The production of top-quark pairs and their main background processes are generated in several subsequent stages. In the first step the pp collisions are simulated as a hard scattering process between the constituents (quarks and gluons) of the two incoming protons using a dedicated PDF set and by taking the formalism described in Section 2.2.1 into account. For this purpose, the matrix element corresponding to the production of top-quarks is calculated at next-to-leading order (NLO) accuracy.

Several different types of MC generators are used in the various studies of the ATLAS collaboration. Examples for generators that are dedicated to the simulation of the matrix element are POWHEG [58], MC@NLO [59], ALPGEN [60] and MADGRAPH [61], while multi-purpose generators such as PYTHIA [62, 63], HERWIG [64] or SHERPA [65] can provide a simulation of whole events (including also parton shower, fragmentation and hadronisation).

During the generation of the matrix element, kinematic variables such as masses, momenta or the spin orientation are set for the outgoing particles. These informations are stored and passed to the second step of event generation, the parton showering. At this stage the emission of gluons from colour-charged particles, involved in the matrix element generation, and photons from electrical charged particles is simulated. Both these photons and gluons split into further partons, which can then produce QED or QCD radiation themself. The parton showering is resumed until a predefined energy threshold is reached.

Figure 3.7 shows exemplary Feynman diagrams corresponding to the LO production of top-quark pairs via gluon-fusion including gluon radiation in the initial (a) and final state (b), respectively. A precise modelling of such radiation effects is of great importance as they directly influence the jet kinematics and multiplicities of the simulated $t\bar{t}$ events.Thus, initial and final state radiation (ISR and FSR) are one of the most important sources for systematic uncertainties related to measurements of the top-quark properties.

During the parton showering also the so-called underlying event, which emerges due to secondary interactions of the spectator partons of the colliding hadrons, is generated. These processes are rather soft and can not be described by perturbative QCD. Therefore, phenomenological models are used, which are tuned to data from dedicated measurements. In the next step, the hadronisation and fragmentation, colourless mesons and baryons are formed from the particles that are produced during the simulation of the matrix element and the parton showering. Subsequently, the decay of unstable particles is initiated. For these procedures the multi-purpose event generators, PYTHIA or HERWIG, are mainly used in this thesis, where both generators approach the tasks differently. The PYTHIA generator is based on the implementation of the Lund model, which splits gluons into quark pairs using the string fragmentation

approach [66], while HERWIG incorporates the cluster fragmentation model [67], which forms colourless clusters from quarks and gluons with low invariant mass and transforms them into hadrons. Independently from all these procedures, the generated events are randomly overlaid with additional inelastic pp interactions in order to model the so-called pile-up in the detector. After the generation of the matrix element, parton showering, fragmentation, underlying event and pile-up interactions, the generated events are either passed through a full simulation of the detector geometry and material distribution based on GEANT4 [68, 69], or through a fast detector simulation [70] based on simplified shower developments in the calorimeter system.

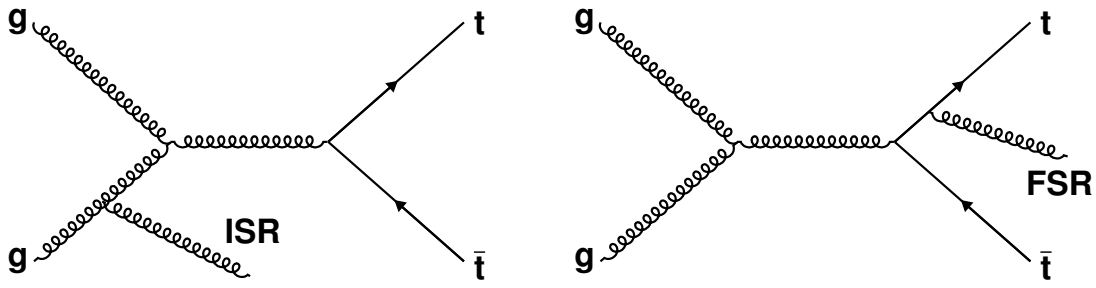

(a) Initial state radiation **(b)** Final state radiation

Figure 3.7: Examples for top-quark pair production via gluon-fusion at a leading order accuracy of the matrix element including the emission of gluon radiation in the initial (a) and final state (b).

3.3 Particle identification and reconstruction

Particles produced in the high energetic pp or lead-lead collisions provided by the LHC pass the several detector components of ATLAS and leave traces in the detector material. These signals are collected, digitalised and read out by the detector electronics and processed by the offline reconstruction software (in the case that the corresponding event is triggered). In this section the reconstruction algorithms that are used by the ATLAS collaboration to identify the physics objects typically occuring in the final state of a $t\bar{t}$ decay such as electrons, muons, jets and neutrinos are described. As the algorithms used to identify these objects rely strongly on the primary vertex, tracks and topological clusters in the calorimeter, their reconstruction procedures are described as well. The various identification techniques for jets containing b-hadrons, called b-tagging, are discussed in more detail in Section 4, while a new calibration method for b-tagging algorithms is extensively presented in Section 8.

3.3.1 Tracks and vertices

The reconstruction of a charged particle track in the Inner Detecor of ATLAS, referred to as tracking, is based on the combination of different algorithms [71]. In a first stage the so-called inside-out algorithm starts the track finding by combining space-points (hits) in the three pixel and the first SCT layers to form a track seed. These seeds are then extended by adding iteratively hits of the subsequent SCT layers to form a track candidate. This is performed by a combinatorial Kalman filter [72]. In a next step, the ambiguities in the association of hits and tracks

are resolved to reduce the fraction of tracks sharing one or more hits in the silicon detectors. Fake tracks are rejected by applying quality cuts, in which a certain number of hits in the pixel and SCT detectors are required. Further cuts limit the number of shared hits and the number of missing measurements (holes) on detector layers that are intersected by the trajectory of the fitted track, where only layers between the first and the last measurement assigned to the fit are taken into account. The track candidates passing these quality requirements are extended into the TRT, where further hits are added.

As the performance of the inside-out algorithm depends on a track seed found in the silicon detector, the trajectories of particles, which do not cause a significant number of Pixel or SCT hits, will most likely not be reconstructed. Thus the final stage of track reconstruction is based on the so-called outside-in algorithm, which searches for unused TRT segments to apply a successive back tracking into the silicon detector [71] in order to increase the tracking efficiency for e.g. tracks stemming from long-lived particles.

Primary vertex candidates are reconstructed by applying an iterative vertex finding algorithm [73] on tracks that are compatible with originating from the interaction region [74], where all tracks with $p_{\mathrm{T}} > 400$ MeV are considered. In the first step, the algorithm searches for the global maximum in the distribution of the z-positions of the selected tracks to find a vertex seed. The position of this seed and nearby tracks are then used to calculate the vertex position by applying a χ^2 fit [75] which removes iteratively tracks that are incompatible with the vertex. Tracks that are displaced by more than 7σ are used as a new vertex seed and the procedure is repeated until no further seed is found in the event. In top-quark analyses the primary-vertex candidates are required to have more than four reconstructed tracks originating from it. From all these candidates, the one with the highest p_T^2 sum of the associated tracks is chosen to be the primary vertex of the event.

Also secondary and tertiary vertices corresponding to the decay of a heavy flavour hadron contained inside a particle jet are reconstructed using the Inner Detector. A short description of the main secondary-vertex finding algorithms used in the efforts of the ATLAS collaboration is given in Section 4.2.3.

3.3.2 Topological clusters

Topological clusters are groups of adjoining calorimeter cells that are designed to follow the development of a particle shower. Their reconstruction is based on the topocluster formation algorithm [76], which is seeded with calorimeter cells, whose signal-to-noise ratio exceeds a value of $S/N = 4$. In a second step of the reconstruction procedure, the seed is combined with all neighbouring cells that have a signal-to-noise ratio above $S/N = 2$ in order to form a so-called topo-cluster. These clusters are extended by adding all adjoining calorimeter cells to it. The properties of such a cluster are reconstructed taking all included calorimeter cells into account. Thus the energy of a topo-cluster is determined from the energy sum of all its components, while its mass is defined to be zero. The calculation of its position relative to the ATLAS coordinate system is based on the weighted averages of the pseudorapidities and azimuthal angles of all associated calorimeter cells, where the absolute cell energies are used as the corresponding weights.

3.3.3 Electrons

Electrons produce, due to their electric charge, tracks in the Inner Detector and bremsstrahlung induced showers in the EM calorimeter. Thus candidates are reconstructed by matching energy deposits (clusters) in the electromagnetic calorimeter to a high-p_{T} track in the Inner Detector.

The size of the clusters is chosen to be 3×7 cells in the EM barrel and 5×5 cells in the EM end-cap regions. These clusters are restricted to a range of $|\eta^{\mathrm{cl}}| < 2.47$ excluding the transition region $1.37 < |\eta^{\mathrm{cl}}| < 1.52$ between the barrel and the end-cap of the EM calorimeter. Stringent cuts are applied on both the associated track and the shape of the cluster of energy deposits corresponding to the induced showers in order to ensure a high quality of the selected object and to reduce the background due to photon conversions, charged pions or other sources. The transverse energy E_{T} of the electron is defined by the ratio of the energy E^{cl} contained in the associated cluster to the hyperbolic cosine of the pseudorapidity η^{trk} of the reconstructed track

$$E_{\mathrm{T}} = \frac{E^{\mathrm{cl}}}{\cosh \eta^{\mathrm{trk}}} \tag{3.6}$$

and is required to be above 25 GeV for electrons used in top-quark studies. Candidates are required to be sufficiently isolated from additional hadronic activity to suppress the selection of electrons stemming from heavy-flavour decays inside jets and to reduce the amount of background corresponding to the misidentification of hadrons faking lepton signatures. In the following studies the so-called mini-isolation is used for this purpose:

$$I^{\ell}_{\mathrm{mini}} = \sum_{\Delta R(\ell,\mathrm{track_i}) < K_{\mathrm{T}}/p^{\ell}_{\mathrm{T}}}^{N^{\mathrm{tracks}}} p_{\mathrm{T}}^{\mathrm{track_i}} \tag{3.7}$$

The transverse momentum of each charged particle track that fulfills $p_{\mathrm{T}}^{\mathrm{track}} > 1$ GeV is summed if its angular separation to the electron candidate is less then $\Delta R(\ell, \mathrm{track}) < K_{\mathrm{T}}/p^{\ell}_{\mathrm{T}}$, where K_{T} is an empirical scale parameter set to 10 GeV [77]. Electrons that satisfy $I^{\ell}_{\mathrm{mini}}/p^{\ell}_{\mathrm{T}} < 0.05$ are finally considered to be isolated. This requirement is by construction looser for high-p_{T} leptons than other isolation criteria used in top-quark analyses at ATLAS, and tighter for low-p_{T} leptons. In addition, electrons stemming from pile-up vertices are rejected by requiring that the absolute value of the longitudinal impact parameter of their associated track, calculated with respect to the primary vertex candidate of the event, is smaller than 2 mm.

A more detailed description about the electron identification and reconstruction techniques and their performance in measurements with the ATLAS detector can be found in the References [78, 79]. This description includes also the exact quality requirements used to select the candidates, whereas in the following studies "tight++" electrons are used.

The quality of the trigger, reconstruction and selection efficiency modelling for electrons as well as their energy resolution and scaling are adjusted using selected $Z \rightarrow ee$ events in the data [79]. The uncertainties corresponding to these measurements are propagated into the studies presented in this thesis.

3.3.4 Muons

Tracks of muon candidates in the spectrometer are built from track segments in each of the three muon stations. For this purpose the so-called Moore algorithm [80] is used, which also extrapolates the tracks to the interaction region in order to determine the track parameters with respect to the primary vertex. Within this extrapolation both multiple scattering and energy losses in the calorimeter system are taken into account. In order to obtain an optimal momentum resolution of the muon candidates, the spectrometer track is combined with information from the Inner Detector. The χ^2_{match} of this track combination is defined as the difference between the outer (MS) and inner track (ID) vectors weighted by their combined covariance matrix

$$\chi^2_{\mathrm{match}} = (T_{\mathrm{MS}} - T_{\mathrm{ID}})^T \, (C_{\mathrm{ID}} + C_{\mathrm{MS}})^{-1} \, (T_{\mathrm{MS}} - T_{\mathrm{ID}}) \tag{3.8}$$

and provides a measure of the quality of these matching procedure. Here T denotes a vector of the ID and MS track parameters, while C corresponds to their covariance matrix [44]. The parameters of the combined muon candidate tracks are either obtained via a statistical combination of both tracks (Staco algorithm [44]) or by a partial refitting (MuId algorithm [81]). In the following studies, muons are used that were reconstructed with the latter algorithm.

The muon candidates are required to have a p_{T} above 25 GeV, at least one hit in the pixel detector, five hits in the SCT and six hits in the TRT if the track has an $|\eta|$ between 0.1 and 1.9. In addition, the combined muon candidate tracks are required to be in the region $|\eta| < 2.5$. To avoid the incorrect identification of a jets' punch-through into the muon system as a muon and to reduce the selection of muons coming from heavy flavour decays within jets, the muon candidates are required to be isolated from hadronic activity. The muon isolation is defined via the Equation 3.7, in the same way as for the electron candidates, where also $I^{\ell}_{\mathrm{mini}}/p^{\ell}_{\mathrm{T}} < 0.05$ is required. As for the electron tracks, the $|z_0|$ of the combined muon track, calculated with respect to the primary vertex, has to be smaller than 2 mm to remove muons from pile-up vertices. To further suppress the contribution of non-prompt muons the significance of the transverse track impact parameter, defined as the ratio of the transverse impact parameter to its uncertainty, has to be smaller than $d_0/\sigma_{d_0} < 3$.

The overall reconstruction efficiency [82] for muon candidates is strongly reduced around $\eta = 0$, where the spectrometer is only partially equipped with muon chambers in order to provide space for services of the Inner Detector and the calorimeters and in the region between the barrel and the end-caps ($1.1 < |\eta| < 1.3$) as the installation of several chambers in this region were incomplete during the Run I of the LHC.

The resolution and scale of the transverse muon momentum as well as the modelling of their triggering, reconstruction and selection efficiencies are adjusted to the observations in data using $Z \rightarrow \mu\mu$ events [82].

3.3.5 Jets

Jets are objects that represent the particle showers induced by a quark, an antiquark or a gluon. For the purpose of jet reconstruction several definitions exist, whereas it is important to use a definition that provides infrared and collinear safety. This means that the addition of infinite partons (infrared safety) or a parton radiated by an infinite small angle (collinear safety) should not change the number and properties of the reconstructed jets. Furthermore it should be applicable to different types of input quantities as hadron momenta, charged particle tracks or energy deposits in the calorimeter. The two most commonly used classes of jet definitions are cone-algorithms [83,84] and sequential recombination algorithms [85]. While algorithms of the first class were extensively used at the Tevatron, the LHC experiments use mainly algorithms of the latter class. The sequential recombination algorithms used in ATLAS (and also in CMS) analyses are based on the calculation of the distance

$$d_{ij} = min\left(p_{\mathrm{T},i}^{2\rho}, p_{\mathrm{T},j}^{2\rho}\right) \cdot \frac{\Delta_{ij}^2}{R^2} \tag{3.9}$$

between each pair of protojets (e.g. particle tracks or energy deposits) i and j considered in the jet clustering procedure. The quantity Δ_{ij} corresponds to the distance of these two objects in the pseudorapidity-azimuthal plane, while $p_{\mathrm{T},i}$ and $p_{\mathrm{T},j}$ are their transverse momenta. The clustering parameter R can be freely chosen in order to control the size of the reconstructed jets, whereas the parameter ρ corresponds to a predefined integer value. During the clustering procedure d_{ij} is calculated for the protojet i with respect to all other protojets in the event. If

d_{ij} is for one protojet pair i, j smaller than $p_{\mathrm{T},i}^{2\rho}$ itself, the protojets i and j are combined (by adding their four-vectors). However, if $p_{\mathrm{T},i}^{2\rho}$ is smaller than the d_{ij}, the protojet i is not used in the clustering process anymore as it is considered as a reconstructed jet.

The class of recombination algorithms is further subdivided by the choice of the parameter ρ, where the k_t algorithm [86] is defined by $\rho = 1$, the Cambridge-Aachen algorithm [87] by $\rho = 0$ and the anti-k_t algorithm [88] by $\rho = -1$. While $\rho = 1$ and $\rho = 0$ lead to an irregular shape of the jets, the case $\rho = -1$ corresponds to a cone-like shape if the distance to the nearest neighbour jet is larger than $2R$. If two jets have an angular separation smaller than $2R$, the jet with the larger transverse momentum will be conical and the other jet will only be partly conical as it misses the components associated to the jet with the higher p_{T}. This feature is caused by the fact that the anti-k_t algorithm prefers to cluster soft protojets to near hard protojets rather then to other close soft protojets (depending also on their Δ_{ij}), while the k_t algorithm tends to cluster first protojets with similar kinematic properties. Each of these variants of the sequential recombination algorithm is infrared and collinear safe. A comparison between the resulting jet shapes (i.e. the active jet areas) is shown for the k_t- and the anti-k_t algorithms in Figures 3.8 (a) and (b), respectively.

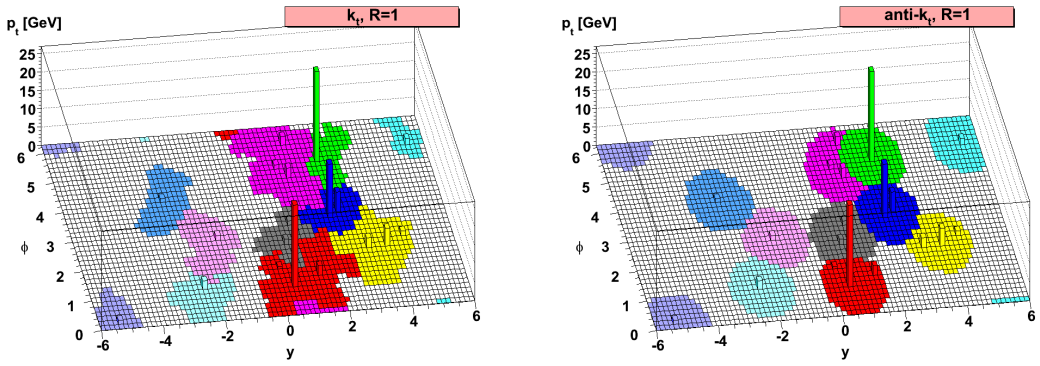

(a) k_t algorithm **(b)** anti-k_t algorithm

Figure 3.8: Shape comparison of the active jet areas for two different jet clustering algorithms. All particles within the active area of a particular jet will be clustered into this jet [88].

Due to its conical shape in isolated topologies the anti-k_t algorithm is the most frequently used jet clustering algorithm in ATLAS analyses, with the distance parameter R set to 0.4. The technical implementation of this algorithm is realised in the FASTJet package [89], which is mainly applied to topological clusters of calorimeter cells, but also tracks, reconstructed in the Inner Detector, can be used for the purpose of jet finding. As track based jets do not include the information of neutral particles, they are not suited to completely reconstruct the kinematics of a hadronic final state. Thus the use of calorimeter jets is preferred in most analysis. However, not all applications need a complete reconstruction of their final states and thus the use of track based jets can be beneficial. An example is given in Section 7, where track based jets are used for the purpose of b-tagging.

Two independent calorimeter based jet collections are used in the following studies. Their distance parameters are chosen to be $R = 0.4$ and $R = 1.0$. The topological clusters used in the reconstruction of these jets are initially determined at the electromagnetic (EM) scale, which correctly measures the energy deposited in the calorimeter by particles produced in electromagnetic showers. With the local cluster weighting method [90] these clusters are calibrated in order to

compensate for differences in the calorimeter response to electromagnetic and hadronic showers. After applying this procedure, the reconstructed jet energies are obtained at the hadronic scale (i.e. the so-called jet energy scale). In addition, the final jet properties (such as the transverse momentum) are corrected with energy and η dependent simulation-based scale factors [90, 91] to compensate for the effects of pile-up, out-of-cluster leakage and dead material.

In the following studies, the narrow radius jets ($R = 0.4$) are required to have a transverse momentum of at least 25 GeV and an absolute pseudorapidity smaller than 2.5, while the large radius jets ($R = 1.0$) have to satisfy $p_T > 300\,\text{GeV}$ and $|\eta| < 2.0$. Jets stemming from a pile-up vertex are rejected by using the so-called jet-vertex fraction r_{JVF} [92]. This quantity is calculated with respect to a certain vertex vtx_j as the p_T sum of all matched tracks originating from vtx_j divided by the p_T sum of all tracks matched to the jet:

$$r_{\text{JVF}}(\text{jet}_i, \text{vtx}_j) = \frac{\sum_k p_\text{T}(\text{trk}_k^{\text{jet}_i}, \text{vtx}_j)}{\sum_n \sum_l p_\text{T}(\text{trk}_l^{\text{jet}_i}, \text{vtx}_n)}. \tag{3.10}$$

The r_{JVF} value gives a measure of how likely jet i emerges from a particular vertex j. So when calculating it for each jet with respect to the primary vertex, a suppression of jets stemming from pile-up vertices or emerging from underlying events is possible, since their r_{JVF} values tend to be low. The computed values are in the range of $[0, 1]$, while a r_{JVF} value of -1 is assigned to those jets, which have no tracks associated. All $R = 0.4$ jets considered in the following studies are required to have a $|r_{\text{JVF}}|$ above 0.5, if the transverse jet momentum is below 50 GeV and the absolute pseudorapidity below 2.4.

The total jet energy scale (JES) uncertainty consists of several components that are measured in a variety of different event topologies (like Z/γ+ jets or dijet) using dedicated methods. A detailed description of the efforts to measure the jet energy scale in the data can be found in References [93, 94]. Contributions are e.g. due to detector effects, the physics modelling, intercalibration for jets with large pseudorapidities or pile-up effects. The JES uncertainty varies from below 2% up to 7% as a function of the jet p_T and η. Additional uncertainties arise from a flavour-specific calorimeter response (i.e. different responses for pions and kaons), the modelling of b-hadron decays or the fact that a substantial fraction of heavy flavour hadron decays contain neutrinos, which interact only weakly with the calorimeter material. The flavour-specific contributions are added in quadrature to the JES uncertainties that are stated above, where the contribution from the term corresponding to jets containing a b-hadron ranges from 0.8% to 2.5%, depending on the particular jet kinematics.

As measurements of the jet energy resolution (JER) in data are found to agree well with the predictions by the simulation [95] no corrections are applied to the simulated jets. However, the impact on the measurements presented in the following is evaluated by smearing the transverse momenta of the simulated jets by 5-20% depending on the jet p_T and η, which corresponds to the uncertainty of the JER measurement in data.

The jet reconstruction efficiency (JRE) is derived using a tag-and-probe method in dijet events, which is based on a ΔR matching procedure between track jets and calorimeter jets. While low-p_T jets (< 20 GeV) show inefficiencies smaller than 3%, jets with a transverse momentum of > 30 GeV were found to be fully efficient [95]. Differences observed between data and the simulation are taken into account by discarding randomly a small fraction of the jets that pass the selection requirements.

The systematic uncertainties related to the jet selection requirements corresponding to the jet vertex fraction r_{JVF} are evaluated by shifting the nominal r_{JVF} cut value up (down) by 6%.

3.3.6 Jet substructure and trimming

Heavy particles produced with a significant boost tend to have highly collimated decay products, which can be contained in a single jet. The substructure and shape [91,96] of such jets are expected to show deviations in comparison to jets induced by light quarks or gluons. Therefore substructure and jet shape related observables can be used to distinguish QCD jets from jets originating from hadronic decays of boosted massive particles as high-p_{T} top-quarks, electroweak bosons or even new particles.

Frequently used substructure quantities are found in the set of the so-called k_t splitting scales $\sqrt{d_{ij}}$, which are calculated by reclustering the constituents of a jet using the k_t algorithm. The variable $\sqrt{d_{12}}$ for example is defined as the k_t-distance

$$\sqrt{d_{ij}} = \min\left(p_{\mathrm{T}}^{i}, p_{\mathrm{T}}^{j}\right) \cdot \Delta R_{ij} \tag{3.11}$$

between the two protojets i and j of the final clustering step. In the environment of a two-body decay of a heavy particle, the final clustering step will likely combine the two decay products, due to the fact that the k_t algorithm tends to combine the hardest components last. Thus the $\sqrt{d_{12}}$ value of such a decay is expected to be approximately half the mass of the decaying particle, while QCD jets will tend to have values in the order of $p_{\mathrm{T}}/10$ [97]. Following this approach further quantities as the splitting scale $\sqrt{d_{23}}$ of the second-to-last step of the reclustering procedure can be defined as well. Another observable that can be used to distinguish between boosted hadronic decaying top-quarks and high-p_{T} QCD jets is the invariant mass, which is derived from the four-momentum sum of all constituents of the jet.

Examples of such substructure related quantities are presented in Figures 3.9 (a) and (b), where the invariant mass and the $\sqrt{d_{12}}$ distribution of jets that originate from boosted hadronical top-quark decays are compared to those corresponding to high-p_{T} QCD jets. Both quantities provide a significant separation strength. For these comparisons, only anti-k_t $R = 1.0$ jets are taken into account that have a p_{T} above 300 GeV and a $|\eta| < 2.0$.
The so-called top-tagging algorithms combine a variety of these quantities to distinguish boosted hadronically decaying top-quarks from high-p_{T} QCD jets. In the studies presented in Section 9, simple rectangular cuts are applied to certain properties of the large radius jets (i.e. the first k_T splitting scale $\sqrt{d_{12}}$ is required to be above 40 GeV and the jet mass must exceed 100 GeV), while more sophisticated top-tagging algorithms are currently validated. Their descriptions can be found for example in References [98, 99].

Since the resolution of the jet mass and substructure quantities degrades dramatically with an increasing contamination of soft QCD radiation induced by pile-up, multiple parton interaction or initial state radiation, various so-called jet grooming techniques are intensively studied by the ATLAS collaboration [91]. These methods are either based on the adaptive modification of jet clustering algorithms or on the selective removal of soft radiation during the reconstruction procedure [100].

One of the most used grooming techniques within ATLAS analyses is the so-called jet trimming [101]. This procedure takes advantage of the fact that the contamination due to multiple parton interaction, pile-up and ISR has a much softer energy spectrum as particles associated to the hard interaction. Constituents of a jet are therefore removed if their transverse momentum relative to that of the jet $p_{\mathrm{T}}^{\mathrm{subjet}}/p_{\mathrm{T}}^{\mathrm{jet}}$ is below a certain threshold f^{cut}, which is typically of the order of a few percent. After the application of the trimming procedure jets are reclustered taking only the remaining constituents into account.

The current implementation of the trimming algorithm includes the reconstruction of R^{sub} sized subjets from the constituents of the jet in study, using the k_t algorithm. In the following

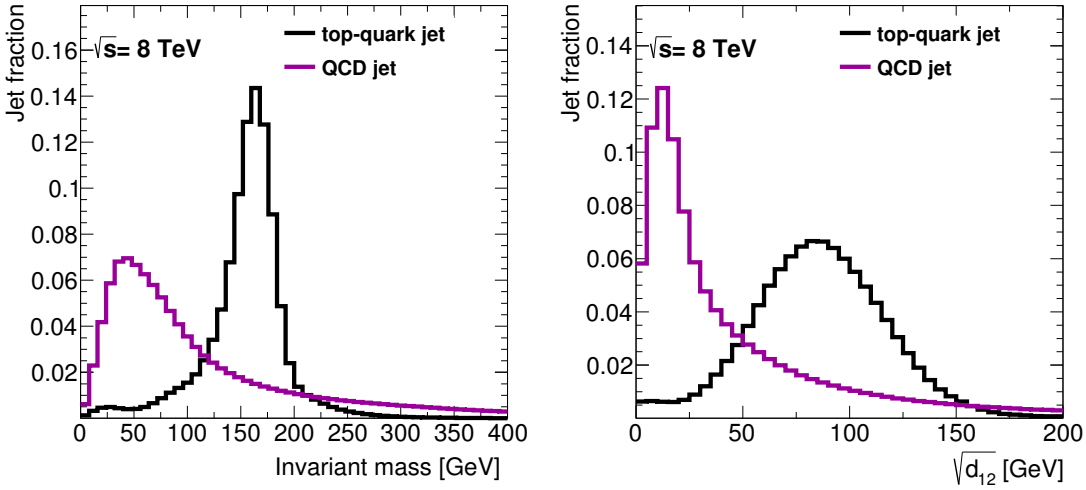

(a) Invariant jet mass

(b) $\sqrt{d_{12}}$

Figure 3.9: Distribution of the invariant mass (a) and the $\sqrt{d_{12}}$ (b) for jets that are reconstructed using topological clusters in the calorimeter system and a distance parameter of $R = 1.0$. Jets obtained from a simulated QCD dijets sample are compared to hadronic top-quark jets. For the latter case only those jets are considered that contain all partons from simulated $t \to bW \to bq\bar{q}$ decays inside a cone of the radius $R = 1.0$ around the jet axis. The corresponding di-jet sample is produced using the PYTHIA generator, while the $t\bar{t}$ decays are obtained using POWHEG+PYTHIA.

studies, R_{sub} is set to 0.3, while the transverse momentum fraction f_{cut} is set to 0.05 [91]. The final properties of the large radius jets are calculated after applying jet trimming. A schematic view of the whole jet trimming procedure is illustrated in Figure 3.10.

Uncertainties related to the energy scale of the large-R jets are evaluated using the γ-jets in situ calibration, the so-called double ratio method [91] and additionally an approach completely based on the predictions of the simulation in order to account for effects due to possible topology dependencies. The same method is also used to derive scale uncertainties on the invariant mass and the $\sqrt{d_{12}}$ for large radius jets [91]. The relative uncertainties on the measured p_{T}, invariant mass and the $\sqrt{d_{12}}$ of the large radius jets are found to vary between 3% and 11% as a function of the jet p_{T} and $|\eta|$.

3.3.7 Neutrinos

As neutrinos interact only weakly with matter, they cross the several detector systems without leaving traces. Hence their identification is only possible exploiting the momentum imbalance in the transverse plane of an event. The corresponding observable is referred to as the missing transverse momentum/energy

$$E_{\text{T}}^{\text{miss}} = \sqrt{\left(E_{\text{x}}^{\text{miss}}\right)^2 + \left(E_{\text{y}}^{\text{miss}}\right)^2} \,. \tag{3.12}$$

In top-quark measurements of the ATLAS collaboration an object based definition of the $E_{\text{T}}^{\text{miss}}$ is used. In this definition topological clusters of the calorimeter are matched to reconstructed

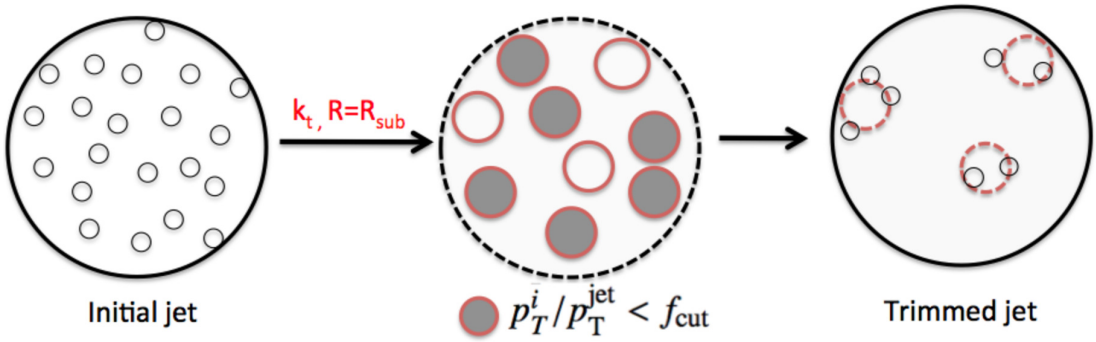

Figure 3.10: Schematic view of the jet trimming procedure [91] in case of the use of subjets. The trimming algorithm takes a jet as input and re-clusters its components into k_T subjets. In the last step all subjets are discarded that have $p_{\mathrm{T}}^{\mathrm{subjet}}/p_{\mathrm{T}}^{\mathrm{jet}} < f^{\mathrm{cut}}$.

objects (such as electrons, muons or jets) and calibrated accordingly. Energy depositions in calorimeter cells not assigned to reconstructed high-p_{T} objects are included in the missing transverse momentum calculation as the so-called cell-out term, which is calibrated to the EM scale. The x- and y-components of the missing momentum are therefore defined as

$$E_{X,Y}^{\mathrm{miss}} = -\left(E_{X,Y}^{RefElec} + E_{X,Y}^{RefJet} + E_{X,Y}^{RefSoftJet} + E_{X,Y}^{RefMuon} + E_{X,Y}^{CellOut}\right) .$$

The electron and muon terms are determined considering all electrons with a $p_{\mathrm{T}} > 10$ GeV and all muon candidates reconstructed by the MuId algorithm. Jets are included in the $E_{\mathrm{T}}^{\mathrm{miss}}$ calculation either at the EM+JES scale if their p_{T} is greater than 20 GeV or as soft jets at the EM scale if their p_{T} is between 7 GeV and 20 GeV.

Sources for systematic uncertainties that are related to the $E_{\mathrm{T}}^{\mathrm{miss}}$ calculation procedure correspond to the energy scale and resolution of calorimeter cells not associated to any reconstructed lepton or jet candidate. The energy scale uncertainty is evaluated by scaling the so-called cell out and soft-jet components up (down) by 8% during the $E_{\mathrm{T}}^{\mathrm{miss}}$ calculation, while the energy resolution uncertainty corresponding to the $E_{\mathrm{T}}^{\mathrm{miss}}$ is calculated by smearing these two components by up to 2.5%.

Chapter 4

Identification of *b*-hadron jets

The identification of jets containing b-hadrons, called b-tagging, is an important ingredient of many physics analyses. Possible applications range from high precision measurements in the top-quark sector to searches for new phenomena, where b-tagging algorithms are used to suppress background processes containing mainly light flavour jets.

The heavy flavour tagging algorithms used in ATLAS are either based on the presence of leptons (electrons or muons) as decay products of c- and b-hadrons or on the relatively long lifetime τ for hadrons containing a b-quark. As their lifetime is in the order of 1.5 ps, b-hadrons that have a transverse momentum of 70 GeV will have therefore an average decay length $\langle L_{xy} \rangle = \beta\gamma c\tau$ of 6.4 mm in the transverse plane before their decay. Such a decay gives rise to a secondary vertex (see Figure 4.1). The impact parameter is the distance of closest approach between an extrapolated track and the primary vertex. This distance tends to be relatively large for tracks stemming from a displaced vertex, while tracks coming from the primary vertex have impact parameters compatible with zero once the tracking resolution has been accounted for.

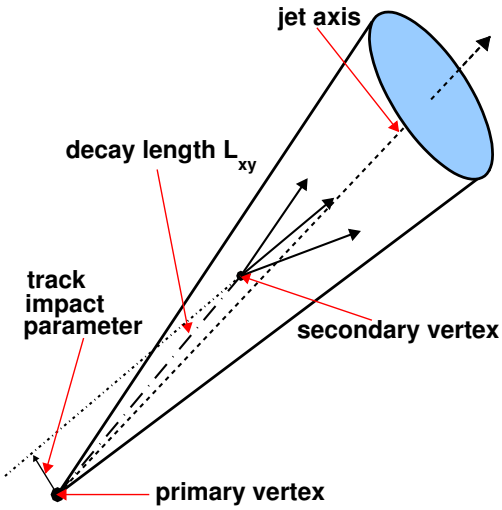

Figure 4.1: Schematic view of a b-hadron decay inside a jet resulting in a secondary vertex with three charged particle tracks. The vertex is significantly displaced with respect to the primary vertex, thus the decay length is macroscopic and well measurable. The track impact parameter, which is the distance of closest approach between the extrapolation of the track and the primary vertex, is shown in addition for one of the secondary tracks.

The ATLAS lifetime-based b-tagging algorithms are subdivided in two categories. The impact parameter based b-tagging algorithms such as IP2D or IP3D [102] use the transverse and longitudinal impact parameter significances $s_{d_0} = d_0/\sigma_{d_0}$ and $s_{z_0} = z_0/\sigma_{z_0}$ (defined as the ratio of the impact parameters to their uncertainties) of all tracks associated to a jet. However, the vertex based b-tagging algorithms such as SV0, SV1 or JetFitter [103, 104] utilize the properties of reconstructed secondary vertices to distinguish between b- and light flavour jets. A short description of how these tools are defined, is given in Section 4.3.

The vertex based b-tagging algorithms have a much higher separation power than the impact parameter ones, but their ability to identify b-jets is limited by the secondary vertex finding efficiency. More sophisticated b-tagging algorithms such as JetFitterCombNN [104] or MV1 [105] use multivariate techniques such as artificial neural networks (ANN) to combine information from the track impact parameters and the secondary vertex to achieve an even higher separation power by also taking the correlations of the various input quantities into account.

4.1 *b*-hadron properties

The lifetime-based b-tagging algorithms used in ATLAS are strongly dependent on the b-hadron properties. In particular the lifetime but also the invariant hadron mass is crucial to distinguish jets containing a b-hadron from those containing just light-flavoured (u, d, s) particles.

About 80.2% of all generated b-quarks hadronise into a B^+ or B^0 meson, 10.5% create a B_S meson and approximately 9.3% produce a b-flavoured baryon. The decay of a ground state b-flavoured hadron occurs via the weak interaction, which is well described by the so-called spectator model. This approach assumes the additional quarks to be spectators, while the b-quark decays predominantly via $b \to cW^*$. The virtual W-boson in this decay can either materialise into a pair of quarks or into a charged lepton and a neutrino. However, as such a decay is a generation changing process and thus suppressed by the CKM matrix, b-hadrons tend to have a relative large lifetime, which is in the order of 10^{-12} s. Decays via $b \to uW^*$ are even more suppressed by the size of the corresponding CKM matrix element, while the decays into a d- or s-quark are required to be mediated via flavour-changing neutral-current, which are forbidden in the SM at tree-level. The main properties of the various b-hadron types are listed in Table 4.1.

Particle	Content	Production fraction [%]	Mass [MeV]	Lifetime [ps]
B^+	ub	40.1 ± 0.8	5279.26 ± 0.17	1.641 ± 0.008
B^0	db	40.1 ± 0.8	5279.58 ± 0.17	1.519 ± 0.007
B_S	sb	10.5 ± 0.6	5366.77 ± 0.24	1.516 ± 0.011
B_c^+	cb	9.3 ± 1.6	6274.5 ± 1.8	0.452 ± 0.033
Λ_b^0	udb		5619.4 ± 1.6	1.425 ± 0.032
Ξ_b^-	dsb		5791.1 ± 2.2	$1.56^{+0.27}_{-0.25}$
Ω_b^-	ssb		6071 ± 40	$1.13^{+0.53}_{-0.40}$

Table 4.1: The main properties of the various b-hadron ground states [12] presented as a statistical combination from CDF [23], D0 [24] and LCHb measurements.

4.2 Key ingredients for *b*-tagging

The key ingredients for the various *b*-tagging algorithms used in ATLAS analyses are the charged particle tracks reconstructed from the information provided by the Inner Detector. All tracks that are associated to a certain jet and pass dedicated quality requirements are used as an input to the ATLAS *b*-tagging algorithms. Several steps of pattern recognition (e.g. reconstruction of secondary vertices) are then applied in order to calculate a so-called *b*-tagging weight. These weights quantify how likely the jets on study contain a *b*-hadron decay. Of similar importance for *b*-tagging is the knowledge of the primary vertex position, as this is used as a reference in the calculation of the track impact parameters and the displacement of the secondary vertex candidates.

The definition of *b*-, *c*-, τ- and light-flavour jets in simulated events is given via the so-called truth flavour labelling. This procedure is currently based on an angular matching of generator level particles to reconstructed jets using their coordinates in the pseudorapidity-azimuthal plane. If a *b*-quark with $p_{\mathrm{T}} > 5$ GeV is found to be inside a cone of radius $\Delta R = 0.3$ around the axis of a jet, this jet is labelled as a *b*-jet. This matching procedure is repeated for *c*-quarks and τ-leptons respectively, if no association to a *b*-quark is possible. A jet is labelled per default as light-flavoured, if no association to one of these particles was successful.

4.2.1 Track-to-jet association

Both, the secondary vertex and the impact parameter based algorithms are applied only to the sub-set of tracks that are assigned to any of the jets contained in a selected event. The association between tracks and their jets is accomplished by a spatial $\Delta R(\mathrm{track}, \mathrm{jet})$-matching procedure [104], where the allowed distance between the two objects dependents on the transverse momentum of the jet:

$$\Delta R\,(p_{\mathrm{T}}) = 0.239 + e^{-(1.22+0.0164 \cdot p_{\mathrm{T}}/\ \mathrm{GeV})} \tag{4.1}$$

This matching function is completely empirical and leads to smaller cones for high-p_{T} jets which are more collimated. It is meant to reduce the number of associated tracks stemming from the fragmentation, the underlying event or from pile-up vertices in order to increase the separation power of the *b*-tagging discriminants. While jets with a p_{T} of 25 GeV get all tracks associated that are within a cone of $\Delta R = 0.43$ around their axis, the corresponding cone for jets with a transverse momentum of 200 GeV has a radius of 0.25. In the case where two or more jets are very close to each other, tracks are always matched to the nearest jet in order to avoid double-counting. The course of the parametrisation function used in the track-to-jet association procedure is shown in Figure 4.2.

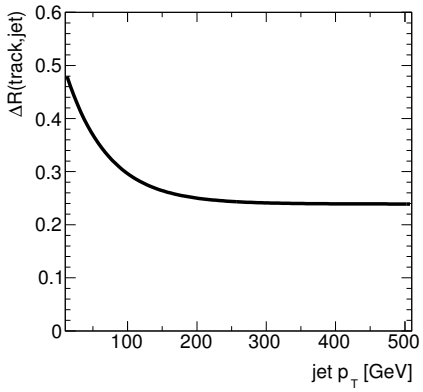

Figure 4.2: Parametrisation function used in the track-to-jet association procedure.

4.2.2 Track selection

Tracks that are associated to a jet have to fulfill certain quality requirements in order to be considered in any of the *b*-tagging algorithm. The aim is to keep the well-measured tracks, while rejecting those coming from material interactions with the silicon layers of the Inner Detector or from the decay of long-living light-flavour particles like K^0_S, Λ^0 or other hyperons.

The impact parameter based taggers as IP3D and IP2D require tight selection cuts on the number of hits in the silicon detector and on the track impact parameters. To be selected, a track must have at least two hits in the Pixel detector of which one has to be in the B-layer and at least seven silicon hits (SCT+pixel) in total. Furthermore, it is required that the transverse track momentum is above 1 GeV and the transverse and longitudinal impact parameters with respect to the primary vertex satisfy $|d_0| < 1\,\text{mm}$ and $|z_0| \cdot \sin\theta < 1.5\,\text{mm}$ respectively, with θ being the track polar angle (see Table 4.2). These selection requirements are often referred to as *b*-tagging quality. In the corresponding track selections of the vertex-based *b*-tagging algorithms (SV0, SV1 and JetFitter) looser criteria are applied to guarantee high vertex finding efficiencies. In particular the cuts on the track p_T and the longitudinal and transverse impact parameters are relaxed, while additional cuts on the uncertainties of the impact parameters σ_{d_0} and σ_{z_0} or the χ^2 of the track fit divided by the number of degrees of freedom (ndof) are applied. The requirement of having a hit in the pixel *B*-layer is also removed in order to not be restricted to decay lengths $\leq 50\,\text{mm}$. For the SV1 algorithm tracks that have more than one shared hit in the pixel- or more than two shared hits in SCT-layers are rejected. A detailed summary of the entire track selection requirements of some ATLAS *b*-tagging algorithms is shown in Table 4.2.

	IP3D/IP2D	SV0	SV1	JetFitter
p_T [GeV]	1.0	0.7	0.7	0.5
B-layer hits	1	0	0	0
pixel hits	2	2	1	1
SCT hits	–	4	4	4
silicon hits	7	7	7	7
max. shared hits	–	1	1	–
max. $\lvert d_0\rvert$ [mm]	1.0	2.0	5.0	7.0
max. σ_{d_0} [mm]	–	1.00	1.00	0.35
max. $\lvert z_0\rvert \cdot \sin\theta$ [mm]	1.5	2.0	25	10
max. σ_{z_0} [mm]	–	2.0	5.0	2.5
max. χ^2/ndof	–	3.0	3.0	3.5

Table 4.2: Track selection requirements for several ATLAS *b*-tagging algorithms.

4.2.3 Reconstruction of secondary and tertiary vertices inside jets

Secondary vertices inside jets can be reconstructed either by an iterative vertex finder (used for the SV0 and SV1 tagger) or by the JetFitter algorithm (used for JetFitterCombNN). The iterative vertex finder reconstructs inclusive vertices containing the decay products of a *b*-hadron and possibly also that of the subsequent *c*-hadron [103] based on a χ^2 minimisation. Using

significantly displaced tracks as input, the iterative algorithm starts by forming vertices of two-track pairs. In the second step vertices originating from material interactions or from long-lived light-flavour particles are reduced by removing two-track pairs if their distance to the primary vertex is compatible with the position of one of the Pixel detector layers or if their invariant mass fit to a K_S^0 meson or a Λ^0 baryon. The inclusive vertex is formed by combining all tracks from the remaining two-track pairs into a fit, which iteratively removes the track with the largest χ^2 contribution until the vertex satisfies certain quality requirements [103].

The JetFitter algorithm [104, 106] exploits the topology of the decay cascade introduced by a b-hadron decay to reconstruct separately the secondary and tertiary vertices. A multi-vertex fit is performed on the assumption that the primary event vertex and the vertices of the weak b- and c-hadron decays lie on a common line defined through the flight direction of the b-hadron. The technical implementation of this procedure is based on a Kalman filter and its main advantage with respect to the iterative vertex finder is the feasibility of reconstructing vertices from single tracks intersecting the flight axis.

The efficiencies to reconstruct a secondary vertex candidate inside a jet using either the JetFitter algorithm or the iterative vertex finder (with the SV1 setup) are displayed in Figure 4.3 (a) and (b) as a function of the jet p_{T} and separately for b-, c- and light-flavour jets. As the JetFitter algorithm can reconstruct both single- and multi-track vertices, its vertex finding efficiencies inside b-jets (up to 90%) are significantly larger than that of the iterative vertex finder with the SV1 setup (up to 75%). However, also its fake rate is substantially larger compared to that of the iterative vertex finder, which becomes obvious in particular for the high p_{T} regime. For jets with a p_{T} around 400 GeV, the vertex finding efficiency inside light-flavour jets increases to 40% for the JetFitter algorithm, while the efficiency of the iterative vertex finder is still only in the order of 10%. The vertex finding efficiency inside c-jets is also significantly larger, by a factor of approximately 2, for the JetFitter algorithm than for the iterative vertex finder.

Most properties of a secondary vertex resulting from the decay of a b-hadron are significantly different compared to those stemming from light-flavour decays. The relatively high b-hadron mass (about 5 GeV) and its long lifetime are particularly important. Examples for vertex based observables that are used in the various ATLAS b-tagging algorithms to identify b-hadrons inside highly-energetic particle jets are listed in Table 4.3.

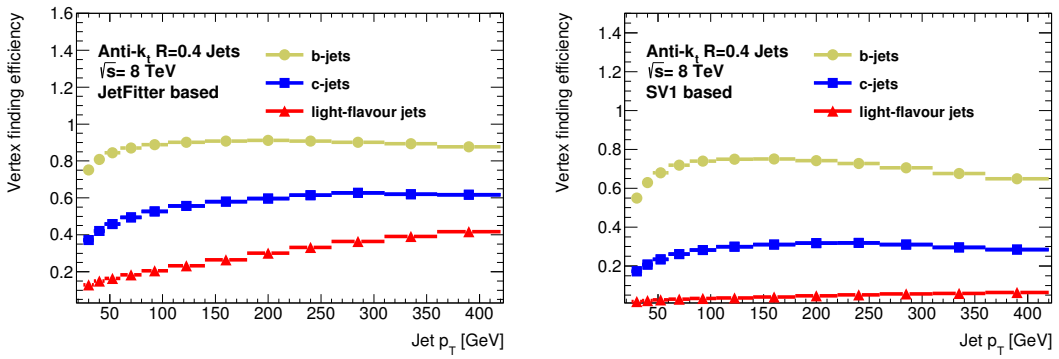

(a) JetFitter algorithm

(b) iterative vertex finder (SV1 setup)

Figure 4.3: Efficiencies to reconstruct a secondary vertex provided by the JetFitter algorithm (a) and the iterative vertex finder (b) as a function of the jet p_{T} presented separately for b-, c- and light-flavour jets. These jets are obtained from a $t\bar{t}$ sample that is simulated using the POWHEG and PYTHIA generators.

Quantity (Symbol)	Definition
$N^{2\text{tv}}$	Number of two-track vertices associated to the jet
$N_{\text{SV}}^{\text{trk}}$	Multiplicity of tracks associated to the displaced vertices
Invariant mass	Invariant mass of all tracks associated to the displaced vertices
Energy fraction	Energy sum of all tracks associated to the displaced vertices divided by the energy sum of all tracks associated to the jet
Transverse decay length L_{xy}	Distance in the xy-plane between the primary and the secondary vertex
Decay length significance	3-dimensional distance between the primary and the secondary vertex divided by its uncertainty
$\Delta R(\text{vertex}, \text{jet})$	Angular separation between the jet axis and the line joining the primary and secondary vertex
Vertex imbalance	Angular separation between the jet axis and the vectorial sum of all tracks fitted to the displaced vertices
$\log_{10}\left(\chi^2/\text{ndof}\right)$	Logarithm of the ratio between the χ^2 obtained from the vertex fit and the number of degrees of freedom
ϕ_{SV}, θ_{SV}, $\sigma_{\phi_{SV}}$, $\sigma_{\theta_{SV}}$	Measured azimuth and polar angle of the secondary vertex obtained from the vertex fit and their uncertainties

Table 4.3: Various properties (and their definitions) of the vertex candidates reconstructed either by the iterative vertex finder or the JetFitter algorithm. The quantity $N_{\text{SV}}^{\text{trk}}$ is equal to zero if the decay topology is only described by single-track vertices (its definition is therefore by construction slightly different for vertices reconstructed with the iterative vertex finder and the JetFitter algorithm). Decay topologies reconstructed by the JetFitter algorithm are further described by the overall number of single- and multi-track vertex candidates associated to the fit. The azimuth and polar angle of the vertex candidates are measured with respect to the detector coordinate system. The decay length significance of a secondary vertex candidate is signed with respect to the jet axis direction analogously to the impact parameter. Both the iterative vertex finder (with the SV1 setup) and the JetFitter algorithm reject vertices that have a negative decay length significance.

4.3 Application of the main ATLAS *b*-tagging algorithms

The ATLAS lifetime-based b-tagging algorithms use information from the track impact parameters and secondary vertices to calculate a continuous b-tagging discriminant. These output quantities are then used to determine whether a jet is tagged as a b-jet candidate or not by applying a cut on them. The corresponding cut values are chosen such that a certain fraction of b-jets obtained from simulated $t\bar{t}$ decays passes this selection requirement. Typical operating points correspond to selection acceptances ranging from 50% to 80% for the lifetime-based tagging algorithms. This section gives a short overview of the lifetime-based b-tagging algorithms that were used in the data recorded by ATLAS during the Run I of the LHC, while a more detailed overview can be found in Reference [107].

4.3.1 Impact parameter based algorithms

The ability of the track impact parameter to distinguish between tracks stemming from a displaced vertex inside a jet from those originating from the primary vertex is increased by considering its sign with respect to the jet direction, as an approximation of the b-hadrons flight path. This sign is calculated separately for the transverse and longitudinal impact parameters, following the prescriptions

$$sgn(d_0) = sgn\left(\sin(\phi^{\text{jet}} - \phi_{PV}^{\text{track}}) \cdot d_0^{\text{track}}\right) \tag{4.2}$$

and

$$sgn(z_0) = sgn\left((\eta^{\text{jet}} - \eta^{\text{track}}) \cdot z_0^{track}\right) \ . \tag{4.3}$$

The sign is positive if the angle between the direction of the jet axis and the line joining the primary vertex to the point of closest approach of the studied track is less than 90° and negative otherwise. While tracks stemming from the decay of a c- or b-hadron tend to be signed positively, tracks not coming from a displaced vertex have a random sign due to the finite resolution of the detector. However a bad measurement of the track properties, the jet direction or the primary vertex position can cause a flip of the impact parameter sign.

The IP2D algorithm relies on a log-likelihood ratio (LLR) method using the signed transverse impact parameter significance s_{d_0} of all tracks matched to a particular jet to calculate the b-tagging discriminant. For each track the measured s_{d_0} is compared to a pre-determined probability density function, testing both the b- and light-flavour jet hypotheses $b(s_{d_0})$ and $u(s_{d_0})$ respectively. The ratio of the resulting probabilities are used to define the track weights w_i, which are summed according to the equation

$$w_{\text{jet}} = \sum_{i=1}^{N^{\text{trk}}} \ln w_i = \sum_{i=1}^{N^{\text{trk}}} \ln \frac{b(s_{d_0})}{u(s_{d_0})} \tag{4.4}$$

to finally obtain the b-tagging weight of the studied jet. As the resolution of the impact parameters is strongly dependent on the track p_{T} or the hit-pattern in the silicon detector layers, it is beneficial to classify the tracks and evaluate their weights separately using a dedicated probability density function for each category. Currently two disjoint classes are used distinguishing whether the selected tracks share a precision hit in the silicon detector or not.

The IP3D algorithm is based on the same formalism as IP2D, but uses instead of the one-dimensional reference distribution of the s_{d_0} measurements, a two-dimensional reference containing both the signed transverse and longitudinal impact parameters and takes therefore also their correlation into account.

4.3.2 Secondary vertex based algorithms

As previously mentioned, both the SV0 and the SV1 algorithms are based on the properties of a displaced vertex reconstructed with the iterative vertex finder (see Table 4.2 for details on the track selection).

While the SV0 tagger is simply defined as the decay length significance signed with respect to the jet direction, the tagging weight of the SV1 algorithm is computed with the same likelihood ratio formalism used for the IP2D and IP3D taggers. As input a two-dimensional reference distribution of the energy fraction and the invariant mass is used as well as two one-dimensional

distributions corresponding to the number of two-track vertices and the $\Delta R(vertex, jet)$. In addition also an a priori knowledge of the vertex finding efficiencies for b-, and light flavour jets is needed.

The b-tagging weight of the JetFitter algorithm is defined by the output value of an artificial neural network, which uses the energy fraction, the invariant mass, the flight length significance and the track multiplicity of the decay cascade reconstructed by the JetFitter algorithm in addition to the number of single- and multi-track vertices as input nodes. The transverse momenta and the pseudorapidities of the jets are included as additional input nodes to take the correlation to the jet kinematics into account. In order to prevent the neural network from separating the different jet flavours using information on their kinematics, a re-weighting technique is applied before the training of the ANN to flatten the p_{T} and η spectra of the b-, c- and light-flavour jets separately. The neural network has three output nodes, that correspond to the b-, c-, and light-flavour jet hypotheses, which are referred to as p_b, p_c and p_u, respectively. With these probabilities a tagging weight is defined as $w_{\mathrm{JetFitter}} = \ln(p_b)/\ln(p_u)$ to separate b- and light flavour jets, while an improved c-jet rejection is obtained using $\ln(p_b)/\ln(p_c)$ as a jet weight.

4.3.3 Combined algorithms

The ability to distinguish between b- and light-flavour jets can be strongly improved by combining the information of the secondary vertex candidates with those of the track impact parameters. In a simple approach the LLR-based algorithms can by unified by simply adding their output values. The combination of the IP3D and SV1 taggers is referred to as the IP3D+SV1 algorithm, which was frequently used in the early ATLAS data taking periods.

A different approach to combine secondary vertex and impact parameter based information is the usage of an artificial neural network, which can also take the correlations between the various jet properties into account. Two different ANN-based b-tagging algorithms were used in ATLAS analysis until now: The JetFitterCombNN algorithm is a simple extension of the neural network used for JetFitter, as an additional input node for the IP3D tagging weight is added. The current ATLAS default tagger, called MV1 [105], is based on an ANN taking the b-tagging weights of the JetFitterCombNN, IP3D and SV1 algorithms as input nodes. Similar to JetFitter, MV1 also takes the correlations to the jet kinematics into account by including the jet p_{T} and η in the ANN. In order to increase the rejection against c-jets, the MV1 architecture can be slightly changed. Instead of the JetFitterCombNN weight, the three jet flavour-hypotheses p_b, p_c and p_u corresponding to the artificial neural network of the JetFitterCombNN algorithm are directly used in the training. The resulting b-tagger is referred to as MV1c.

4.3.4 Expected performance of the various b-tagging algorithms

The performance of a b-tagging algorithm is quantified by the b-tagging efficiency ε_b and the rejection rates for τ-, c- and light-flavour jets. The b-tagging efficiency is defined as the fraction of b-hadron jets that are tagged by the b-tagging algorithm, while the rejection rate of a certain jet flavour i is simply the inverse of the corresponding mis-tagging efficiency ε_i (fraction of τ-, c- or light-flavour jets tagged mistakenly as a b-jet).

A comparison of the expected performance corresponding to some of the previously introduced b-tagging algorithms can be found in Figure 4.4, which shows the light-flavour rejection rate as a function of the b-tagging efficiency for jets stemming from simulated $t\bar{t}$ decays. Each working point on these curves corresponds to a different cut on the discriminant of the various taggers. Since the MV1 algorithm shows a much better light-flavour rejection for a given b-tagging efficiency compared to the other tagging tools, it is currently the default b-tagger in

ATLAS. However, as different signal processes have different needs in terms of rejecting a certain jet flavour more dominantly, both the b-tagging algorithm and the working point should be chosen such that it is optimal to the corresponding analysis. Nevertheless, the 70% operating point of the MV1 algorithm is most frequently used. The corresponding tagging efficiencies for b-, c- and light-flavour jets are shown as a function of the jet p_{T} and $|\eta|$ in Figures 4.5 (a) and (b) respectively. While the tagging efficiencies for c-jets range from 15% to 25% at this working point, the tagging efficiencies for light-flavour jets is in the order of a few per mille for low and medium p_{T} jets and rises to the percentage level for jets with a p_{T} above 250 GeV.

The tagging efficiency for b- and c-jets is flat in the $|\eta|$ range that corresponds to the barrel region of the Inner Detector and decreases continuously for increasing $|\eta|$ values above $|\eta| > 1.2$. This decrease is based on the fact that the forward region of the Inner Detector contains more material than the barrel region, which leads to a degradation of the track finding efficiency. However, the mis-tagging efficiency for light-flavour jets is approximately flat over the whole range of $|\eta|$ values.

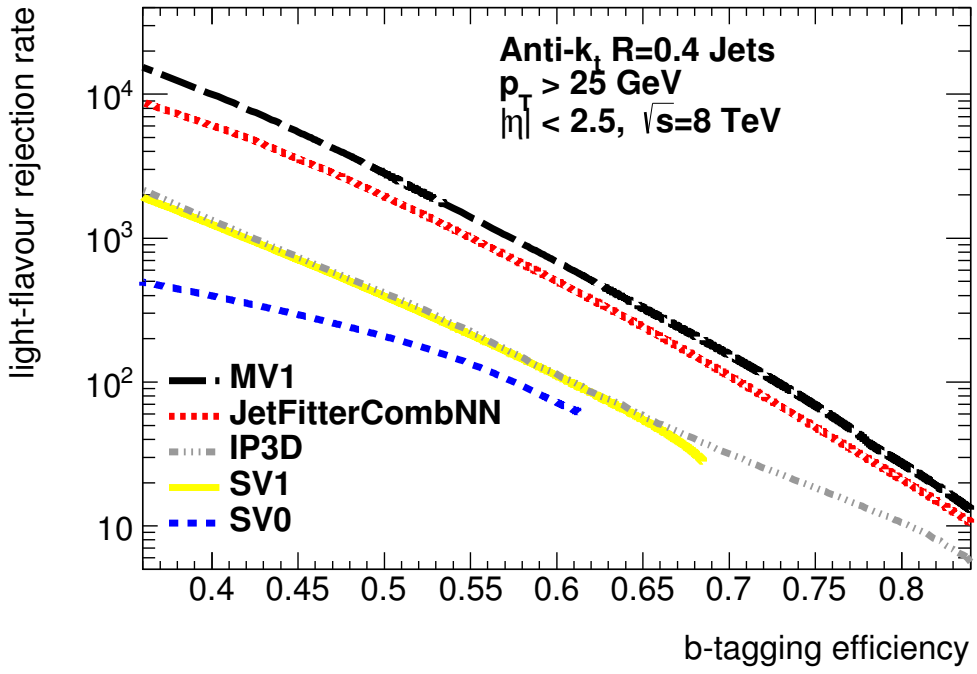

Figure 4.4: The light-flavour rejection rate as a function of the b-tagging efficiency for different b-taggers available at ATLAS. The jets are extracted from a $t\bar{t}$ sample that is simulated using the POWHEG and PYTHIA generators. As it can be seen, the MV1 tagger (presented as a black dashed line) shows a significantly better rejection power for light-flavour jets than all the other tagging algorithms presented here. Also the other ANN based tagger, the JetFitter algorithm (presented as a red dashed line), is much better than the three standalone taggers (SV0, SV1 and IP3D).

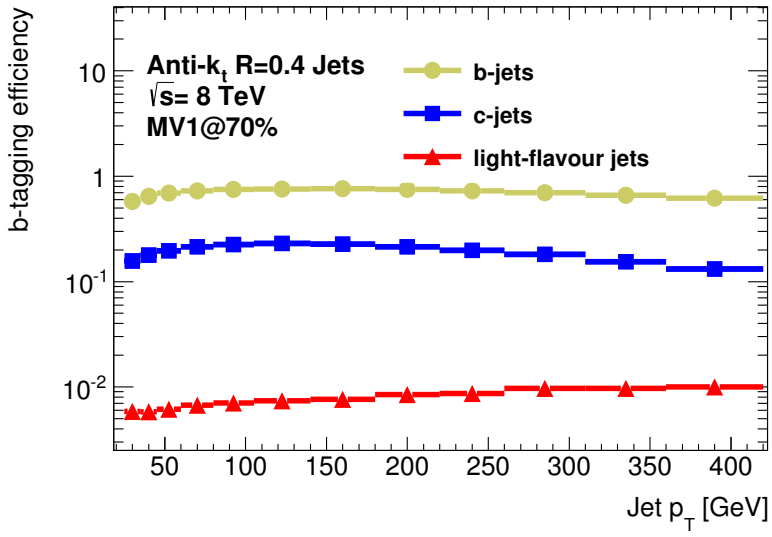

(a)

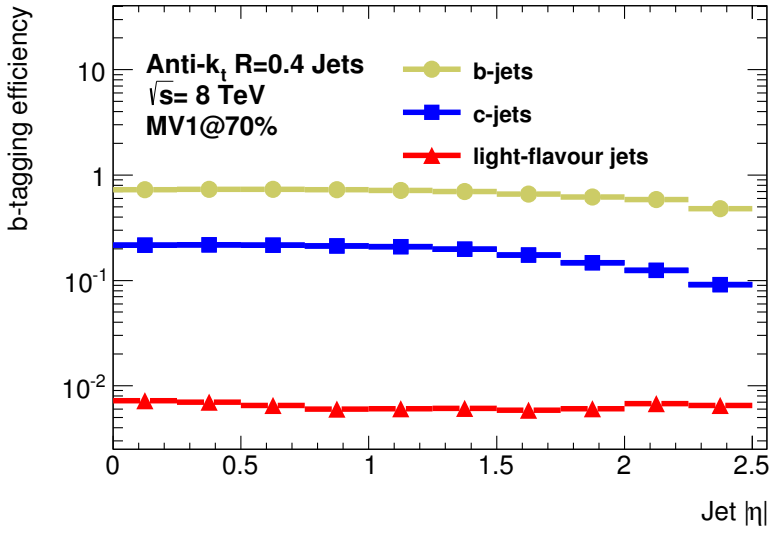

(b)

Figure 4.5: Tagging efficiencies corresponding to the MV1 algorithm for b-, c- and light-flavour jets are presented as well as a function of the jet p_{T} (a) and $|\eta|$ (b) for a representative working point corresponding to an overall b-tagging efficiency of 70%.

4.3.5 Calibration of b-tagging algorithms

Due to the imperfect modelling of the detector and its response to incoming particle showers, the usage of approximations in the generation of the fragmentation and hadronisation or the fact that many Monte Carlo models depend strongly on inputs from previous measurements (e.g. branching ratios of heavy flavour decays) the simulation does not describe the performance of the various b-tagging algorithms perfectly. In order to use a certain b-tagging algorithm in a physics analysis the b-tagging efficiency of the tagger and its mis-tagging efficiencies for c- and

light-flavour jets have to be measured in data and compared to the expectations provided by the simulation. This procedure is called calibration and the corresponding results are presented in the form of p_{T} or η dependent data-to-simulation scale factors:

$$\kappa_{\varepsilon_i}^{\mathrm{data/sim}}(p_{\mathrm{T}},\eta) = \frac{\varepsilon_i^{\mathrm{data}}(p_{\mathrm{T}},\eta)}{\varepsilon_i^{\mathrm{sim}}(p_{\mathrm{T}},\eta)}, \tag{4.5}$$

in which the measured tagging efficiency in data is divided by the tagging efficiency in simulated events. The corresponding inefficiency scale factors are defined as

$$\kappa_{\varepsilon_i}^{\mathrm{ineff.}}(p_{\mathrm{T}},\eta) = \frac{1-\kappa_{\varepsilon_i}^{\mathrm{data/sim.}}(p_{\mathrm{T}},\eta)\cdot\varepsilon_i^{\mathrm{sim.}}(p_{\mathrm{T}},\eta)}{1-\varepsilon_i^{\mathrm{sim}}(p_{\mathrm{T}},\eta)}\ . \tag{4.6}$$

Both, the tagging efficiency and the inefficiency scale factors are calculated separately for the three different flavour types ($i = b, c, \mathrm{light}$) using dedicated calibration methods, which aim to select samples that predominantly contain jets of a certain flavour to probe for the b-tagging efficiency for this particular jet flavour.

Mis-tagging efficiencies for light-flavour jets $\varepsilon_{\mathrm{light}}$ and their corresponding scale factors were measured by ATLAS in the Run I data by either applying a template likelihood fit to the invariant mass spectrum of vertices reconstructed by the iterative vertex finder (with the SV0 setup) [108] or by using the negative tag method [105]. The calibration of c-jets is based on the so-called D^* method, while the measurement of the b-tagging efficiencies ε_{b} is performed either on a sample of jets containing soft muons or on a jet sample obtained from $t\bar{t}$ candidate events. For the muon based approaches either the so-called system8 or the $p_{\mathrm{T}}^{\mathrm{rel}}$ [109] method can be used to measure the b-tagging efficiency, while a variety of different $t\bar{t}$ based methods exist of which the combinatorial likelihood approach in dileptonic top pair events [110] gives currently the most precise results with combined statistical and systematic uncertainties between 2%-8%. The results of the b-tagging efficiency calibration efforts corresponding to the ATLAS default flavour-tagging algorithm, MV1 (evaluated at an operating point that matches an overall b-tagging efficiency of 70%), provide scale factors for b-jets that are consistent with unity within their combined statistical and systematic uncertainties. However, the b-tagging scale factors for c-jets and light-flavour jets tend to be different from 1.0. They range from 0.9 to 1.0 (1.1 to 1.5) for c-jets (light-flavour jets) and have combined statistical and systematic uncertainties of 8% to 15% (15% to 40%).

In each physics analysis which uses b-tagging, the scale factors are calculated per jet in the simulation as a function of their flavour i, their transverse momentum p_{T} and their pseudorapidity η. A final b-tagging based event weight $w^{\mathrm{b-tag}}$ is obtained by the product sum of all these (in)efficiency scale factors

$$w^{\mathrm{b-tag}} = \prod_{j=0}^{N^{\mathrm{jets}}} \kappa_{\varepsilon_i}^{j}(p_{\mathrm{T}},\eta)\ . \tag{4.7}$$

The systematic uncertainties that arise due to the use of b-tagging are evaluated by shifting the values of the b-tagging calibration scale factors up/down by the total uncertainties of the measurements (full envelope approach). In order to properly take into account the correlation of the b-tagging uncertainties across the various jet p_{T} bins, the so-called eigenvector approach can be used, instead of full envelope approach. The eigenvectors are obtained from the total covariance matrix of the flavour-specific scale factors and their number is equal to the number of bins of the corresponding b-tagging calibration measurement. The according eigenvalues are then used in order to vary the scale factors properly during the calculation of the b-tagging uncertainties.

Chapter 5

Selection and reconstruction of top-quark pair candidate events

The studies presented in Sections 8 and 9 are based on a selected sample of top-quark pair candidates decaying into a final state containing high-p_{T} objects such as a charged lepton, a neutrino (i.e. a large amount of missing transverse momentum) and at least four jets. Decays into the single lepton channel (see Figure 5.1) offer a relative large branching fraction (compared to the dilepton channel), a clear signature in the detector system and thus a relatively low contribution due to non-$t\bar{t}$ backgrounds (compared to the all-hadronic channel). In addition, this decay channel provides the possibility to reconstruct the complete $t\bar{t}$ system and its invariant mass. Therefore, the single lepton channel is an ideal channel to e.g. search for $t\bar{t}$ resonances.

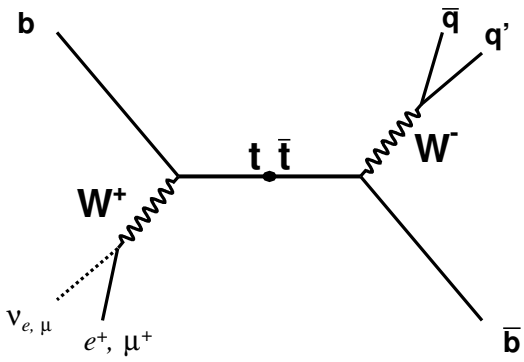

Figure 5.1: Schematic view of a single lepton $t\bar{t}$ decay at parton level (i.e. a decay into a final state with one charged lepton, one neutrino, two b-quarks and two additional quarks from the hadronic decay of a W-boson.

The various BSM theories summarised in Section 2.2.2 predict new heavy particles that decay predominantly into top-quark pairs. As the possible mass range of these hypothetical particles extend to several TeV, the resulting top-quarks might be produced with a significant Lorentz boost. The decay products of a boosted top-quark (or any other highly boosted particle) can be strongly collimated and their signatures in the calorimeter system might even have a significant overlap. While the merging between an electron or a muon and a jet can often still be resolved by applying dedicated isolation requirements and correction techniques, the overlap of two or more particle showers can lead to the problem that the reconstructed jets do not resemble sufficiently the initial partons. Thus the decay of a highly boosted top-quark candidate into a hadronic final state is reconstructed as one single jet, using a large-radius parameter $R = 1.0$ during the jet clustering (see Figure 5.2). Further dedicated selection requirements are used to increase the

sensitivity to search for $t\bar{t}$ candidate events produced with a large invariant mass. This event category is referred to as the boosted decay channel, while events which are assumed to have well-separated physics objects in the final state are classified into the so-called resolved decay channel. This section describes the techniques used to select and reconstruct both boosted and resolved top-quark candidate events having a final state containing exactly one charged lepton, missing transverse momentum and at least four jets. In addition, the methods used to estimate the remaining non-$t\bar{t}$ background contributions are summarised as well.

This chapter introduces the various selection and reconstruction requirements used to identify possible $t\bar{t}$ candidates for both boosted and resolved event topologies. In addition, also the relevant background sources are explained as well as the methods with which these processes are estimated.

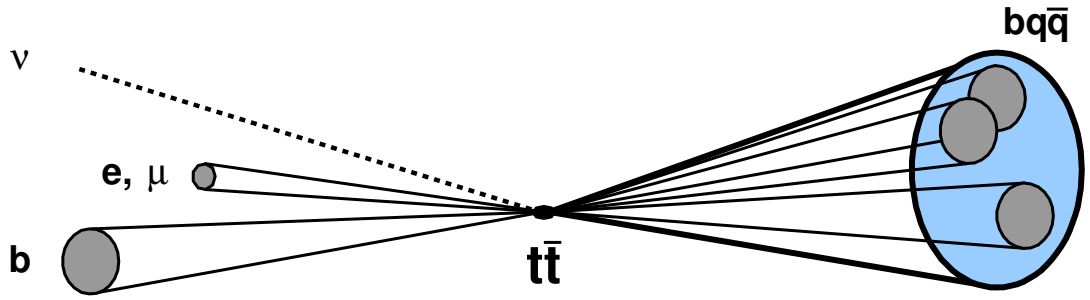

Figure 5.2: Schematic view of the decays of a boosted top- and antitop-quark into a final state containing leptons and jets. The decay products on both the leptonic and hadronic side of the event are strongly collimated and their signatures might overlap in the calorimeter system. As the standard narrow-cone jet algorithms might fail to resolve the hadronic side of the event, the $t \to bW \to bqq$ decay is reconstructed as one single large-radius jet in order to recover sensitivity.

5.1 Event preselection

Top quark pair candidate events decaying into a final state of exactly one charged lepton, missing transverse momentum and jets are selected by requiring that the appropriate single-lepton trigger has fired. The lepton trigger decisions are based on information at the event filter level using a logical OR of two single-electron or two single-muon triggers with transverse momentum thresholds of 24 GeV for leptons isolated from hadronic activity and further lepton candidates and 36 GeV or 60 GeV for non-isolated muons and electrons. Motivated by the decay of a W-boson into a high-energetic charged lepton and neutrino, exactly one electron or one muon that passes the full object definition requirements that are described in Sections 3.3.3 and 3.3.4 (including isolation) has to be identified within the acceptance of the detector. Additionally, the lepton candidate has to be matched to the triggered object.

The minimal distance ΔR between a lepton candidate and a selected jet in the η-ϕ-plane is not allowed to be less than 0.2 for electron candidates and not less than $0.04 + 10\ \text{GeV}/p_{\text{T}}^{\mu}$ for muon candidates. Leptons that fail this requirement are removed from the event. For electrons with $0.2 < \Delta R < 0.4$ to the nearest jet, a dedicated overlap and correction procedure is applied in order to take into account that the energy deposits of the electron candidate into the calorimeter system can substantially affect the direction of the jet axis. In such a case, the four-vector of the

electron is subtracted from the jet four-vector. If the track associated to the electron candidate is originally considered in the calculations of the jet vertex fraction, it is removed and the r_{JVF} value is re-calculated. The corrected jet is removed from the event if it fails the jet selection requirements on the transverse momentum, the energy, the pseudorapidity and the jet vertex fraction. The electron is removed if the corrected jet still passes these requirements and the ΔR between the two objects is smaller than 0.2 (in this case the electron four-vector is added again to the jet). Such an overlap removal becomes beneficial in particular in decays of top-quark pairs that are produced with an invariant mass above 1 TeV, as the lepton and jet candidates of such events tend to have a relatively low angular separation.

The missing transverse momentum $E_{\mathrm{T}}^{\mathrm{miss}}$, which corresponds to the neutrino transverse momentum, is required to be at least 20 GeV for each selected candidate event. This requirement is meant to reject events containing only non-prompt and fake leptons (i.e. multijet production processes in which such leptons originate for example from heavy-flavour decays inside jets). A further suppression of this background is realised by using the transverse mass of the W-boson:

$$m_{\mathrm{T},W} = \sqrt{2p_{\mathrm{T}}^{\ell}E_{\mathrm{T}}^{\mathrm{miss}}(1-\cos\phi_{\ell\nu})} \tag{5.1}$$

where $\phi_{\ell\nu}$ corresponds to the azimuthal angle between the lepton candidate and the $E_{\mathrm{T}}^{\mathrm{miss}}$ vector in the x-y-plane of the detector. For both the electron and muon channel the sum of $m_{\mathrm{T},W}$ and $E_{\mathrm{T}}^{\mathrm{miss}}$ has to be larger than 60 GeV. Further cuts are applied to remove events that fail dedicated quality requirements. Therefore events are removed if they contain a noise burst in the LAr calorimeter or any jet with $p_{\mathrm{T}} > 20\,\mathrm{GeV}$ that is identified as noise in the calorimeter or out-of-time activity with respect to the considered pp collision. Events are also rejected, if they contain at least one electron whose reconstructed track is also associated to a muon. Additional requirements on the jet multiplicity are applied to the candidate events, where the particular selection that is chosen depends on whether the event is categorised into the so-called resolved or the boosted decay channel. The definition of these two channels is given in the following.

Boosted decay channel

In order to optimise the selection of events containing high-p_{T} top-quarks decaying into a fully hadronic final state, at least one anti-k_t $R = 1.0$ jet $j_{1.0}$ that passes the object definitions given in Sections 3.3.5 and 3.3.6 has to be selected in the event. In the case that more than one large-radius jets was found, the highest p_{T} jet is considered as the top-quark candidate. In addition, at least one anti-k_t $R = 0.4$ jet $j_{0.4}$ has to be found within $\Delta R(\ell, j_{0.4}) < 1.5$ to the charged lepton ℓ to enable the reconstruction of the leptonic top-quark decay.

As a large fraction of the top-quark and top-antiquark (in the boosted decay channel) are expected to be emitted back-to-back, the azimuthal angle between the charged lepton and the large-radius jet has to fulfill $\Delta\phi(\ell, j_{1.0}) > 2.3$. Furthermore, the angular separation between the $R = 1.0$ jet and the $R = 0.4$ jet that is used in the reconstruction of the leptonic top-quark decay is required to fulfill $\Delta R(j_{0.4}, j_{1.0}) > 1.5$ in order to avoid a double counting of cluster energies in the reconstruction of the invariant $t\bar{t}$ mass. To further reduce the selection of processes not containing the decay of a top-quark, at least one anti-k_t $R = 0.4$ jet in the event has to be b-tagged using the MV1 algorithm at an operating point that matches an overall efficiency of 70% in a simulated $t\bar{t}$ sample. The corresponding cut value on the jet weight of the MV1 algorithm is 0.7892.

Resolved decay channel

Events that are expected to have only well separated electrons, muons and jets (i.e. physics objects whose signals do not significantly overlap in the various detector systems) are classified in the so-called resolved category. Candidate events from this decay channel are required to contain at least four anti-k_t $R = 0.4$ jets. As for the boosted decay channel, these jets have to fulfill the kinematic requirements stated in Section 3.3.5. In addition, at least one of them has to be tagged as a b-jet using again the MV1 algorithm at the 70% operating point.

5.2 Event reconstruction

The current strategy of the ATLAS collaboration in searches for new heavy bosons decaying into top-quark pairs is to probe the invariant mass spectrum of the $t\bar{t}$ system for an excess in data with respect to the prediction of the Standard Model. In order to reconstruct the invariant mass of the $t\bar{t}$ system, the four-vectors of both the hadronically and leptonically decaying top-quarks have to be determined. The methods used for this purpose depend on whether the corresponding events are selected in the boosted or the resolved decay channel.

The reconstruction of the leptonic top-quark candidate requires the knowledge of the neutrino four-vector. However, the momentum imbalance of an event (see Section 3.3.7) provides only the neutrino p_x and p_y components approximated by E_x^miss and E_y^miss respectively. It does not give any information on the longitudinal momentum or the pseudorapidity of the neutrino. For top-quark pair decays into single-lepton final states, the longitudinal component of the neutrino momentum can be calculated by applying an on-shell W-boson mass constraint to the $E_\mathrm{T}^\mathrm{miss}$+lepton system. Nevertheless, this procedure requires the majority of the missing transverse momentum to stem from the neutrino, instead of mis-reconstruction of jets or leptons. Solving this problem, which is done for example in Reference [111], gives the longitudinal neutrino momentum

$$p_\mathrm{z}^{\nu\pm} = \frac{\mu \cdot p_\mathrm{z}^\ell}{p_T^{\ell\,2}} \pm \sqrt{\frac{\mu^2 \cdot p_\mathrm{z}^{\ell\,2}}{p_\mathrm{T}^{\ell\,2}} - \frac{E^{\ell\,2} \cdot E_T^{\mathrm{miss}\,2} - \mu^2}{p_\mathrm{T}^{\ell\,2}}}\,, \tag{5.2}$$

where the abbreviation $\mu = \frac{m_W^2}{2} + p_\mathrm{T}^\ell \cdot E_\mathrm{T}^\mathrm{miss} \cos\Phi_{\ell\nu}$ is used. This equation provides either two, one or zero real solutions. If it does not have an existing real solution, the missing momentum vector is rotated until exactly one real solution is found. If this procedure leads to ambiguities, the rotation which provides the minimal change in the $E_\mathrm{T}^\mathrm{miss}$ is chosen.

The $t\bar{t}$ decay in the resolved decay channel is reconstructed by a χ^2 minimisation procedure, which uses a constraint on the expected top-quark and W-boson masses and on the event kinematics. All selected anti-k_t $R = 0.4$ jets, the charged lepton and both solutions for the longitudinal neutrino momentum (if two exist) are taken into account to find the jet-neutrino assignment corresponding to the smallest

$$\chi^2_\mathrm{total} = \underbrace{\left(\frac{m_{jj} - M_{W_h}}{\sigma_{M_{W_h}}}\right)^2}_{\chi^2_{W_h}} + \underbrace{\left(\frac{m_{jjj} - m_{jj} - M_{t_h - W_h}}{\sigma_{M_{t_h - W_h}}}\right)^2}_{\chi^2_{t_h - W_h}} + \underbrace{\left(\frac{m_{j\ell\nu} - M_{t_\ell}}{\sigma_{M_{t_\ell}}}\right)^2}_{\chi^2_{t_\ell}} + \underbrace{\left(\frac{(p_{\mathrm{T},jjj} - P_{\mathrm{T},t_h}) - (p_{\mathrm{T},j\ell\nu} - P_{\mathrm{T},t_\ell})}{\sigma_{P_\mathrm{T}\ \mathrm{diff}}}\right)^2}_{\chi^2_{p_\mathrm{T}\ \mathrm{diff}}}$$

value. The first and second terms ($\chi^2_{W_h}$ and $\chi^2_{t_h-W_h}$) in this equation correspond to the mass constraints on the W-boson and the top quark on the hadronic side of the event, where M_{W_h} and $\sigma_{M_{W_h}}$ represent the average value and the standard deviation of the mass distribution of the hadronically decaying W bosons. As the invariant masses of the two and three jet combinations m_{jj} and m_{jjj} are strongly correlated to each other, the W-boson mass is subtracted from the mass of the hadronically decaying top quark (which leads to $M_{t_h-W_h}$ and $\sigma_{M_{t_h-W_h}}$) in order to decouple both terms. The two-jet combination is assigned to the hadronically decaying W-boson, while the three-jet combination is assigned to the hadronically decaying top-quark.

The contribution $\chi^2_{t_\ell}$ corresponds to the $t \to bW \to b\ell\nu$ decay in the event, and the fourth term includes information on the expected event kinematics and constrains the p_T difference of the leptonically and hadronically decaying top quark candidates to the predictions of the simulation. Included in the last two terms are the mass of the combined jet-lepton-neutrino system $m_{j\ell\nu}$, the expected average mass of the leptonically decaying top quark M_{t_ℓ}, the expected average transverse momenta of the hadronic and leptonic top quarks P_{T,t_h} and P_{T,t_ℓ} as well as the corresponding standard deviations $\sigma_{M_{t_\ell}}$ and $\sigma_{P_\mathrm{T}\,\mathrm{diff}}$. For each event only the assignment corresponding to the smallest χ_total value is considered in the following measurements.

All parameters, contained in the χ^2_total expression (i.e. masses, momenta and their standard deviations), that are denoted by a capital letter are kept constant during the minimisation procedure. Their values are obtained from simulated $Z' \to t\bar{t}$ decays with resonance masses in the range of 0.5 TeV and 2 TeV and were found to be $M_{W_h} = 82.4$ GeV, $M_{t_h-W_h} = 89.0$ GeV, $M_{t_\ell} = 166.0$ GeV, $\sigma_{W_h} = 9.6$ GeV, $\sigma_{M_{t_h-W_h}} = 15.7$ GeV, $\sigma_{M_{t_\ell}} = 17.5$ GeV, $P_{\mathrm{T},j\ell\nu} - P_{\mathrm{T},t_\ell} = 0.43$ GeV and $\sigma_{p_\mathrm{T}\,\mathrm{diff}} = 46.1$ GeV (as described in Reference [36]). The calculation of these values is based on the invariant mass distribution that is obtained combining jets, which are ΔR matched to the corresponding decay products (i.e. the generator level partons) of the leptonically and hadronically decaying top-quarks.

In addition to the previously mentioned selection requirements used to identify possible $t\bar{t}$ decays, the candidate events are also required to have a $\log_{10}(\chi^2_\mathrm{total}) < 0.9$. This cut is introduced in order to further remove non-$t\bar{t}$ backgrounds and also to ensure that dominantly well-reconstructed top-quark pair decays are used for the following analyses.

Top-quark pair candidate events passing the boosted selection requirements are reconstructed from the the vectorial sum of the four-momenta of the neutrino, the charged lepton, the jet with the largest p_T inside $\Delta R < 1.5$ to the charged lepton (as a b-jet candidate) and the large-radius jet. If Equation 5.2 has two real solutions, the one with the smallest $|p_z|$ is used in this reconstruction procedure.

5.3 Prediction of signal and background processes

In order to measure any of the top-quark properties precisely a good knowledge about the various top-quark production and decay modes as well as their main background contributions is required. Indeed the single lepton $t\bar{t}$ decay channel has a clear signature in the detector. However, several other processes can have the same signature in terms of lepton and jet multiplicities in the final state. Such background events contain particle jets that tend to be produced with relatively small angles with respect to the beam axis, while their energy spectrum is expected to be relative low. Particle jets stemming from a top-quark decay are emitted rather centrally into the detector and tend to have much higher energies due to the large top-quark mass. Thus the signal-to-background ratio S/B can be improved by optimising the adjustment of the selection requirements to the underlying event kinematics.

The most dominant background processes for the investigation of $t\bar{t}$ decays into final states with one charged lepton, missing transverse momentum and at least four jets is the production of a W-boson in association with jets, followed by processes involving single top-quarks, which have much lower event rates but a rather similar event topology. Smaller background contributions arise due to the production of Z+jets events or dibosons (WW, WZ and ZZ) in association with jets. Also QCD multijet events can mimic the topology of a $t\bar{t}$ decay, if e.g. a heavy-flavour particle (as a c- or b-hadron) inside a particle jet decays into either an electron or a muon. This type of background is only relevant due to its large production rates and is usually estimated completly data-driven using approaches like the matrix element method, which is briefly described in Section 5.3.3.

Exemplary Feynman diagrams visualising the production of W- and Z-bosons in association with jets, and diboson events are shown in Figures 5.3 (a-f), while exemplary Feynman diagrams of the single top-quark production were already presented in Figures 2.3 (f-h).

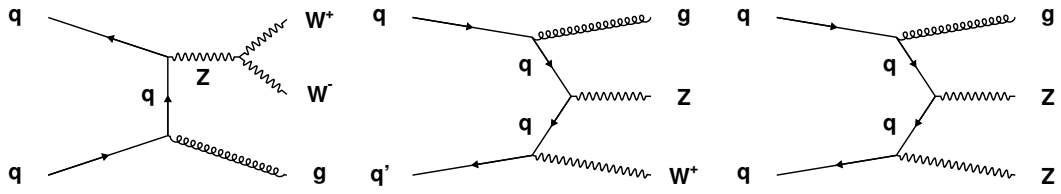

(a) dibosonic WW production **(b)** dibosonic WZ production **(c)** dibosonic ZZ production

(d) $W + c$ production **(e)** W+jets production **(f)** Z+jets production

Figure 5.3: Examples for Feynman diagrams depicting important background processes for top-quark physics: The production modes of diboson events (WW, WZ, ZZ) in association with jets (a-c) as well as the associated production of a W/Z-boson and jets (d-f) are presented.

5.3.1 Modelling of the various signal and background processes

The simulated signal and background samples used in the following studies are briefly described below: The production of $t\bar{t}$ events (according to the SM predictions) is simulated by the POWHEG r2129 [112] generator at next-to-leading order (NLO) accuracy of the matrix element using the CT10 parton distribution function (PDF) sets [33]. Parton showering and underlying events are modelled by PYTHIA v6.4.26 [62] with the Perugia 2011C tune [113]. Systematic effects corresponding to the generation of the matrix element or the modelling of parton showering and fragmentation are studied by using samples of $t\bar{t}$ events that are produced with alternative generators. For this purpose the MC@NLO v.4.03 [59] and the POWHEG generators are interfaced to HERWIG v6.52 [64] with the AUET2 tune and JIMMY [114] for the modelling of the hadronisation and the underlying event, respectively. The uncertainties arising

from the choice of the Monte Carlo generator and the associated matching between the matrix element and the parton shower are estimated by comparing the results obtained with the $t\bar{t}$ sample produced by POWHEG+HERWIG to those from a sample generated by MC@NLO+HERWIG, while the dependence on the fragmentation and parton shower modelling is estimated comparing samples that are produced with POWHEG+PYTHIA and POWHEG+HERWIG. In both cases, the full difference of the results obtained with these samples is assigned as a systematic uncertainty.

The impact of the initial and final state radiation (ISR/FSR) is estimated by using two different setups of the AcerMC v3.7 [115] generator, which is interfaced to PYTHIA v6.4.26. Both generators are used with the AUET2B tune. In these AcerMC setups, the parameter $1/\Lambda_{QCD}^{ISR}$, the maximum parton virtuality in space-like parton showers, and Λ_{QCD}^{FSR}, the FSR infrared cut-off, are varied in order to increase or decrease the additional jet activity produced in association with $t\bar{t}$ events. Both parameters are chosen such that the amount of additional radiation is increased (decreased) in a range consistent with experimental findings [116, 117]. The uncertainty is calculated as $1/2$ of the difference between the results derived with these two samples.

Events containing the associated production of a top-antitop pair and a vector boson ($t\bar{t}$ + V) are generated by MadGraph v5 [61] at leading-order using the PDF set CTEQ6L1 [118] and PYTHIA v6.4.26 for parton shower and fragmentation. Its production cross-section is normalised to the NLO predictions. An uncertainty of 13% is assumed to be on the cross-section for top-quark pairs produced in association with a W-boson [119] and 14% for the associated production with a Z-boson [120].

Single top-quark production in the s- and t-channel or in association with a W-boson are simulated like the $t\bar{t}$ events by using POWHEG and PYTHIA to generate matrix element and parton shower including the PDF sets CT10F4 [33] and CT10. The overlap at higher orders between the Wt-channel and top-quark pair processes is handled by the so-called diagram removal scheme [121]. The production cross-sections for these three channels have uncertainties of 4% for both the s- and t-channel and 7% for the associated production of a top-quark and a W-boson [122]. Per additional jet an extra uncertainty of 24% is added in quadrature, leading in total to an uncertainty of 34% for the s- and t-channel and 25% on the normalisation of the Wt-channel.

For all top-quark involved processes a top-quark mass of 172.5 GeV is assumed and the branching ratio of the $t \to Wb$ decay is set to 1. The $t\bar{t}$ production cross-section corresponding to this particular top-quark mass is computed at NNLO accuracy in QCD calculations including the resummation of NNLL soft gluon bremsstrahlung leading to 253^{+13}_{-15} pb for $\sqrt{s} = 8\,\text{TeV}$ [28, 123–126].

However, as the kinematic distribution of the top-quark decay products are strongly correlated to the top-quark mass, it has to be investigated to what extent the following measurements are affected by a variation of the top-quark mass. For this purpose, samples, generated by POWHEG and PYTHIA, corresponding to $m_{\text{top}} = 170.0$ GeV and $m_{\text{top}} = 175.0$ GeV are used separately instead to the nominal $t\bar{t}$ sample. The nominal cross-section of the mass variation samples is scaled to the cross-section corresponding to a top-quark mass of 172.5 GeV, as the total normalisation uncertainty already includes a contribution due to the lack of knowledge of the exact top-quark mass (in order to avoid a double-counting of uncertainties). The uncertainty due to the top-quark mass variation is calculated as $1/4$ of the difference between the results derived with these two samples.

Events containing the production of a single vector boson (W or Z) are simulated in association with up to five additional partons using the multileg LO generator ALPGEN [60] and the CTEQ6L1 PDF set interfaced to PYTHIA 6.426, used with the P2011C tune, for parton

showering and fragmentation. To avoid a double-counting of events having the same partonic configurations produced by both the matrix element and the parton shower evolution, the MLM matching procedure [127] is performed. Samples of the W+jets production are generated separately for the sub processes W+light-flavour jets, $Wc\bar{c}$+jets, $Wb\bar{b}$+jets and Wc+jets, while samples for the process Z+jets are generated for Z+light-flavour jets, $Zc\bar{c}$+jets and $Zb\bar{b}$+jets. As the W/Z+jets final states containing c- or b-jets can be produced in the same configuration for several of these subsamples, the heavy-flavour-overlap-removal [128] is applied in order to avoid a double counting of the corresponding heavy-flavour contributions.

For the predictions of the W+jets background dedicated systematic uncertainties have to be taken into account that are related to the parameter choices in the setup of the ALPGEN generator (shape uncertainty). The dominant systematic uncertainties arising from the use of the ALPGEN generator (referred to as "iqopt3" and "ptjmin10") are evaluated by varying so-called scale and MLM matching parameters. Hence, the first term corresponds to a variation of the functional form of the factorisation and renormalisation scale used in ALPGEN, while for the calculation of the "ptjmin10" term, the minimum p_{T} value of the partons considered during the matrix element generation are changed from 15 GeV to 10 GeV.

The Z+jets normalisation uncertainty depends on the number of jets in the final state [129]. A basic uncertainty of 4% is assumed and an additional term of 24% per jet is added in quadrature, leading to a total uncertainty of 48% for the four-jet bin. The inclusive cross-sections of the W/Z + jets samples are normalised to the NNLO predictions obtained from the FEWZ package [130].

The diboson (WW, WZ and ZZ) production is simulated at NLO accuracy with up to 3 additional partons using the PDF set CT10 and SHERPA v.1.4.1 [65] for the generation of the matrix element and parton shower. For these dibosonic events a basic uncertainty of 5% from the inclusive cross-section is taken into account, together with an additional term of 24% per jet is added in quadrature (as for Z + jets events). This leads to a total uncertainty of 34% for a requirement of at least four jets, as two of the required jets are assumed to originate from one of the well-described hadronic gauge bosons decays.

QCD dijet events are generated by PYTHIA8 v8.1.60 using the AU2 tune [131] and the CT10 PDF set. These samples were generated with the same number of events for each of several disjoint phase space regions, where the transverse momentum of the leading jet is the classification criteria. In total seven different dijet samples are used with bin edges of 20 GeV, 80 GeV, 200 GeV, 500 GeV, 1000 GeV, 1500 GeV, 2000 GeV and ∞.

In addition various BSM Monte Carlo samples are used. The process $Z' \rightarrow t\bar{t}$ [132] is simulated using the default settings of PYTHIA v8.165 [63] for both the matrix element and parton shower generation. The PDF set MSTW2008LO [133] is used to produce samples for various Z' masses ranging from 0.4 TeV to 3 TeV, in which the assumed Z' width is of the order of 3% of its mass and therefore small compared to the detector resolution. While the kinematic distribution for this process are generated at LO accuracy, the cross-section is normalised in order to match the NLO calculations by applying a scale factor of 1.3 [134]. The hypothetical decay of a Kaluza-Klein-gluon g_{KK} into a $t\bar{t}$ pair [135] is simulated at LO for masses in the range from 0.4 TeV to 3 TeV and for a g_{KK} width of 15.3% using the MadGraph5 v1.3.33 generator [61] interfaced to PYTHIA8 v8.1.65 with AU2 tune and the MSTW2008LO PDF set. Additional g_{KK} samples with assumed masses of 1 TeV, 2 TeV and 3 TeV are produced for which the width ranges from 10% to 40% of the g_{KK} mass.

The production and decay of Kaluza-Klein gravitons, G_{KK}, are simulated using the MadGraph generator for the matrix element, the CTEQ6L1 as the PDF set and PYTHIA8 v8.1.75 with the AU2 tune for the fragmentation and parton showering. The parameters of the studied

model are chosen such that they match those from the scenario described in References [40], which leads to resonances with widths between 3% and 6% of their mass. For such gravitons the decay to light fermions are strongly suppressed. In addition, the branching ratio to photons is insignificant, while decays into $t\bar{t}$, W^+W^-, ZZ or hh are dominant.

A further BSM process corresponding to the decay of a Higgs-like spin-0 resonance into a top-quark pair [136] is simulated with the MadGraph generator assuming effective couplings [137] of the Higgs-like particle. The CTEQ6L1 parametrisation is used to provide the PDF information, while PYTHIA8 is chosen for the fragmentation and parton showering. Various samples are produced to cover resonance masses ranging from 0.4 TeV to 3 TeV, in which the width of the resonance is set to be 0.66% of its mass. Interference effects with the SM processes are ignored for all these signal hypotheses.

The simulated events are generated at a centre-of-mass energy $\sqrt{s}$ of 8 TeV and passed afterwards through either the full or the fast ATLAS detector simulation [68, 69]. The simulated events are overlaid with additional inelastic pp interactions, which are simulated with PYTHIA8, in order to match the pile-up conditions observed in the ATLAS data recorded during the 2012 run of the LHC. The cross-sections for the various Monte Carlo samples used in the following studies are listed in detail in the Tables A.1, A.2, A.3, A.4, A.5, A.6, A.7 and A.8, which are contained in the appendix.

The uncertainties corresponding to the use of a particular PDF set for the generation of the various Monte Carlo samples are evaluated by re-weighting the selected events according to the PDF4LHC recommendations [138]: combining the 68% C.L. uncertainties on the CT10, NNPDF2.3 [139] and MSTW2008NLO PDF sets.

The effect of changes in the performance of the tile calorimeter during the data-taking period was checked by using two different simulated $t\bar{t}$ samples with different numbers of dead modules, covering the variations seen during data-taking [1]. The corresponding uncertainties are also calculated as $1/2$ of the difference between the results derived with these two samples.

5.3.2 Charge asymmetry

The associated production of W-bosons in association with jets is one of the most important backgrounds to top-quark analysis. Its kinematics are predicted with LO accuracy, while the production cross-section is known from NNLO calculations.

However, both the overall normalisation and the heavy flavour composition of this background are not described sufficiently by the simulation. Thus they have to be determined using data-driven techniques, while the shape of the various kinematic distributions of the W+jets

[1] Due to a variety of reasons, several modules of the hadronic tile calorimeter were temporarily or permanently defective throughout the 2012 data taking periods of the ATLAS detector. One particular tile module was even kept inactive for the full dataset and thus had to be considered as defective during the detector simulation as well. Calorimeter cells contained on the affected modules are not available for energy measurements. Indeed the cluster energy is corrected by extrapolating from the energy content of cells neighbouring the inactive modules, still this procedure becomes very inaccurate for high p_{T} clusters due to their collimated energy deposits. As a consequence, both the measurements of the jet energy and direction can be substantially affected by this issue.

While the simulated signal and background samples take only one permanently inactive tile module into account, three further modules were affected for 29%, 36% and 82% of the collected integrated luminosity. In order to estimate the impact, this inconsistency between the data taking conditions and the detector simulation has on the b-tagging calibration results, an alternative sample of top quark pairs is generated for which these four tile modules are completely deactivated. While the default Monte Carlo samples underestimate the corresponding effects on the calibration results, the alternative $t\bar{t}$ sample provide an conservative overestimation. Hence it is possible to derive dedicated systematic uncertainties corresponding to $1/2$ of the difference between the results obtained with these two samples.

background is taken from the simulation. The normalisation of the W+jets background is estimated using the so-called charge asymmetry method, which relies on the fact that positively charged W-bosons (e.g via $u\bar{d} \rightarrow W^+$) are produced more often in proton-proton collisions than negatively charged W-bosons (e.g. via $d\bar{u} \rightarrow W^-$), due to a relative difference in the quark and antiquark distribution functions. In contrast to the overall production rates for W+jet events, the ratio of cross-sections $r_{\text{asym}} = \frac{\sigma(pp \rightarrow W^+)}{\sigma(pp \rightarrow W^-)}$ is expected to be relatively well modelled with uncertainties in the order of a few percent [133]. As the main backgrounds to a dedicated W+jets selection (as top-quark pairs, QCD multijet and Z+jets events) do not provide a charge asymmetry, the total number of W+jets events in data $N_{W^+} + N_{W^-}$ can be estimated via the equation

$$N_{W^+} + N_{W^-} = \frac{r_{\text{asym}} + 1}{r_{\text{asym}} - 1} \cdot (N^+_{\text{data}} - N^-_{\text{data}}) \, . \tag{5.3}$$

Here $N^{\pm}_{\text{data}}$ denotes the selected number of events having a positively/negatively charged lepton. This number is measured in data for a given event selection, while the asymmetry ratio r_{asym} is taken from the simulation. However, as the associated production of top-quark pairs and vector-bosons, single top-quarks and diboson events provide a source for additional charge asymmetry, their contributions to N^+_{data} and N^-_{data} are subtracted from the measurements in data. The results obtained via the Equation 5.3 are then used to scale the predicted normalisation of the W+jets background to the event yields in data.

The relative fractions of W-bosons produced in association to light flavour F_{ll}, and heavy flavour jets F_c, F_{cc} and F_{bb} are fixed by performing a template fit of the predicted b-tag multiplicity distribution to the observations in data. The control region is defined by keeping the event selection criteria the same as in the signal region except for the requirement on the jet multiplicity. The fit is performed in the two jet bin. Four separate templates are used as the simulated W+jets events are subdivided into the processes W+light, $Wc\bar{c}$, $Wb\bar{b}$ and Wc, while the data is subtracted by the contribution due to the other processes. The resulting flavour fractions are extrapolated to higher-jet multiplicities and used to correct the predictions of the simulation accordingly. Since the charge asymmetry is different between $Wb\bar{b}$ and $Wc\bar{c}$ on the one hand and Wc on the other, the results provided by Equation 5.3 vary if the fractions F_c, F_{cc}, F_{bb} and F_{ll} change. Therefore the charge asymmetry method and the template fit are applied iteratively until stable results are reached. The normalisation scale factors k_{CA} obtained after applying this procedure to the resolved decay channel are 1.03 ± 0.01 (0.98 ± 0.01) for the electron (muon) channel. The corresponding scale factors for the relative flavour fractions are listed in Table 5.1 separately for the electron and the muon channel, while further details on their measurement can be found in Reference [36].

The measurement of the charge asymmetry is repeated for the boosted channel, due to the fact that the large difference in the covered phase space region (with respect to the resolved decay channel) can bias the resulting normalisation scale factors. The control region of the W+jets background in the boosted decay channel is defined by removing the b-tagging and $\Delta\phi(\ell, j_{1.0}) > 2.3$ requirements as well as the cuts on the mass and the $\sqrt{d_{12}}$ of the large-radius jet. As the statistics of the 2012 dataset is not sufficient to measure the heavy flavour fractions separately for the boosted channel, the scale factors obtained in the resolved channel are used instead to correct the relative fractions of W+light, $Wc\bar{c}$, $Wb\bar{b}$ and Wc events passing the boosted selection requirements. The normalisation scale factors k_{CA} obtained in the boosted channel are 0.89 ± 0.06 and 0.81 ± 0.05 for the electron and muon channel, respectively. The determination of the W+jets normalisation scale factors and the corresponding heavy flavour fractions in data are repeated for all relevant systematic uncertainties. Thus when shifting e.g. the jet

energy scale up/down for the Monte Carlo based processes (i.e. $t\bar{t}$, Z+jets, single top-quarks and diboson events) the normalisation of the W+jets background is also changed.

Channel	k_{bb}, k_{cc}	k_c	k_{ll}	k_{CA}
Electron	1.36 ± 0.07	0.70 ± 0.03	0.93 ± 0.00	1.03 ± 0.01
Muon	1.52 ± 0.08	0.66 ± 0.03	0.87 ± 0.00	0.98 ± 0.01

Table 5.1: Scale factors k_{bb}, k_{cc}, k_c, k_{ll} and k_{CA} (including their statistical uncertainties) used to correct the relative flavour fractions and the normalisation of the W+jets background in the resolved decay channel presented separately for final states containing electrons and muons.

5.3.3 Background from non-prompt and fake lepton sources

The remaining contribution due to the production of QCD multijets events is estimated using the so-called matrix method [140] in both the electron and the muon channel. Events from this background type do not contain a prompt charged lepton but reconstructed leptons that can originate for example from a heavy flavour decay or from a jet misidentification.

The matrix method applied to the data is based on the definition of two differently strict lepton selection requirements. While the tight (T) lepton definition has to be equal to the requirements used in the final event selection, less strict cuts on the isolation and quality definitions are applied in order to classify leptons into the loose (L) category. Hence, the sample of selected tight leptons is a subsample of the loose lepton category. The aim of this method is to estimate the number of events containing exactly one non-prompt lepton passing the tight selection requirements. This is approached by disentangling the total number of events containing exactly one lepton passing the selection requirements of the loose category according to:

$$N_L = N_{\text{prompt}} + N_{QCD} \ . \tag{5.4}$$

Here N_{prompt} is the number of events that contain prompt leptons ($t\bar{t}$, single-top, W/Z+jets and diboson), while N_{QCD} gives the number of selected QCD multijet events, i.e. sources for non-prompt leptons. Following this approach, the number of events having exactly one lepton being defined as tight, can be written as:

$$N_T = \varepsilon \cdot N_{\text{prompt}} + f \cdot N_{QCD} \ , \tag{5.5}$$

where ε and f are the efficiencies for prompt and non-prompt leptons that are selected with the loose requirements to pass also the tight lepton definitions. Solving Equation 5.4 for N_{prompt} and inserting the corresponding expression in Equation 5.5, it becomes possible to estimate the QCD contribution to the signal region via

$$N_{QCD} = \frac{1}{\varepsilon - f} \left(\varepsilon \cdot N_L - N_T \right) \ . \tag{5.6}$$

In order to obtain two independent event samples, which means that their correlations do not have to be taken into account, the loose lepton category is split into two disjoint subsamples

$N_L = N_T + N_A$, which contain either events with a lepton candidate passing the tight selection requirements N_T or those events having exactly one lepton that fails the tight requirements N_A. Using this relation, Equation 5.6 can be re-written as:

$$N_{QCD} = \frac{1}{\varepsilon - f}\left((\varepsilon - 1) \cdot N_T - \varepsilon N_A\right) \ . \tag{5.7}$$

However, it is required to know both the total event yields and the shape of all relevant kinematic distributions (as e.g. the lepton and jet p_{T}) in order to estimate the impact of the non-prompt lepton background to the mass spectrum of the selected $t\bar{t}$ candidates. The shapes of the various kinematic distributions required in the following studies are obtained by applying Equation 5.7 on each candidate event individually, setting (N_T, N_A) to $(0, 1)$ or $(1, 0)$ depending whether or not the lepton of the loose category passes or fails the tight object definitions.

Crucial for the estimation of the non-prompt lepton background via the matrix method is the determination of the reconstruction efficiencies ε and f. Their measurement is performed in a control region in data, which is defined by inverting, relaxing or removing certain event and object selection requirements. Hence, the missing transverse energy and the transverse W-boson candidate mass have to fulfill $E_{\mathrm{T}}^{\mathrm{miss}} < 20$ GeV and $E_{\mathrm{T}}^{\mathrm{miss}} + m_{\mathrm{T},W} < 60$ GeV. In addition the cut on the $\log_{10}(\chi^2)$ is removed for events assigned to the resolved channel, while the selection criteria for the large-radius jet are changed to $p_{\mathrm{T}} > 100$ GeV, $\sqrt{d_{12}} > 0$ GeV and $m < 70$ GeV for events from the boosted decay channel. Both reconstruction efficiencies ε and f are measured as a function of the lepton p_{T}, the ΔR between the lepton and its closest jet and the p_{T} of this jet, while the corresponding uncertainties are evaluated by altering the definition of the control regions.

The estimation of the non-prompt lepton background is performed for each of the two lepton channels separately, where the isolation requirements are removed for both electron and muon candidates to define the loose lepton category. The corresponding normalisation uncertainties were found to be 20.1% for e+jets events and 22.6% for μ+jets events in the resolved channel and 19.4% (e+jets) and 18.9% (μ+jets) in the boosted decay channel. Further details on the extraction of the efficiencies for prompt and non-prompt leptons ε and f can be found in Reference [36], while the matrix method formalism is also extensively explained in Reference [140].

Chapter 6

A new *b*-tagging algorithm dedicated to identifying *b*-jets in boosted top-quark decays

The identification of isolated *b*-jets was studied intensively in the Monte Carlo simulation adapted to the expected conditions of pp collisions at centre-of-mass energies of 7 TeV and 8 TeV as well as in the data that was recorded by the ATLAS detector during the LHC runs in 2011 and 2012. As searches for new physics will gradually probe higher and higher masses, the corresponding analyses will focus more strongly on event topologies containing highly boosted massive particles such as top-quarks, W-, Z- or Higgs-bosons. Since top-quarks and Higgs-bosons predominantly decay into final states including *b*-quarks the importance of understanding the performance of the ATLAS *b*-tagging algorithms (which are summarised in Section 4.3) in dense environments (i.e. a topology containing several close-by jets) will increase. The following chapter demonstrates the main problems related to the identification of *b*-jets inside the dense environments of boosted top-quark decays (i.e. the degradation of the *b*-hadron direction resolution and the contamination with tracks from nearby light-flavour decays). In addition, the development of a new set of multivariate analysis (MVA) based *b*-tagging algorithms is described. The corresponding taggers are referred to as MVb and MVbCharm. The choice of their input quantities and training procedures are modified with respect to the current ATLAS *b*-tagging tools to take the conditions of boosted topologies better into account. The performance of these new taggers is extensively tested in both boosted and resolved event topologies using information that is obtained from Monte Carlo simulation and compared to the current ATLAS default *b*-tagger, MV1. A first validation of these tools is shown in Chapter 8, where the predicted distributions of the most important input quantities and their MVA outputs are compared to data that was measured by the ATLAS detector in the 2012 run of the LHC. A complete calibration of the *b*-tagging efficiencies corresponding to the MVb tagger is demonstrated in this Chapter additionally for a representative operating point using a new developed approach. This method is dedicated to measurements of *b*-tagging efficiencies in dense jet environments (i.e. in hadronic top-quark decays) in order to probe whether the performance of these new tagging algorithms is compatible in data and in the simulation.

6.1 Problems related to the identification of *b*-jets inside dense environments

A crucial feature of highly boosted massive particles is their strongly collimated decay products. The angular separation ΔR in the $\eta - \phi$-plane between the decay products of a particle with the mass m and the transverse momentum p_{T} can be approximated in case of a 2-body decay [91] by

$$\Delta R \approx \frac{2m}{p_{\mathrm{T}}} \,. \tag{6.1}$$

Hence the decay products of a top-quark with a transverse momentum of $p_{\mathrm{T}}^{\mathrm{top}} = 450$ GeV tend to have an angular separation smaller than 0.8, which is twice the radius of the jets that are typically used for b-tagging purposes in ATLAS. For ΔR values below this threshold, the standard jet reconstruction techniques start failing to resolve the decay products of a hadronic final state individually. This leads for example to the problem that the reconstructed jets might not sufficiently resemble the partons from the decay $t \to bW \to bq\bar{q}$, as the particle showers corresponding to more than one parton could be combined into one jet. These effects are irrelevant for most of the SM top-quark pair production as only about 1% of all the top-quarks are produced with a p_{T} of more than 450 GeV. However, these problems become more important in e.g. searches for $t\bar{t}$ resonances. In $Z' \to t\bar{t}$ events simulated with a Z' mass of 1 TeV, approximately 12% of all top-quarks are predicted to be produced with a p_{T} exceeding this threshold. For resonance masses of 1.5 TeV and 2.5 TeV, these fractions even increase to about 58% and 72%, respectively. These numbers indicate impressively how important it is to develop dedicated reconstruction techniques in order to be sensitive to search for new heavy particles decaying into top-quark pairs.

Figure 6.1 visualizes the p_{T} dependence of the angular separation ΔR between the W-boson and the b-quark in simulated top-quark decays (generated using both POWHEG and PYTHIA), as well as the p_{T} dependence of the minimal separation between the b-quark and the two resulting partons stemming from the $W \to q\bar{q}$ decay.
The identification of b-hadrons inside the dense environment of a boosted hadronic top-quark decay or also in a boosted $H \to b\bar{b}$ decay is much more demanding than in resolved topologies as tracks can easily be assigned to the wrong source if the decay products are close to each other. A further shortcoming under these conditions is the degradation of the resolution of the b-hadron direction which is approximated by the axis of the corresponding reconstructed jet in certain steps of the calculation of any b-tagging related quantity. As additional activity next to a jet can change the axis direction considerably, this approximation might no longer be valid. Therefore it is important to investigate the performance of the various ATLAS b-tagging algorithms and their input quantities for b-jets that overlap partially or are merged completely with a particle shower induced by the partons resulting from the $W \to q\bar{q}$ decay. A simple approach to study the b-tagging performance in hadronic top-quark decays is to calculate for each reconstructed b-jet the minimal distance to the quarks (at generator level) that originate from the $W \to q\bar{q}$ decay

$$\Delta R^{\mathrm{min}} = \min\{\Delta R(b\text{−jet}, q), \Delta R(b\text{−jet}, \bar{q})\} \tag{6.2}$$

and probe the b-tagging efficiency of the different taggers as a function of this quantity. This approach is of course only applicable in the simulation, whereas reconstructable variables are

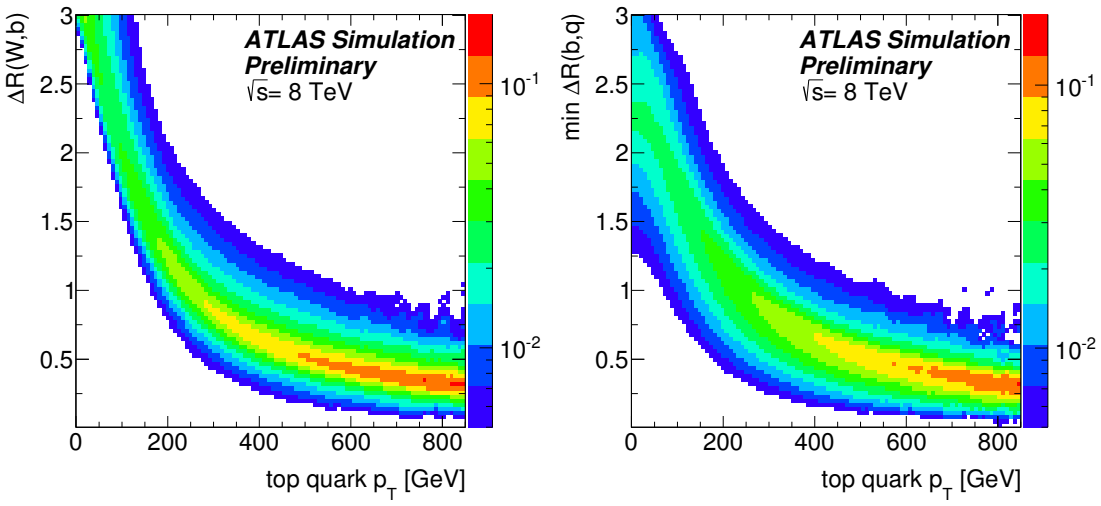

(a) $\Delta R(W,b)$ vs. top p_{T} [7]

(b) $\min \Delta R(b,q)$ vs. top p_{T} [7]

Figure 6.1: Angular distance ΔR between the W-bosons and b-quarks in $t \to bW$ decays as a function of the transverse momentum of the top-quark (a), and smallest distance ΔR^{min} in the $\eta - \phi$-plane between the b-quark and the decay products of the W-boson in $t \to bW \to bq\bar{q}$ decays (b) as a function of the top-quark p_{T}. The distributions are normalised column-wise in the p_{T} bins and the colour coding corresponds to the fraction of considered top-quarks. Both distributions correspond to the particle information at the generator level after the emission of initial and final state radiation and are obtained from $t\bar{t}$ decays simulated using POWHEG+PYTHIA.

essential to understand the performance in data. However, this quantity allows the identification of those variables used in the various b-tagging algorithms that are sensitive to a jet overlap. Hence b-jets are classified according to their distance to the nearest W-boson decay product, so that jets are considered as merged if their ΔR^{min} is smaller than the size of the radius parameter used in the jet clustering procedure, which is $R = 0.4$ in these studies.

Figure 6.2 (a) shows the b-tagging efficiency of the current ATLAS default tagger, MV1, as a function of this quantity separately for three different jet p_{T} regions. The chosen operating point corresponds to an overall b-tagging efficiency of 70% for b-jets selected from the simulated SM $t\bar{t}$ sample according to the object definition criteria described in Section 3.3.5. It can be seen that the tagging performance is degraded noticeably if the distance between a b-jet and the W-boson decay products decreases. The total loss of efficiency due to a partial overlapping or even a complete merging of the b-jet with a decay product of the W-boson seems to be only slightly dependent on the jet p_{T} and an overall loss by a factor of 1.7 can be observed from the highest to the lowest considered ΔR^{min} values. The same comparisons for the JetFitterCombNN, the IP3D, the SV1 and the SV0 taggers reveal that the degradation effect occurs regardless of whether the studied b-tagger is based on the track impact parameters, the secondary vertex properties or a neural network combining both. The dependence of the b-tagging efficiency on the ΔR^{min} between the b-quark jets and the hadronic decay products of the W-boson are displayed in Figures 6.2 (b-e). This ΔR dependence is similar for all these b-tagging algorithms. In addition, the total loss in their b-tagging efficiency is found to be in the same order of magnitude as for the MV1 tagger.

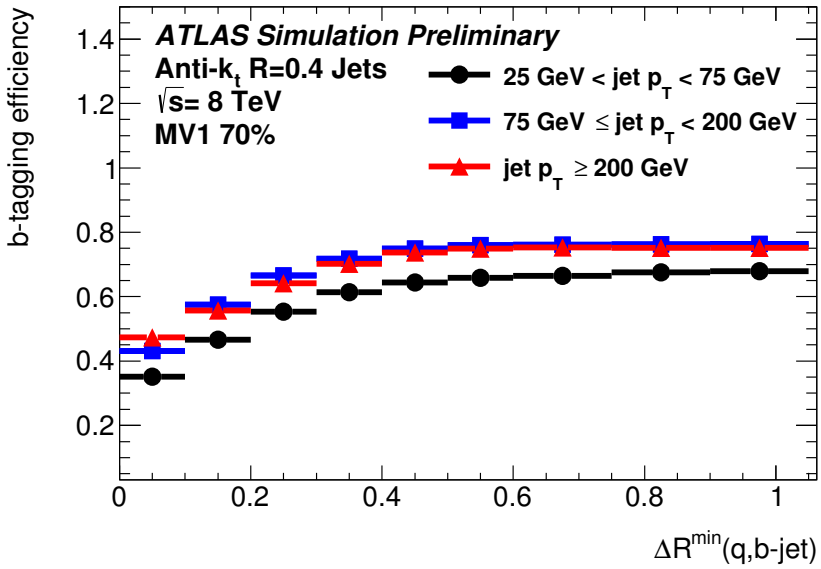

(a) Neural network based tagger (MV1) [7]

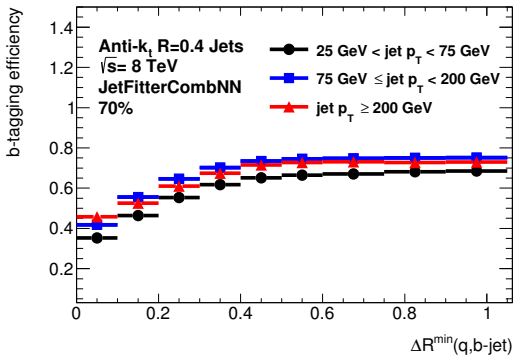

(b) Neural network based tagger (JetFitterCombNN)

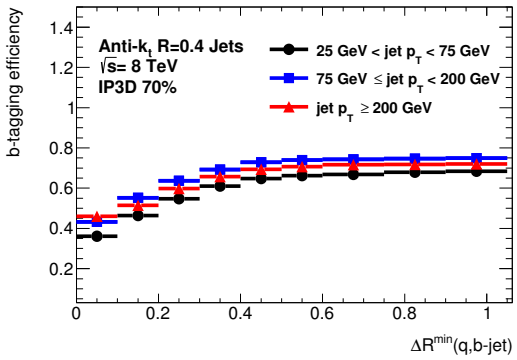

(c) Impact parameter based tagger (IP3D)

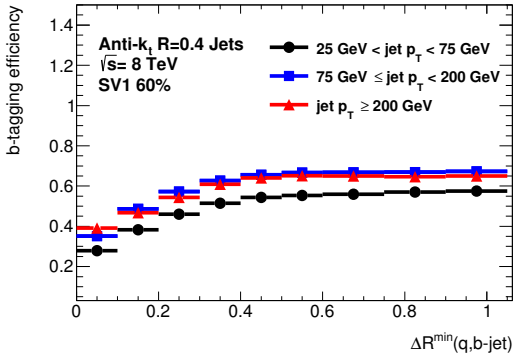

(d) Secondary vertex based tagger (SV1)

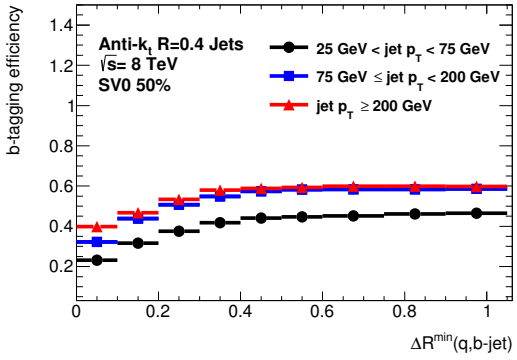

(e) Secondary vertex based tagger (SV0)

Figure 6.2: The b-tagging efficiencies' dependence on the ΔR^{min} between the b-quark jets and the closest hadronic decay product of the W-boson stemming from top-quark decays for the MV1 algorithm (a) as well as for the JetFitterCombNN (b), the IP3D (c), the SV1 (d), and the SV0 (e) taggers. The chosen working points correspond to an overall b-tagging efficiency of 70% for all these algorithms, except for the SV1 and the SV0 taggers, which are investigated at operating points that correspond to b-tagging efficiencies of 60% and 50%, respectively. Jets obtained from simulated SM $t\bar{t}$ decays are classified into three different p_{T} regions and studied separately.

The following sections are dedicated to study in more detail possible reasons for the performance loss of the main ATLAS b-tagging algorithms observed in boosted hadronic top-quark decays. In this context, it is studied to what extent effects like the degradation of the jet axis direction resolution (in Section 6.1.1) or the contamination with tracks from nearby light-flavour decays (in Section 6.1.2) contribute to the degradation of performance of these b-tagging algorithms.

6.1.1 Shift of the jet axis

One of the major problems connected to b-tagging in dense environments is the resolution of the b-jet direction, which is here quantified by the angular separation between the flight direction of a b-hadron at generator level and the axis direction of the associated jet at reconstruction level $\Delta R(b\text{−hadron, jet})$. Additional activity in the calorimeter clusters next to those stemming from a b-jet can skew the jet axis away from the flight direction of the b-hadron, if the non-b-hadron component next to the jet has enough energy.

When the distance in the $\eta - \phi$-plane between the b-jet axis and the b-hadron flight direction becomes too large, tracks from the b-hadron decay might no longer be matched to the jet and therefore not be taken into account in the calculation of the several b-tagging discriminants. Related to this problem is also a degradation of the reconstruction efficiency for secondary vertices, a change of the vertex properties and a reduction in the ability to determine correctly the sign of the track impact parameters. As a consequence of these effects, the performance of the various b-tagging algorithms degrades considerably with increasing ΔR values.

The b-tagging efficiency as a function of the jet axis shift $\Delta R(b\text{−hadron, jet})$ is shown in Figure 6.3 (a) for the current ATLAS default b-tagger at an operating point corresponding to an overall efficiency of 70%. Jets with a p_{T} below 75 GeV show a total efficiency loss by a factor of 4 over the full range of ΔR values. For jets with a transverse momentum between 75 GeV and 200 GeV a total loss by a factor of 7 is observed as their b-tagging efficiency decreases from 80% for jets that are perfectly aligned to the b-hadron flight direction ($\Delta R = 0$) to 12% for jets that have a ΔR larger than 0.25. The b-tagging efficiency for jets with $p_{\mathrm{T}} > 200$ GeV decreases from 80% to 5%, which corresponds to a reduction by a factor of 16. The b-tagging efficiency degradation is more pronounced for high-p_{T} jets due to the smaller radius used in the track-to-jet association procedure, which was explained in Section 4.2.1.

Again, the same comparisons are performed for the JetFitterCombNN, the IP3D, the SV1 and the SV0 taggers. Their b-tagging efficiencies' dependence on the $\Delta R(b\text{−hadron, jet})$ are displayed in the Figures 6.3 (b-e). It is shown that a degradation effect, similar to that of the MV1 algorithm, occurs for all studied b-tagging algorithms (regardless of whether they are based on the track impact parameters, the secondary vertex properties or a neural network combining both). When comparing the performance loss of the various b-tagging algorithms in more detail, it becomes obvious that the vertex-based b-tagging algorithms (i.e. SV0 and SV1) are more sensitive to a shift of the jet axis than the b-taggers that are based on the track impact parameters (i.e. the IP3D tagger).

For the IP3D tagger the b-tagging efficiency for jets that have a ΔR larger than 0.25 and a p_{T} below 75 GeV is decreased by a factor of 3 with respect to those jets that are perfectly aligned to the b-hadron flight direction. Jets with a p_{T} in the range between 75 GeV and 200 GeV show a total efficiency loss by a factor of 5 over the full range of ΔR values, while a reduction by a factor of 8 is seen for jets with a p_{T} above 200 GeV. The b-tagging efficiencies corresponding to the SV1 (SV0) algorithm are reduced by factors of 5 (4), 8 (5), and 18 (9) for these three p_{T}

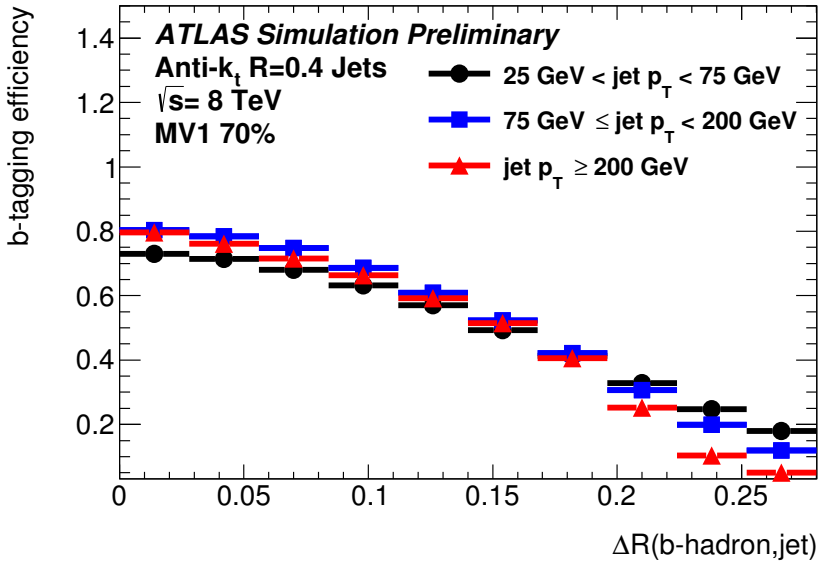

(a) Neural network based tagger (MV1) [7]

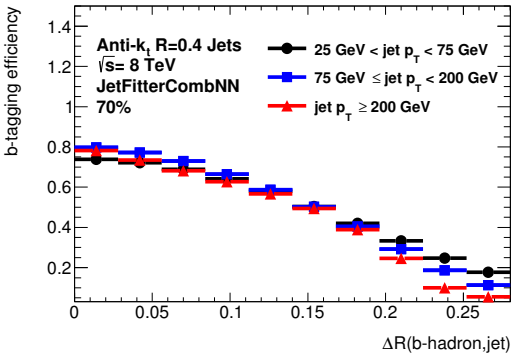

(b) Neural network based tagger (JetFitterCombNN)

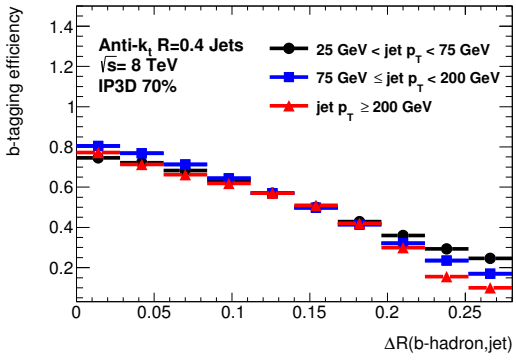

(c) Impact parameter based tagger (IP3D)

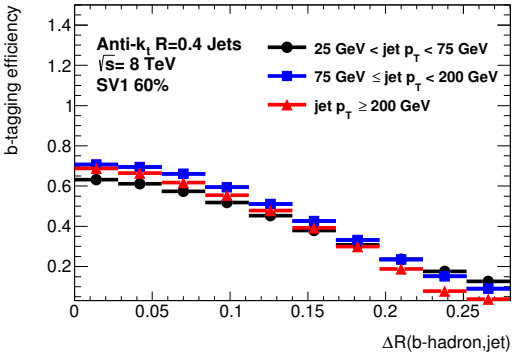

(d) Secondary vertex based tagger (SV1)

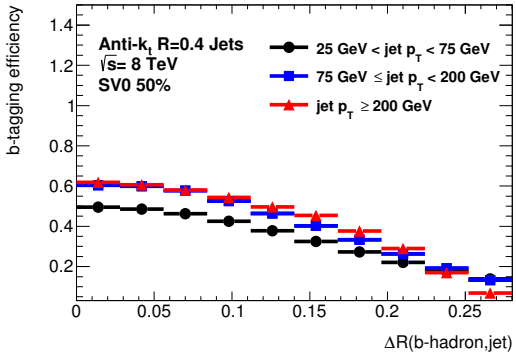

(e) Secondary vertex based tagger (SV0)

Figure 6.3: The b-tagging efficiency of the MV1, JetFitterCombNN, IP3D, SV1 and SV0 taggers as a function of the angular separation between the jet axis and the b-hadron $\Delta R(b-\text{hadron}, \text{jet})$. The chosen operating points correspond to overall b-tagging efficiencies of 70%, 60% and 50%. Jets obtained from simulated SM $t\bar{t}$ decays are classified into three different p_{T} regions and studied separately.

regions. The dramatic decrease of the b-tagging efficiencies corresponding to the vertex-based b-tagging algorithms with increasing ΔR values is simply caused by the degradation of the vertex reconstruction efficiencies of the corresponding vertex finders (i.e. the JetFitter algorithm or the iterative vertex finder). This is related to the problem that in case where the track-to-jet association procedure loses several tracks stemming from the b-hadron decay, the vertex fit might fail.

However, the loss of tracks in the track-to-jet association procedure is not the only reason for a decrease of the vertex finding efficiencies of both the JetFitter algorithm and the iterative vertex finder (using the SV1 setup). The shift of the jet axis can also have an influence on the sign of the decay length of a reconstructed secondary vertex, which might be flipped from positive to negative (or vice versa). Such a flip of the sign of the decay length degrades the vertex finding efficiency as both the JetFitter algorithm and the iterative vertex finder (applied with the SV1 setup) reject secondary vertex candidates having a negative decay length.

The efficiency to find a secondary vertex in a b-jet using the iterative vertex finder with the SV1 setup or the JetFitter algorithm is displayed in Figures 6.4 (a) and 6.4 (b) as a function of the angular separation $\Delta R(b\text{−hadron}, \text{jet})$ between the b-hadron flight direction and the jet axis. Both vertex finders show qualitatively a similar behaviour for increasing ΔR values. But as the JetFitter algorithm is capable of reconstructing single-track vertices, its finding efficiency is consistently higher than that of the iterative vertex finder. In the lowest p_{T} bin, about 90% (70%) of all jets that are perfectly aligned to the b-hadron flight direction have a secondary vertex reconstructed with the JetFitter algorithm (iterative vertex finder based on the SV1 setup). The efficiency decreases to approximately 40% (30%) for jets with a $\Delta R > 0.25$ to the nearest b-hadron. The loss of the vertex finding efficiency in jets having a large angular separation to the b-hadron flight direction $\Delta R(b\text{−hadron}, \text{jet}) > 0.18$ is more pronounced for high-p_{T} b-jets as their ΔR-cone used in the track-to-jet association procedure is smaller.

The reduction of the vertex finding efficiency for large values of the angular separation between the b-hadron and the jet axis is the main reason for a decrease of the b-tagging efficiency, but

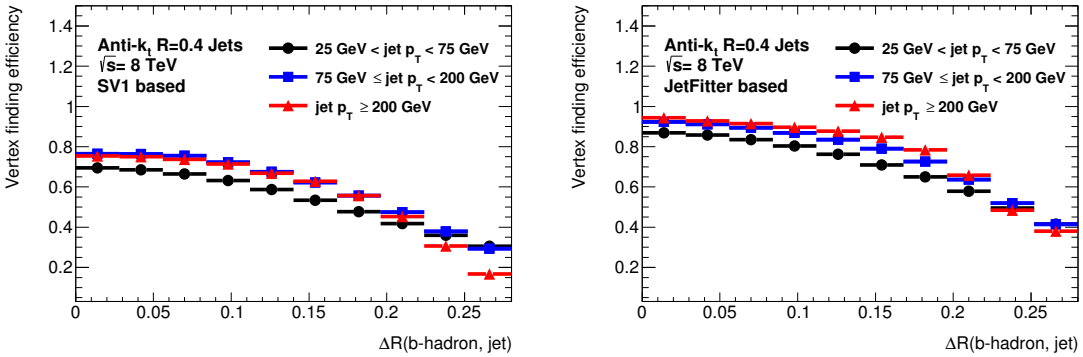

(a) iterative vertex finder (using the SV1 setup)

(b) JetFitter algorithm

Figure 6.4: Secondary vertex finding efficiencies of the iterative vertex finder using the SV1 setup (a) and the JetFitter algorithms (b) as a function of the angular separation between the jet axis and the b-hadron direction $\Delta R(b\text{−hadron}, \text{jet})$. The vertex finding efficiencies are displayed for reconstructed b-jets that are obtained from SM $t\bar{t}$ decays, which are simulated using the POWHEG and PYTHIA generators. Jets are classified into three different p_{T} regions and studied separately.

other effects can also appear. Figures 6.5 (a) and (b) show the average number of tracks associated to the secondary and tertiary vertices that are reconstructed within a selected b-jet using either the iterative vertex finder (with the SV1 setup) or the JetFitter algorithm as a function of the $\Delta R(b-\text{hadron}, \text{jet})$. For vertex candidates that are reconstructed with the iterative vertex finder, the average track multiplicity is decreased by a factor of 1.4 to 1.6 over the full range of ΔR values, while the average track multiplicity of the vertices that are reconstructed with the JetFitter algorithm are decreased by a factor of up to 3. For both algorithms, the decrease is more pronounced for the high-p_{T} b-jets.

As the number of tracks assigned to a secondary vertex decreases with increasing angular separation between the flight direction of the b-hadron and the axis direction of the associated jets, other vertex properties like the invariant mass or the energy fraction are distorted. In addition, also a decline of the secondary vertex quality is observed since vertex properties like the $\log_{10}(\chi^2/\text{ndof})$ or the significance of the measured 3-dimensional decay length are substantially affected by a shift of the jet axis direction, as the uncertainty on the vertex position increases if information (i.e tracks) are missing. The $\Delta R(b-\text{hadron}, \text{jet})$ dependence of the average decay length significance is displayed in Figure 6.6 (a), where a decrease by a factor of 2.6 to 3.2, depending on the kinematics of the studied jets, is observed over the full range of ΔR values. To conclude, the vertex properties become more and more dissimilar to the reference distribution used in the training of a MVA-based b-tagger, if the number of missing tracks at the displaced vertices increases or if the quality of these vertices declines.

Similarly to the sign of the decay length, the sign of the track impact parameter is calculated with respect to the jet axis as an approximation of the b-hadron flight direction and therefore depends strongly on the resolution of the jet direction. With increasing values of the angular separation between the jet and the b-hadron, the fraction of tracks for which the impact parameter sign is flipped from positive to negative increases substantially.

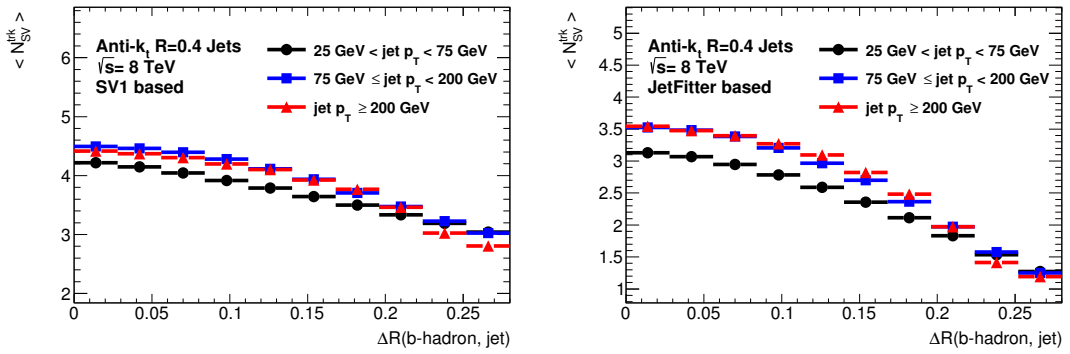

(a) SV1 based **(b)** JetFitter based

Figure 6.5: Average number of tracks associated to the secondary vertex candidates as a function of the angular separation between the jet axis and the b-hadron flight direction for vertices reconstructed with the iterative vertex finder using the SV1 setup (a) and the JetFitter algorithm (b). These properties are investigated for selected b-jets that are obtained from SM $t\bar{t}$ decays, which are simulated using the POWHEG and PYTHIA generators. Jets are classified into three different p_{T} regions and studied separately.

In order to quantify the importance of this effect, the average fraction of tracks that have a positively signed transverse impact parameter is studied as a function of the $\Delta R(b-\text{hadron}, \text{jet})$ for three different p_{T} regions and displayed graphically in Figure 6.6 (b). For these curves only those tracks are considered that are both successfully matched to a b-jet and stem directly from the b-hadron decay cascade (using information at the generator level). It is shown that on average 85% to 93% (with the exact value depending on the transverse momentum of the jet) of all b-hadron tracks inside the studied jets have a positively signed transverse impact parameter, in case the axis of the probed jets is perfectly aligned to the flight direction of the initial b-hadron. With increasing ΔR values a significant decrease in the average track fraction is observed. For ΔR values above 0.25, the average fraction of tracks with a positively signed transverse impact parameter per jet ranges between 38% and 50%. Thus a decrease by a factor of down to 0.4 is seen for jets with a p_{T} above 200 GeV and approximately 0.5 for jets with a p_{T} below 200 GeV.

Therefore, the impact parameter based taggers (IP3D or IP2D), which use the signed transverse and longitudinal track impact parameter significance as an input, are also strongly affected by the jet axis shift. However, the dependence that the shift of the jet axis direction has on the IP3D and IP2D taggers is reduced, as the sign of the track impact parameters is calculated with respect to the line connecting the secondary and primary vertex instead of the jet axis direction if the studied jet has a reconstructed secondary vertex.

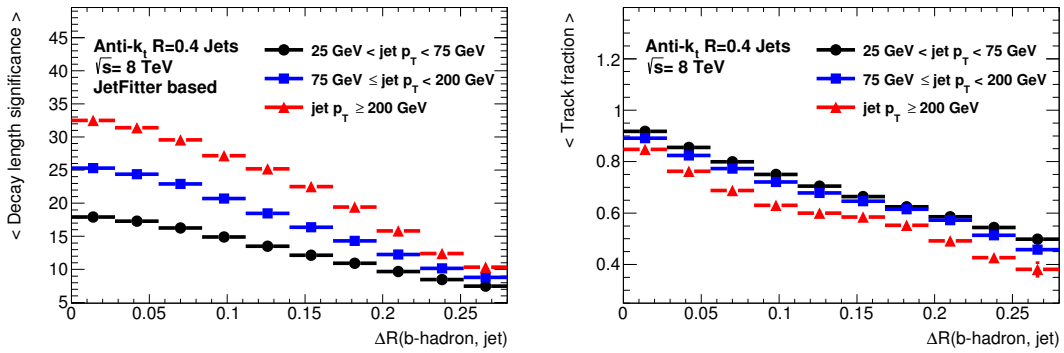

(a) JetFitter based **(b)** track based

Figure 6.6: Average decay length significance (a) for vertices reconstructed with the JetFitter algorithm as well as the average fraction of b-hadron tracks inside a flavour labelled b-jet that have a positive impact parameter sign. Both jet properties are shown as a function of the angular separation between the b-hadron flight direction at generator level and the axis direction of the associated jet. The track fractions are determined using only those jets which contain at least four tracks associated to the decay products of the b-hadron (using information at the generator level). Both studies are based on selected b-jets that are obtained from SM $t\bar{t}$ decays, which are simulated using the POWHEG and PYTHIA generators. Jets are classified into three different p_{T} regions and studied separately.

6.1.2 Light-flavour contamination

Even if the jet axis is not shifted substantially away from the flight direction of the b-hadron, additional activity close-by a b-jet can still lead to a contamination with tracks from light-flavour

decays. Several b-jet properties are sensitive to such a contamination. As most b-tagging algorithms are based on pre-defined reference distributions corresponding to several jet properties, the performance of these b-taggers will degrade with an increasing contamination of tracks from light-flavour decays. The most crucial differences between tracks resulting from heavy and light-flavour decays appear in the distributions of their transverse and longitudinal impact parameter significance. As the jet weights of the IP2D and IP3D taggers are calculated using the impact parameter significance of all tracks associated to a particular jet, both are good examples of quantities that are strongly influenced by a contamination with light-flavour tracks. In order to quantify the effect that an increasing contamination has on the performance of any b-tagging algorithm, the track purity is defined for a b-jet as the number of tracks associated to the b-hadron decay divided by the total number of tracks assigned to the jet. A low track purity is strongly correlated with a high contamination with tracks from light-flavour quarks or gluon fragmentation and vice versa. Figure 6.7 (a) and (b) show the b-tagging efficiencies of the IP3D and MV1 algorithms as a function of this quantity for three different jet p_{T} regions and an operation point corresponding to an overall efficiency of 70%. It can be seen that the b-tagging efficiencies for both taggers decrease considerably if the track purity declines to smaller values. In the displayed range of track purity values the efficiency is decreased by a factor of 2.6-2.8 for the IP3D tagger (with the exact value depending on the transverse momentum of the jet) and by a factor of 1.7-2.1 for the MV1 algorithm. As the IP3D tagger is based only on information concerning the track impact parameters its performance is more affected than that of the MV1 tagger. However, the MV1 algorithm uses the IP3D jet weight as an input to its neural network. Thus the strong dependence on additional tracks from light-flavour decays is propagated to it.

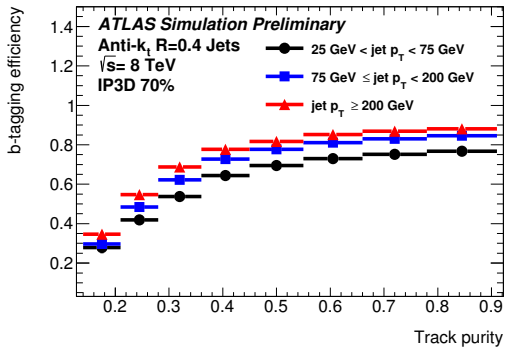

(a) b-tagging efficiency (IP3D) vs. purity [7]

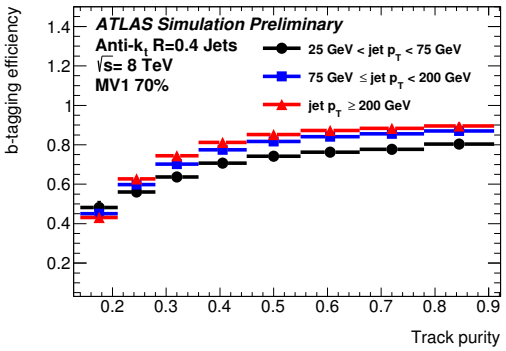

(b) b-tagging efficiency (MV1) vs. purity [7]

Figure 6.7: b-tagging efficiencies of the IP3D (a) and MV1 (b) algorithms as a function of the track purity of the studied jets. The results are shown separately for three different jet p_{T} ranges and correspond to an operating point that has an overall efficiency of 70%. To ensure that a low track purity is related to a contamination with tracks from light-flavour decays, rather than to the missing of tracks from the b-hadron decay, only those jets that contain at least three tracks associated to the decay products of the b-hadron are considered. The jets used for this study are obtained from a sample of SM $t\bar{t}$ decays, which are simulated using the POWHEG and PYTHIA generators.

6.1.3 Influence on the *b*-tagging related quantities

After discussing the impact that a jet axis shift or a contamination with tracks from light-flavour decays has on the performance of the current ATLAS *b*-tagging algorithms, the various input quantities of the MVA based taggers are studied individually. The aim is to identify those quantities that are affected the most if a *b*-jet contains also particles coming from a hadronic *W*-boson decay. Examples are shown in Figure 6.8. In addition, further quantities are presented (in Section 6.2) that are not yet used in any of the current high performance algorithms, but promise to be beneficial for the identification of *b*-jets in boosted topologies. For this purpose, the various *b*-tagging related properties of single and merged *b*-jets are compared to each other. Here the previous definition of a merged jet (those containing two ΔR-matched quarks from the $t \to bW \to bq\bar{q}$ decay) is used.

Most of the *b*-tagging related quantities are strongly dependent on the jet kinematics. As the p_{T} spectra for single and merged *b*-jets are different, a re-weighting has to be applied in order to make their properties comparable. After this procedure, the p_{T} distribution (at the reconstruction level) of both jet types are identical in shape. Since light-flavour jets are included in the following comparisons the same re-weighting technique is applied to them as well.

Examples of quantities that are strongly influenced by a jet overlap (as they loose some of their strength to separate between *b*- and light-flavoured jets) are the jet weights of the IP2D and IP3D taggers, the energy fraction as well as the uncertainties on the θ or ϕ coordinates of the reconstructed vertices or the so-called vertex imbalance. Quantities like the total track multiplicity at the displaced vertices, the invariant mass of these tracks, the number of two-track vertices, the $\log_{10}\left(\chi^2/\mathrm{ndof}\right)$ of the vertex fit, the transverse decay length or the decay length significance are more stable. In general, the quantities based only on charged particle tracks associated to the displaced vertices are less affected than those which also depend on other tracks within the jet. This means that the impact on quantities like the energy fraction are related to a change in the jet properties, rather than to a change in the vertex properties, as additional tracks from light-flavour decays are intrinsically rejected by the vertex fit. However, as the contamination with additional tracks from light-flavour decays and the shift of the jet axis lead to a degradation of the quality of the vertex fit (i.e. causing higher uncertainties on the obtained vertex position or an increase in the fraction of jets that have only single-track vertices reconstructed), quantities such as the decay length significance or the total track multiplicity at the displaced vertices show at least a small influence due to a jet overlap.

Conclusions concerning the degree of the vertex quality degradation in merged *b*-jets can be for example drawn from the first bin of the distribution that corresponds to the track multiplicity at the secondary vertex, as this bin represents the number of jets, which have only single-track vertices reconstructed. The distribution of this quantity is shown separately for the inclusive *b*-jet sample, for merged *b*-jets and also for light-flavour jets in Figure 6.9 (b). For the inclusive *b*-jet sample, 18% of all jets contain only single-track vertices, while this fraction increases to approximately 24% for the merged *b*-jets. Thus an increase by a factor of 1.3 is observed.

Examples for distributions corresponding to quantities that are sensitive to a jet overlap and those which are not are presented in Figures 6.8 (a) to (f) and in Figures 6.9 (a) to (f). As a reminder, the exact definitions of the several quantities that are based on the reconstruction of displaced vertices are given in Table 4.3.

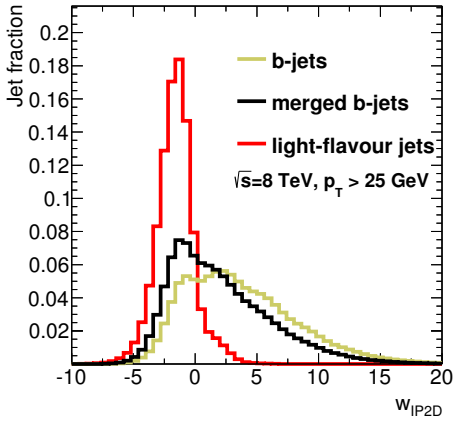

(a) IP2D weight

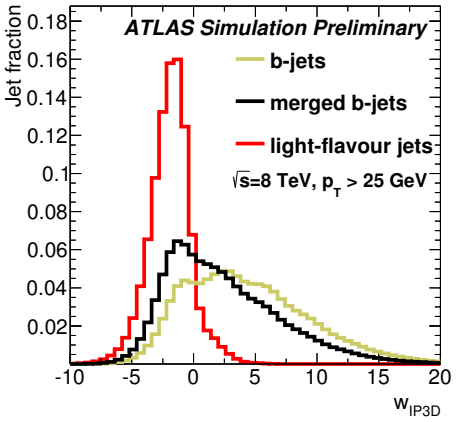

(b) IP3D weight [7]

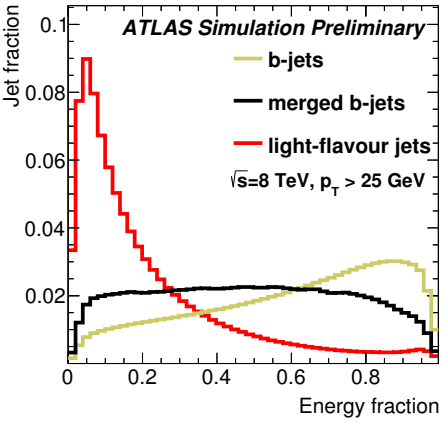

(c) energy fraction (JetFitter based) [7]

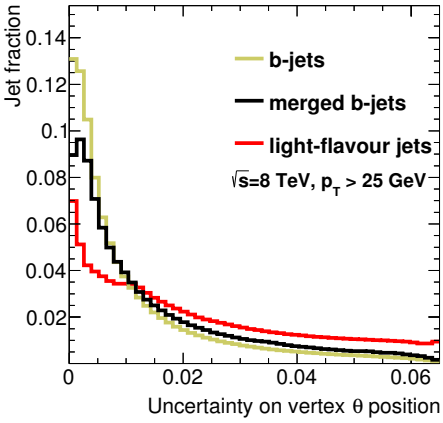

(d) uncertainty on vertex θ position (JetFitter based)

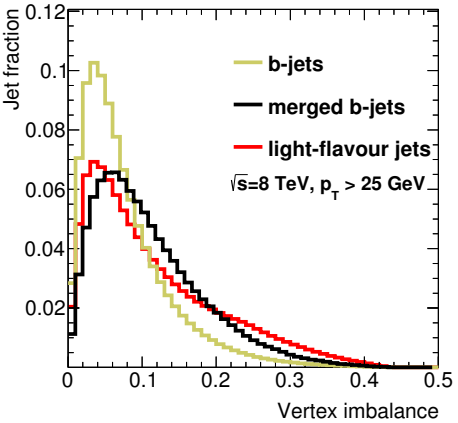

(e) vertex imbalance (JetFitter based)

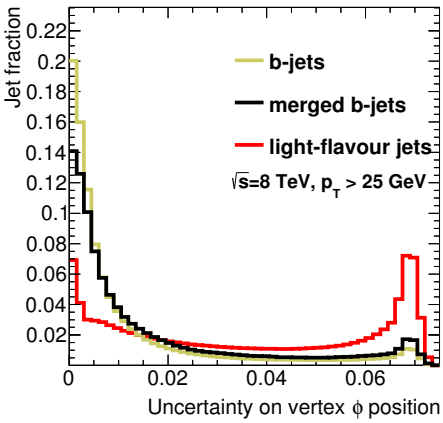

(f) uncertainty on vertex ϕ position (JetFitter based)

Figure 6.8: Distributions of the IP2D and IP3D jet weights (a-b), the energy fraction (c), uncertainty on the θ coordinate (d), the vertex imbalance (e), as well as the uncertainty on the ϕ coordinate (f) of the reconstructed vertices are presented for the inclusive b- (yellow), merged b- (black) and light-flavour jets (red). Each distribution is individually normalised to unit area. The considered jets stem from simulated $t\bar{t}$ decays that are generated with $\sqrt{s} = 8$ TeV and have $p_{\mathrm{T}} > 25$ GeV and $|\eta| < 2.5$.

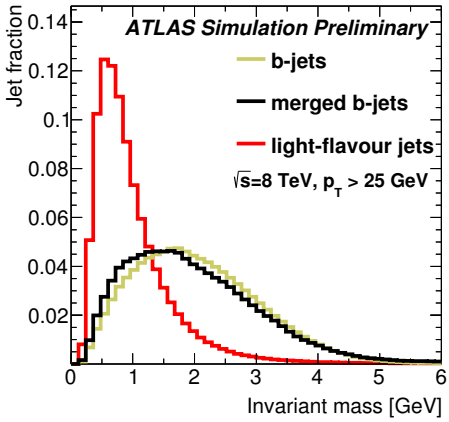

(a) invariant mass (SV1 based) [7]

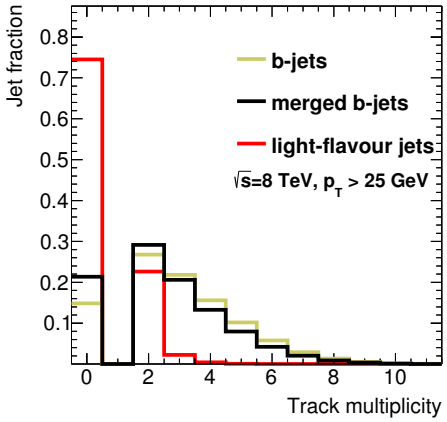

(b) track multiplicity at the secondary vertex (JetFitter based)

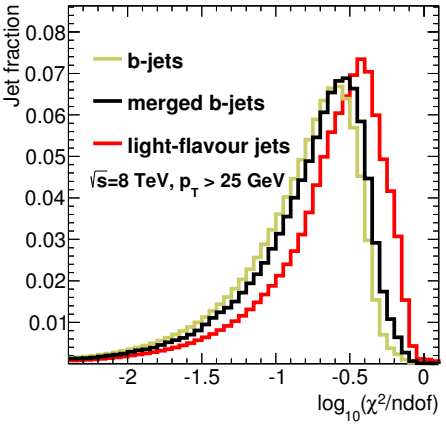

(c) $\log_{10}\left(\chi^2/\text{ndof}\right)$ (JetFitter based)

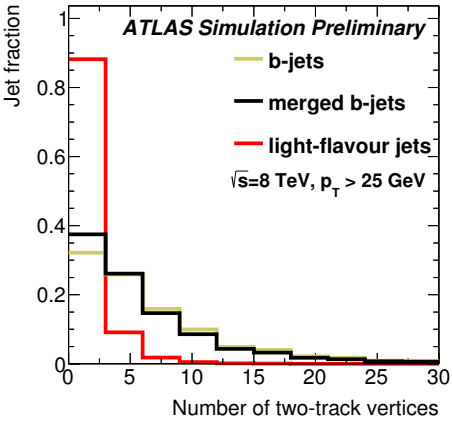

(d) number of two-track vertices (JetFitter based) [7]

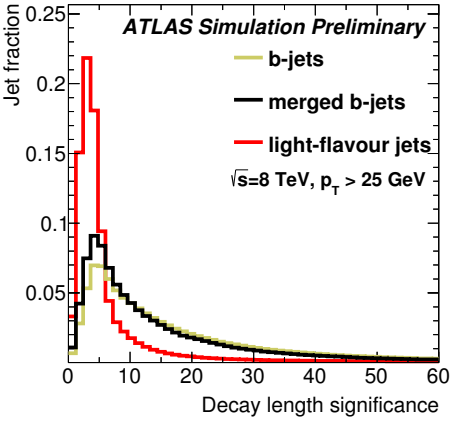

(e) decay length significance (SV1 based) [7]

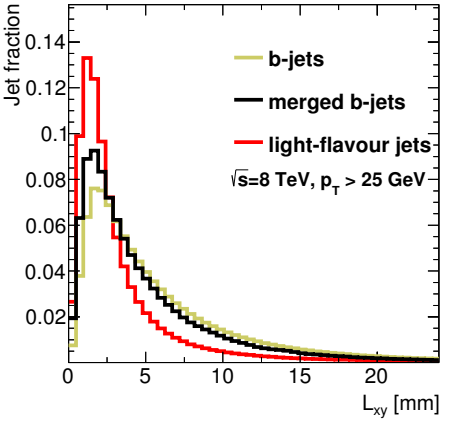

(f) transverse decay length (SV1 based)

Figure 6.9: Distributions of the invariant mass (a), the track multiplicity at the secondary vertex (b), the $\log_{10}\left(\chi^2/\text{ndof}\right)$ (c), the number of two-track vertices (d), the decay length significance (e) and the transverse decay length (f) are presented for the inclusive b- (yellow), merged b- (black) and light-flavour jets (red). Each distribution is individually normalised to unit area. The considered jets stem from simulated $t\bar{t}$ decays that are generated with $\sqrt{s} = 8$ TeV and have $p_{\text{T}} > 25$ GeV and $|\eta| < 2.5$.

6.2 Alternative quantities

The previously discussed quantities are already used by several of the ATLAS b-tagging algorithms. Additional variables can provide new information that might help to distinguish between light- and heavy-flavour jets or improve the stability of a b-tagging algorithm with respect to the effects connected to dense environments. In order to achieve this goal, possible new input quantities should not show a dramatic loss of their separation strength between b- and light-flavour jets under such conditions.

Quantities that describe the shape of a jet are good candidates as the fragmentation of b- and light-flavour quarks is very different due to the large mass difference of these two quarks [141]. An example for such a shape-related quantity is the so-called jet width w_{jet}, which is defined as the p_{T} weighted average distance ΔR between the tracks associated to a jet and its axis direction:

$$w_{\text{jet}} = \frac{\sum_{i=1}^{N} p_{\text{T}}^{\text{trk}_i} \Delta R(\text{trk}_i, \text{jet})}{\sum_{i=1}^{N} p_{\text{T}}^{\text{trk}_i}} \,. \tag{6.3}$$

The distribution of the jet width is shown in Figure 6.10 (a), where for jets that do not have any charged particle tracks associated, the width is set to 0. It can be seen that this quantity provides indeed a small separation between the inclusive b- and the light-flavour jets. For merged b-jets this separation strength is even increased.

As the IP2D and IP3D weights for b-hadron jets are strongly affected by an increase of the additional tracks stemming from light-flavour quarks or gluon fragmentation, it is beneficial to use mainly tracks that have a relative large and positively signed impact parameter significance. A simple approach to obtain one single variable from these tracks is given by the so-called TrackCounting algorithm, which was one of the first b-tagging algorithms designed for the early LHC data recorded by the ATLAS detector. The algorithm uses all tracks that pass certain quality requirements and arranges them in decreasing order of their signed transverse impact parameter significance. Possible discriminants are defined by the d_0 significance of the track at each position of that sequence, but previous studies suggested the use of the information of the second or third highest ranked track [102]. As tracks stemming from light-flavour decays tend to have low d_0 significances, tracks from additional hadronic activity nearby a b-jet will be likely to be ranked at a lower position than the tracks of the b-hadron decay products. The resilience to the addition of extra tracks outweighs the degradation due to the shift of the jet axis at high-p_{T}. Thus the output of the TrackCounting algorithm is much less affected for b-jets containing also tracks coming from the hadronic W-boson decay than the IP2D and IP3D jet weights. Another quantity investigated in this context is the multiplicity of tracks with a large transverse impact parameter significance $|d_0/\sigma_{d_0}| > 1.8$. Its distribution for single b-, merged b- and light-flavour jets is presented in Figure 6.10 (b) next to that of the d_0 (c) and the z_0 (d) significance of the track with the third highest-ranking. These four quantities are calculated using all tracks that are associated to the studied jets by the p_{T} dependent ΔR matching procedure defined in Section 4.2.1. The corresponding track selection is identical to that of the IP2D and IP3D taggers.

The energy fraction is one of the quantities affected most by a jet overlap, but simultaneously it also provides a high separation between heavy and light-flavour jets. By scaling its values with the ratio of the track multiplicity matched to the jet to the number of tracks associated to the vertex fit, a better stability with respect to a contamination with additional tracks is obtained. The corresponding quantity is shown in Figure 6.10 (e) and (f) for vertex candidates reconstructed with the iterative vertex finder (using the SV1 setup) and the JetFitter algorithm.

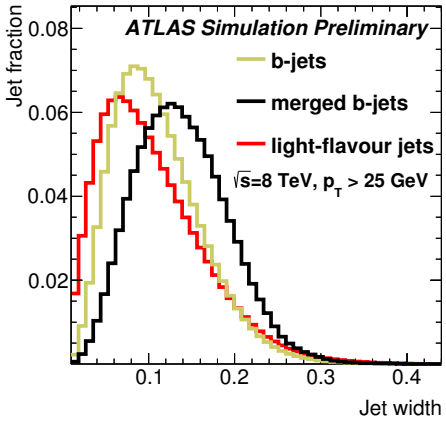

(a) jet shape based

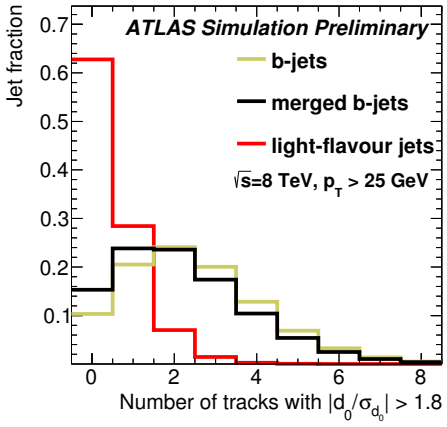

(b) IP based

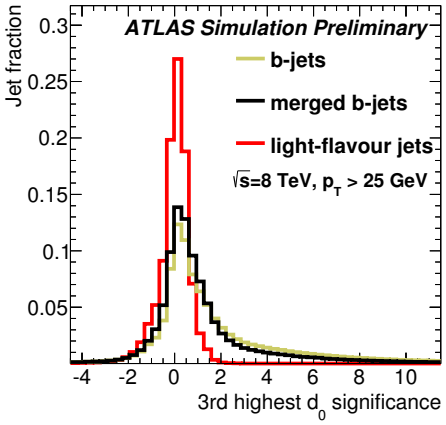

(c) IP based

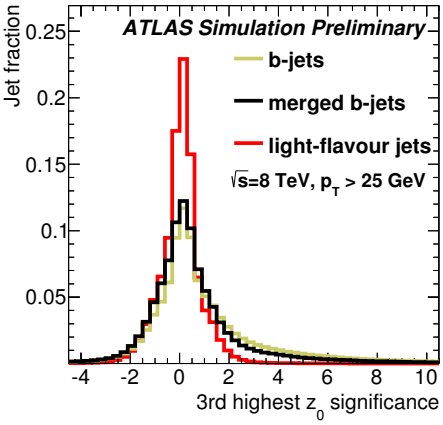

(d) IP based

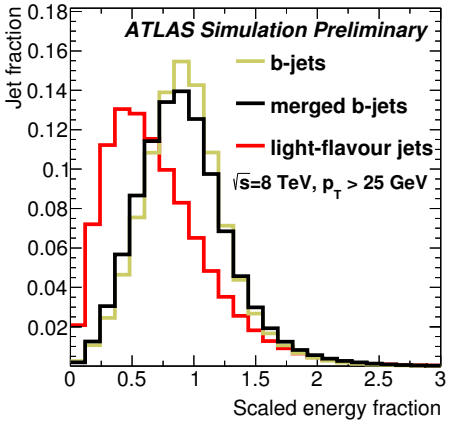

(e) SV1 based

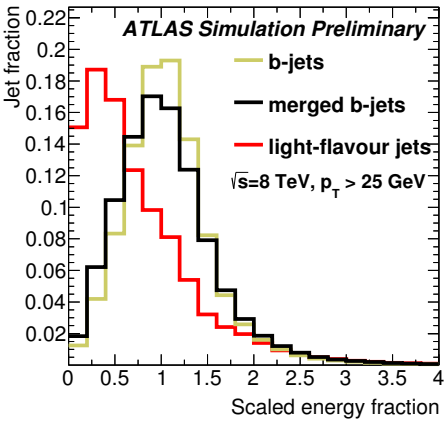

(f) JetFitter based

Figure 6.10: Distribution of the jet width (a), the number of tracks having a d_0 significance above 1.8 (b), the d_0 (c) and the z_0 (d) significance of the track with the third-highest ranking of its signed d_0 significance, as well as the scaled energy fraction corresponding to vertices reconstructed with the iterative vertex finder (using the SV1 setup) (e) or the JetFitter algorithm (f) presented for inclusive b-, merged b- and light flavour jets stemming from $t\bar{t}$ events that are generated at $\sqrt{s} = 8$ TeV. Only jets that have $p_{\mathrm{T}} > 25$ GeV and $|\eta| < 2.5$ are considered. Each distribution is individually normalised to unit area [7].

6.3 Development of new *b*-tagging algorithms dedicated to identifying *b*-jets in boosted topologies

The performance of the *b*-tagging algorithms that are currently used in the various ATLAS analyses strongly degrades in the dense environments of boosted hadronic top-quark decays. As shown above, this is mainly due to an increasing misalignment between the jet axis and the *b*-hadron flight direction or due to a contamination with additional tracks from light-flavour decays. Related to these two effects is the problem that some of the jet properties are topology dependent. Thus they might show considerable deviations from the reference distribution used in the training of a MVA based *b*-tagger. Therefore a new *b*-tagging algorithm is developed that is intended to be less sensitive to the effects described in Sections 6.1.1 and 6.1.2. In contrast to the MV1 or JetFitterCombNN algorithms, the training procedure (including the handling of the jet kinematics) of this algorithm emphasizes more strongly the high p_{T} and dense environment regimes. The previously discussed quantities are used as inputs for the new tagger, with the quantities introduced in Section 6.2 providing an improved stability to the performance of the *b*-jet identification in boosted topologies. In addition to these quantities further variables are used in the training. From the vertices that are reconstructed with the iterative vertex finder (with the SV1 setup) the number of two-track vertices, the energy fraction and the transverse decay length are included, while from the vertices reconstructed with the JetFitter algorithm the vertex imbalance, the track multiplicity at the secondary vertex, the $\log_{10}(\chi^2/\mathrm{ndof})$, the invariant mass, the decay length significance and both the uncertainties of the measured azimuth and polar angles are added. With the jet weight of the IP2D tagger, a further IP based quantity is used. The full list of input quantities can be seen in Table 6.1.

Boosted decision trees are trained using *b*-jets as signal and light-flavour jets as background. However, as for some event signatures the dominant background processes mainly contain *c*-jets, the procedure is repeated training *b*- against *c*-jets. The boosted decision trees resulting from these training cycles are referred to as the MVb and MVbCharm algorithms in the following.

6.3.1 Multivariate separation of *b*-, *c*- and light-flavour jets using boosted decision trees

Decision trees are based on a sequence of binary decisions in order to classify objects or events as either signal- or background-like. Each decision is made by applying a rectangular cut on one of the properties $\mathbf{x} = \{x_1, .., x_n\}$ of the object (event) on study. Figure 6.11 demonstrates the principle of such a decision tree. The process is started at the so-called root node of the tree which contains the whole statistics inserted into the trainings phase. The sample is then split into two subsamples (daughter nodes) by applying a cut on one of the properties x_i of the studied objects (events). In this process the quantity and cut value, used to split the sample, are chosen such that the difference between the separation index of the parent node and the sum of the separation indices of the two daughter nodes

$$I^{\text{parent node}} - \left(I^{\text{daughter node 1}} + I^{\text{daughter node 2}}\right) \tag{6.4}$$

is maximised. The most widely used separation criteria for decision trees is the so-called Gini index defined as

$$I_{\text{gini}} = \left(\sum_{i=1}^{n} W_i\right) P \cdot (1 - P) \tag{6.5}$$

with W_i being the predefined weight of the i-th object (event) on study and P being the signal purity

$$P = \frac{\sum_{i=1}^{n} W_i^S}{\sum_{i=1}^{n} W_i^S + \sum_{i=1}^{n} W_i^B} \,. \tag{6.6}$$

For each daughter node, the process is repeated selecting again the quantity providing the best separation improvement and splitting the sample into two parts. The splitting at a node is stopped as soon as a certain abort criterion (e.g. minimum number of events) is reached and the node is called either signal or background leaf depending on the majority of contained events.

Decision trees are in some sense similar to cut-based analyses but instead of selecting only one hypercube in the phase space spanned by the object (event) properties they are able to classify several disjoint phase space regions as either signal- or background-like.

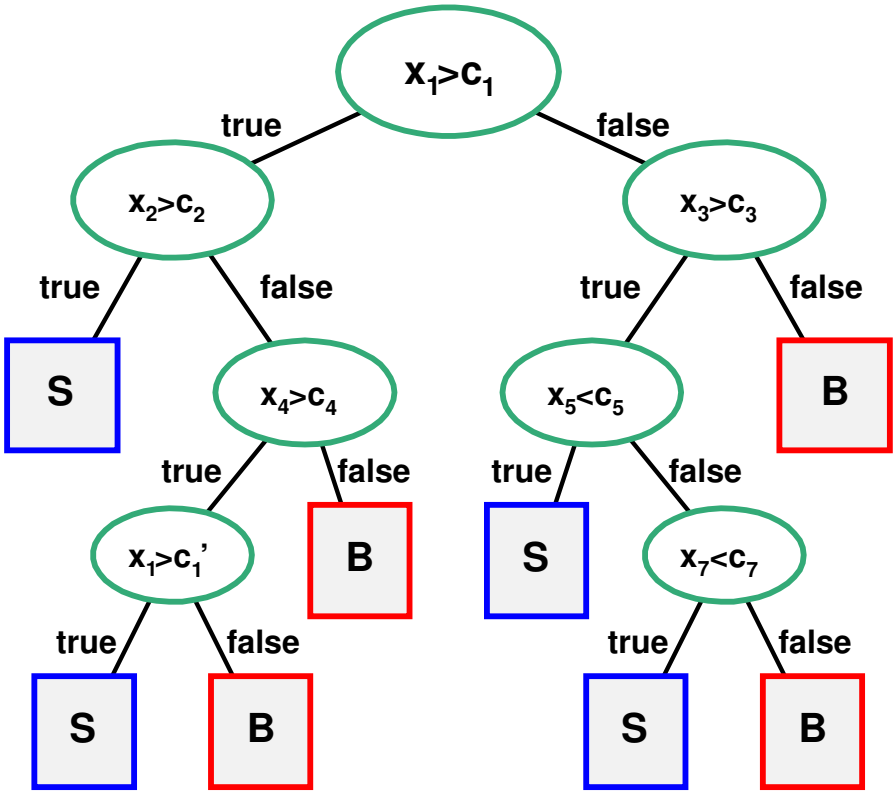

Figure 6.11: Schematic view of an exemplary decision tree, which can be used to classify events (or objects) as either signal (S) or background (B) depending on the signal purity of the leave node (represented as boxes) in which they end up. Nodes that are neither dominated by signal nor background events are represented as ellipses. The classification is performed by applying a sequence of binary decisions using rectangular cuts on the discriminating variables $\mathbf{x} = \{x_1, .., x_n\}$. The selection of the quantities, used to split the event sample, and their corresponding cut values $\mathbf{c} = \{c_1, .., c_n\}$ are performed independently at each node such that the difference between the separation index of the parent node and the sum of the separation indices of the two daughter nodes is maximised. Thus some of the variables can be used several times in one decision tree to split the event sample, while other quantities might not be used at all.

Single decision trees are very unstable, statistical fluctuations or even small changes in the training sample can have dramatic effects on their performance. Therefore a technique called boosting can be applied to obtain more reliable results. Boosting, which extends the concept of one single decision tree to many trees (forest), does not only increase the statistical stability, but can also lead to a significant improvement of the separation strength.

The so-called AdaBoost (adaptive boost) algorithm [142,143], is the most common boosting algorithm, used in high energy physics. It relies on the re-weighting of events that were misclassified during the training phase of a previous decision tree. The weight w of a given event, which was misclassified during the training of the i-th tree is therefore transformed according to

$$w \to w \cdot \exp\left(\beta \ln\left(\frac{1 - r_i^{\text{err}}}{r_i^{\text{err}}}\right)\right) , \tag{6.7}$$

where r_i^{err} is the misclassification rate of the i-th decision tree and β is a free parameter. Before starting the training of the $(i+1)$-th tree, the weights of the entire event sample are normalised such that their sum remains constant with respect to that of the first tree.

While the classifier of a single tree is defined to be $y(\mathbf{x}) = 1$ for signal- and $y(\mathbf{x}) = 0$ for background-like events, the boosted event classifier is given by the weighted sum over all trees:

$$y^{\text{boost}}(\mathbf{x}) = \frac{1}{N^{\text{trees}}} \sum_{i=1}^{N^{\text{trees}}} \beta \cdot \ln\left(\frac{1 - r_i^{\text{err}}}{r_i^{\text{err}}}\right) \cdot y_i(\mathbf{x}) \tag{6.8}$$

where N^{trees} is the number of trees used in the training and $y_i(\mathbf{x}) = 1$ if the object (event) was classified as signal during the training of the i-th tree, $y_i(\mathbf{x}) = -1$ otherwise.

6.3.2 Training and testing of the BDT

The training of the boosted decision trees, on which the MVb tagger relies, is performed by using the BDT implementation of the TMVA package [143]. In the chosen setup, the AdaBoost algorithm is used with the parameter β set to 0.5 for boosting a total of 1000 trees. Each of these trees has a maximum depth of five nodes. In order to protect against overtraining, the minimum number of events at these leaf nodes is not allowed to be less than 1% of the overall number of events in the training sample. The input data set is split randomly into a training and a testing sample, which are compared to check for overtraining. The two samples contain b-jets as signal and either c- or light-flavour jets as background. These jet flavour types are taken from a mixture of simulated $t\bar{t}$, dijet and $Z' \to t\bar{t}$ events. As both the MVb and MVbCharm taggers are meant to be dedicated to the identification of b-jets in dense environments, only those events from the $t\bar{t}$ and $Z' \to t\bar{t}$ samples are considered that have an invariant $t\bar{t}$ mass above 0.7 TeV (calculated at the generator level). This is done in order to emphasise the changed properties of overlapping jets during the training of the boosted decision trees. The obtained jets are additionally required to have a p_{T} between 25 GeV and 800 GeV. In order to enrich the statistics in the high-p_{T} region, jets stemming from dijet events are also included in the training if their transverse momentum is between 100 GeV and 800 GeV.

Since most b-tagging related quantities depend strongly on the kinematic properties of the jets, additional information and therefore additional separation power is obtained by taking the correlation of the BDT input quantities to the jet p_{T} and $|\eta|$ into account. However, only the correlation of the jet η and p_{T} to the input quantities should be used to distinguish between b-, c- and light-flavour jets and not the shape of the p_{T} and η distribution itself. Otherwise an

unwanted dependence on the event topology could be introduced to the training results. One approach to deal with the correlations to the jet kinematics is to subdivide the phase space into several disjoint regions and train in each region independently. Following this approach five $|\eta|$ regions with bin boundaries at (0.0, 0.4, 0.8, 1.2, 1.8, 2.5) are defined such that they follow the geometry of the Inner Detector with three bins corresponding to the barrel region ($|\eta| \leq 1.2$) and one for each the overlap ($1.2 < |\eta| \leq 1.8$) and the end-cap regions ($|\eta| \geq 1.8$). Hence five separate boosted decision trees are trained for the MVb and MVbCharm algorithm. As the jet p_{T} has a much stronger correlation to the properties of the secondary vertex or the impact parameter based quantities, it is included as an additional input quantity into the training of the BDT. To avoid an artificial training on the shape of the transverse momentum distribution for different jet flavours the c- and light-flavour jet samples are re-weighted in such a way that their p_{T} distributions are identical in normalisation and shape to that of the b-jets.

A final set of 23 input quantities is considered during the training of the MVb and MVbCharm taggers. Table 6.1 lists all these variables and their relative importance for jets with $|\eta| < 0.4$ (as an example). The importance is evaluated by taking into account how often a particular quantity is used to split decision tree nodes, and summing up the squares of the corresponding separation indices times the number of events (sum of weights) contained at each of these nodes [144].

In particular, the number of two-track vertices calculated by the iterative vertex finder (SV1), the jet weight of the IP3D algorithm, the transverse flight length, the energy fraction (by the JetFitter algorithm), the width and the transverse momentum of the jets (due to its correlation with other quantities) are ranked relatively high in each of the five different $|\eta|$ regions when training b- against light-flavour jets. In the training of the boosted decision trees that correspond to the MVbCharm tagger (i.e. when training b- against c-jets), the number of two-track vertices reconstructed using the iterative vertex finder (SV1) is by far the most important of all the input quantities within each of the five different $|\eta|$ bins. Also the output weight of the IP3D tagger, the decay length significances of displaced vertices reconstructed by either the iterative vertex finder or the JetFitter algorithm, the energy fraction, the track multiplicity of the displaced vertices or the invariant mass of the displaced vertices that are reconstructed with the JetFitter algorithm appear to be relatively important for the separation between b- and c-jets. The exact values of the relative importance corresponding to these and all other quantities that are used in the training of the MVbCharm algorithm are shown in Table 6.1 next to the values obtained in the training of b- against light-flavour jets. The contribution of the new defined variables (see Section 6.2) to an improved b-tagging stability in dense jet environments is studied briefly in Section 6.4.5.

Examples of linear correlation coefficients for all input quantities of the MVb and MVbCharm taggers are presented in Figures 6.12 (a) and (b) as well as in Figure 6.13 separately for b-, c- and light-flavour jets. Their values are obtained studying all jets with $|\eta| < 0.4$ stemming from the sample mixture mentioned above. Large values of the linear correlation coefficient for a pair of input quantities might lead to a low ranking of at least one of these two quantities, even if they have both a high separation strength between signal and background. Such a case is seen for example for the invariant mass and the energy fraction of the vertices that are reconstructed with the iterative vertex finder. Their linear correlation coefficients are 0.88, 0.93 and 0.88 for b-, light-flavour and c-jets, respectively. Further examples for quantities that have relatively large correlation coefficients with at least one of the other input variables are the jet weights of the IP3D and IP2D taggers, the number of two-track vertices, and in particular the track multiplicity at the secondary vertex, while the uncertainties on the secondary vertex positions $\sigma_{\theta_{SV}}$ and $\sigma_{\theta_{SV}}$ as well as the vertex imbalance have relative strong negative correlations with several other input quantities. This feature is observed not only for b-, but also for c- and light-flavour jets.

In addition, it is shown that vertex properties, which are defined with both the iterative vertex finder and the JetFitter algorithm, do not necessarily have a strong linear correlation with each other. For example, the correlation coefficient for the two invariant mass definitions are 0.51, 0.36 and 0.26 for b-, c- and light-flavour jets, respectively. These results are mainly related to the difference in the vertex finding efficiencies of the JetFitter algorithm and the iterative vertex finder. Due to the fact that input quantities which are strongly correlated with several other variables can still provide useful information, non of the previously mentioned quantities are excluded from the training of the MVb and MVbCharm taggers.

Variable	MVb	MVbCharm
w_{IP3D}	6.80	5.23
w_{IP2D}	3.44	1.42
Number of two-track vertices (SV1)	19.32	19.30
Number of two-track vertices (JetFitter)	3.75	3.82
Energy fraction (JetFitter)	6.98	4.93
$\log_{10}(\chi^2/\text{ndof})$ (JetFitter)	1.86	1.07
Number of tracks with $\lvert d_0/\sigma_{d_0}\rvert > 1.8$	2.85	2.65
Energy fraction (SV1)	3.07	3.76
Decay length significance (JetFitter)	3.72	6.54
3rd highest d_0 significance	2.85	2.80
Jet p_T	4.62	4.23
L_{xy}	4.95	3.79
Invariant mass (SV1)	2.61	7.74
Scaled energy fraction (SV1)	4.38	2.79
Invariant mass (JetFitter)	2.84	4.99
Jet width	5.63	3.20
Scaled energy fraction (JetFitter)	7.21	3.95
3rd highest z_0 significance	1.28	1.44
$\sigma_{\theta_{SV}}$ (JetFitter)	3.06	3.60
Decay length significance (SV1)	3.31	2.69
Track multiplicity at SV (JetFitter)	1.73	6.26
Vertex imbalance (JetFitter)	1.29	1.20
$\sigma_{\phi_{SV}}$ (JetFitter)	2.46	2.58

Table 6.1: Importance of the various input quantities of the MVb (middle column) and the MVbCharm (right column) algorithms presented for the boosted decision trees that are trained using jets with $|\eta| < 0.4$. The exact values of the variable importances are normalised to all variables together having an importance equal to one. These numbers are presented in percent. The quantities that were introduced in Section 6.2 with the intention to improve the tagging performance in dense jet environments are printed in bold letters.

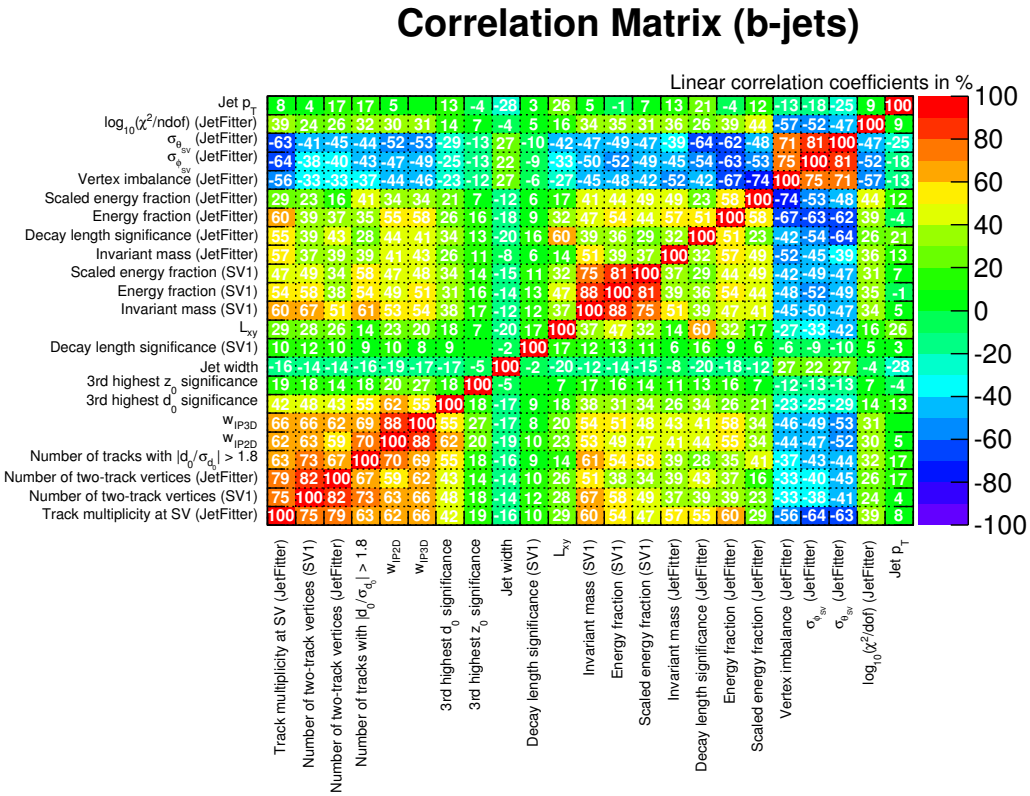

(a) *b*-jets

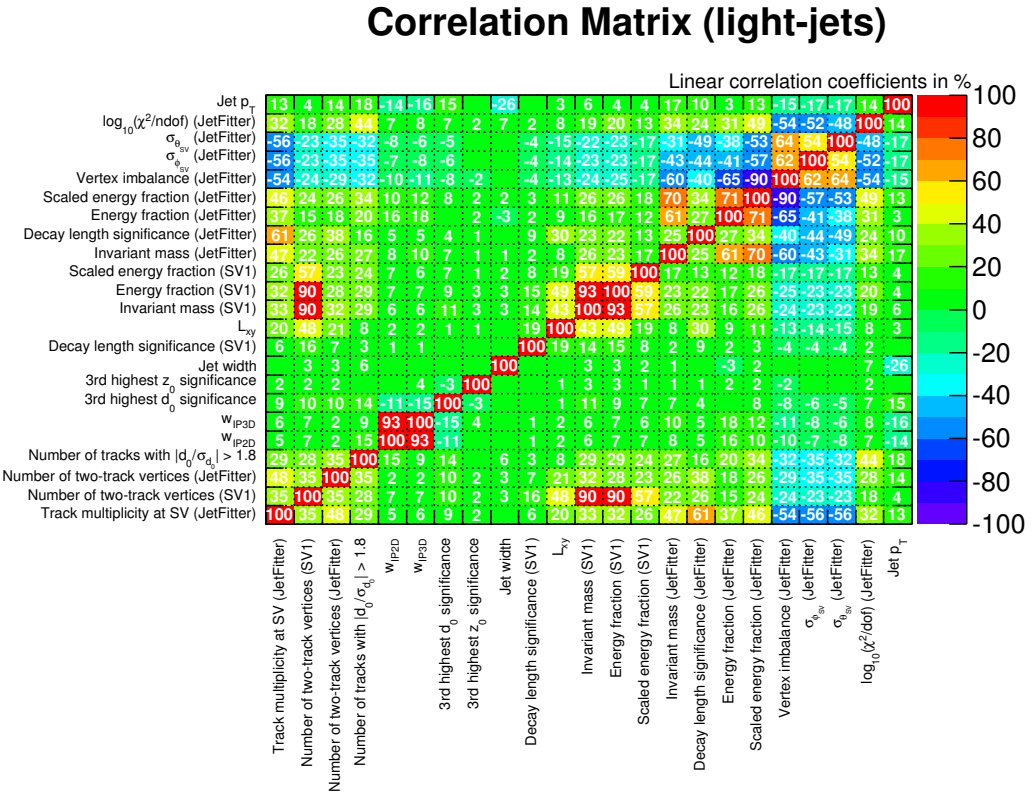

(b) light-flavour jets

Figure 6.12: Matrices of the linear correlation coefficients for all input quantities of the MVb and MVbCharm taggers displayed separately for *b*- (a) and light-flavour (b) jets that stem from a mixture of simulated $t\bar{t}$, $Z' \rightarrow t\bar{t}$, and dijet events and satisfy $|\eta| < 0.4$.

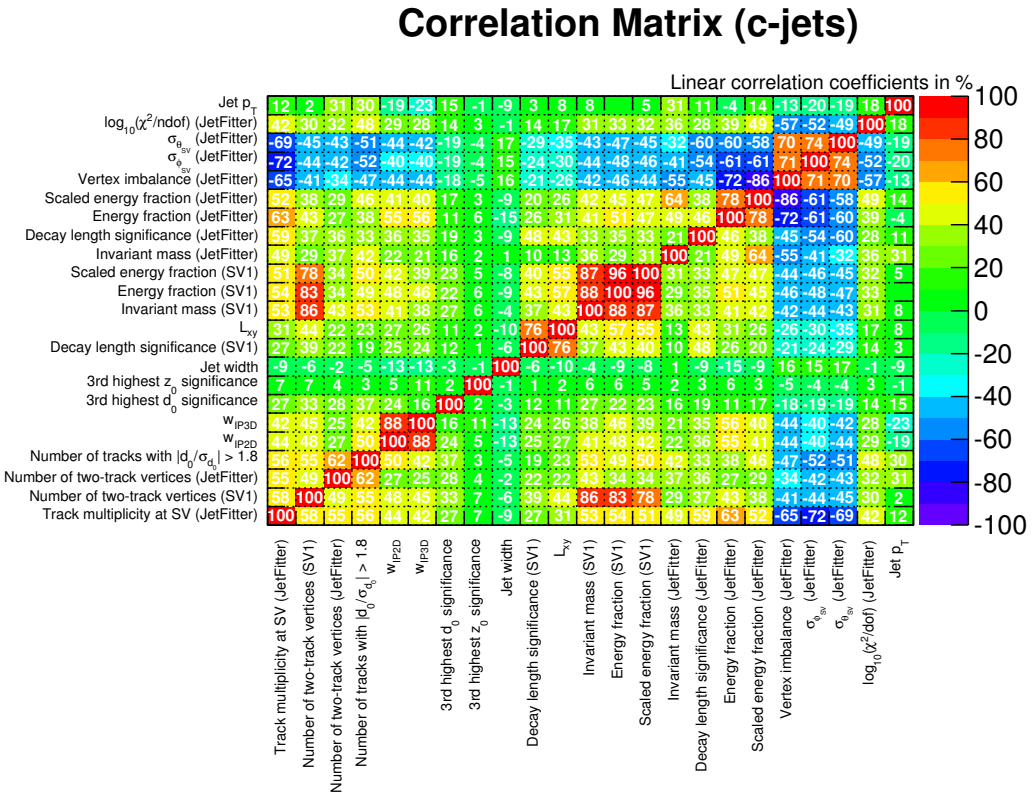

(a) *c*-jets

Figure 6.13: Matrix of the linear correlation coefficients for all input quantities of the MVb and MVbCharm taggers shown for *c*-jets that stem from a mixture of simulated $t\bar{t}$, $Z' \rightarrow t\bar{t}$, and dijet events and satisfy $|\eta| < 0.4$.

6.4 Expected Performance of the MVb and MVbCharm taggers

The discriminants of the MVb and MVbCharm *b*-tagging algorithms are calculated as the object classifier of the underlying boosted decision trees (via Equation 6.8). Their distribution for all selected *b*-, *c*- and light-flavour jets stemming from a SM $t\bar{t}$ sample that is simulated using the POWHEG and PYTHIA generators are displayed in Figures 6.14 (a) and (b) respectively. Both tagging weights show a good separation between *b*- and light-flavour jets. However, as the MVbCharm tagger is trained with *b*-jets against *c*-jets, its rejection power with respect to light-flavour jets is less strong, while its ability to reject charm jets is considerably improved compared to MVb.

The shape of the MVb weight distribution for *b*-jets reveals some very distinct features, as it has four local maxima. Each of these peaks corresponds to an accumulation of jets having similar properties in the quantities relevant to *b*-tagging. In general jets having no vertex found with either the JetFitter algorithm or the iterative vertex finder are most likely considered to be background-like, whereas jets having a reconstructed multi-track vertex tend to be classified as signal. To be more specific, the peak around w_{MVb} values of -0.2 is dominated by *b*-jets having no reconstructed vertex, while the peak around w_{MVb} values of approximately 0.2 is mostly populated by *b*-jets containing a vertex reconstructed by either the JetFitter or the iterative

vertex finder. Jets having a vertex reconstructed by both tools correspond mainly to the maxima in the regions around 0.6 and 0.95. The exact MVb output weight depends of course also on the vertex properties (as for example the track multiplicity, the invariant mass or the energy fraction) or on the impact parameter (or shape) based quantities of these jets.

The output weight distribution of the MVbCharm tagger for b-jets shows in principle a somewhat similar structure as the corresponding distribution of the MVb weights. However, the local maxima are less strong pronounced. This is mainly due to the fact that a significant fraction of the c-jets contain a secondary vertex candidate. Thus the fact whether a jet has a reconstructed vertex or not is a less strong classification criteria in the BDT training, while the characteristic shapes of the various vertex and impact parameter based quantities become more important to separate b- and non-b-jets.

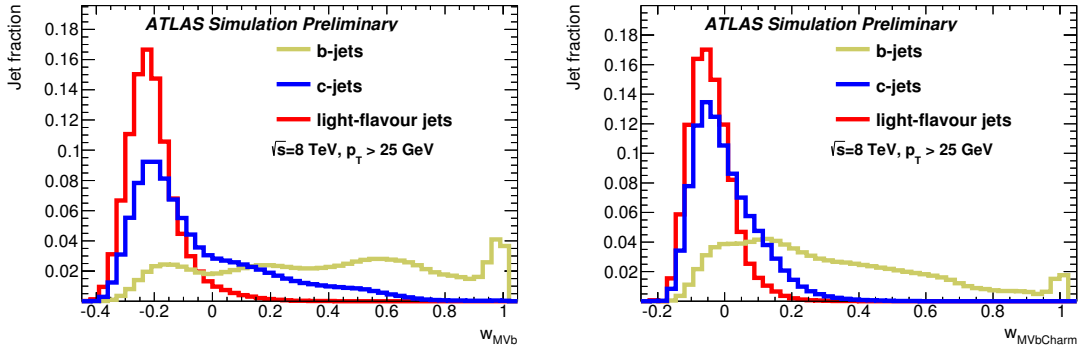

(a) MVb weight [7]

(b) MVbCharm weight [7]

Figure 6.14: Distribution of the MVb (a) and the MVbCharm (b) output weights for all b-, c-, and light-flavour jets stemming from SM $t\bar{t}$ events that are simulated with $\sqrt{s} = 8$ TeV using the POWHEG and PYTHIA generators. Only jets with $p_{\mathrm{T}} > 25$ GeV and $|\eta| < 2.5$ are considered.

In addition, the distributions of the correlation between the MVb and MVbCharm weights are shown in the Figures 6.15 (a), (b) and (c) for b-, c- and light-flavour jets separately. While both weights appear to be highly correlated for b- and light-flavour jets, the correlation between these two quantities is less pronounced for c-jets. The correlation coefficient ρ corresponding to the MVb and MVbCharm jet weights equals 0.877 for b-, 0.688 for c- and 0.747 for light-flavour jets. Hence both weights could be combined in order to obtain a high separation strength against both c- and light-flavour jets. A quantification of the b-tagging efficiency and the charm and light-flavour rejection strength of both taggers is presented in the following section. In addition their performance is compared to the current ATLAS default b-tagging algorithm, MV1.

6.4.1 Rejection rates for charm and light-flavour jets

The expected performance of the MVb and MVbCharm taggers is compared to that of the MV1 and the JetFitterCombNN algorithm in Figure 6.16. Their rejection rates for light-flavour jets are shown as a function of the b-tagging efficiency ε_b. Each working point on these curves corresponds to a different cut on the discriminant of these taggers, Also their relative performance with respect to MV1, the current ATLAS default b-tagger, is shown. The evaluation is performed using jets that are either from simulated $t\bar{t}$ events produced according to the Standard Model predictions (a) or from events in which a hypothetical Kaluza-Klein gluon with the mass $m_{g_{KK}} = 2.5$ TeV decays to a boosted $t\bar{t}$ system (b). The basic difference of these two samples

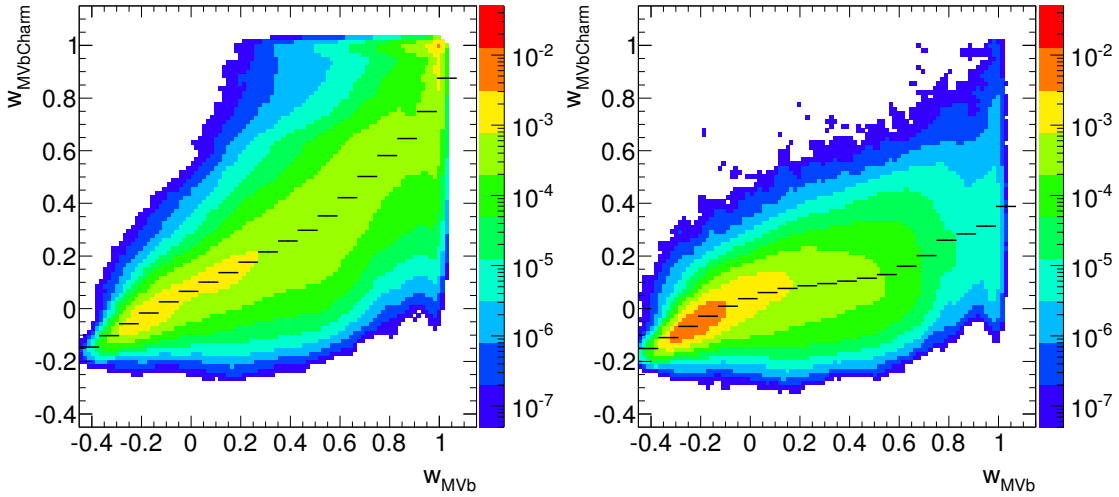

(a) b-jets

(b) c-jets

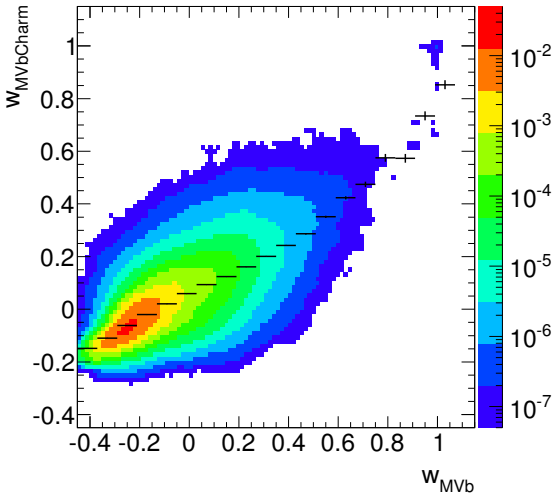

(c) light-flavour jets

Figure 6.15: Distributions of the correlation between the output weights of the MVb and the MVbCharm taggers shown separately for the three different jet flavour types. The colour coding shows the fraction of jets contained in each plot. Overlaid to the two-dimensional distributions are the average value of the MVbCharm weights (dashed line) corresponding to each w_{MVb} bin. The considered jets are required to have $p_{\mathrm{T}} > 25$ GeV and $|\eta| < 2.5$ and stem from $t\bar{t}$ events that are simulated with $\sqrt{s} = 8$ TeV using the POWHEG and PYTHIA generators.

is the distribution of their top-quark p_{T}. While the top-quarks produced according to the SM production mechanisms are mainly of low transverse momentum, a large fraction of the top-quarks from the $g_{KK} \rightarrow t\bar{t}$ samples have a transverse momentum above 400 GeV and provide therefore an ideal scenario to test the performance of the MVb and MVbCharm taggers, which are developed exactly for such environments. The MVb tagger shows a similar performance compared to the MV1 tagger in the SM $t\bar{t}$ sample for working points corresponding to the in-

teresting range of b-tagging efficiencies ($0.65 < \varepsilon_b < 0.85$). As the MVb tagger uses not only the IP3D weight as input, but also the IP2D weight, the jet width and the number of tracks with a large impact parameter significance, its performance is strongly improved with respect to the MV1 and JetFitterCombNN algorithm for jets having no reconstructed vertex. This becomes obvious in particular due to the large improvements of the MVb tagger with respect to the other algorithms for b-tagging efficiencies above 87%.

Also working points corresponding to b-tagging efficiencies between 50% and 60% show an improved light-flavour rejection rate (up to a factor of 1.3). In events where a high mass resonance of the KK-gluon decays into boosted top-antitop pairs, the performance of MVb is even better, by a factor of 1.5-2.5 (depending on the chosen working point).

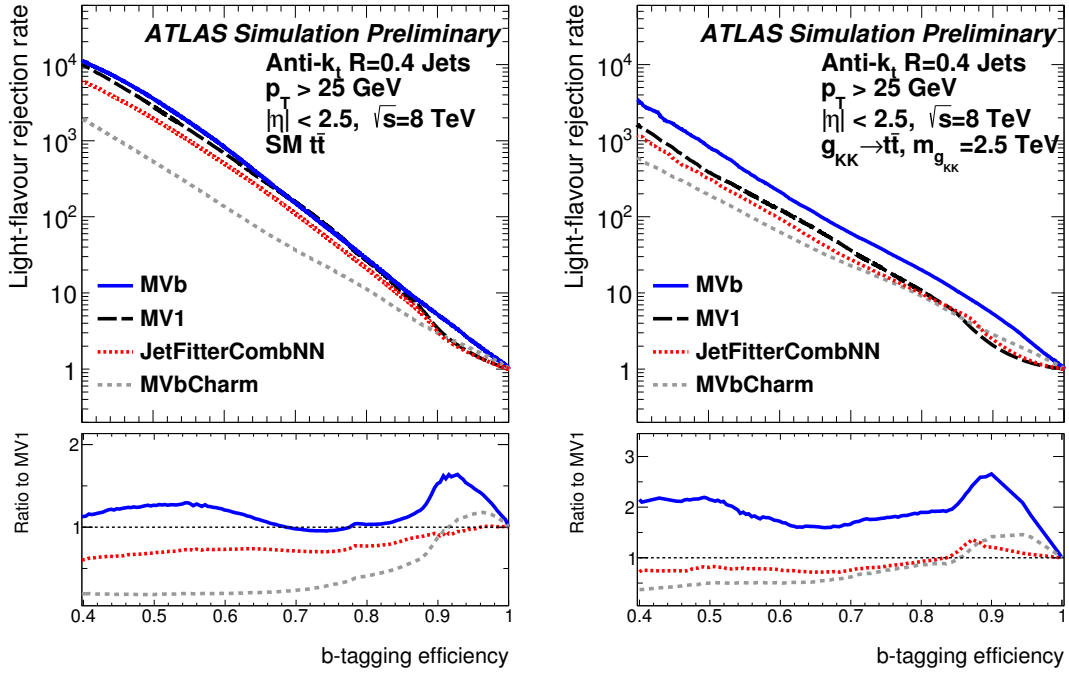

(a) SM $t\bar{t}$ **(b)** BSM model

Figure 6.16: Light-flavour rejection rates as a function of the b-tagging efficiency for jets stemming from two samples of simulated $t\bar{t}$ events produced either according to the SM predictions (a) or from the decay of a Kaluza-Klein gluon (b). The performance of the MVb tagger (presented as a blue line) is compared to the MV1 (black line), JetFitterCombNN (red line) and the MVbCharm (gray line) taggers [7].

The overall performance of the MVbCharm tagger (in terms of the light-flavour rejection rate) is significantly worse than the performance of the other taggers in both the SM and the BSM $t\bar{t}$ sample and for working points corresponding to b-tagging efficiencies below 85%. But as light-flavour jets are not included in its training procedure, this behaviour is expected. Nevertheless, its light-flavour rejection rate is improved with respect to MV1 for $\varepsilon_b > 90\%$. As for the MVb algorithm, this is also related to the fact that MVbCharm uses more input quantities than the MV1 tagger, which are not depending on the reconstruction of displaced vertices.

Rejection rates for c-jets are displayed in Figure 6.17 for the MVb, MVbCharm and MV1 taggers as a function of the corresponding b-tagging efficiency. Additionally the performance

of the MV1c tagger, which is a modified version of MV1 and provides a better charm rejection, is shown. The performance of these taggers is again compared separately for a SM (a) and a BSM (b) $t\bar{t}$ sample.

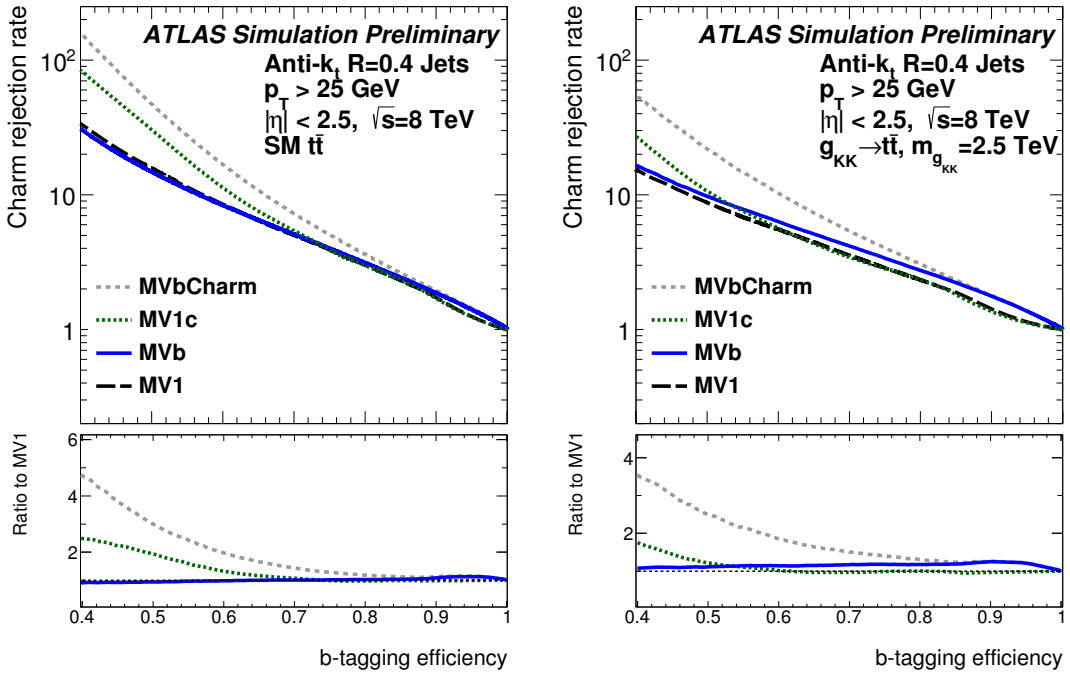

(a) SM $t\bar{t}$ **(b)** BSM model

Figure 6.17: Charm rejection rates as a function of the b-tagging efficiency for jets stemming from two samples of simulated $t\bar{t}$ events produced either according to the SM predictions (a) or from the decay of a high mass resonance (b). The performance of the MVb (presented as a blue line) and the MVbCharm (gray line) tagger is compared to the performance of the MV1 (black line) and the MV1c (green line) algorithm [7].

It can be seen that the charm rejection rate of the MVb tagger appears to be very similar in the SM $t\bar{t}$ sample compared to the MV1 algorithm for any given b-tagging efficiency below 90%. The charm rejection rates corresponding to b-tagging efficiencies above 90% are, like the light-flavour rejection rates, improved with respect to those of the MV1 tagger due to the fact that MVb uses more input quantities that do not rely on the reconstruction of a secondary vertex. The same trend is observed in the comparison between MVb and MV1c for efficiencies above 70%, while the performance of MV1c is better for efficiencies below 70%. However, the performance of the MVbCharm algorithm is significantly better compared to the other b-taggers for any working point. Its charm rejection rate is improved with respect to MV1c by a factor of 1.5 for working points corresponding to efficiencies between 60% and 70%. The same tendency can be observed in the jet sample obtained from the $g_{KK} \rightarrow t\bar{t}$ decays with the difference that the performance of MVb is improved with respect to MV1c for working points corresponding to b-tagging efficiencies above 50%.

The light-flavour rejection rates of the MVb and MVbCharm taggers are presented as a function of the jet p_{T} and η in Figure 6.18. A representative operating point corresponding to an overall b-tagging efficiency of 70% (in the whole $t\bar{t}$ sample) is chosen to compare them to

the rejection rates of the MV1 algorithm. While the rejection rates of these three taggers behave qualitatively very similarly over the full range of the jet pseudorapidity values, significant differences can be observed for the jet p_{T}. The rejection rate of the MV1 tagger has its maximum for jets with low transverse momentum and decreases continuously with increasing p_{T}. MVb and MVbCharm however have their maximum in the rejection factor for jets with a p_{T} around 120 GeV. For increasing jet p_{T} values both these taggers show a continuously decreasing of their light-flavour rejection rates. Still, the light-flavour rejection of MVb is superior to that of the MV1 algorithm in a range between 60 GeV and 320 GeV, whereas it is similar for high-p_{T} jets and slightly lower for jets with a transverse momentum below 60 GeV.

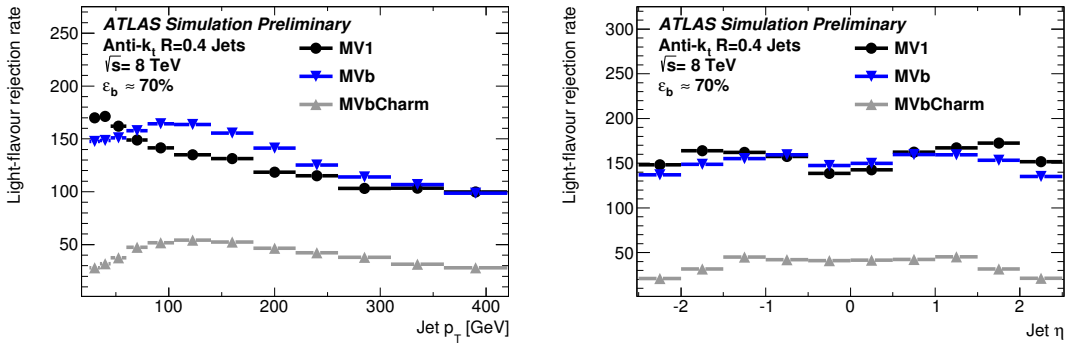

(a) light-flavour rejection vs. p_{T}

(b) light-flavour rejection vs. η

Figure 6.18: Rejection rates for light-flavour jets corresponding to the MV1, MVb and MVbCharm algorithms as a function of the jet p_{T} (a) and η (b). The taggers are compared at an operating point corresponding to a b-tagging efficiency of 70% using jets that stem from SM $t\bar{t}$ decays, which are simulated using the POWHEG and PYTHIA generators [7].

The charm rejection rates for these three taggers are shown in Figures 6.19 (a) and (b) as a function of the jet p_{T} and η using the same operating point. The performance of MVbCharm is strongly improved with respect to MV1c and MVb in a p_{T} range between 50 GeV and 250 GeV and in an η range between -1.5 and 1.5. For a jet p_{T} above 300 GeV or for jet $|\eta|$ values above 2.0, the charm rejection rates of the MV1c tagger become superior to those of MVbCharm. At the same time, the b-tagging efficiencies of the MV1c tagger decrease more strongly with increasing jet p_{T} and η values than those of the other taggers. Thus, the differences in the overall performance of the three taggers are less dramatic in these phase space regions as indicated by Figures 6.19 (a) and (b).

The course of the charm rejection rates of the MVbCharm algorithm are in general qualitatively very similar to its light-flavour rejection rates, while the rejection rates of MVb behave qualitatively similar compared to those of MV1c. As a function of the jet p_{T}, the charm rejection rates of the MVbCharm tagger increase for increasing p_{T} values until the maximum is reached at approximately 120 GeV. For a p_{T} value above this threshold a continious decreasing is observed. In an η range corresponding to the barrel region of the Inner Detector, the c-jet rejection rate corresponding to MVbCharm is almost constant, while it decreases in the forward region. In contrast to this, the c-jet rejection rates of both the MV1c and MVb taggers have their minimum for low $|\eta|$ values and increase with increasing $|\eta|$.
Precise values of the rejection rates corresponding to τ-, c- and light-flavour jets are highlighted in Table 6.2 for various working points of the MVb tagger. The b-tagging efficiencies corresponding to these working points range from 45% to 85% and were calculated in the SM $t\bar{t}$

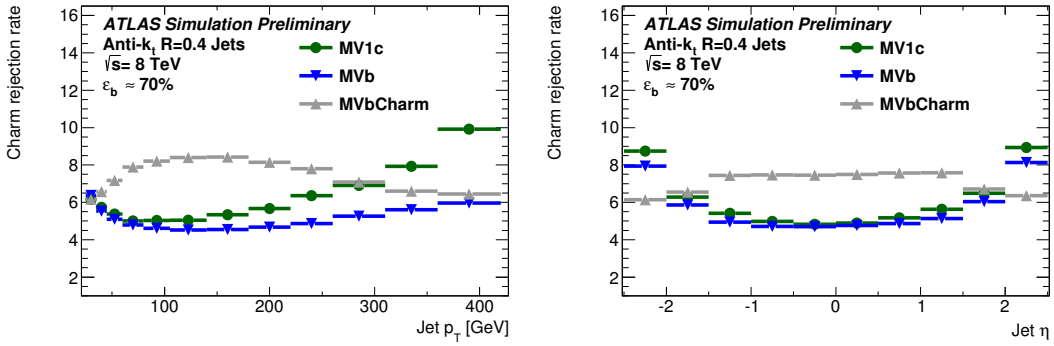

(a) charm rejection vs. p_{T}

(b) charm rejection vs. η

Figure 6.19: Rejection rates for charm jets corresponding to the MV1c, MVb and MVbCharm algorithms as a function of the jet p_{T} (a) and η (b). The taggers are compared at an operating point corresponding to a b-tagging efficiency of 70% using jets that stem from SM $t\bar{t}$ decays, which are simulated using the POWHEG and PYTHIA generators [7].

sample. Operating points corresponding to b-tagging efficiencies of 60%, 70% and 80% in this sample are defined by a cut of 0.2748, 0.1471 and 0.0023 on the MVb output quantity, respectively. The c- and τ-jet rejection rates of the working point corresponding to a b-tagging efficiency of 70% are 5.11 and 13.8 respectively and are therefore even slightly improved with respect to the values obtained by the MV1 tagger (5.04 and 13.6) at an equivalent working point.

The τ-, c- and light-flavour rejection rates corresponding to the MVbCharm algorithm are displayed in Table 6.3. For this b-tagger working points matching an overall b-tagging efficiency of 60%, 70% and 80% are defined by applying cuts of 0.1753, 0.1121 and 0.0477 on the discriminant, respectively. While the light-flavour rejection rates corresponding to these working points are sufficiently lower than that of the MVb or MV1 algorithm, the rejection rates for c-jets are improved by a factor of 1.4 for the 70% operating point and by a factor 2 for the 60% operating point.

operation point	weight cut	light rejection	charm rejection	τ rejection
MVb@45%	0.4737	6667	21	57
MVb@50%	0.4109	3568	15	39
MVb@55%	0.3435	1774	11	30
MVb@60%	0.2748	828	8.4	23
MVb@65%	0.2097	356	6.5	18
MVb@70%	0.1471	152	5.1	14
MVb@75%	0.0798	66	4.0	9.4
MVb@80%	0.0023	28	3.1	6.0
MVb@85%	−0.0774	12	2.4	3.9

Table 6.2: Summary of the performance of the MVb tagger, in which the rejection rates for τ-, c- and light-flavour jets are shown for various working points. The corresponding values have been extracted from a sample of $t\bar{t}$ decays generated by POWHEG+PYTHIA.

operation point	weight cut	light rejection	charm rejection	τ rejection
MVbCharm@45%	0.2936	1032	85	325
MVbCharm@50%	0.2495	532	47	166
MVbCharm@55%	0.2103	274	27	81
MVbCharm@60%	0.1753	138	17	43
MVbCharm@65%	0.1429	69	11	25
MVbCharm@70%	0.1121	37	7.3	16
MVbCharm@75%	0.0807	21	5.1	10
MVbCharm@80%	0.0477	11	3.6	6.7
MVbCharm@85%	0.0143	5.7	2.6	4.5

Table 6.3: Summary of the performance of the MVbCharm tagger, in which the rejection rates for τ-, c- and light-flavour jets are shown for various working points. The corresponding values have been extracted from a sample of $t\bar{t}$ decays generated by POWHEG+PYTHIA.

6.4.2 Identification of b-jets in boosted top-quark decays

An alternative presentation of the performance comparison between the MVb, MVbCharm and the current ATLAS default b-tagger, MV1, is presented in Figures 6.20 (a) and (b), where the efficiency dependence on the minimal distance of a b-jet to the quarks originating from the hadronic decay of a W-boson and the jet axis shift are shown. As both quantities are very sensitive to a jet overlap, they are perfect candidates to display the improvement from the MVb and MVbCharm taggers compared to the current ATLAS tools when they are applied to dense environments. The jet sample that is used for these comparisons are obtained from the decays of a KK-gluon into a pair of top-quarks, which are simulated with a KK-gluon mass of 2.5 TeV using PYTHIA8 and an operating point that matches an overall b-tagging efficiency of 70% (evaluated in the SM $t\bar{t}$ event sample) is chosen to compare the performance of the three tagging algorithms.

Figure 6.20 (a) shows that the performance of the MV1, MVb and MVbCharm algorithms is almost identical for b-jets obtained from the $g_{KK} \rightarrow t\bar{t}$ event sample, if these jets have an angular separation ΔR larger than 0.4 to the decay products of the hadronic W-boson decays (i.e. when the b-jets are isolated). The performance of all three tagging algorithms decreases substantially if this angular separation tends to smaller values. However, the performance loss of the MVb and MVbCharm algorithms is less significant with respect to the performance loss of the MV1 tagger. An improvement by a factor of up to 1.8 for the MVb and a factor of up to 2.2 for the MVbCharm algorithms are shown over the full range of ΔR values. In addition, it can be seen that the performance of the different taggers is very similar for a given working point if the alignment between the b-hadron and the jet is perfect, as it is shown in Figure 6.20 (b). Indeed the b-tagging efficiency of the MVb and MVbCharm taggers decreases as well for increasing values of the angular separation between the b-hadron and the jet. The loss of efficiency is however less significant and an improvement by a factor of up to 1.5 is shown for the various ΔR values. In a comparison between the Figure 6.20 (a) and Figure 6.2 (a), a difference in the efficiency loss can be observed, which is mainly due to the different kinematics of the top-quarks and their decay products. The same holds for the results presented in Figures 6.20 (b) and 6.3.

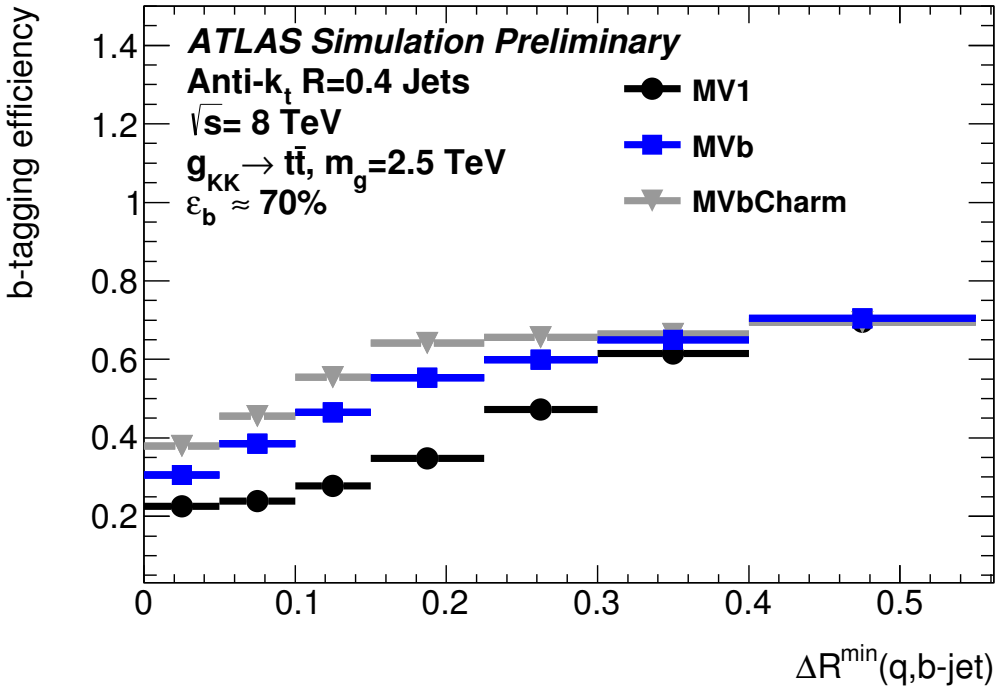

(a) b-tagging efficiencies vs. ΔR^{min}

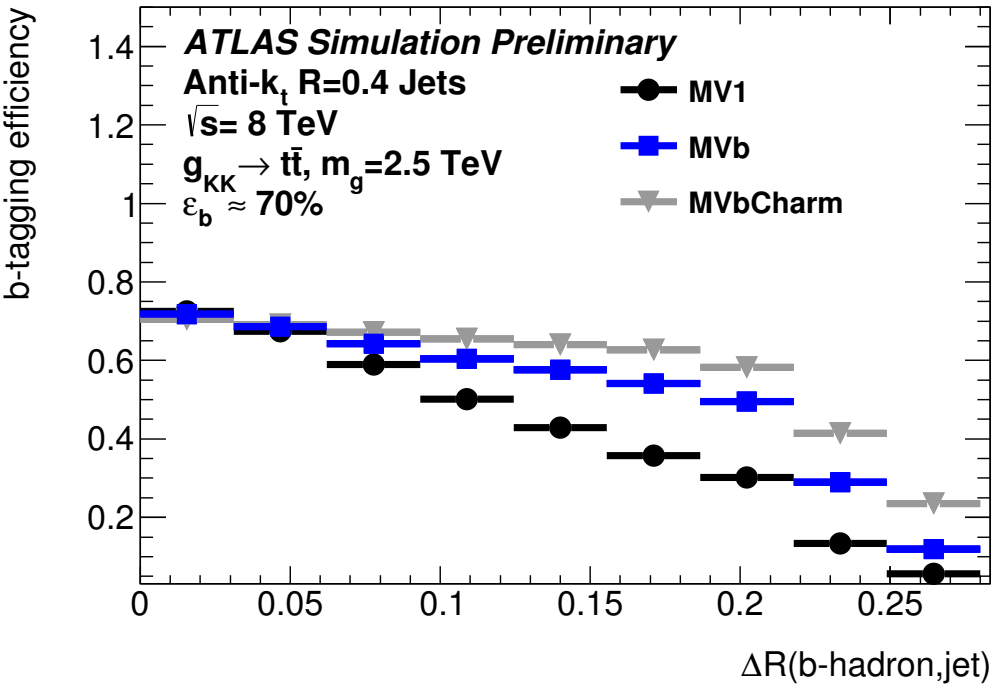

(b) b-tagging efficiencies vs. $\Delta R(b-\text{hadron, jet})$

Figure 6.20: b-tagging efficiencies of the MV1, MVb and MVbCharm algorithms as a function the ΔR between the reconstructed b-jets and the nearest quark from the $W \rightarrow q\bar{q}$ decay (a) and of the distance between the flight direction of the b-hadron and the b-jet axis (b) [7]. Both plots are evaluated for a sample containing $g_{KK} \rightarrow t\bar{t}$ events with a KK-gluon mass of 2.5 TeV. The algorithms are compared for a working point corresponding to 70% in the SM $t\bar{t}$ sample.

6.4.3 Performance in non-top-quark final states

In order to demonstrate that the MVb and MVbCharm algorithm do not only improve the identification of b-jets in strongly boosted hadronic top-quark decays but also in other topologies, both taggers are applied to further extreme scenarios. Their performance is compared to the MV1 tagger. In the following, jets from the decays of a hypothetical Randall-Sundrum graviton with the mass $m_{G^*} = 2$ TeV are used for this purpose as well as high-p_{T} jets from the QCD dijet production. Both comparisons are performed for a representative working point corresponding to an overall efficiency of 70% as evaluated for all three taggers in the SM $t\bar{t}$ sample.

Figure 6.21 (a) displays the b-tagging efficiency of the MVb, MVbCharm and the MV1 algorithm for jets stemming from the $G^* \rightarrow hh \rightarrow b\bar{b}b\bar{b}$ decay as a function of the transverse momentum of the Higgs boson from which the corresponding b-jets originated. The Higgs bosons appearing in these decays are assumed to have a mass of 125 GeV and Standard Model like properties. For a Higgs p_{T} below 400 GeV all taggers show a very similar performance since the two resulting b-hadrons are often clustered into two individual jets. With increasing p_{T} of the Higgs bosons the angular separation between the two hadrons will decrease and it becomes more likely that both will be clustered into one jet. As can be seen, the performance of both the MVb and MVbCharm algorithms is degraded less than for the MV1 tagger, although they do not exploit the double b-hadron topology resulting into two secondary vertices. As for the comparisons performed in Section 6.4.2, the b-tagging efficiencies of the MVbCharm algorithm are slightly larger for this operating point than the efficiencies of the MVb algorithm. However, the light-flavour rejection rates of the MVbCharm algorithm corresponding to the same operating point are significantly smaller with respect to those of the MVb tagger.

In addition, the ratio between the b-tagging efficiency ε_{b} and the mis-tagging efficiency for light-flavour jets is shown in Figure 6.21 (b) for a operation point corresponding to an overall efficiency of 70% and as a function of the transverse momentum of the jets obtained from the sum of the simulated QCD dijet samples described in Section 5.3.1. In the search for heavy resonances decaying into a $b\bar{b}$ final state, jets are investigated whose transverse momentum extends to values above the TeV scale. Thus a good b-tagging performance for high-p_{T} jets is highly desirable. Indeed the MVb tagger shows a significantly better performance for high-p_{T} jets obtained from QCD dijet events than the MV1 algorithm since the ratio between the b-tagging efficiency and the light-flavour rejection rate corresponding to MVb is improved by a factor of 1.2 to 2 with respect to MV1. This particular representation is chosen as not only the light-flavour rejection rates of the MV1 and MVb algorithms decrease strongly with increasing jet p_{T} (see Figure 6.18 (a)), but also their b-tagging efficiency itself if the transverse momenta of the studied jets exceed values of 500 GeV. Thus a fair performance comparison at very high p_{T} is not possible from studying only the light-flavour rejection rate. These two comparisons underline that both the MVb and the MVbCharm tagger are not only better adjusted to identify b-jets in boosted top-quark decays but also in the decay of a boosted boson into two b-quarks or in the case of high b-jet transverse momentum.

6.4.4 Combination of the MVb and MVbCharm algorithms

In order to increase the b-tagging performance both in terms of the charm and light-flavour rejection, the MVb and the MVbCharm algorithms can be combined. For this purpose, the decision whether a jet is b-tagged or not can be made by placing a two-dimensional cut on the output weights of these two tagging algorithms (i.e. a jet is considered to be b-tagged if both its MVb and MVbCharm output weights exceed certain threshold values).

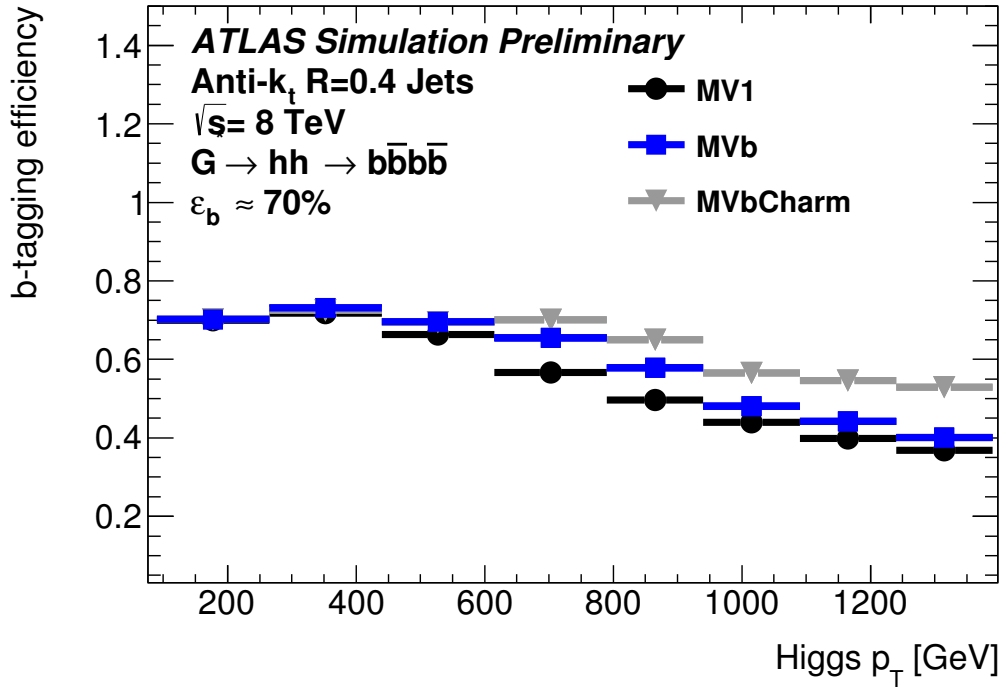

(a) $G^* \to hh \to b\bar{b}b\bar{b}$

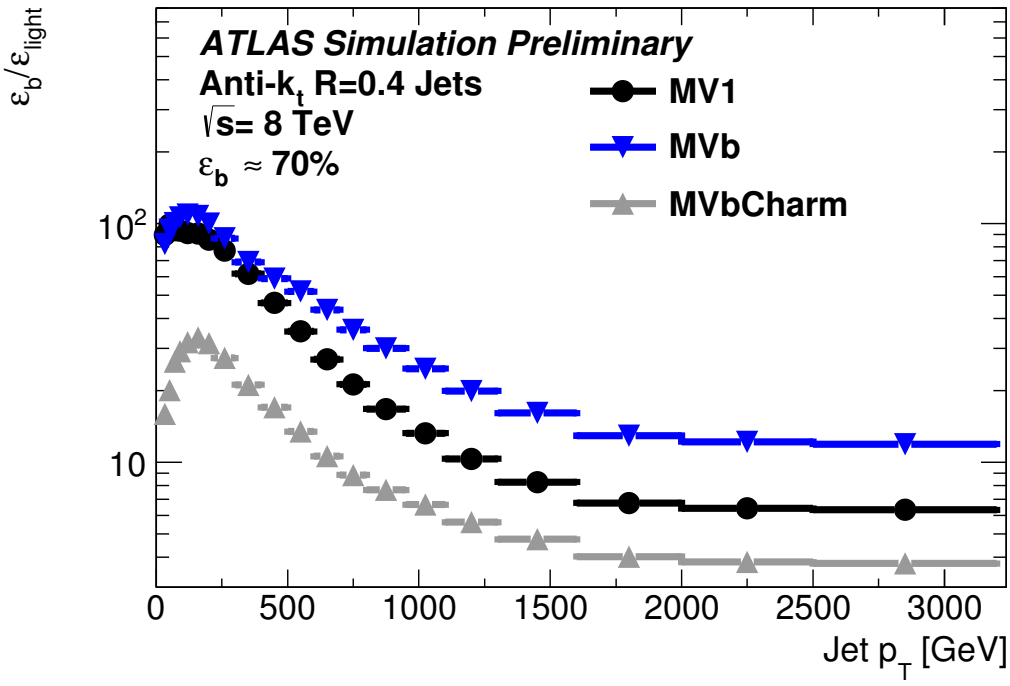

(b) QCD dijet

Figure 6.21: Performance comparison between the MV1, MVb and MVbCharm taggers in jet samples obtained from the decay of a hypothetical Randall-Sundrum graviton with the mass $m_{G^*} = 2$ TeV (a) or from the sum of the QCD samples described in Section 5.3.1 but without applying the event weights corresponding to the sample cross-section (b). Shown are the b-tagging efficiency as a function of the Higgs p_T and the ratio $\varepsilon_b/\varepsilon_{light}$ as a function of the jet p_T respectively. Both comparisons are performed for a working point corresponding to an overall efficiency of 70% [7].

A variety of different operating points is obtained for this combined tagger (referred to in the following as MVbComb) by independently varying the thresholds on the two output weights. From all the possible operating points, the one is chosen that maximises the following expression:

$$\varepsilon_{\mathrm{b}} \cdot \left(1 - \frac{N_{\mathrm{l}-jets}^{\mathrm{tagged}} + N_{\mathrm{c}-jets}^{\mathrm{tagged}} + N_{\tau-jets}^{\mathrm{tagged}}}{N_{\mathrm{l}-jets}^{\mathrm{total}} + N_{\mathrm{c}-jets}^{\mathrm{total}} + N_{\tau-jets}^{\mathrm{total}}} \right) , \tag{6.9}$$

where, the N_i^{tagged} denote the number of c-, τ-, and light-flavour jets that pass the particular b-tagging requirement, while the N_i^{total} represent the total number of c-, τ-, and light-flavour jets contained in the investigated event sample. Such an operating point has the maximal rejection of non-b-jets (i.e. the sum of c-, τ- and light-flavour jets) for a given b-tagging efficiency. In order to obtain not one but several operating points, this procedure can be performed allowing only two-dimensional cuts on the output weights of the MVb and MVbCharm algorithms that provide particular values for ε_{b}. Using this strategy, four different operating points are derived, which match overall b-tagging efficiencies of around 60%, 70%, 80% and 85%, respectively. The determination of these operating points is performed based on a selected jet sample obtained from $Z' \rightarrow t\bar{t}$ events that are simulated with a resonance mass of $m_{Z'} = 0.5$ TeV, whose decays provide a relative similar event kinematic compared to the $t\bar{t}$ decays that are produced according to the SM predictions. The exact definition (i.e. the threshold values of the MVb and MVbCharm output weights) of these four operating points and their expected performance in a jet sample obtained from SM $t\bar{t}$ decays generated with POWHEG and PYTHIA are presented in Table 6.4. Their performance is quantified by the rejection rates for c-, τ- and light-flavour jets. For the operating point that matches a b-tagging efficiency of 60%, the rejection rates for c-, τ- and light-flavour jets are 16, 65 and 275 respectively, while the corresponding rejection rates of the 70% efficiency operating point are 6.2, 20 and 109.

Operating point	Threshold values	Light rejection	Charm rejection	τ rejection
MVbComb@60%	$w_{MVb} > 0.139$ & $w_{MVbCharm} > 0.154$	275	16	65
MVbComb@70%	$w_{MVb} > 0.111$ & $w_{MVbCharm} > 0.040$	109	6.2	20
MVbComb@80%	$w_{MVb} > -0.015$ & $w_{MVbCharm} > -0.044$	25	3.3	6.4
MVbComb@85%	$w_{MVb} > -0.085$ & $w_{MVbCharm} > -0.092$	11	2.4	3.9

Table 6.4: Definition of four exemplary b-tagging operating points corresponding to the combination of the MVb and MVbCharm algorithms (referred to as MVbComb), which is based on a two-dimensional cut on the output weights of these two taggers. Rejection rates for light-flavour, c- and τ-jets are displayed additionally. The presented values have been extracted from a sample of $t\bar{t}$ decays generated by POWHEG and PYTHIA. The considered jets are required to have $p_{\mathrm{T}} > 25$ GeV and $|\eta| < 2.5$.

In order to compare these four operating points to equivalent operating points of the MVb algorithm, the number of b-jets passing the particular b-tagging requirement divided by the sum of b-tagged c- τ- and light-flavour jets is studied in a sample of SM $t\bar{t}$ decays. For the MVbComb algorithm this ratio is predicted to be 31 at the 60% operating point, while the MVb algorithm provides a value of 19 at this operating point. Operating points that match b-tagging efficiencies of 70%, 80% and 85% for the MVbComb algorithm correspond to values of 14, 5.7 and 3.4 respectively, while the MVb tagger provides values of 12, 5.7 and 3.4 for these two efficiencies. To conclude, the ratios obtained after applying a two-dimensional cut on the output weights of

the MVb and MVbCharm algorithms are improved by factors of 1.6 and 1.2 with respect to the MVb algorithm when comparing operating points that match b-tagging efficiencies of 60% and 70%. For b-tagging efficiencies of 80% and 85%, no significant difference can be observed between the performance of these two tagging algorithms.

The performance of the MVbComb tagger is displayed in Figures 6.22 (a) and (b) in terms of its light-flavour and charm rejection rates separately for the operating points that match overall b-tagging efficiencies of 60%, 70% and 80%. These rejection rates are presented as a function of the jet p_{T} for jets that stem from a sample of SM $t\bar{t}$ decays, which are simulated using the POWHEG and PYTHIA generators. The curves of the light-flavour rejection rates have qualitatively a very similar shape for all three presented operation points. Starting from the low-p_{T} region, the light-flavour rejection rates increase continuously until a maximum is reached for jet p_{T} values around 120 GeV. The light-flavour rejection rates decrease again continuously to lower values for a jet p_{T} above approximately 120 GeV. The curve of the charm rejection rates of the operating point that provides a tagging efficiency of 60% is qualitatively very similar to the curves of the light-flavour rejection rates (as it also shows a peak at p_{T} values around 120 GeV), while the charm rejection rates corresponding to the operating points that match b-tagging efficiencies of 70% and 80% appear to be rather flat over the presented p_{T} range. The curves of the charm and light-flavour rejection rates corresponding to the MVbComb algorithm are in general qualitatively very similar to those of the MVb and MVbCharm algorithms.

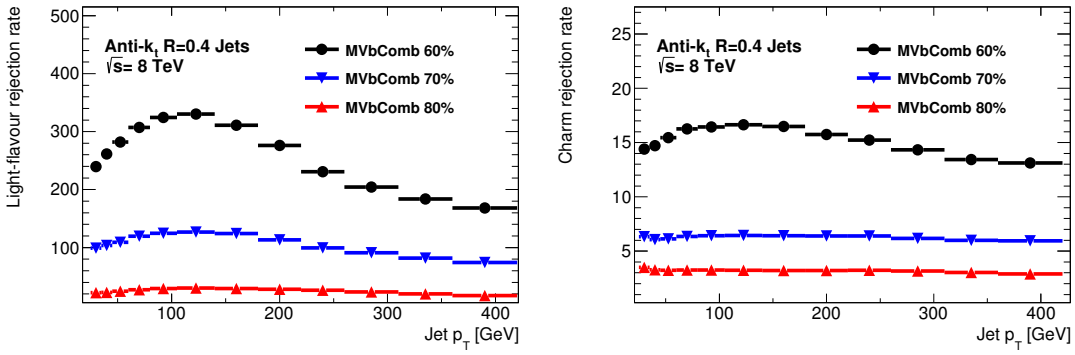

(a) light-flavour rejection vs. p_{T}

(b) charm rejection vs. p_{T}

Figure 6.22: Rejection rates for light-flavour (a) and charm (b) jets corresponding to three different operating points of the MVbComb algorithm as a function of the jet p_{T}. The considered jets are obtained from a sample of SM $t\bar{t}$ decays that are simulated using the POWHEG and PYTHIA generators.

6.4.5 Impact of the new introduced input quantities on the performance of the MVb tagger

The performance of the MVb tagger is substantially improved with respect to the MV1 algorithm for dense jet environments and for the high-p_{T} regime. In order to quantify to what extent these improvements depend on the new input quantities that are introduced in Section 6.2, the training of the MVb tagger is repeated and several quantities (i.e. the number of tracks with $|d_0/\sigma_{d_0}| > 1.8$, the scaled energy fractions, the jet width, the d_0 and z_0 significances of the track with the third highest-ranking as well as the vertex imbalance) are removed from the list of input

quantities of the underlying boosted decision trees. This version of the MVb tagger is referred to in the following as MVb*.

Figures 6.23 (a) and (b) show the light-flavour rejection rates of the MV1 algorithm and of both the MVb and MVb* taggers as a function of their b-tagging efficiency. Two different jet samples are used in order to compare the performance of these three taggers. The simulated jets are obtained either from SM $t\bar{t}$ events or from events in which a hypothetical Kaluza-Klein gluon with the mass $m_{g_{KK}} = 2.5$ TeV decays to a boosted $t\bar{t}$ system. In addition, the relative performance with respect to MVb is presented for the MVb* and the MV1 algorithms at the bottom of each plot. In the jet sample obtained from SM $t\bar{t}$ decays, the performance of the MVb* algorithm is reduced by a factor of around 0.9 for operating points corresponding to b-tagging efficiencies ranging from 40% to 80% and by a factor of around 0.8 for b-tagging efficiencies above 80%. However, the MVb* tagger performs still significantly better than the MV1 algorithm, when comparing b-tagging efficiencies below 60% or above 80%. For the jet sample that is obtained from events in which a high mass resonance of the KK-gluon decays into boosted top-antitop pairs, the performance of the MVb* tagger is even reduced with respect to MVb by a factor of up to 0.6 for b-tagging efficiencies below 80%, while its performance with respect to MV1 is still better by a factor of 1.1-2.2 (depending on the chosen operating point).

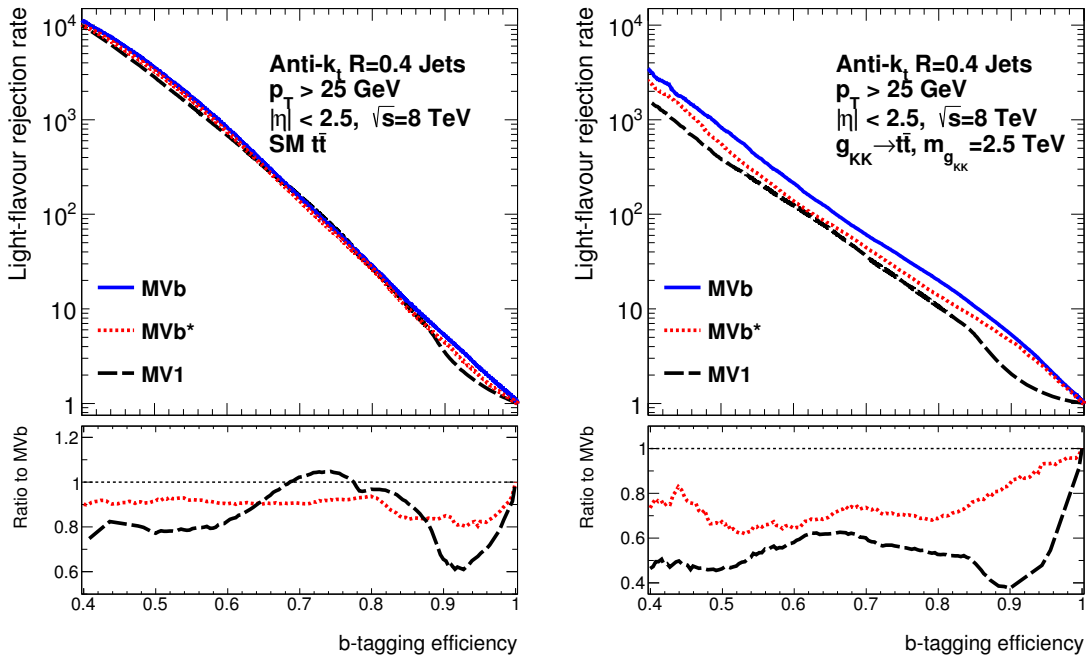

(a) SM $t\bar{t}$ **(b)** BSM model

Figure 6.23: Light-flavour rejection rates as a function of the b-tagging efficiency for jets stemming from two samples of simulated $t\bar{t}$ events produced either according to the SM predictions (a) or from the decay of a Kaluza-Klein gluon (b). The performance of the standard setup of the MVb tagger (presented as a blue solid line) is compared to the performance of the MVb* (red dashed line) and the MV1 (black dashed line) taggers.

In addition, the b-tagging efficiency dependence on the $\Delta R(b-\text{hadron}, \text{jet})$ is compared in Figure 6.24 for the MVb, MVb* and the MV1 algorithms using a representative operating point that matches an overall b-tagging efficiency of 70%. This comparison is performed again in a sample of jets that is obtained from $g_{KK} \rightarrow t\bar{t}$ events. For ΔR values below 0.06, the b-tagging efficiencies of these three taggers are very similar. However, the performance of the MVb* algorithm degrades more strongly than the performance of the standard setup of MVb, if the ΔR between the flight direction of the b-hadron and the jet axis increases. Hence, the b-tagging efficiency of the MVb* algorithm is reduced by a factor of down to 0.7 with respect to the MVb tagger. Still, the tagging efficiency of MVb* is better by a factor of up to 1.2 with respect to the MV1 algorithm.

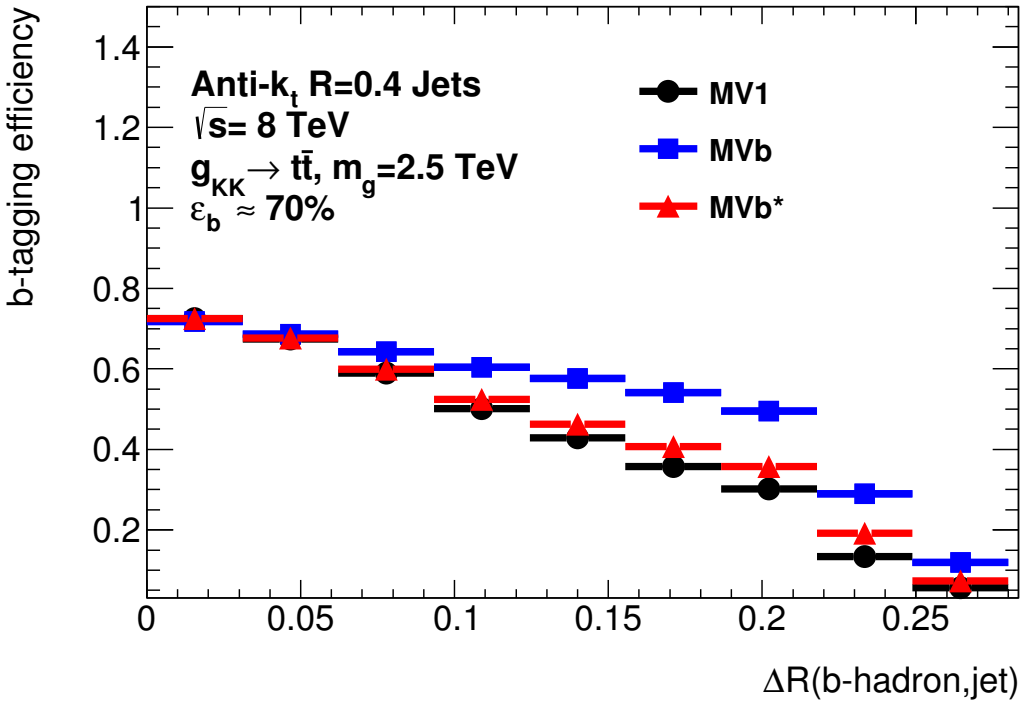

Figure 6.24: b-tagging efficiencies of the MV1, MVb and MVb* algorithms as a function of the angular separation between the flight direction of the b-hadron and the b-jet axis. These curves are evaluated for a jet sample obtained from $g_{KK} \rightarrow t\bar{t}$ events with a KK-gluon mass of 2.5 TeV. The algorithms are compared for an operating point corresponding to a b-tagging efficiency of 70% in the SM $t\bar{t}$ sample.

Figure 6.25 displays the ratio between the b-tagging efficiency ε_{b} and the mis-tagging efficiency for light-flavour jets corresponding to the MVb, MVb* and the MV1 algorithm as a function of the transverse jet momentum using again an operating point that matches an overall efficiency of 70%. The jet sample used for this purpose is obtained from the sum of the simulated QCD dijet samples described in Section 5.3.1.

According to the $\varepsilon_{\text{b}}/\varepsilon_{\text{light}}$ curves, significant differences in the performance of the MVb and MVb* algorithms are shown both for jet p_{T} values below 75 GeV and above 300 GeV. The performance of the MVb* tagger is particularly worse than the performance of the MVb algorithm in the high-p_{T} regime, where the performance differences between these two taggers range up to a factor of approximately 1.4. Nevertheless, the performance of the MVb* algorithm

is still significantly better with respect to the performance of the MV1 algorithm for p_{T} values in a range between 100 GeV and 250 GeV and also for p_{T} values above 500 GeV.

To conclude, the performance improvements of the MVb tagger with respect to the MV1 algorithm in dense jet environments, appear to be mainly caused by the new introduced input quantities (i.e. the number of tracks with $|d_0/\sigma_{d_0}| > 1.8$, the scaled energy fractions, the jet width, the d_0 and z_0 significances of the track with the third highest-ranking as well as the vertex imbalance) and of a lesser extent due to the changed training procedures. Also in the high-p_{T} regime, the new input quantities provide a significant contribution to the improved performance of the MVb tagger. For high jet p_{T} values, the impact of the changed training conditions on the b-tagging performance seems to be significant as well.

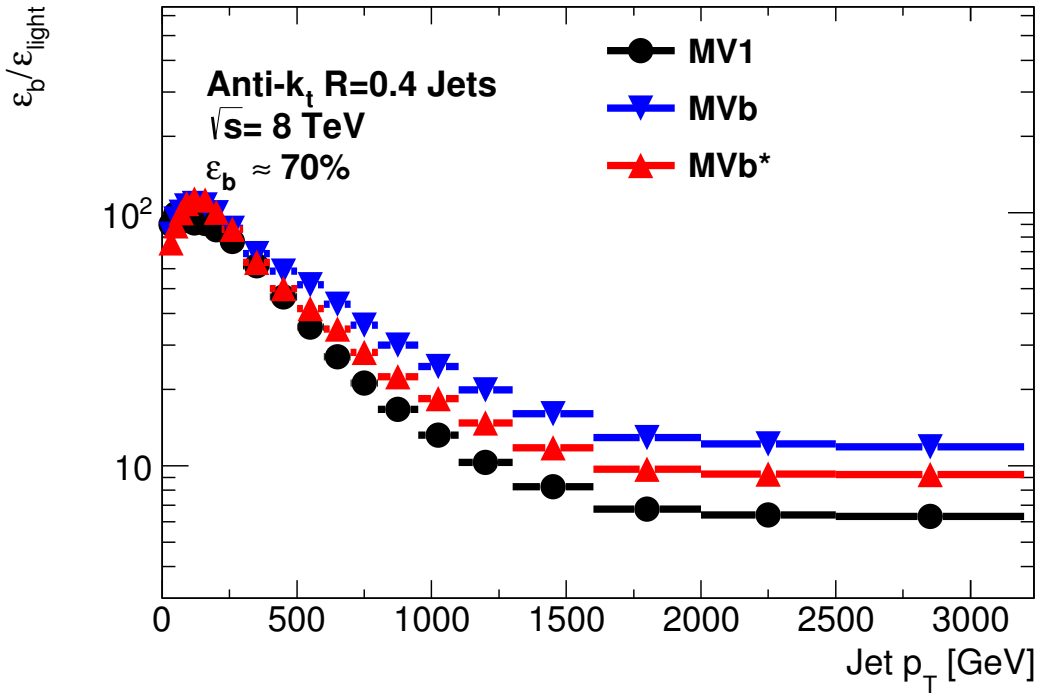

Figure 6.25: Performance comparison between the MV1, MVb and MVb* taggers in a jet sample that is obtained from the sum of the QCD dijet samples described in Section 5.3.1 but without applying the event weights corresponding to the sample cross-section. The b-tagging efficiency times the light-flavour rejection rate $\varepsilon_{\mathrm{b}}/\varepsilon_{\mathrm{light}}$ is shown as a function of the jet p_{T}. The algorithms are compared for an operating point that corresponds to a b-tagging efficiency of 70% in the SM $t\bar{t}$ sample.

Chapter 7

b-tagging with track based jets

Up to now the process of b-tagging was based on using jets reconstructed from adjoining clusters in the calorimeter system in order to approximate the flight direction of the b-hadron. As previously shown this approach runs into problems for topologies containing partons emitted with a small angular separation, since the reconstructed jets often do not resemble well enough the partonic structure of such events. However, new developments within the ATLAS collaboration strive for the usage of jets clustered directly from tracks as an alternative approach [8].

The selection requirements applied to the tracks entering the track jet clustering can be chosen to be close to the track selection requirements used by the various b-tagging tools. Thus it is guaranteed that almost all track based jets provide at least some b-tagging related information. A further advantage is that track based jets are expected to be relatively pile-up insensitive as stringent cuts on the transverse and longitudinal track impact parameters can be used to remove a substantial fraction of the tracks stemming from pile-up vertices. Thus track jets corresponding to low-p_{T} b-hadrons can be easily studied, while this is more difficult for calorimeter jets, due to the large contamination with low momentum jets stemming from pile-up vertices.

In addition, the clustering of these track based jets is completely independent from the reconstruction of the calorimeter based jets, which are used to measure the four-momentum of a hadronically decaying particle (such as $t \rightarrow bW \rightarrow bq\bar{q}$). This allows the disentangling of the measurement of energies or masses and the process of b-tagging. The track based jets could then be optimised in order to obtain the best b-tagging performance, while the calorimeter jets can still be optimised to give the best interpretation of the hadronic final state. A b-tagged track jet can be easily matched to any calorimeter based object applying either a ghost or a simply ΔR based association procedure [8] in order to b-tag the whole calorimeter based object.

The main disadvantage of track based jets is the fact that they do not include any information concerning electrically neutral particles. Thus the p_{T} of a track based jet, which is defined as the p_{T} of the four-momentum sum of all considered Inner Detector tracks, correspond to only about 60% (on average) of what is measured in the calorimeter system.

Connected to the efforts that aim to use track based jets for the purpose of b-tagging are studies investigating the feasibility to use small distance parameters R in the jet clustering procedure. In particular, track jet collections with $R = 0.4$, $R = 0.3$ and $R = 0.2$ are used. In order to motivate the use of such small-R jets for the purpose of b-tagging, Figure 7.1 presents the average distance in the η-ϕ-plane between a b-hadron with a certain transverse momentum and the charged particle tracks associated directly to its decay products $\Delta R(\mathrm{track}, b\mathrm{-hadron})$. In addition, also the ΔR curves are displayed that correspond to the 95.4%- and 99.6%-quantiles meaning that 95.4% (99.6%) of all tracks associated to the b-hadron decay have a ΔR smaller than the value given by the corresponding lines. Each of these curves show a characteristic $1/p_{\mathrm{T}}$ dependence (similar to Equation 6.1).

It can be seen that the average angular separation between the flight direction of a b-hadron with a transverse momentum of 20 GeV and its tracks is $\Delta R \approx 0.2$, while the 95.4%- and

99.6%-quantiles correspond to ΔR values of 0.4 and 0.7, respectively. For these low-p_{T} cases the standard-sized jets seem to be required to capture a sufficient fraction of the b-hadron decay products. However, for a b-hadron p_{T} of around 50 GeV these values decrease already to approximately 0.1, 0.2 and 0.3, while for for b-hadrons with a transverse momentum above 100 GeV the angular separation corresponding to the 99.6%-quantile is below $\Delta R = 0.2$. Thus for the medium- and high-p_{T} regime, clustering parameters substantially smaller than the standard-size of $R = 0.4$ are sufficient in order to reconstruct the decay of a b-hadron via a jet.

This chapter gives a short motivation for a possible application of the track jet based b-tagging to the top-quark sector, mainly on boosted hadronic top-quark decays, and describes the retraining of the MVb and MVbCharm algorithms for track jet collections corresponding to clustering parameters of $R = 0.4$, $R = 0.3$ and $R = 0.2$, respectively.

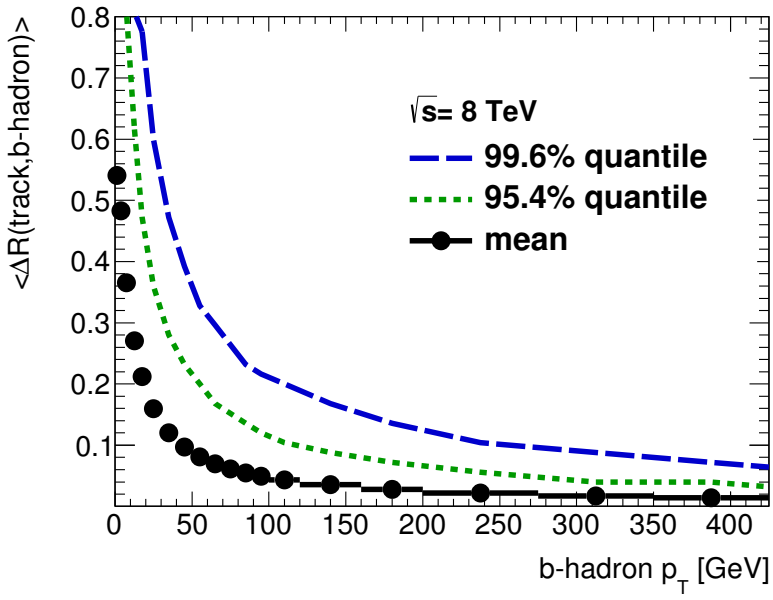

Figure 7.1: Average angular separation between a b-hadron and the tracks corresponding to its decay products $\langle \Delta R(\mathrm{track}, b-\mathrm{hadron}) \rangle$ presented as a function of the b-hadron p_{T} (as black markers). In addition, the two quantiles corresponding to 95.4% (green dashed line) and 99.6% (blue dashed line) of all tracks matched to the studied b-hadrons are shown as well. The simulated b-hadron decays stem from a sample of SM $t\bar{t}$ decays, which is produced with the POWHEG and PYTHIA generators.

7.1 Selection of tracks and track based jets

The track based jets used in the following studies are clustered with the anti-k_t algorithm applied to reconstructed Inner Detector tracks using distance parameters of $R \in \{0.4, 0.3, 0.2\}$. The tracks that are used in the jet clustering need to have a transverse momentum of at least 0.5 GeV. Here the direction of the track vector is evaluated at the position of the primary vertex. Further it is required that the tracks have at least one hit in the Pixel detector and at least six hits in total in the whole silicon layers of the Inner Detector. These hit requirements are chosen such that a track jet can be reconstructed even if the corresponding heavy flavour hadron decays relatively late (behind the first or second pixel layer). The transverse and longitudinal impact parameters

measured with respect to the primary vertex are required to fulfill $d_0 < 1.5$ and $z_0 \cdot \sin(\theta) < 1.5$, respectively to discard low quality tracks, but also tracks stemming from pile up vertices (as their longitudinal impact parameters are relatively large compared to tracks corresponding to the hard interaction).

In the following studies, the reconstructed track based jets are required to contain at least two tracks, have a transverse momentum above 7 GeV and an absolute pseudorapidity below 2.5. To further suppress track based jets that appear not to be compatible with the primary vertex but rather stem from pile-up vertices, the so-called "OriginIndex" formalism is used. Within this approach the jet vertex fraction (defined in Equation 3.10), is evaluated for each jet with respect to both the primary and pile-up vertex candidates contained in the particular event. If the value of the jet vertex fraction calculated with respect to the primary vertex is larger than the values obtained after calculating it with respect to all the pile-up vertices, the jet is considered within the analysis. The *b*-tagging based properties corresponding to these track jet collections are calculated using the exactly same processes and algorithms as for the calorimeter based jets.

Truth flavour labelling

Also the truth flavour labelling of these track based jets is performed as for the calorimeter jets based on a spatial matching of generator level particles to the reconstructed objects (as described in Section 4.2). However, it is taken into account that the small-R jets have a reduced active area with respect to the standard-sized jets. Thus the matching of a particle to a jet is considered to be successful if their angular separation is smaller than 0.3 for the $R = 0.4$ and $R = 0.3$ track jet collections and smaller than 0.2 for the $R = 0.2$ track based jets.

7.2 Performance of track based jets in boosted top-quark decays

Figure 7.1 indicates that distance parameters smaller than $R = 0.4$ are sufficient to cluster the decay products of medium- and high-p_{T} b-hadrons into one single jet. The expected main advantage of such small-R jets is that they are capable to resolve more often (than the standard-sized jets) the dense environments of e.g. a boosted hadronic top-quark decay completely. Thus the b-tagging related problems corresponding to the merging of two partons into one single jet (i.e. degradation of the resolution of the hadron flight direction) are reduced.

The performance of the three previously mentioned track jet collections are individually studied in terms of their ability to e.g. resolve boosted hadronically decaying top-quarks that stem from $Z' \rightarrow t\bar{t}$ events with various $m_{Z'}$ values. These track based jets are also compared to jets reconstructed from topological clusters in the calorimeter system with $R = 0.4$, as this is the current default jet collection used for b-tagging purposes in ATLAS. Figure 7.2 (a) presents the number of jets matched to the generator level particles that stem from top-quarks decaying via $t \rightarrow bW \rightarrow bq\bar{q}$, while Figure 7.2 (b) displays the angular separation between the flavour-labelled b-jets and their associated b-hadrons. For both comparisons, the matching between a $R = 0.2$ ($R = 0.3$ or $R = 0.4$) track based jet and a generator-level particle is considered successful, if the ΔR between these two objects is smaller 0.2 (0.3). It is shown that with decreasing distance parameter, used in the jet clustering, the structure of a boosted hadronic top-quark decay can be resolved more often. For an exemplary Z' mass, simulated with the PYTHIA8 generator at a resonance mass of 2 TeV, approximately 60% of all hadronic top-quark decays have a track jet associated to each of the three quarks of the $bq\bar{q}$ system. This amount decreases to about 40% (20%) if track based jets with distance parameters of $R = 0.3$ ($R = 0.4$) are used instead. In the comparison between the calorimeter and track based jets,

both clustered with $R = 0.4$, no significant difference is found. The distributions of the angular separation between the flavour-labelled b-jets and their corresponding b-hadrons in Figure 7.2 (b) convey a similar impression. The jet collection with the smallest distance parameter R gives a significantly better resolution of the jet axis direction than the other jet collections. In the comparison between calorimeter and track based jets, the latter class seems to provide in general a better alignment between b-hadron and jet axis, which should be explainable for example due to their lower pile-up sensitivity. As a reminder: The various b-tagging algorithms use the jet axis as an approximation of the b-hadron direction (e.g. in the procedure of track-to-jet association). Thus a worse alignment between the jet axis and the b-hadron direction automatically leads to an decrease in the b-tagging performance (see again Figure 6.3).

However, the performance of a particular jet collection is strongly dependent on the event topology and its kinematics, which becomes obvious considering the distributions that are displayed in Figures 7.2 (c) and (d) for further resonance mass points. In these figures, the number of jets matched to the generator level particles of the $t \to bW \to bq\bar{q}$ decays are presented for $Z' \to t\bar{t}$ events with resonance masses of 1 TeV and 3 TeV, respectively. For a resonance mass of 1 TeV, the average top-quark p_{T} is substantially reduced with respect to the 2 TeV events. Therefore, the expected angular separation between the decay products of the top-quarks is larger and a significant fraction of $t \to bW \to bq\bar{q}$ decays ($\sim 60\%$) is completely resolved using $R = 0.4$ jets. While the $R = 0.3$ jet collection shows the best performance in this particular kinematic region, the $R = 0.2$ track based jets seem to perform slightly worse with respect to the 2 TeV sample. This is mainly due to the fact that the b-hadron p_{T} spectrum is substantially softer for a resonance mass of 1 TeV and the fraction of $R = 0.2$ jets that fail the p_{T} selection requirement is larger than for the $R = 0.3$ jets as fewer tracks are considered in the clustering process. In total, approximately 70% (60%) of all the hadronic top-quark decays can be completely resolved using $R = 0.3$ ($R = 0.2$) track based jets. For the $Z' \to t\bar{t}$ event sample produced with a resonance mass of $m_{Z'} = 3$ TeV, the fraction of hadronic top-quark decays that are completely resolved using $R = 0.2$ track based jets is decreased by a factor of 1.2 (from 60% to 50%) with respect to the event sample produced with a resonance mass of 2 TeV. Therefore, even smaller clustering parameters could be beneficial in the case of such large resonance masses. To conclude, the choice of jet collection (i.e. the choice of the distance parameter R used in the jet clustering) should be carefully adjusted to the expected topology of a studied phase space region.

An additional approach to compare the performance of the various track jet collections to each other and to the calorimeter based jet collection is presented in Figure 7.3. Within this figure, the efficiency to find a reconstructed jet around the flight direction of a b-hadron as a function of the hadron p_{T} is shown separately for the three track jet collections and the calorimeter jets. In general all the studied jet classes perform very similar. Significant differences are only observable for a b-hadron p_{T} in the range between 15 GeV and 40 GeV, while the efficiency to match a jet with a b-hadron increases to almost 100% for each collection when the b-hadron p_{T} reaches a value of around 75 GeV. In the low-p_{T} region, the track based jets clustered with $R = 0.4$ and $R = 0.3$ show a matching efficiency that is increased by a factor of approximately 2 and 1.7, respectively with respect to the calorimeter jets. However, this is not an entirely fair comparison as these matching efficiencies strongly depend on the chosen selection requirements on the jet p_{T}. Nevertheless, it is possible to conclude that using small-R track based jets do not lead to a substantial loss in associating low-p_{T} b-hadrons and jets. Anyhow, as the b-hadron p_{T} spectrum in boosted top-quark decays extends to several hundred GeV, the low-p_{T} region of the b-hadron p_{T} spectrum is anyhow of lesser importance.

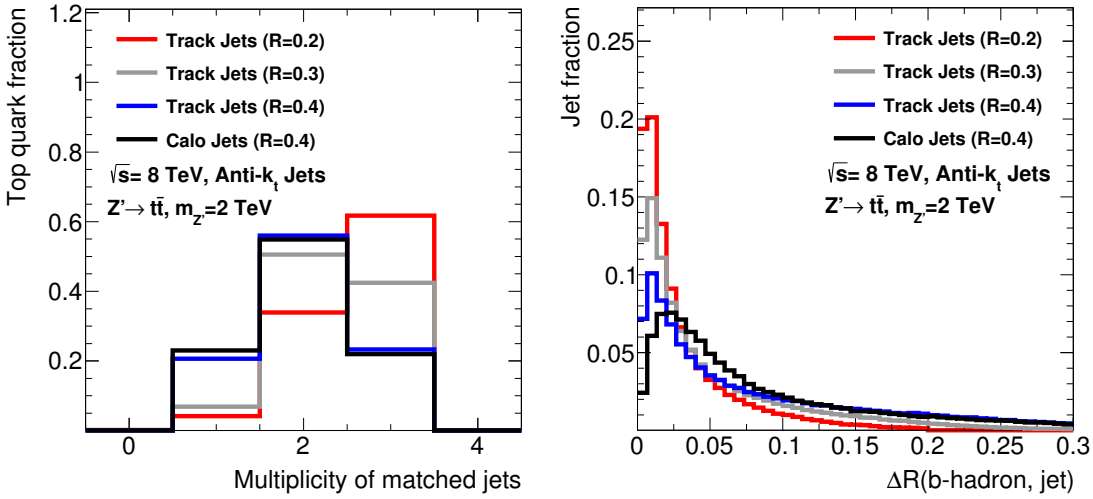

(a) **(b)**

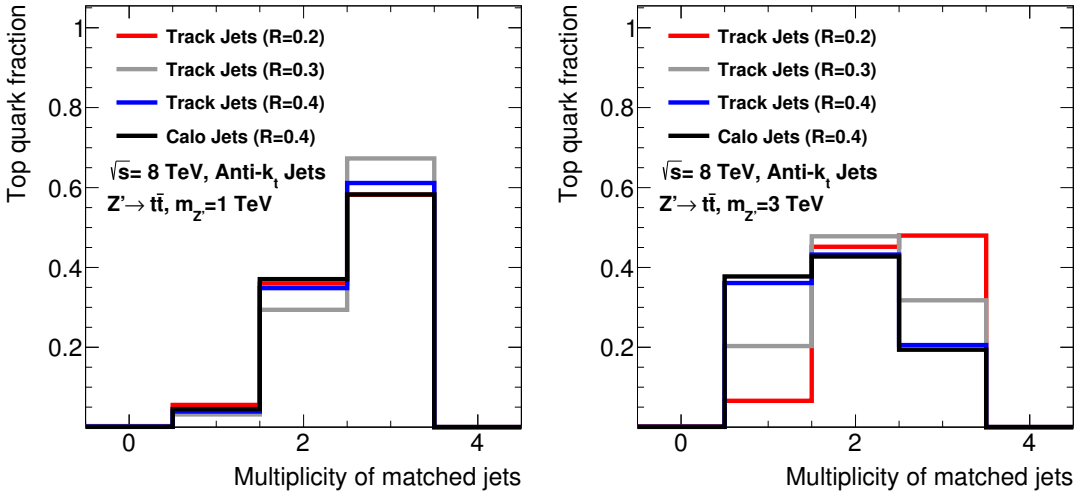

(c) **(d)**

Figure 7.2: Number of jets matched to the generator level particles that stem from top-quarks decaying via $t \to bW \to bq\bar{q}$ into a hadronic final state. The top quarks are produced in the decay $Z' \to t\bar{t}$ for resonance masses of 1 TeV (c), 2 TeV (a) and 3 TeV (d), respectively. In addition, the angular separation between the flavour-labelled b-jets and their associated b-hadrons is shown for jets stemming from $Z' \to t\bar{t}$ decays, in which the resonance mass is 2 TeV (b). All distributions are individually normalised to unit area. Compared are various jet collections reconstructed with the anti-k_t algorithm from either topological clusters in the calorimeter system or tracks from the Inner Detector. The various $Z' \to t\bar{t}$ event samples are simulated with Pythia8.

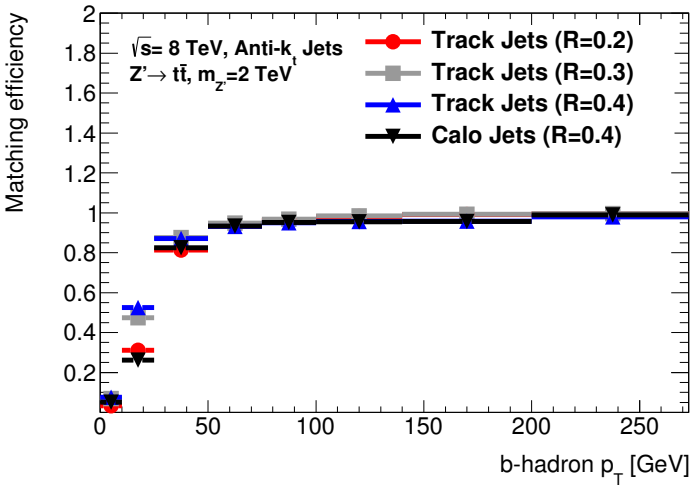

Figure 7.3: Efficiency to find a reconstructed jet around the flight direction of a b-hadron as a function of the hadron p_{T}. Presented are matching efficiencies corresponding to three different track jet collections clustered with a distance parameter $R \in \{0.2, 0.3, 0.4\}$ and a calorimeter jet collection clustered with $R = 0.4$. Both, the b-hadrons and jets stem from $Z' \rightarrow t\bar{t}$ decays that are simulated with Pythia8 for a resonance mass of $m_{Z'} = 2$ TeV.

7.3 Retraining the MVb and MVbCharm algorithms for track based jets

Jets that are clustered independently from each other using different distance parameters show differences in their kinematics and in particular in their b-tagging related properties (even when they correspond to the same parton). Thus, the performance of a b-tagging algorithm that is developed by training on a certain jet collection might not be optimal for another jet collection. Thus a retraining of the MVb and the MVbCharm algorithms for each of the three track jet collection is needed in order to exploit the full potential of both these algorithms.

For this purpose the same boosted decision tree setup is used as described in Section 6.3.2. Again the jet p_{T} is included into the training, while five independent boosted decision trees are trained in the same $|\eta|$ regions that were previously considered for the calorimeter based jets. Also the same re-weighting scheme is applied in order to obtain identical p_{T} spectra for b-, c- and light-flavour jets. However, the jet-flavour composition and the corresponding p_{T}-spectra of the different training samples are slightly different for the various track jet collections due to the dependence between the chosen clustering parameter and the jet kinematics.

The training statistics is obtained from b-, c- and light-flavour jets with a p_{T} between 7 GeV and 600 GeV stemming from simulated $t\bar{t}$ decays that are produced with the POWHEG and PYTHIA generators and dijet events generated with PYTHIA8. The dijet samples contain again the same number of events for each of several disjoint phase space regions, where the transverse momentum of the leading jet is the classification criteria. In total six different dijet samples are used for the retraining with bin edges of 0 GeV, 20 GeV, 80 GeV, 200 GeV, 500 GeV, 1000 GeV, 1500 GeV. In order to emphasize the boosted and high-p_{T} regime, only jets stemming from events containing a $t\bar{t}$ decay corresponding to an invariant $t\bar{t}$ mass (at generator level) above 0.7 TeV are considered, while jets originating from the dijet event samples are only taken into account if their transverse momentum is above 70 GeV.

As for the calorimeter jets, the training of the MVb algorithm for track based jets is based on using b-jets as signal and light-flavour jets as background, while for the MVbCharm algorithm c-jets are used as the background. In total 22 input quantities are considered during the retraining of both taggers. Table 7.1 lists separately for each of the three different track jet collections all these variables and their relative importance for an exemplary region corresponding to $|\eta| < 0.4$.

Comparing the ranking of the MVb and MVbCharm input quantities according to their importance in the training, no significant differences can be seen for the various track jet collections (i.e. it is not the case that a quantity, which is extremely important for one jet collection is almost not considered when training another jet collection). The same holds for the comparison to the variable ranking related to the training with calorimeter based jets (see Table 6.1). However, the relative importance of a certain quantity may indeed be very different when comparing the training results of two track jet collections to each other.

The quantities that receive the largest relative importance when training b- against light-flavour jets are the number of two-track vertices, the output weight of the IP3D tagger, the transverse decay length L_{xy} and also the energy fraction at the secondary vertex for vertices reconstructed by both, the iterative vertex finder and the JetFitter algorithm. When training b-against c-jets, also the number of two-track vertices and the jet weight of the IP3D tagger are the most important input quantities. Further important quantities are the invariant mass and the track multiplicity of the secondary vertices.

7.4 Performance of the retrained MVb and MVbCharm algorithms for the various track jet collections

The previously shown comparisons between the three different track jet collections were dedicated to study the ability of resolving the partonic structure of boosted hadronically decaying top-quarks. It was shown that the $R = 0.3$ and in particular the $R = 0.2$ track based jet collections represent the partonic structure of the studied $Z' \rightarrow t\bar{t}$ events significantly better than the $R = 0.4$ track jets, in case that the resonance masses were $m'_Z = 2$ TeV (or higher). However, this does not guarantee that the b-tagging performance (in terms of b-tagging efficiency as well as charm and light-flavour rejection) is better for the small R jet collections in these topologies than for the $R = 0.4$ jets. In order to draw any conclusions, the b-tagging performance of the MVb and MVbCharm taggers is probed both in resolved and boosted event topologies. Due to the fact that calorimeter and track based jets are not easily comparable in terms of their b-tagging performance, only the track based jets are considered in the following studies.

Figure 7.4 (a) shows the light-flavour rejection rates as a function of the b-tagging efficiency corresponding to the MVb tagger, while 7.4 (b) displays the c-jet rejection rates as a function of the b-tagging efficiency corresponding to the MVbCharm tagger. These figures compare the b-tagging performance of the two tagging algorithms applied to the three different track jet collections to each other. The considered jets are obtained from a sample of simulated $Z' \rightarrow t\bar{t}$ events that are generated with a resonance mass $m_{Z'}$ of 2 TeV using PYTHIA8. Both comparisons show that the $R = 0.2$ and the $R = 0.3$ track jet collections provide a substantially better b-tagging performance in boosted top-quark decays with respect to the $R = 0.4$ track based jets. While the light-flavour rejection rates of the MVb tagger applied to the $R = 0.2$ ($R = 0.3$) track based jets are improved with respect to the $R = 0.4$ track based jets by a factor of up to 1.8 (1.4) depending on the studied operating point, the charm rejection rates of the MVbCharm tagger are increased by a factor of up to 1.5 (1.25). A similar comparison was performed for jets from

Variable	anti-k_t $R = 0.2$	anti-k_t $R = 0.3$	anti-k_t $R = 0.4$
w_{IP3D}	12.86	17.46	17.54
w_{IP2D}	4.70	10.34	6.72
Number of two-track vertices (SV1)	14.89	5.50	8.50
Energy fraction (JetFitter)	4.30	3.56	4.98
$\log_{10}(\chi^2/\text{ndof})$ (JetFitter)	2.28	2.09	2.38
Number of tracks with $\lvert d_0/\sigma_{d_0}\rvert > 1.8$	7.69	3.69	7.56
Energy fraction (SV1)	4.06	8.02	4.37
Decay length significance (JetFitter)	3.84	3.59	4.96
3rd highest d_0 significance	3.74	3.06	2.88
Jet p_T	2.16	3.56	3.50
L_{xy}	4.76	5.92	3.94
Invariant mass (SV1)	4.42	5.40	2.53
Scaled energy fraction (SV1)	4.06	4.54	3.85
Invariant mass (JetFitter)	3.16	4.02	4.07
Jet width	1.93	3.97	5.76
Scaled energy fraction (JetFitter)	2.62	2.15	1.59
3rd highest z_0 significance	2.60	1.77	2.81
$\sigma_{\theta_{SV}}$ (JetFitter)	2.22	3.18	1.80
Decay length significance (SV1)	1.53	2.33	2.86
Track multiplicity at SV (JetFitter)	3.25	2.78	3.26
Vertex imbalance (JetFitter)	5.21	1.48	2.45
$\sigma_{\phi_{SV}}$ (JetFitter)	3.89	1.59	1.67

(a) Training: b- versus light-flavour jets

Variable	anti-k_t $R = 0.2$	anti-k_t $R = 0.3$	anti-k_t $R = 0.4$
w_{IP3D}	5.35	7.76	8.66
w_{IP2D}	2.28	3.04	2.75
Number of two-track vertices (SV1)	29.98	36.96	34.37
Energy fraction (JetFitter)	5.03	4.59	2.95
$\log_{10}(\chi^2/\text{ndof})$ (JetFitter)	1.47	3.01	1.77
Number of tracks with $\lvert d_0/\sigma_{d_0}\rvert > 1.8$	1.86	1.23	3.46
Energy fraction (SV1)	4.26	2.99	4.52
Decay length significance (JetFitter)	5.16	3.88	3.76
3rd highest d_0 significance	2.67	2.10	3.25
Jet p_T	2.66	2.38	2.68
L_{xy}	2.78	3.03	4.10
Invariant mass (SV1)	8.48	4.06	5.43
Scaled energy fraction (SV1)	1.11	2.99	2.08
Invariant mass (JetFitter)	6.33	5.82	5.26
Jet width	4.93	2.54	2.71
Scaled energy fraction (JetFitter)	4.76	1.18	1.72
3rd highest z_0 significance	1.28	2.43	1.98
$\sigma_{\theta_{SV}}$ (JetFitter)	1.38	2.41	0.67
Decay length significance (SV1)	1.05	1.17	1.03
Track multiplicity at SV (JetFitter)	4.42	4.25	4.57
Vertex imbalance (JetFitter)	1.28	1.40	1.16
$\sigma_{\phi_{SV}}$ (JetFitter)	1.49	0.93	1.14

(b) Training: b- versus c-jets

Table 7.1: Importance of the various input quantities of the boosted decision trees that are used in order to retrain the MVb and MVbCharm algorithms in the region $|\eta| < 0.4$ for the three different track jet collections. The values are normalised in each row to all variables together having an importance equal to one. The shown numbers are given in percent.

a $Z' \rightarrow t\bar{t}$ event sample using a generated resonance mass $m_{Z'}$ of 3 TeV. The corresponding results are similar to those obtained when $m_{Z'} = 2$ TeV was used to simulate the $Z' \rightarrow t\bar{t}$ decays.

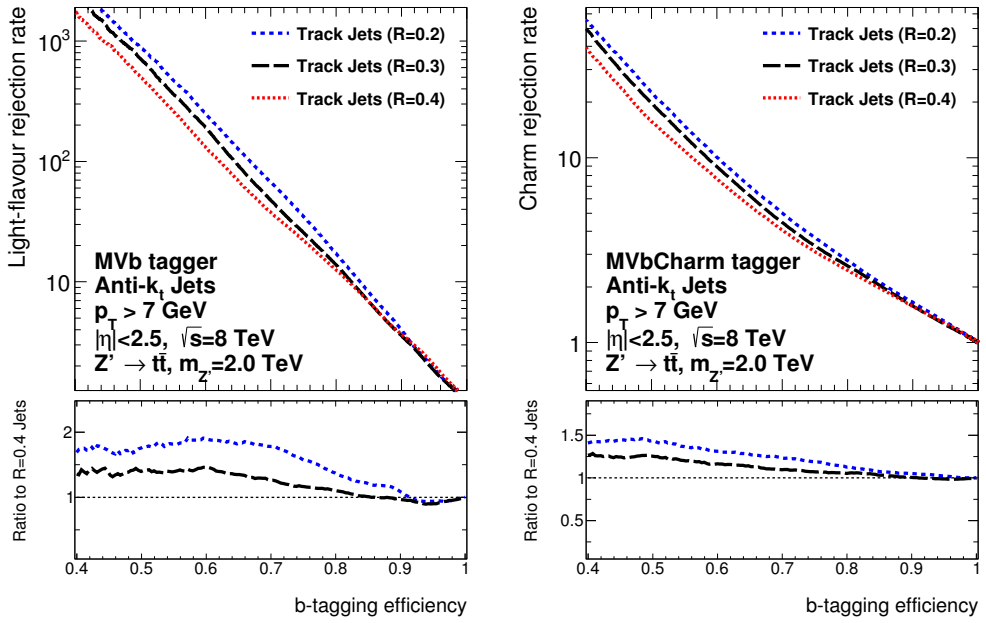

(a) light-flavour vs. b-jets

(b) c- vs. b-jets

Figure 7.4: Light-flavour (a) and charm (b) rejection rates as a function of the b-tagging efficiency corresponding to the MVb (a) and MVbCharm (b) algorithms for the three different track jet collections. All considered track based jets stem from a sample of simulated $Z' \rightarrow t\bar{t}$ events that are generated with a resonance mass $m_{Z'}$ of 2.25 TeV using PYTHIA8. The performance curves corresponding to the $R = 0.2$ track based jets are displayed as a blue line, while the $R = 0.3$ and $R = 0.4$ track based jets are represented by a black and a red line, respectively.

In Figures 7.5 (a) and (b), the same comparisons between the various track jet collections are performed based on jet samples that are obtained from SM $t\bar{t}$ decays, which are simulated using POWHEG and PYTHIA. Jets from these samples have a significantly softer p_{T} spectrum with respect to the jets stemming from the $Z' \rightarrow t\bar{t}$ events. In addition, the fraction of b-jets that are merged with a particle shower induced by the partons resulting from the $W \rightarrow q\bar{q}$ decays are also substantially reduced with respect to these BSM events. In contrast to the BSM samples, the b-tagging performance (in terms of light-flavour rejection) of the $R = 0.2$ track based jets is worse in this particular phase space region compared to the $R = 0.3$ and the $R = 0.4$ track based jets. For an operating point corresponding to a b-tagging efficiency of 80%, the light-flavour rejection rates of the MVb algorithm applied to the $R = 0.2$ track based jets is smaller by a factor of 0.9 with respect to the performance of the MVb algorithm retrained and applied to the $R = 0.4$ track based jets. This performance ratio difference decreases down to a value of 0.5 for b-tagging efficiencies around 60%. The corresponding performance differences of these two track jet collections are much less pronounced for the charm rejection of the MVbCharm algorithm, which is displayed in Figure 7.5 (b). At a b-tagging efficiency of 70% the performance of the $R = 0.2$ and the $R = 0.4$ track based jets is almost the same, while for an efficiency of 50% the performance difference is still below 10%. When comparing the performance of the MVb and MVbCharm taggers after applying them to the selected $R = 0.4$ and $R = 0.3$ track based jets no

significant difference in terms of charm or light-flavour rejection is observed for the jet samples obtained from SM $t\bar{t}$ events.

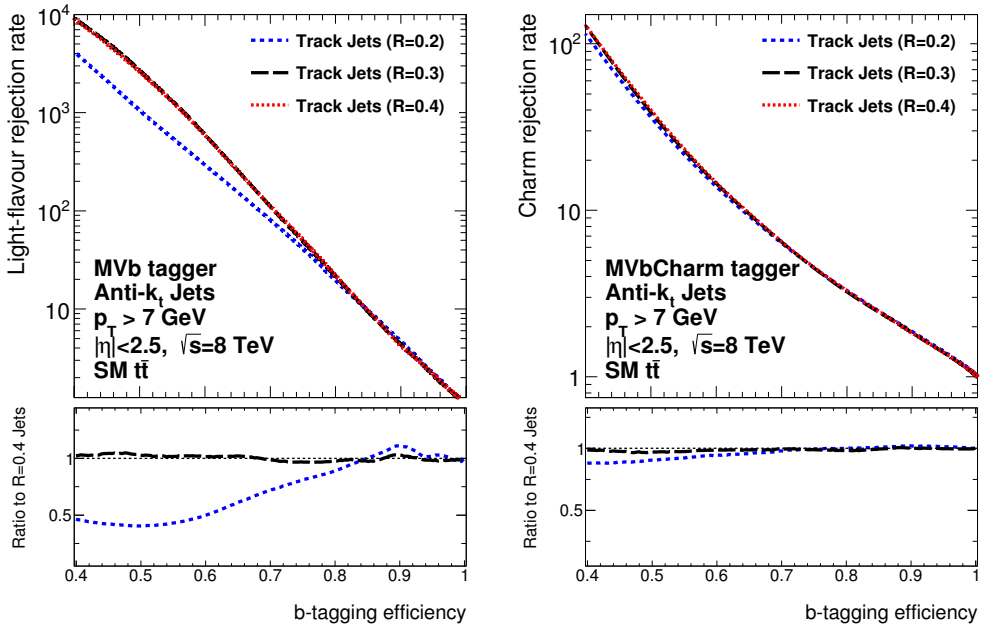

(a) light-flavour vs. b-jets

(b) c- vs. b-jets

Figure 7.5: Light-flavour (a) and charm (b) rejection rates as a function of the b-tagging efficiency corresponding to the MVb (a) and MVbCharm (b) algorithms for the three different track jet collections. All considered track based jets stem from a sample of simulated SM $t\bar{t}$ events that are generated using POWHEG and PYTHIA. The performance curves corresponding to the $R = 0.2$ track based jets are displayed as a blue line, while the $R = 0.3$ and $R = 0.4$ track based jets are represented by a black and a red line, respectively.

Also for track based jets it appears to be beneficial to combine the information provided by the MVb and MVbCharm algorithms in order to obtain an optimised b-tagging performance. This is done by using again the same procedure as described in Section 6.4.4 in order to derive for each of the three track jet collections one operating point that matches an overall b-tagging efficiency of 70%. Details on the rejection rates for the various jet flavour-types and the exact definition (i.e. the threshold values of the MVb and MVbCharm output weights) of the derived operating points are presented for each of the three different track based jet collections in Table 7.2. The expected performance in terms of the charm, τ- and light-flavour rejection rates corresponding to these operating points are evaluated individually for each track jet collection within a sample of jets that are obtained from SM $t\bar{t}$ decays, which are simulated using the POWHEG and PYTHIA generators. For track based jets that are clustered using a distance parameter $R = 0.4$, the rejection rates for c-, τ- and light-flavour jets are 5.6, 12 and 87 respectively, while the corresponding rejection rates for the $R = 0.3$ ($R = 0.2$) track jets are 6.0 (6.0), 10 (11) and 68 (58). Comparing these numbers to the rejection rates corresponding to a similar operating point evaluated for the combination of the MVb and MVbCharm algorithms for calorimeter based jets (see again Table 6.4), it becomes obvious that the light-flavour jet rejection rates according to any of the various track based jet collections are substantially lower. This is mainly due to the fact that a significant fraction of the light-flavour jets reconstructed with information of the

calorimeter system has none or only very few charged particle tracks (passing the b-tagging related track selection requirements) associated to and thus do not provide sufficient b-tagging relevant information. These jets are very unlikely to be b-tagged and their existence leads to a sizeable increase of the rejection rates of the calorimeter based jets relative to the track jet collections.

Track jet collection	Threshold values	Light rejection	Charm rejection	τ rejection
$R = 0.4$	$w_{MVb} > 0.118$ & $w_{MVbCharm} > 0.016$	87	5.6	12
$R = 0.3$	$w_{MVb} > 0.097$ & $w_{MVbCharm} > 0.064$	68	6.0	10
$R = 0.2$	$w_{MVb} > 0.097$ & $w_{MVbCharm} > 0.058$	58	6.0	11

Table 7.2: Rejection rates for light-flavour, c- and τ-jets corresponding to the combination of the MVb and MVbCharm algorithms (referred to as MVbComb) at an operating point that matches an overall b-tagging efficiency of 70%. The set of rejection rates are presented for track based jets that are clustered using distance parameters of $R = 0.2$, $R = 0.3$ or $R = 0.4$. Each operating point is defined by a two-dimensional cut on the output weights of the MVb and MVbCharm algorithms The presented values have been extracted from a sample of $t\bar{t}$ decays generated by POWHEG and PYTHIA. The considered track based jets are required to have $p_{\mathrm{T}} > 7$ GeV.

The light-flavour rejection rates of the MVbComb tagger are displayed as a function of the jet p_{T} in Figure 7.6 for the three different track jet collections at an operating point that matches a b-tagging efficiency of 70%. The curves of the light-flavour rejection rates have qualitatively for all three track jet collections a very similar shape. The small performance differences in each of the several p_{T} regions can be explained by the fact that jets clustered with a different distance parameter are dissimilar in their kinematics. Thus the boosted decision trees used to retrain the MVb and MVbCharm algorithms provide slightly different results in a particular phase space region.

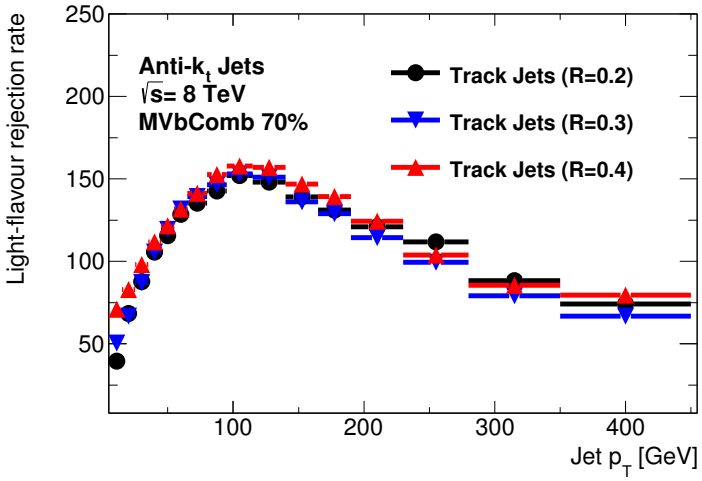

Figure 7.6: Light-flavour rejection rates presented as a function of the jet p_{T} corresponding to an operating point of the MVbComb algorithm that matches an b-tagging efficiency of 70%. Jets from three different track jet collections are taken from a sample of SM $t\bar{t}$ decays that are simulated using the POWHEG and PYTHIA generators.

Chapter 8

Calibration of the main ATLAS *b*-tagging algorithms in dense jet environments

The calibration of b-tagging algorithms using top-quark pair events as standard candles is well established. With the good understanding of the ATLAS detector and the data measured with it, b-tagging efficiencies have been measured with a precision of 2% for jets with a p_{T} around 100 GeV using a combinatorial likelihood approach applied to $t\bar{t}$ dilepton events [110]. However, as the focus of the Run II of the LHC will be shifted towards event topologies containing highly boosted objects leading to dense environments (including several close-by or even merged jets), a measurement of the b-tagging efficiencies is required not only as a function of the jet p_{T} and η, but also as a function of quantities that are sensitive to a merging of several partons from the hard interaction into one single jet.

A good example for a quantity that is highly sensitive to dense jet environments is the angular separation between the flight direction of a b-hadron and the jet axis $\Delta R(b-\mathrm{hadron}, \mathrm{jet})$. The performance of the various b-tagging algorithms used in ATLAS decrease strongly for increasing ΔR values as it was shown in Chapter 6. Thus, it is of great importance to probe whether this performance loss is equally strongly pronounced in the simulation and in data. However, this quantity is only accessible using information from the simulation and therefore not suitable for the purpose of a b-tagging calibration. Nevertheless, if a jet contains a reconstructed secondary vertex, the direction of the line joining the primary and secondary vertex candidates can be used as an approximation of the b-hadron flight direction in order to define a similar quantity $\Delta R(\mathrm{vertex}, \mathrm{jet})$. This quantity does not rely on generator level information.

Figures 8.1 (a) and (b) display the angular separation between the jet axis and the line joining the primary and the secondary vertices $\Delta R(\mathrm{vertex}, \mathrm{jet})$ as a function of the ΔR between the flight direction of the associated b-hadron and the jet for vertex candidates that are either reconstructed with the iterative vertex finder (using the SV1 setup) or the JetFitter algorithm. Both two-dimensional distributions show some asymmetry between the investigated quantities. A relevant fraction of the vertices reconstructed with the iterative vertex finder (see Figure 8.1 (a)) tends to relative large $\Delta R(\mathrm{vertex}, \mathrm{jet})$ values, even though the angular separation between the true flight direction of the b-hadron and the jet axis is relatively small. For vertices reconstructed with the JetFitter algorithm, a slightly opposite tendency is shown: In a significant fraction of cases in which the corresponding $\Delta R(b-\mathrm{hadron}, \mathrm{jet})$ values are relatively large, the reconstructed vertices tend to have relative small $\Delta R(\mathrm{vertex}, \mathrm{jet})$ values (see Figure 8.1 (b)). Nevertheless, the correlation between these two quantities seems to be relatively strong, thus $\Delta R(\mathrm{vertex}, \mathrm{jet})$ appears to be a very promising candidate for the calibration of b-tagging algorithms in dense environments, as it is expected to sufficiently describe the angular separation between the flight direction of a b-hadron candidate and the jet axis.

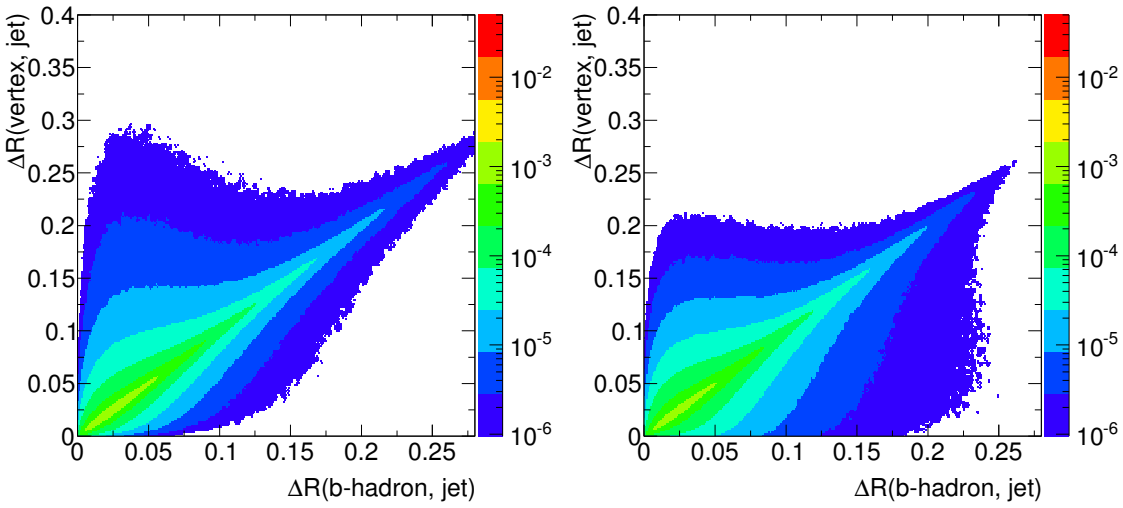

(a) SV1 based

(b) JetFitter based

Figure 8.1: Two-dimensional distribution of the angular separation between the line joining the primary and secondary vertex and the jet axis for jets that are spatially matched to a b-hadron (with $\Delta R < 0.3$) as a function of the ΔR between the flight direction of the corresponding hadron and the jet axis. In order to be considered, the jets are required to fulfill $p_{\mathrm{T}} > 25$ GeV and $|\eta| < 2.5$, while the b-hadrons must satisfy $p_{\mathrm{T}} > 5$ GeV. The colour coding represents the fraction of jets contained in a particular bin. The considered b-jets stem from $t\bar{t}$ decays that are simulated with the POWHEG and PYTHIA generators at a centre-of-mass energy of 8 TeV.

A further quantity that is suited for the purpose of b-tagging calibration in crowded jet environments is the angular separation between the probe jet and its nearest neigbouring jet ΔR^{min}, which has the advantage that it does not require any b-tagging based information (for example, the presence of a secondary vertex) in order to be calculated. Thus this quantity can be calculated for each selected jet in contrast to the $\Delta R(\mathrm{vertex}, \mathrm{jet})$.

This chapter describes the measurement of the b-tagging efficiencies of the MVb and MV1 algorithms in data for a representative operating point that matches an overall b-tagging efficiency of 70%. The obtained results are compared to the predictions by the simulation, in order to calibrate them (see 4.3.5). The corresponding data-to-simulation efficiency scale factors $\kappa = \varepsilon_b^{\mathrm{data}}/\varepsilon_b^{\mathrm{sim.}}$ are measured as a function of the p_{T}, η, $\Delta R(\mathrm{vertex}, \mathrm{jet})$, and ΔR^{min} of the selected probe jets. For this purpose a b-jet enriched sample is used that is obtained from selected $t\bar{t}$ candidate events with a final state containing exactly one charged lepton and at least four jets. Although the dileptonic $t\bar{t}$ based calibration methods have previously proven to provide more precise calibration results, they are not suited for these studies due to the relatively low jet multiplicities[1] contained in $t\bar{t}$ dilepton events.

Previous attempts to measure b-tagging efficiencies and the corresponding data-to-simulation scale factors using semileptonic $t\bar{t}$ candidate events are documented in detail in Reference [145]. Examples for such approaches are the kinematic selection method or the kinematic fit method. However, their systematic uncertainties were significantly larger with respect to the dilepton based methods, while they were less limited in statistics.

[1] As such events do not provide dense jet environments

8.1 Selection of the event and *b*-jet sample

The *b*-tagging efficiencies and the corresponding data-to-simulation calibration scale factors need to be measured in an unbiased sample of *b*-jets that is selected without using any *b*-tagging related information. Instead, the event topology of $t\bar{t}$ decays can be exploited using the invariant top-quark and *W*-boson masses as well as the expected event kinematics in order to identify *b*-jets stemming from hadronic top-quark decays. For this purpose, the χ^2 minimisation procedure, which is explained in Section 5.2, is used to fully reconstruct top-quark pair candidate events in data that decay into a final state of one charged lepton and at least four jets.

In order to be considered, a candidate event has to pass the full preselection requirements that are described in Section 5.1. In this χ^2 minimisation procedure, for each event only the jet assignment corresponding to the smallest χ^2_{total} value is considered in the following measurements. Additional requirements are introduced in order to decrease both the number of incorrectly-reconstructed $t\bar{t}$ decays and contaminations due to the backgrounds. Thus a selected candidate event is required to have a $\log_{10}(\chi^2_{\text{total}}) < 0.9$. In addition, the jet assigned to stem from the leptonic top-quark decay is required to be *b*-tagged (tag), while the two jets assigned to the hadronic *W*-boson decay are required to be not *b*-tagged (anti-tag). For this purpose the MV1 algorithm is used at an operating point that matches an overall efficiency of 70% in a simulated $t\bar{t}$ sample. The corresponding value of the MV1 output weight has to be larger (smaller) than 0.7892 in the case of the tag (anti-tag) requirement.

The measurement of the *b*-tagging efficiencies of the various algorithms in data is finally performed on a jet sample that contains only the *b*-jet candidates on the hadronic side of the events. The hadronic side of the semileptonic $t\bar{t}$ events is chosen in this context as it provides a higher jet multiplicity (and thus a more dense jet environment) than the leptonic side of the events. However, some of the measurements of the *b*-tagging efficiencies and the corresponding scale factors presented in the following are performed as well using the *b*-jet candidate on the leptonic side in order to study whether the results are consistent or not. In this case, the $\log_{10}(\chi^2_{\text{total}}) < 0.9$ and the anti-tag requirements have to be fulfilled as well. An additional control sample for the validation of the *b*-tagging efficiencies of *c*- and light-flavour jets corresponding to the MVb algorithm is obtained by requiring the *b*-jet candidates on both the leptonic and the hadronic side of the event to be *b*-tagged (double-tag). Again, the selected event has to satisfy $\log_{10}(\chi^2_{\text{total}}) < 0.9$. The two jets that are assigned to the hadronic *W*-boson decay are the corresponding probe jets. Thus the anti-tag requirement is not applied to obtain this jet sample.

Figure 8.2 shows the *b*-tagging efficiency of the *b*-jets associated to the hadronic side of the reconstructed top-quark decays as a function of the jet p_{T} (a) and $|\eta|$ (b) for an operating point of the MVb algorithm that matches an overall efficiency of 70%. The efficiency curves correspond to the cases that both the tag and the anti-tag requirements are applied, that only the *b*-tagging requirement on the *b*-jet candidate is applied to the leptonic side of the $t\bar{t}$ decay and that neither of these requirements is used to select the $t\bar{t}$ candidate events. Furthermore, the tagging efficiency of the *b*-jet corresponding to the hadronic side of the event is also presented for the case that both the *b*-jet candidate on the leptonic side and at least one jet associated to the hadronic *W*-boson decay are *b*-tagged (tag & mis-tag requirement).

In addition to these efficiency curves, the ratios of the *b*-tagging efficiencies obtained after applying the tag (tag & anti-tag) requirement to the efficiencies extracted from the "pre-tag" (i.e. no *b*-btagging requirement is applied) sample are shown as well. The difference between the four sets of *b*-tagging efficiencies is below the percent level and thus negligible compared to the expected statistical or systematic uncertainties on the *b*-tagging efficiency measurement. Furthermore, as this bias is expected to exist in both the simulation and the data, the correspond-

ing effect can be assumed to be further decreased when calculating the data-to-simulation ratios. Therefore, no corrections are required to be applied to the calibration results obtained with this tag and probe method (T&P).

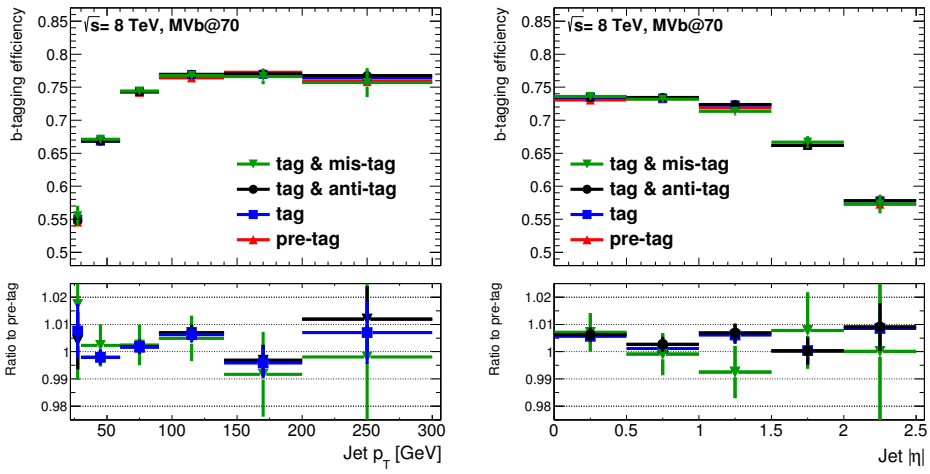

(a) b-tagging efficiency vs. the jet p_{T} **(b)** b-tagging efficiency vs. the jet $|\eta|$

Figure 8.2: b-tagging efficiencies of the b-jets that are associated by the χ^2 minimisation procedure to the hadronic top-quark decay as a function of the jet p_{T} (left) and $|\eta|$ (right) for an operating point of the MVb algorithm that matches an overall efficiency of 70%. The curves are shown separately for the case that both the tag and the anti-tag requirement are applied (black line), that only the b-tagging requirement is applied (blue line) and that neither of this requirements (pre-tag) is used to select the $t\bar{t}$ candidate events (red line). Also the efficiencies are shown (as a green line) that correspond to the case that both the b-jet candidate on the leptonic side and at least one jet associated to the hadronic W-boson decay are b-tagged (tag & mis-tag requirement). The ratios of the b-tagging efficiencies obtained after applying either the "tag", the "tag & anti-tag" or the "tag & mistag" requirements to the efficiencies extracted from the "pre-tag" sample are shown additionally at the bottom of each plot.

Corrections

The measurements of the unfolded top-quark p_{T} spectrum performed on the 2011 $\sqrt{s} = 7$ TeV data showed significant deviations with respect to the predictions of the POWHEG and PYTHIA generators [146]. Thus the average p_{T} of the top and anti-top-quark obtained from the 8 TeV simulation are reweighted using data-to-simulation scale factors based on the $\sqrt{s} = 7$ TeV findings (as no equivalent measurement for the 8 TeV data is yet available). The systematic uncertainties corresponding to the top-quark p_{T} reweighting are assessed by repeating the following measurement, but without applying the corresponding data-to-simulation scale factors to the simulated $t\bar{t}$ events. The full difference will be taken as a systematic uncertainty.

8.1.1 Event yields

The final event yields that are obtained after the event selection and reconstruction procedures (including the the cut on the reconstructed χ^2_{total} value, as well as the tag and anti-tag requirements) are applied to the ATLAS data and the simulation and are summarised in Table 8.1 (a).

In total 48207 (46579) events are observed in the electron (muon) channel, while approximately 44500 (42900) events are predicted by the Monte Carlo simulation and the data-driven background estimations. Considering the total uncertainties on the selection acceptance for both the signal and background processes, the predictions by the simulation and the data collected by the ATLAS detector are compatible with each other. The dominant background contributions after the full event selection and reconstruction arise from the associated production of a W-boson and jets, single top-quarks and the fake lepton background, while the backgrounds due to the Z+jets and diboson production are substantially smaller. The background contamination in the selected event sample is 14% and 10% for the electron and muon channel, respectively.

The number of events passing the double-tag requirements (i.e. events in which both the b-jet candidates on the leptonic and the hadronic side are b-tagged) are represented in Table 8.1 (b). The expected background contaminations in the e+jets and μ+jets channels of this event sample are 4% and 3%, respectively.

Source	$N_{e\text{+jets}}$	$N_{\mu\text{+jets}}$
$t\bar{t}$	38400 ± 4800	38500 ± 5000
$t\bar{t}+V$	101 ± 14	101 ± 15
W + jets	2050 ± 380	2180 ± 310
Z + jets	430 ± 220	200 ± 110
Diboson	58 ± 22	52 ± 20
Single top	1410 ± 320	1460 ± 340
Fake lepton background	2070 ± 520	365 ± 91
Total prediction	44500 ± 4900	42900 ± 5000
Observed	48207	46579

(a) Number of events passing the tag and anti-tag requirements

Source	$N_{e\text{+jets}}$	$N_{\mu\text{+jets}}$
$t\bar{t}$	26300 ± 5100	26000 ± 5200
$t\bar{t}+V$	101 ± 6	102 ± 6
W + jets	186 ± 36	235 ± 46
Z + jets	69 ± 15	32 ± 21
Diboson	2 ± 1	2 ± 1
Single top	548 ± 57	596 ± 70
Fake lepton background	257 ± 64	18 ± 4
Total prediction	27500 ± 5100	27000 ± 5200
Observed	29394	27928

(b) Number of events passing the double-tag requirement

Table 8.1: Number of events passing the full event selection and reconstruction procedure dedicated to identify $t\bar{t}$ candidates decaying into a final state with exactly one charged lepton and at least four jets. Table (a) presents the number of events that pass the cut on the $\log_{10}(\chi^2_{\text{total}})$ as well as the tag and anti-tag requirements, while Table (b) presents the number of events that pass the double-tag requirement and also the cut on the $\log_{10}(\chi^2_{\text{total}})$. The event yields are shown separately for the predicted signal and background processes and the observations in data. The uncertainties correspond to the total systematics relevant for this analysis.

Figures 8.3 (a) and (b) show data-to-simulation comparisons of the χ^2_{total} distribution of the events passing the full selection and reconstruction procedures (including the tag and the anti-tag requirements but not the cut on the corresponding $\log_{10}(\chi^2_{\text{total}})$ value) separately for the electron plus jets and muon plus jets channel. The sum of the individual processes predicted by the simulation and estimated by the matrix method are compared to the data. In these distributions (and also in the following), the non-prompt and fake lepton backgrounds, diboson and single top-quark events as well as the associated production of a Z-boson and jets are summarised as one single component (referred to as "others"). The contribution that is denoted by $t\bar{t}$ contains both the top-quark pair production and the associated production of top-quark pairs and a vector boson. In addition, data-to-simulation ratios are shown at the bottom of each plot. Considering the total uncertainties on the selection acceptance for both the signal and background processes, the predictions by the simulation and the observations in data are compatible with each other over almost the full range of $\log_{10}(\chi^2_{\text{total}})$ values. Only in the low statistic regions, obvious differences between the data and the simulation are seen for both lepton plus jets channels. In addition, the observations in data are almost constantly above the predictions by the simulation. This offset is in the order of 8%, but is not expected to impact the measurements presented in the following significantly, as the applied method depends not on the total normalisation but only on the modelling of the flavour composition of the selected jet sample.

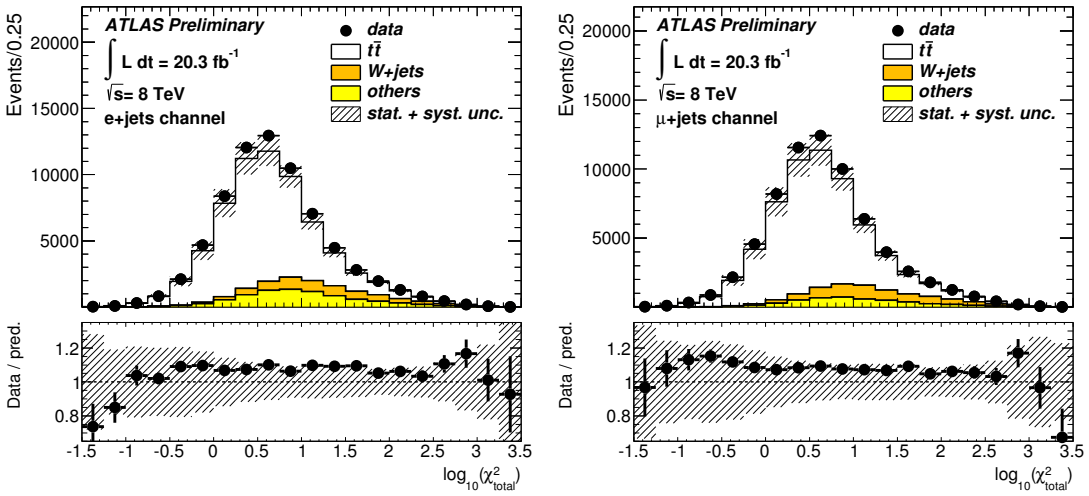

(a) $\log_{10}(\chi^2_{\text{total}})$ (e+jets channel) [9]

(b) $\log_{10}(\chi^2_{\text{total}})$ (μ+jets channel) [9]

Figure 8.3: Distribution of the minimum χ^2_{total} obtained from the reconstruction of the top-quark pair candidates after the full event selection (including the tag and the anti-tag requirements but not the cut on the corresponding $\log_{10}(\chi^2_{\text{total}})$ value) was applied (a-b). The simulated Monte Carlo samples are normalised according to their predicted cross-sections to an integrated luminosity of 20.3 fb^{-1}. Data-to-simulation ratios are shown at the bottom of each plot [9].

Data-to-simulation comparisons for the relevant kinematic properties of the selected probe jets (i.e. the b-jet candidate on the hadronic side of the reconstructed events) are displayed in Figures 8.4 (a-d) for the e+jets and μ+jets channels separately. The transverse momenta, Figures 8.4 (a-b), and the pseudorapidities, Figures 8.4 (c-d), of these jets are shown. Again, data-to-simulation ratios are presented at the bottom of each plot. These distributions are obtained after applying the full selection and reconstruction requirements to the candidate events (including the tag and the anti-tag requirements and also the cut on the corresponding $\log_{10}(\chi^2_{\text{total}})$ value).

For these quantities, the predictions by the simulation and the observations in data are compatible with each other over the full range of η values and up to a transverse momentum of 350 GeV, considering the total uncertainties on the selection acceptance for the signal and background processes. As no significant difference is observed between the e+jets and μ+jets channel, the b-tagging calibration results are presented in the following section based on the combination of both channels.

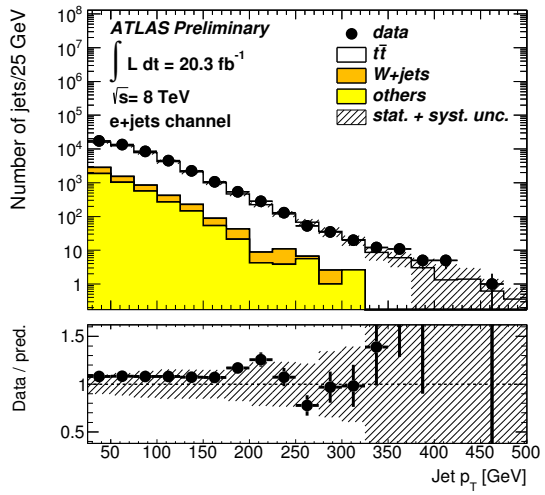

(a) Probe jet p_{T} (e+jets channel)

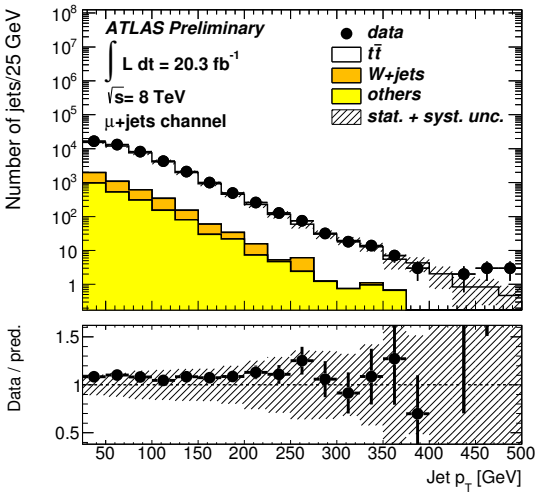

(b) Probe jet p_{T} (μ+jets channel)

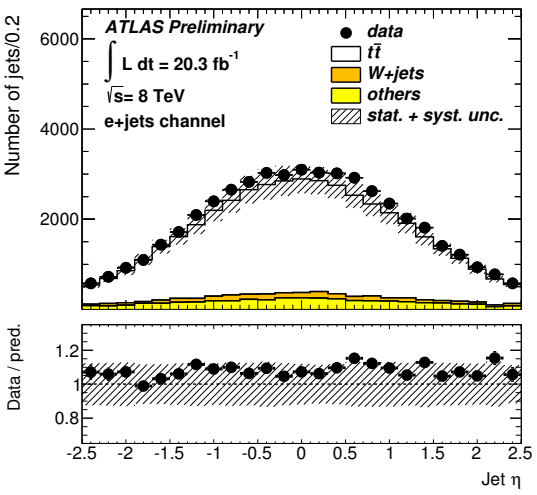

(c) Probe jet η (e+jets channel)

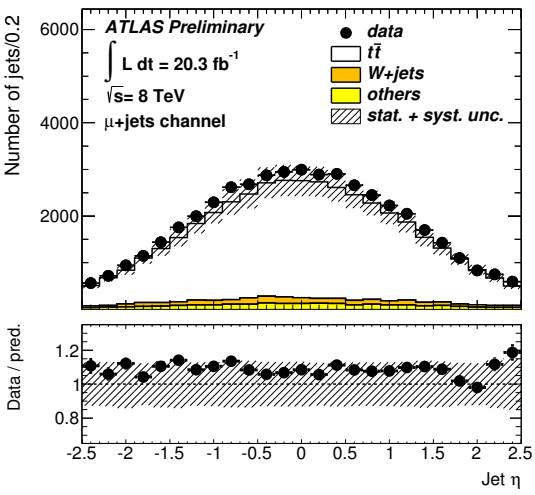

(d) Probe jet η (μ+jets channel)

Figure 8.4: Distribution of the transverse momentum (a-b) and the pseudorapidities (c-d) of the selected probe jets displayed separately for the electron plus jets (left column) and muon plus jets (right column) channel. The simulated Monte Carlo samples are normalised according to their predicted cross-sections to an integrated luminosity of 20.3 fb^{-1}. Data-to-simulation ratios are shown at the bottom of each plot [9].

Data-to-simulation comparisons for the angular separation between the line joining the primary and secondary vertex and the jet axis $\Delta R(\text{vertex}, \text{jet})$ and the angular separation between the probe jet and its nearest neigbouring jet ΔR^{min} (i.e. further quantities, which will be used in the calibration of the MVb and the MV1 algorithms) are displayed in the Figures 8.5 (a-c), where the distributions of the $\Delta R(\text{vertex}, \text{jet})$ are shown separately for secondary vertex candidates reconstructed by either the iterative vertex finder (a) or the JetFitter algorithm (b). In order to highlight the difference between b- and non b-jets, these distributions are subdivided into the various jet flavours, where the contribution due to the non-prompt and fake lepton background is subtracted from the observations in the data collected by the ATLAS detector. Jets originating from τ lepton decays are included in the distribution of the light-flavour jets. In general, the distributions observed in the data and the predictions by the simulation are compatible with each other considering the total systematic uncertainties. Only for $\Delta R(\text{vertex}, \text{jet}) < 0.02$, when studying vertices corresponding to the JetFitter algorithm, or ΔR^{min} values above 2.5, significant differences between the data and the simulation are observed.

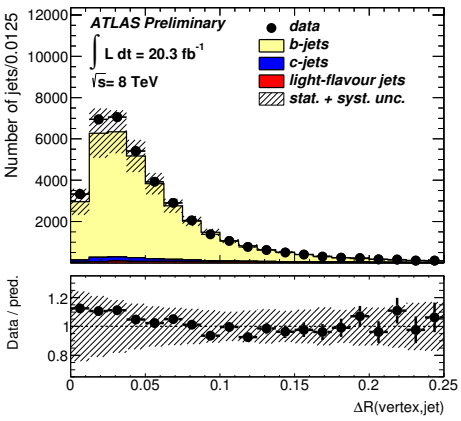

(a) $\Delta R(\text{vertex}, \text{jet})$ (SV1 based)

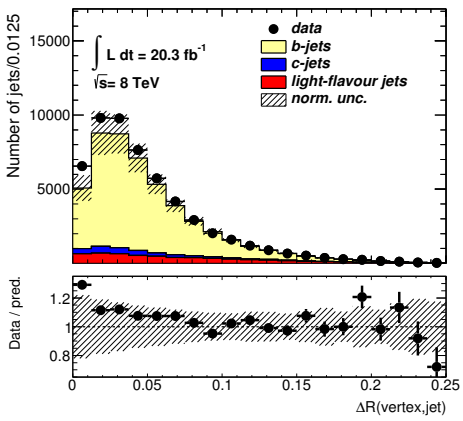

(b) $\Delta R(\text{vertex}, \text{jet})$ (JetFitter based)

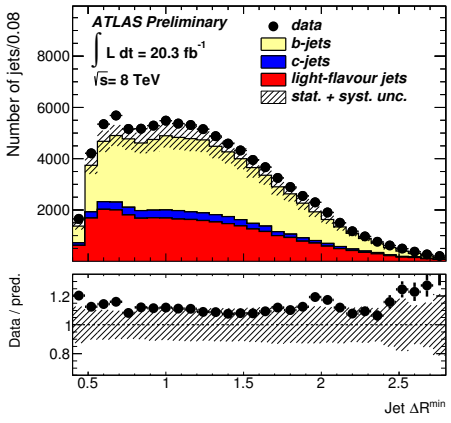

(c) ΔR^{min}

Figure 8.5: Distribution of the $\Delta R(\text{vertex}, \text{jet})$ for secondary vertex candidates contained in the selected probe jets (a-b) as well as their ΔR^{min} (c). The predictions from the simulation are subdivided into the three different jet flavour types. The simulated samples are normalised according to their predicted cross-sections to an integrated luminosity of 20.3 fb^{-1}. Ratios of the data and the simulation are shown as well at the bottom of each plot [9].

Figures 8.6 (a-c) show the distribution of the output weights of the MVb, MVbCharm and MV1 taggers for all probe jets contained in the selected event sample in a data-to-simulation comparison. It is shown, that the output weight of the MVb algorithm is not very well modelled in the background dominated region (i.e. a difference in the normalisation, but also in the shape is seen for w_{MVb} values below 0.1). Also the output weight of the MV1 algorithm shows significant differences between the observations in data and the predictions in the simulation. In general, these disagreements are negligible, as the calibration will correct for them. However, it has to be assured that these differences are due to a mismodelling of the b-tagging related properties of the b-jet candidates and not due to incorrect predictions of the flavour composition of the selected probe jet sample.

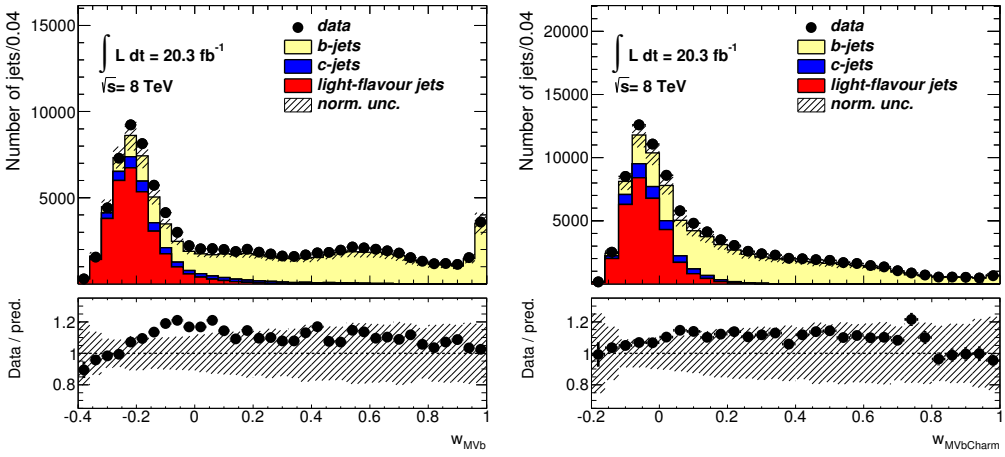

(a) MVb weight

(b) MVbCharm weight

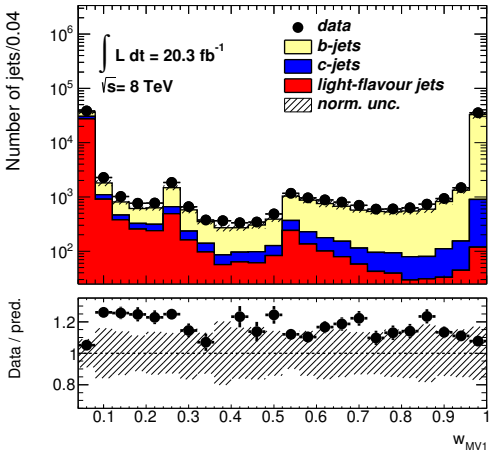

(c) MV1 weight

Figure 8.6: Distribution of the output weights of the MVb (a), MVbCharm (b) and MV1 (c) taggers for all probe jets contained in the selected event sample. The predictions by the simulation are subdivided into the three different jet flavour types. The simulated Monte Carlo samples are normalised according to their predicted cross-sections to an integrated luminosity of 20.3 fb^{-1}. In addition, ratios of the data and the simulation are shown at the bottom of each plot.

Data-to-simulation comparisons for some of the input quantities of the MVb and MVbCharm algorithms

In order to make sure that the observed shape and normalisation discrepancies that are shown for the output weight of the MVb tagger are rather caused by a mismodelling of the b-, c- and light-flavour contributions than by a mismodelling of the relative jet flavour fractions, several input quantities of the MVb and MVbCharm are studied in the probe jet sample but also in a dedicated control sample. This control sample is obtained by selecting events that have both the b-jet candidates on the leptonic and the hadronic side of the event b-tagged with the MV1 algorithm. Jets that are assigned by the χ^2 minimisation procedure to stem from the hadronic W-boson decay are most likely c- or light-flavoured. Examples for quantities that indicate a mismodelling of c- and light-flavour jet properties are presented in Figures 8.7 (a-d), where the number of tracks with $|d_0/\sigma_{d_0}| > 1.8$ (a), as well as the track multiplicity (b), the $\log_{10}(\chi^2/\text{ndof})$ and the invariant mass of the secondary vertices (reconstructed with the JetFitter algorithm) are shown. In addition, also the distribution of the MVb output weight is presented, in Figure 8.7 (e), as obtained from this control sample. Similar to the probe jet sample, a shape and normalisation disagreement is observed for w_{MVb} values below 0.1.

In addition, certain input quantities of the MVb and MVbCharm taggers show also significant data-to-simulation disagreements in their shape and normalisation for b-jets. This can be seen in Figures 8.8 (a-f), where data-to-simulation comparisons for the energy fraction, the invariant mass and the decay length significance are shown for vertices that are either reconstructed with the JetFitter algorithm or the iterative vertex finder (using the SV1 setup). In particular, the energy fraction shows significant shape differences in the comparisons between the predictions and the observations, while the shapes of invariant mass and the decay length significance seem to be modelled more reasonable. Both the invariant mass and the decay length significance depend only on the reconstruction of the secondary vertices, while the energy fraction depends also strongly on the additional number of tracks associated to a jets. As the values of the energy fraction that are observed in data tend to be larger than those predicted by the simulation, it can be concluded that the Monte Carlo prediction seems to overestimate the activity of additional tracks contained in a b-jet.

The distributions that are displayed in Figures 8.5 (a) and (b), in Figures 8.7 (a-d) as well as in Figures 8.8 (a-e) take only the subset of probe jets into account that contain a secondary vertex candidate, which is either reconstructed with the JetFitter algorithm or the iterative vertex finder (using the SV1 setup). According to the predictions by the simulation, 42.2% of these jets have a secondary vertex reconstructed with the iterative vertex finder, while 58.2% have a vertex found by the JetFitter algorithm. The JetFitter vertex candidates can be further classified depending whether they correspond to a single- or a multi-track topology. 12.6% of the probe jets contain only single-track vertices, while 45.6% contain at least one vertex candidate composited by two or more tracks. The corresponding fractions in data are 40.4%, 13.2 and 45.3%, respectively. The predictions in the simulation and the observation in data are compatible with each other within the statistical and systematic uncertainties. A summary of these numbers is also presented in Table 8.2.

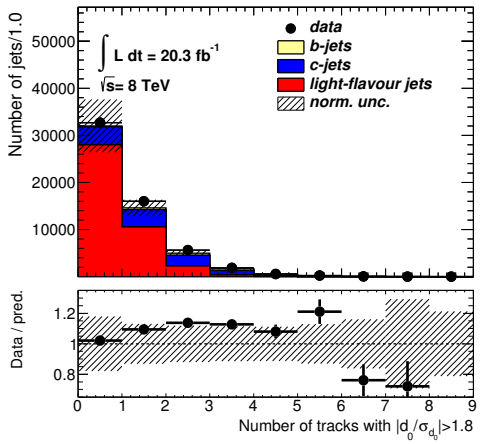

(a) Number of tracks with $|d_0/\sigma_{d_0}| > 1.8$

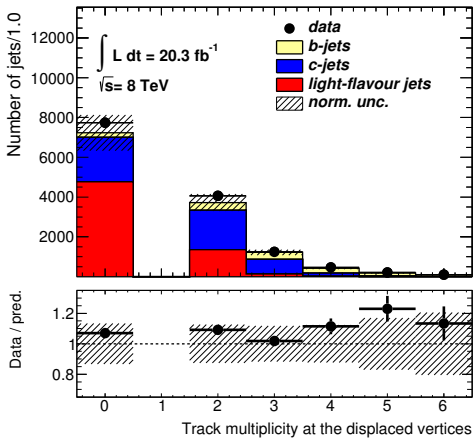

(b) Track multiplicity at the displaced vertices (JetFitter based)

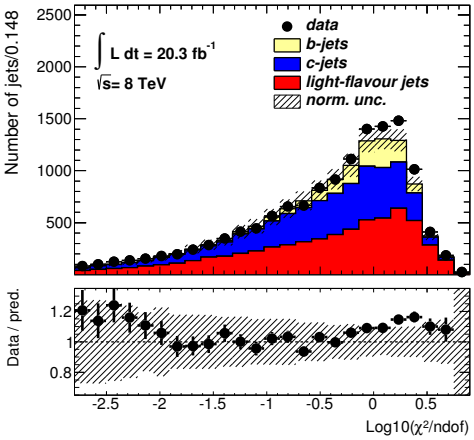

(c) $\log_{10}(\chi^2/\text{ndof})$ (JetFitter based)

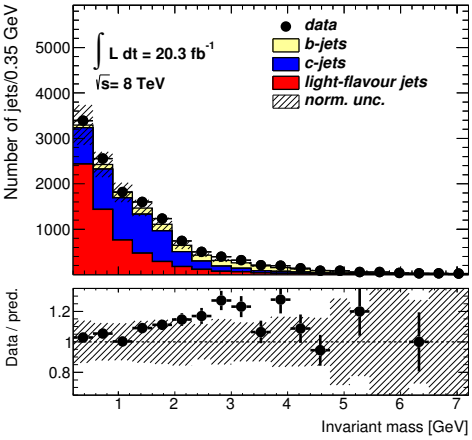

(d) Invariant mass (JetFitter based)

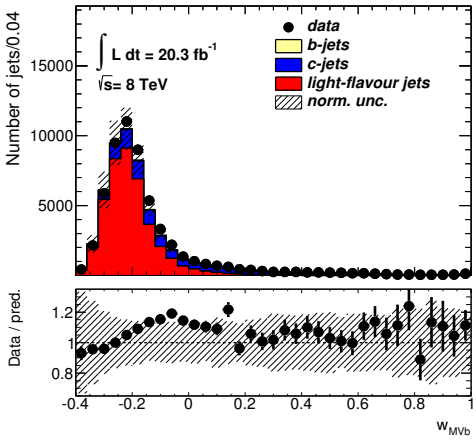

(e) MVb output weight

Figure 8.7: Distribution of several input quantities of the MVb and MVbCharm taggers (a-d) as well as the MVb output weight (e) for jets contained in the charm and light-flavour jet control region. The predictions by the simulation are subdivided into the three different jet flavour types. The simulated Monte Carlo samples are normalised according to their predicted cross-sections to an integrated luminosity of 20.3 fb^{-1}. In addition, ratios of the data and the simulation are shown at the bottom of each plot.

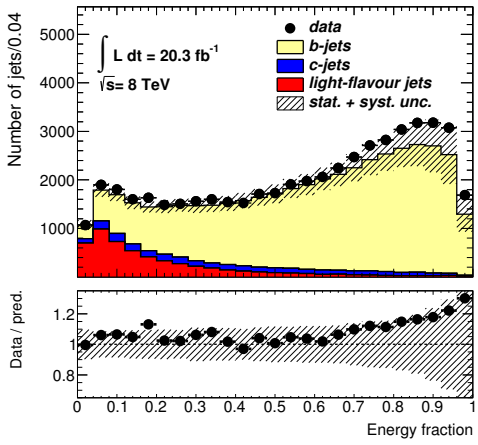

(a) Energy fraction (JetFitter)

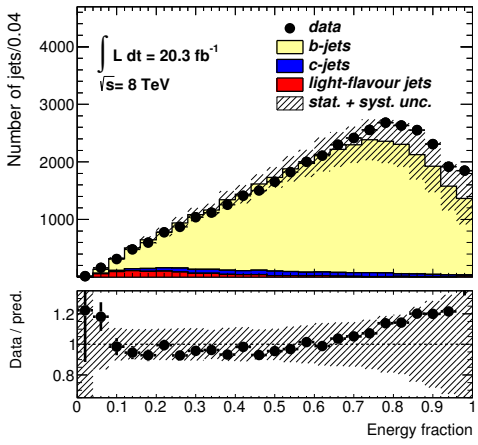

(b) Energy fraction (SV1)

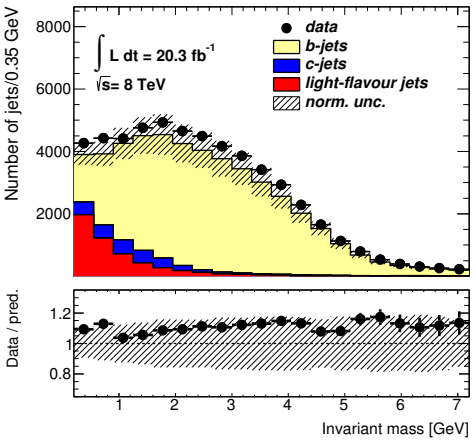

(c) Invariant mass (JetFitter)

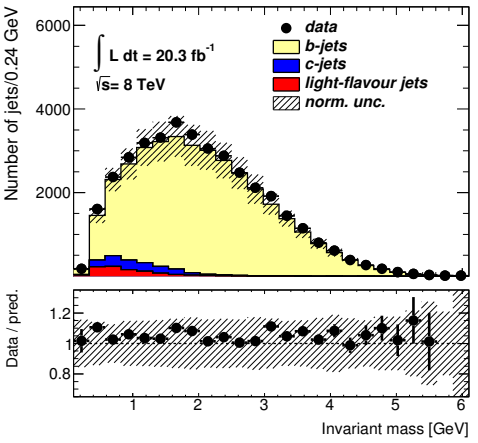

(d) Invariant mass (SV1)

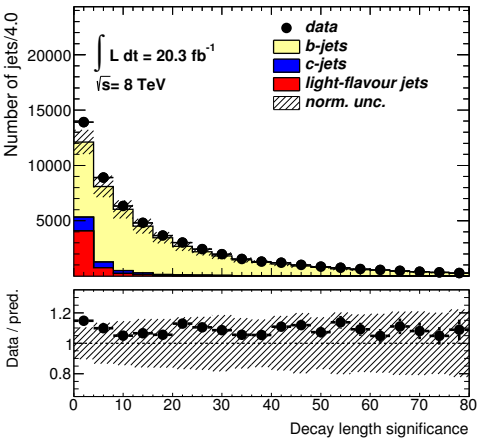

(e) Decay length significance (JetFitter based)

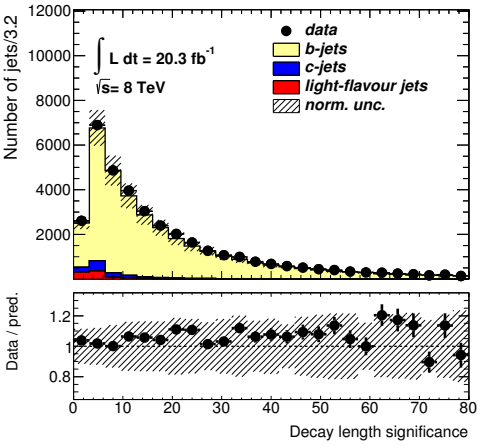

(f) Decay length significance (SV1 based)

Figure 8.8: Distribution of the energy fraction (a-b), the invariant mass (c-d) and the decay length significance (e-f) for vertices reconstructed with the JetFitter algorithm (left column) or the iterative vertex finder (right column). The predictions by the simulation are subdivided into the three different jet flavour types. The simulated Monte Carlo samples are normalised according to their predicted cross-sections to an integrated luminosity of 20.3 fb^{-1}. In addition, ratios of the data and the simulation are shown at the bottom of each plot.

	Simulation	Data
JetFitter (single-track)	12.6 ± 0.6%	13.2 ± 0.1%
JetFitter (multi-track)	45.6 ± 3.0%	45.3 ± 0.2%
iterative vertex finder (SV1 setup)	42.2 ± 2.8%	40.4 ± 0.2%

Table 8.2: Fraction of probe jets that contain a secondary vertex candidate reconstructed with the iterative vertex finder (using the SV1 setup) and the JetFitter algorithm presented separately for the predictions by the simulation and the measurements in data. The vertices reconstructed with the JetFitter algorithm are further subdivided depending whether they correspond to a single-track or a multi-track topology. The uncertainties of the predictions by the simulation correspond to the expected total systematics relevant for the determination of the fraction of jets containing a secondary vertex candidate, while the uncertainty on the observations in data is restricted to the statistics.

8.2 Measurement of the *b*-tagging efficiency in data

The measurement of the b-tagging efficiency in data is performed by probing the b-jet candidate on the hadronic side of the $t\bar{t}$ decay. As the jet sample that is obtained after applying the full event selection and reconstruction requirements still contains a significant fraction of c- and light-flavour jets, this contamination has to be taken into account. Thus the same approach as in the so-called kinematic selection method, which is described in Reference [145], is used to calculate the b-tagging efficiency in data. This method requires a precise knowledge of the flavour composition of the selected jet sample that is described by the relative fractions of b-, c- and light-flavour jets f_b, f_c and f_{light}, respectively. These quantities are calculated with respect to the overall number of jets contained in the sample. As the non-prompt and fake lepton background is determined by estimations based on data, the flavour of the corresponding jets is unknown and therefore an additional term f_{fake} has to be introduced so that the flavour fractions add up to unity:

$$f_b + f_c + f_{\text{light}} + f_{\text{fake}} = 1 \tag{8.1}$$

Assuming that the simulation and the estimations of the non-prompt and fake lepton background predicts the flavour fractions of this sample sufficiently accurate, then the relation

$$f_{\text{tag}} = \varepsilon_b f_b + \varepsilon_c f_c + \varepsilon_{\text{light}} f_{\text{light}} + \varepsilon_{\text{fake}} f_{\text{fake}} \ , \tag{8.2}$$

in which f_{tag} denotes the fraction of jets that is b-tagged with a certain tagger and operating point, can be used to derive the b-tagging efficiency:

$$\varepsilon_b = \frac{1}{f_b} \cdot \left(f_{\text{tag}} - \varepsilon_c f_c - \varepsilon_{\text{light}} f_{\text{light}} - \varepsilon_{\text{fake}} f_{\text{fake}} \right) \tag{8.3}$$

Both the tagging efficiency corresponding to jets from the fake lepton background and the fraction of b-tagged jets have to be measured in the data, while all other quantities can be retrieved from the predictions by the simulation. However, the mis-tag efficiencies ε_c and ε_l for c- and light-flavour jets respectively, are corrected using the most recent data-to-simulation calibration scale factors measured with the D^* and negative tag methods [105]. While f_{tag} is obtained from events passing the full event selection and reconstruction requirements, the b-tagging efficiency for jets coming from the non-prompt and fake lepton background $\varepsilon_{\text{fake}}$ is extracted from dedicated control regions in data (as is described in Section 8.2.2).

In order to validate the results obtained with Equation 8.3, a closure-test is performed. In this test, the b-tagging efficiencies predicted by the simulation are compared to the tagging efficiencies that are obtained when also f_{tag} is taken from the simulation. The corresponding findings are displayed as a function of the jet p_{T} in Figure 8.9. The calculated b-tagging efficiencies are compatible with the predicted b-tagging efficiencies within their statistical uncertainties. These b-tagging efficiencies are evaluated at an operating point that matches an overall tagging efficiency of 70%, whereas the sample of simulated jets is obtained after applying the full selection and reconstruction procedures to the signal and background processes that were previously discussed.

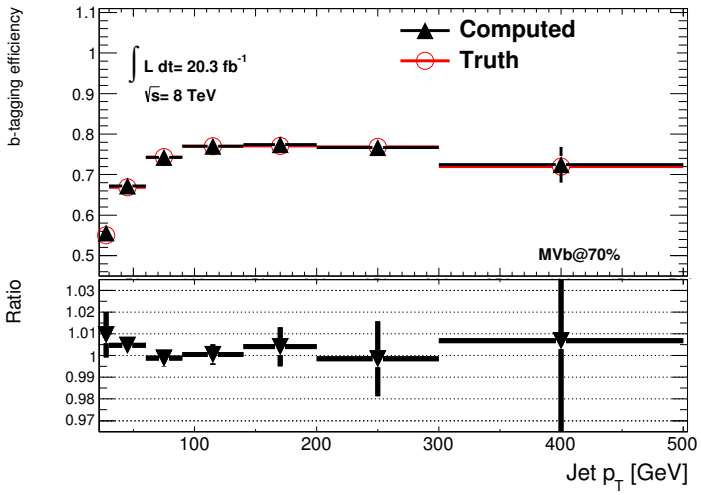

Figure 8.9: Comparison between the b-tagging efficiencies' dependence on the jet p_{T} as predicted by the simulation (referred to as "truth") and the calculations via Equation 8.3 ("computed") both corresponding to the MVb algorithm applied at a representative operating point that matches an overall b-tagging efficiency of 70%.

8.2.1 Flavour composition of the selected jet sample

A precise knowledge of the flavour composition of the probe jet sample is essential for the measurement of the b-tagging efficiency via Equation 8.3. However, the precision to which these fractions are known depends strongly on the quality of the kinematic reconstruction of $t\bar{t}$ candidate events. Systematic effects on the reconstruction method will lead to systematic uncertainties on the flavour fractions and thus also on the measured b-tagging efficiencies.

The relative flavour fractions f_i are studied in the following section as a function of various jet and vertex properties. Figures 8.10 (a-c) display the fraction of b-, c- and light-flavour jets as well as the fraction of jets stemming from the non-prompt and fake lepton background as a function of the probe jet p_{T} and the probe jet $|\eta|$ as well as a function of the angular separation between the probe jet and its nearest neigbouring jet ΔR^{min}. Each figure shows the corresponding flavour fractions together with their total systematic uncertainties.

For jets with a transverse momentum between 25 GeV and 30 GeV, the b-jet fraction is around 35% and rises continually to values of approximately 75% for jets with a p_{T} above 300 GeV. Light-flavour jets give the second largest contribution to this sample. Their fraction is between approximately 20% and 40% in the range from 30 GeV to 500 GeV and about 55% for jets with a p_{T} below 30 GeV, where their contribution is larger than the b-jet fraction. The

contamination due to jets from the non-prompt and fake lepton background is below 2% over the full p_{T} region, while the fraction of c-jets is in each p_{T} bin in the order of 5% to 7%.

In measurements as a function of the jet $|\eta|$, the b-jet fraction of the probe jet sample decreases from approximately 60% for $|\eta| < 1.0$ to about 45% for $|\eta|$ values above 2.0, while the fraction of light-flavour jets increases accordingly from 35% to 45%. The contribution of c-jets and from jets corresponding to the non-prompt and fake lepton backgrounds are for each $|\eta|$ bin below 7% and 5%, respectively.

The relative flavour fractions are almost constant for ΔR^{min} values above 1.0, while the b-(light-flavour) contribution decreases (increases) from about 60% (35%) to 45% (40%) for a decreasing ΔR^{min}. The ΔR^{min} dependence on both the c-jet fraction and the fraction of jets stemming from the non-prompt and fake lepton background is similar to their p_{T} and $|\eta|$ dependence.

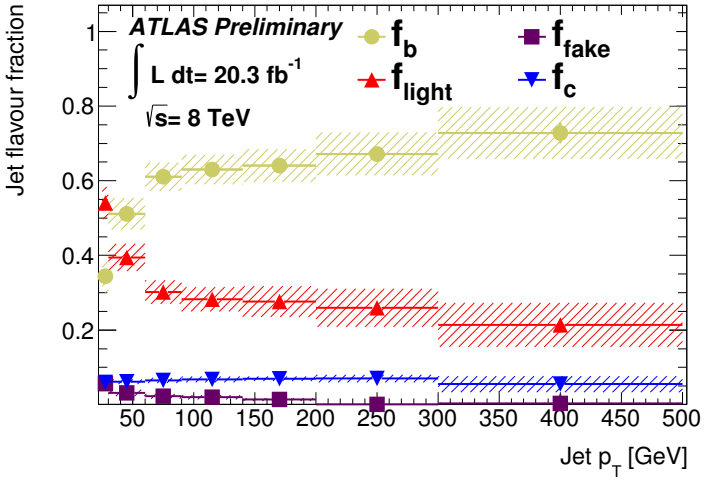

(a) Flavour fractions as a function of the jet p_{T} [9]

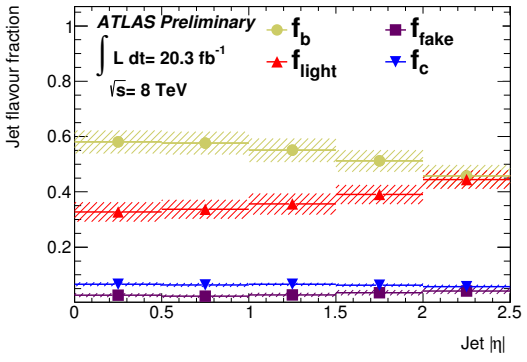

(b) Flavour fractions as a function of the jet $|\eta|$ [9]

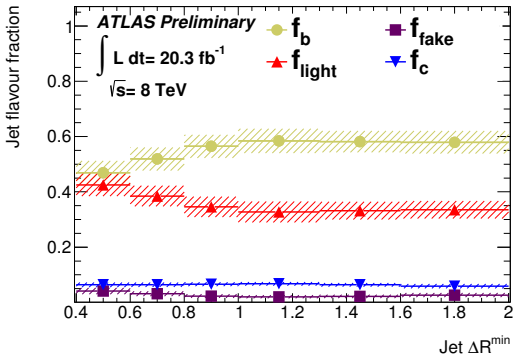

(c) Flavour fractions as a function of the ΔR^{min} [9]

Figure 8.10: Expected jet flavour composition of the selected probe jet sample obtained using the b-jet candidates from the hadronic side of the reconstructed events. The relative flavour fractions are presented in various bins of the jet p_{T} (a) and $|\eta|$ (b) and the ΔR to the nearest neighbouring jet (c). In addition, the total systematic uncertainties on the flavour fractions are presented as shaded areas as well.

The expected jet flavour composition of the selected jet sample is shown as a function of the ΔR(vertex, jet) for single- and multi-track vertices reconstructed with the JetFitter algorithm or the iterative vertex finder in Figures 8.11 (a), (b) and (c), respectively. In case the measurements of the b-tagging efficiencies and the corresponding data-to-simulation scale factors are performed as a function of the ΔR(vertex, jet), the fractions of c- and light-flavour jets as well as the fraction of jets stemming from the non-prompt and fake lepton background are below the percent level for ΔR(vertex, jet) values below 0.15, if only multi-track vertices reconstructed by either the JetFitter algorithm or the iterative vertex finder are used. The light-flavour fraction increases to a few percent for angular separation above 0.15. For single-track vertices, the b-jet fractions are significantly lower. For ΔR(vertex, jet) values below 0.025, f_b is approximately 55% and decreases to about 40% for ΔR(vertex, jet) $>$ 0.15. The fraction of light-flavour jets increases over the studied range of ΔR(vertex, jet) values from about 30% to 50%, while the fraction of c-jets decreases from about 15% to 5%.

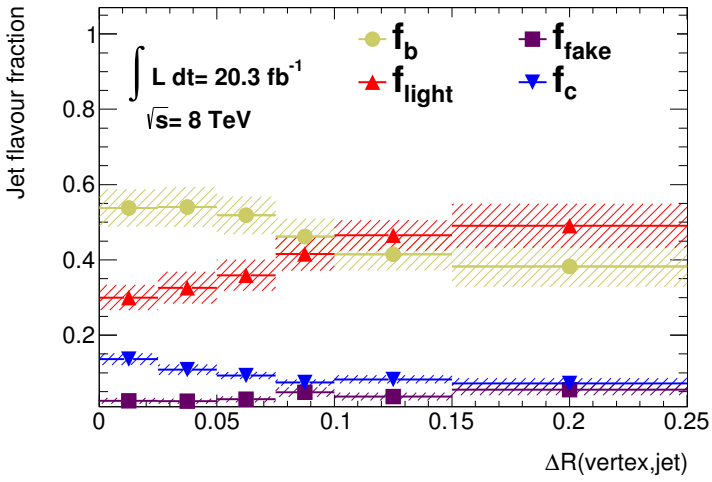

(a) single-track vertices based on JetFitter

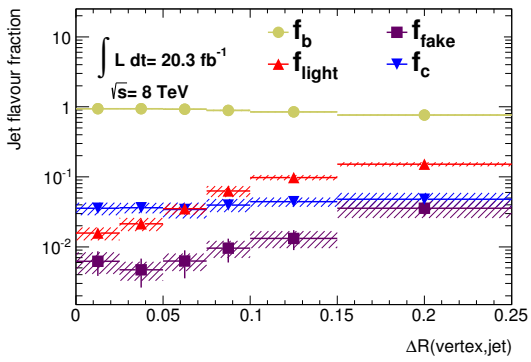

(b) multi-track vertices based on JetFitter

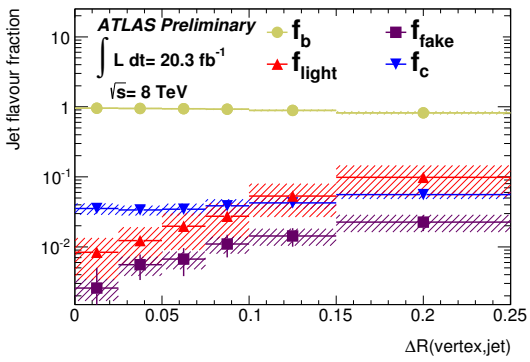

(c) multi-track vertices based on SV1) [9]

Figure 8.11: Expected jet flavour composition of the selected jet sample obtained using the b-jet candidates from the hadronic side of the reconstructed events. The relative flavour fractions are presented as a function of the ΔR(vertex, jet) for single- and multi-track vertices reconstructed with the JetFitter algorithm (a-b) or the iterative vertex finder (f). In addition, the total systematic uncertainties on the flavour fractions are presented as shaded areas as well.

The probe jet sample used for these studies are obtained using the b-jet candidates stemming from the reconstructed hadronic top-quark decays of the events that are listed in Table 8.1 (a). However, if the b-jet candidate on the leptonic side of the event is used to obtain the probe jet sample (instead of the b-jet candidate on the hadronic side), the b-jet fraction is significantly increased.

For jets with a p_{T} below 30 GeV the b-jet fraction is of the order of 30%. The fraction of light-flavour jets is around 60% in this region, while the fraction of c-jets and jets from the non-prompt and fake lepton background are both approximately 5%. For a probe jet p_{T} exceeding 200 GeV, the b-jet fraction rises to 85%-90% and the light-flavour fraction decreases to around 5%-10%. These flavour fractions are displayed as a function of the probe jet p_{T} in Figure 8.12 together with their total systematic uncertainties.

Both the c- and light-flavour contribution of the two jet samples studied in this context originate mainly from incorrectly reconstructed top-quark decays (i.e. candidate events in which the χ^2 minimisation procedure has assigned the wrong permutation of jets to the decay products of the top-quark). Only 10% to 20% of the selected c- and light-flavour jets stem from vector bosons produced in association with jets or from single top-quark events.

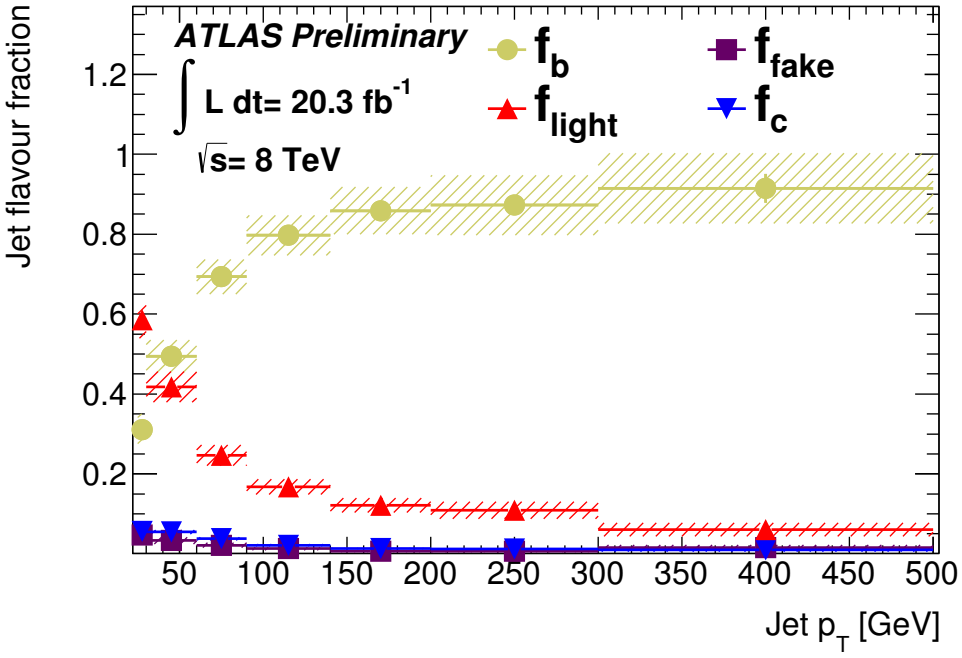

Figure 8.12: Expected jet flavour composition of the selected b-jet sample shown as a function of the jet p_{T} in case that the b-jet candidate on the leptonic side of the event is used. In addition, the total systematic uncertainties on the flavour fractions are presented as shaded areas as well [9].

8.2.2 Measurement of the b-tagging efficiency for jets from the non-prompt lepton background

The b-tagging efficiencies for jets from the non-prompt and fake lepton background $\varepsilon_{\mathrm{fake}}$ are determined directly in a control region in data without using the templates obtained from the application of the matrix method in the signal region (due to their limited statistics). An or-

thogonal jet sample (CR1) is obtained by inverting the selection requirements on the missing transverse momentum, the transverse W-boson candidate mass and the logarithm of the χ^2_{total} obtained by the kinematic fit. The corresponding cut values are set to $E_{\text{T}}^{\text{miss}} < 20$ GeV, $E_{\text{T}}^{\text{miss}} + m_{\text{T},W} < 60$ GeV and $\log_{10}(\chi^2_{\text{total}}) > 0.9$, respectively. In addition, the only events taken into account are those that contain a reconstructed lepton candidate that is classified into the loose category but does not fulfill the tight lepton definition (in order to minimise the contribution of events providing prompt leptons). All jets contained in this sample are used to determine $\varepsilon_{\text{fake}}$ (i.e. the fraction of b-tagged jets).

The measurement of $\varepsilon_{\text{fake}}$ is repeated changing the selection requirements on the $E_{\text{T}}^{\text{miss}}$, $E_{\text{T}}^{\text{miss}} + m_{\text{T},W}$ and $\log_{10}(\chi^2_{\text{total}})$, to check to what extent the estimated $\varepsilon_{\text{fake}}$ depends on the control region definition. Thus the second and third control regions (CR2 and CR3) are defined by $E_{\text{T}}^{\text{miss}} > 20$ GeV and $E_{\text{T}}^{\text{miss}} + m_{\text{T},W} < 60$ GeV as well as $E_{\text{T}}^{\text{miss}} < 20$ GeV and $E_{\text{T}}^{\text{miss}} + m_{\text{T},W} > 25$ GeV, where the $\log_{10}(\chi^2_{\text{total}})$ is required to be above 0.9 for both regions. The fourth control region (CR4) is defined by $E_{\text{T}}^{\text{miss}} < 20$ GeV and $E_{\text{T}}^{\text{miss}} + m_{\text{T},W} < 60$ GeV, while no cut on the $\log_{10}(\chi^2_{\text{total}})$ value is applied. The definition of these four control regions is summarised in Table 8.3.

	Definition
CR1	$E_{\text{T}}^{\text{miss}} < 20$ GeV, $E_{\text{T}}^{\text{miss}} + m_{\text{T},W} < 60$ GeV, $\log_{10}(\chi^2_{\text{total}}) > 0.9$
CR2	$E_{\text{T}}^{\text{miss}} > 20$ GeV, $E_{\text{T}}^{\text{miss}} + m_{\text{T},W} < 60$ GeV, $\log_{10}(\chi^2_{\text{total}}) > 0.9$
CR3	$E_{\text{T}}^{\text{miss}} < 20$ GeV, $E_{\text{T}}^{\text{miss}} + m_{\text{T},W} > 60$ GeV, $\log_{10}(\chi^2_{\text{total}}) > 0.9$
CR4	$E_{\text{T}}^{\text{miss}} < 20$ GeV, $E_{\text{T}}^{\text{miss}} + m_{\text{T},W} < 60$ GeV

Table 8.3: Definition of the four control regions that are used to estimate the b-tagging efficiency for jets from the non-prompt and fake lepton background $\varepsilon_{\text{fake}}$ and its corresponding uncertainties from data. The central value of $\varepsilon_{\text{fake}}$ is obtained from CR1, while the uncertainties are calculated from CR2, CR3 and CR4.

The different results obtained in the additional three control regions (CR2, CR3 and CR4) are used to estimate a systematic uncertainty on $\varepsilon_{\text{fake}}$. For each bin, the value with the largest variation with respect to the results of the first control region defines the uncertainty in the corresponding phase space region. This uncertainty is then propagated into the measurement of the b-tagging efficiency in data and their corresponding data-to-simulation scale factors.

The b-tagging efficiencies of the MVb algorithm at an illustrative operating point that matches an overall efficiency of 70% for jets from the non-prompt and fake lepton background and their systematic uncertainties (i.e. the envelope of the $\varepsilon_{\text{fake}}$ differences per bin) are compared to the predicted b-tagging efficiencies for b-, c- and light-flavour jets as a function of the jet p_{T} and η in Figures 8.13 (a) and (b) respectively, while their ΔR^{min} dependence is shown in Figure 8.13 (c). The overall b-tagging efficiency for jets from the non-prompt and fake lepton background is approximately 10% and thus larger by a factor of up to 10 with respect to the overall b-tagging efficiency for light-flavour jets and smaller by a factor of up to 0.5 compared to b-tagging efficiency for c-jets. The $\varepsilon_{\text{fake}}$ values decrease with increasing jet p_{T} and $|\eta|$ values and are almost constant as a function of ΔR^{min}. The systematic uncertainties assigned to $\varepsilon_{\text{fake}}$ range between 20% and 42% as a function of the jet p_{T}, between 19% and 41% as a function of the jet $|\eta|$ and between 19% and 53% as a function of the angular separation between the probe jet and its nearest neigbouring jet.

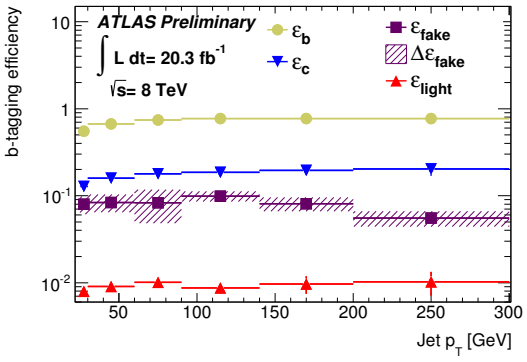

(a) *b*-tagging efficiencies as a function of the jet p_{T} [9]

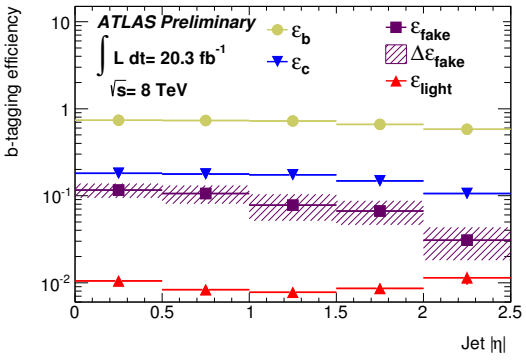

(b) *b*-tagging efficiencies as a function of the jet $|\eta|$ [9]

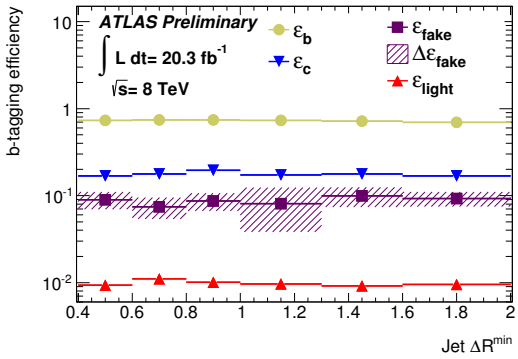

(c) *b*-tagging efficiencies as a function of the ΔR^{min} [9]

Figure 8.13: *b*-tagging efficiency for *b*-, *c*- and light-flavour jets (extracted from the simulation) as well as for jets stemming from the non-prompt and fake lepton background (obtained from a control region in data) corresponding to the MVb algorithm at an operating point that provides an overall efficiency of 70%. The systematic uncertainties assigned to $\varepsilon_{\mathrm{fake}}$ (shaded areas) correspond to the envelope of the different results obtained from the various control regions. Both the efficiencies of the various jet flavours and the uncertainties on $\varepsilon_{\mathrm{fake}}$ are shown as a function of the probe jet p_{T} (a), η (b) and ΔR^{min} (c).

8.2.3 Validation of the *b*-tagging efficiency for *c*- and light-flavour jets corresponding to the MVb algorithm

The mis-tagging efficiencies corresponding to the MVb algorithm are not yet calibrated for *c*- and light-flavour jets. However, the scale factors corresponding to the most recent $\varepsilon_{\mathrm{light}}$ and ε_{c} measurements for the MV1 tagger using the D^* and negative tag methods [105] are used to correct the expected *b*-tagging performance for the simulated *c*- and light-flavour jets, as the corresponding scale factors for the MVb algorithm are expected to be roughly in the same order of magnitude. However, the uncertainties on the scale factors, which are used in the calibration of the MVb tagger, are inflated in order to be conservative. In order to justify this approach, the *b*-tagging performance of the jets assigned to the hadronic *W*-boson decay is studied in data. The findings are afterwards compared to the prediction by the simulation corrected by the data-to-simulation scale factors corresponding to the MV1 algorithm.

For this purpose events are selected that have both the *b*-jet candidates on the hadronic and the leptonic side *b*-tagged using the MV1 algorithm at an operating point that matches an

overall efficiency of 70%. The jet sample obtained this way consists of 4% b-, 20% c- and 76% light-flavour jets. However, after applying a b-tag requirement on these jets using the MVb algorithm at an operating point of 70% efficiency, the fraction of c-jets is approximately 60% and dominates over the b- and light-flavour components (33% and 7%, respectively). Thus the b-tagging rate, defined as the number of b-tagged jets divided by the total number of jets is strongly sensitive to the b-tagging performance of the c-jets. A comparison between this quantity as measured in the data and as predicted by the simulation is displayed in Figure 8.14 as a function of the jet p_{T}. The b-tagging rates in data and in the simulation is compatible with each other for most p_{T} bins within 1σ of the mis-tagging uncertainties corresponding to c-jets. The remaining deviations are covered if the mis-tagging uncertainties for c-jets are inflated by a factor of 1.25. Thus the b-tagging efficiency for c-jets will be shifted up/down by 10%-19% (instead of $8\% - 15\%$) depending on the jet kinematics, in order to evaluate the corresponding uncertainties on the b-tagging calibration results of the MVb algorithm. The total uncertainties due to the b-tagging efficiency for light-flavour jets are inflated as well by the same factor. Thus $\varepsilon_{\mathrm{light}}$ will be changed by 19%-50% (instead of $15\% - 40\%$), with the exact value depending on the jet kinematics, during the calibration of the MVb algorithm.

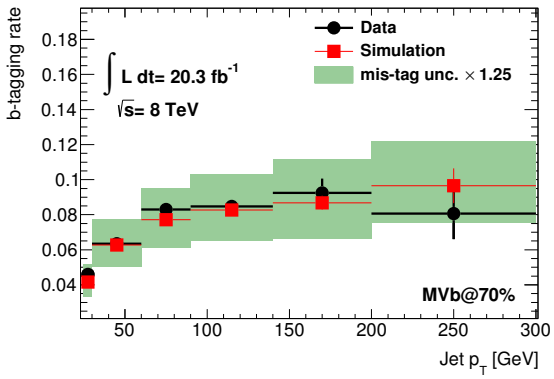

Figure 8.14: The b-tagging rates for the MVb tagger, displayed as a function of the p_{T} of the jets that are associated to the hadronic W-boson decays in fully reconstructed $t\bar{t}$ single lepton candidate events. In these events, the b-jet candidates on the hadronic and the leptonic side are required to be b-tagged using the MV1 algorithm. The b-tagging rates are shown for the predictions by the simulation (red lines) and the measurements in data (black dots). In addition, the mis-tagging uncertainties for c-jets corresponding to the MV1 algorithm (as measured by the D^* method) and increased by 25% are presented (green filled area).

8.3 Results

The following section is dedicated to present in detail the measurement of the b-tagging efficiencies for the MVb (in Section 8.3.1) and the MV1 (in Section 8.3.2) algorithms as obtained by applying the tag and probe (T&P) method (further calibration results for e.g. the MVbCharm and the MVbComb taggers are presented in Appendix B). The corresponding results are compared to the predictions by the simulation directly using the truth labelling, in order to determine the data-to-simulation correction scale factors.

The systematic uncertainties on the measured b-tagging efficiencies and their scale factors are evaluated one at a time, by replacing the nominal jet sample with a modified sample ob-

tained after varying a particular property of the simulated objects. The largest contributions are expected to arise from systematics that lead to a significant change in the flavour composition of the selected jet sample. The total systematic uncertainty is finally obtained by summing the individual systematics uncertainties in quadrature.

During the calculations of the various systematic uncertainties corresponding to the measurement of the b-tagging scale factor $\kappa = \varepsilon_b^{\text{data}}/\varepsilon_b^{\text{sim.}}$, the denominator is kept constant at the value obtained from the nominal jet sample. This is done to only consider the impact of the various systematics on the method used to extract the b-tagging efficiency from the data (through a change of the expected flavour fractions), but not the impact on the predicted b-tagging performance in the simulation. Thus a double counting of systematic uncertainties is avoided once the b-tagging calibration scale factors are applied to physics analyses. Exceptions are made for the jet energy scale and resolution, for which the denominator is changed as well in order to correlate the systematic variation of the b-tagging efficiency measurement with the corresponding systematic variation of the analysis. This approach is needed in the case that a certain source of systematic uncertainty (e.g. JES and JER) affects both the measured b-tagging efficiency and, more directly, the observables of the analysis to which the corresponding b-tagging scale factors are applied to. The same procedure is applied for all other b-tagging calibration measurements.

The measurement of the b-tagging efficiencies and the corresponding scale factors is performed for the two b-taggers as a function of the probe jet p_{T}, the probe jet $|\eta|$, the ΔR between the probe jet and its nearest neighbouring jet as well as the angular separation $\Delta R(\text{vertex}, \text{jet})$ between the axis of the probe jet and the line joining the primary and the secondary vertices. For this purpose, displaced vertices are used that are reconstructed with the iterative vertex finder (using the SV1 setup) or the JetFitter algorithm. The measurements corresponding to the vertex candidates based on the JetFitter algorithm are subdivided into single- and multi-track vertices.

8.3.1 Calibration results corresponding to the MVb algorithm

The results of the b-tagging calibration measurements for the MVb algorithm are presented in Figures 8.15 and 8.16 for the combined e + jets and μ + jets channel. The b-tagging efficiencies of the MVb tagger are shown for both the predictions from the simulation and the data collected by the ATLAS detector during the 2012 run of the LHC applying the single-lepton (SL) tag and probe (T&P) method (i.e. the approach that is described in Section 8.2). The corresponding data-to-simulation scale factors are shown as well. A representative working point corresponding to an overall b-tagging efficiency of 70% is chosen to demonstrate the performance of this algorithm. This operating point is obtained by defining a jet as b-tagged if the output of the MVb algorithm exceeds a value of 0.1471.

The measurement is separately performed as a function of the probe jet p_{T}, displayed in Figures 8.15 (a) and (b), the probe jet $|\eta|$, displayed in Figures 8.15 (c) and (d), the ΔR between the probe jet and its nearest neighbouring jet, displayed in Figures 8.15 (e) and (f), as well the angular separation between the axis of the probe jet and the line joining the primary and the secondary vertices $\Delta R(\text{vertex}, \text{jet})$, displayed in Figures 8.16 (a-f). The measurement of the b-tagging efficiency as a function of the $\Delta R(\text{vertex}, \text{jet})$ is performed separately for jets having a vertex reconstructed with either the iterative vertex finder, in Figures 8.16 (a-b), or the JetFitter algorithm, whose vertices are subdivided into multi- and single-track topologies, in Figures 8.16 (c-f). The results corresponding to these three measurements are not inclusive due to the requirement of a reconstructed displaced vertex. The fractions of jets that contain such a vertex are listed in Table 8.2.

The measurements as a function of the probe jet p_{T}, η and ΔR^{min} provide calibration scale factors that are compatible with unity within their combined statistical and systematic uncertainties. The b-tagging calibration scale factors corresponding to the measurements as function of the $\Delta R(\mathrm{vertex}, \mathrm{jet})$ are also compatible with unity within their total uncertainties. A detailed break-down of all the relevant systematic uncertainties on the measured scale factors is given in Tables 8.4 (a-b), 8.5 (a-b) and 8.6 (a-b) for the various p_{T}, $|\eta|$, ΔR^{min} and $\Delta R(\mathrm{vertex}, \mathrm{jet})$ bins.

The dominant contributions to the total systematic uncertainties are due to the choice of the Monte Carlo generator, the initial and final state radiation and the jet energy resolution. Smaller systematic uncertainties are related for example to the choice of the fragmentation and hadronisation model, the normalisation of the signal and background processes, or to the b-tagging efficiencies for c- and light-flavour jets. Also the systematic uncertainties arising due to defective tile modules have a relative small contribution to the total uncertainties for a jet p_{T} below 300 GeV. Contribution due to the lepton energy (momentum) scale and resolution and their identification, reconstruction and triggering efficiency uncertainty have a negligible effect on the measurements of the b-tagging efficiencies. The same holds for uncertainties related to the resolution of the missing transverse momentum, the jet reconstruction efficiencies, the jet vertex fraction and the choice of the "iqopt3" and "ptjmin10" parameter (i.e the W+jets shape uncertainties).

Systematic uncertainties such as the jet energy scale and resolution as well as the initial and final state radiation show a strong p_{T} or $|\eta|$ dependence, as their contribution to the total uncertainties decreases for increasing p_{T} values, while their contribution increases for increasing $|\eta|$ values. On the other hand, the systematic uncertainties related to the top-quark p_{T} reweighting or the defective tile modules become more relevant at higher jet p_{T} values.

As measurements as a function of the $\Delta R(\mathrm{vertex}, \mathrm{jet})$ implicitly require the reconstruction of a secondary vertex, an additional systematic uncertainty is introduced (referred to as light-flavour jet normalisation) in order to account for a possible mismodelling of the vertex finding efficiency in light-flavour jets ε_1^{SV}. This uncertainty is calculated by scaling the normalisation of the light-flavour jet contribution successively up and down by 50% and comparing the corresponding results. This 50% shift is justified by the size of the systematic uncertainties of the b-tagging calibration scale factors for light-flavour jets [105] and becomes particularly important at ΔR values above 0.075.

The combined statistical and systematic uncertainty is below 7% in the p_{T} range between 60 GeV and 200 GeV, below 9% in the range from 200 GeV to 300 GeV and about 14% for jets with a p_{T} above 300 GeV. However, the measurement above 300 GeV is strongly dominated by the statistical uncertainty.

In the measurements as a function of the jet $|\eta|$, the total uncertainties range from 7% for low $|\eta|$ values to about 9% in the outermost $|\eta|$ region, whereas in measurements as a function of the ΔR^{min}, total uncertainties between 6% and 10% are obtained.

The systematic uncertainties corresponding to the efficiency and scale factor measurements as a function of the $\Delta R(\mathrm{vertex}, \mathrm{jet})$ using exclusively multi-track vertices range between 1% to 3% for vertices reconstructed with the iterative vertex finder and between 1% to 4% for vertices reconstructed with the JetFitter algorithm. These uncertainties are substantially smaller with respect to the measurements as a function of the jet p_{T}, η and ΔR^{min}, which is in particular related to the additional requirement of a reconstructed displaced vertex inside the studied jets and therefore a much higher b-jet purity of the probe jet sample. For single-track vertices the total uncertainties range from 10% to 18% and have a significant contribution due to the statistical limitations.

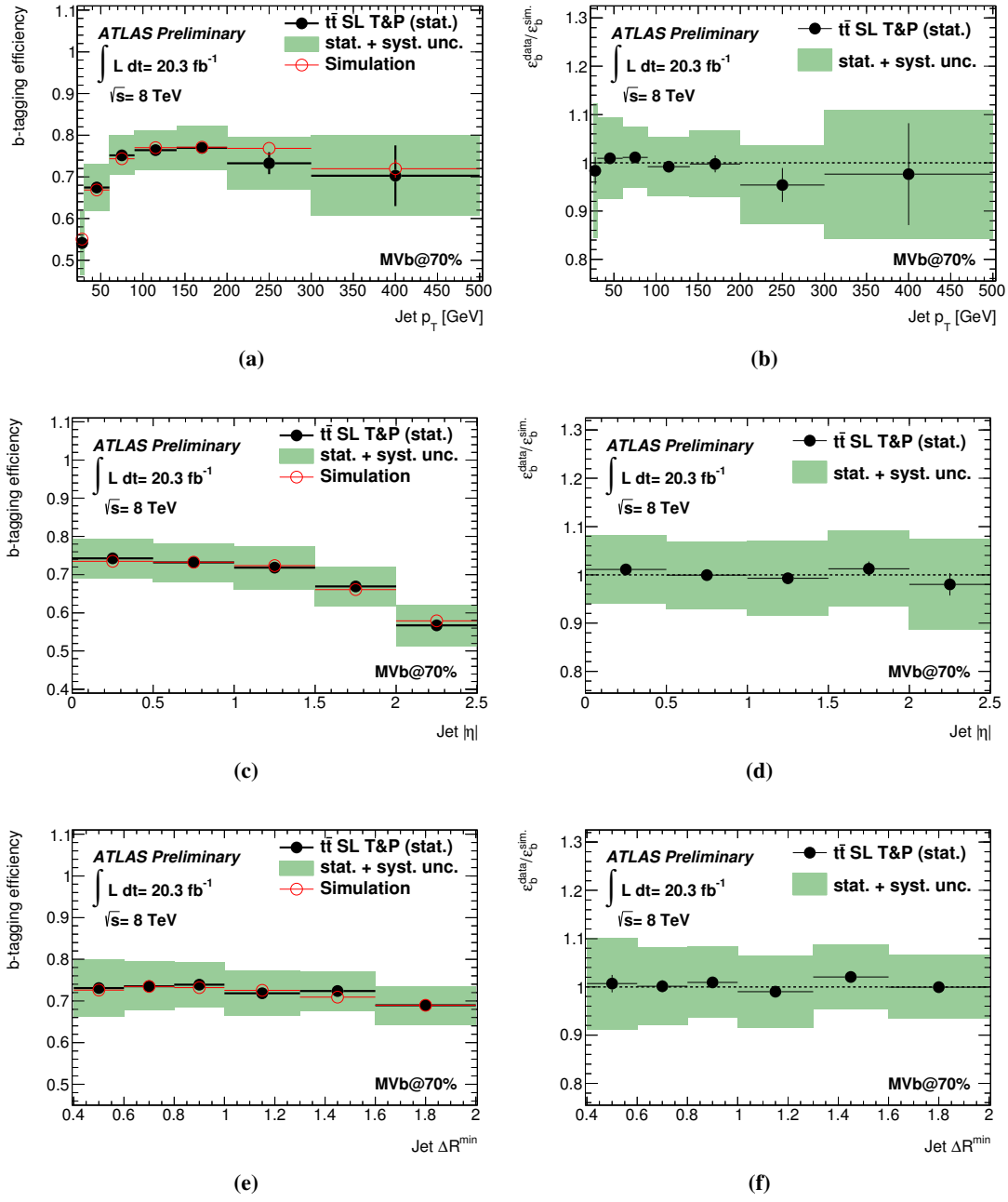

Figure 8.15: The *b*-tagging efficiencies for the MVb algorithm corresponding to an operating point of an overall efficiency of 70% as a function of the transverse momentum (a), the absolute pseudorapidity (c) and the ΔR^{min} (e) of the jets contained in the sample of $t\bar{t}$ single lepton (SL) candidate events. The *b*-tagging efficiencies are shown for the predictions by the simulation (as a red line) and the measurements in data by the tag and probe (T&P) method (as black dots). The total uncertainties of these measurements are displayed as well (by the green filled area). The uncertainties on the predicted tagging efficiencies are based only on the the Monte Carlo statistics. The corresponding data-to-simulation scale factors are presented in addition also as a function of the jet p_{T} (b), $|\eta|$ (d) and ΔR^{min} (f) [9].

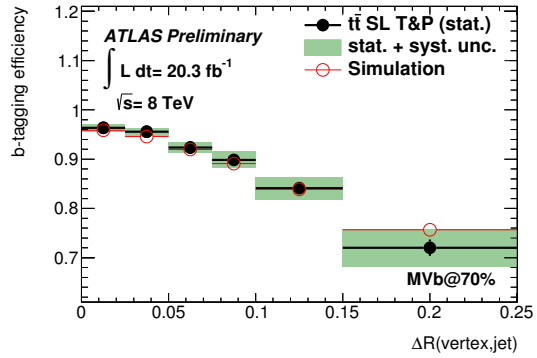

(a) multi-track vertex (SV1)

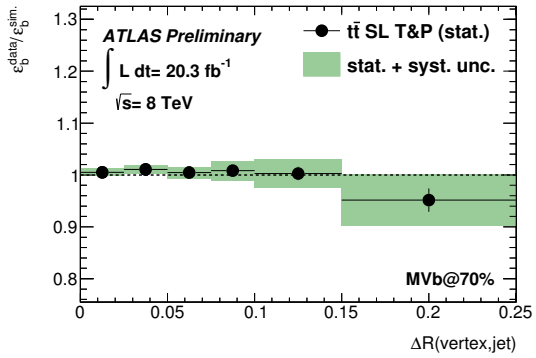

(b) multi-track vertex (SV1)

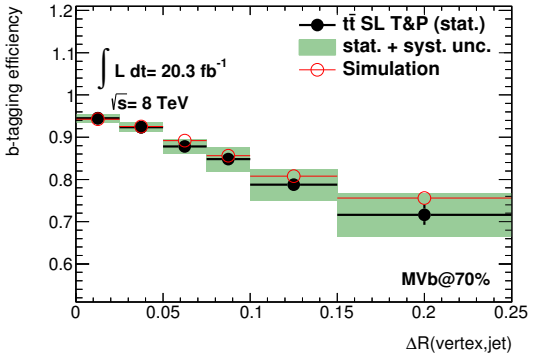

(c) multi-track vertex (JetFitter)

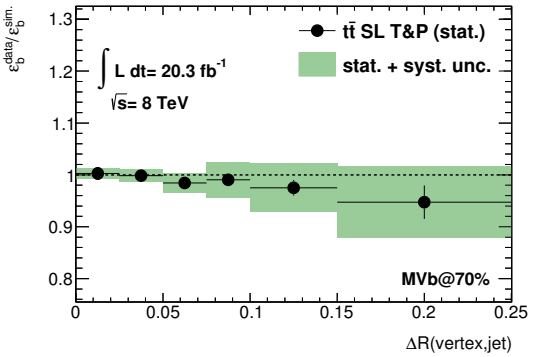

(d) multi-track vertex (JetFitter)

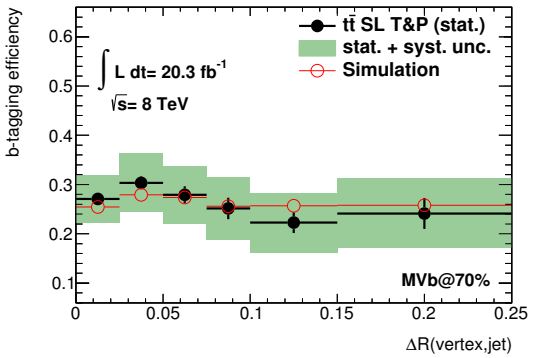

(e) single-track vertex (JetFitter)

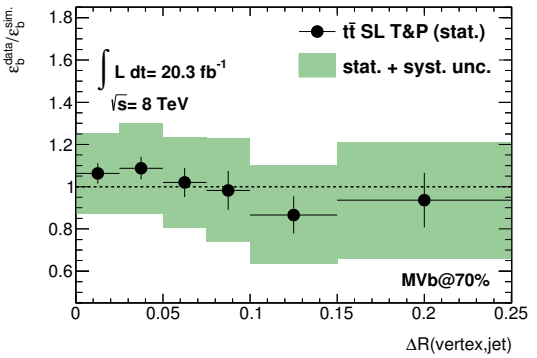

(f) single-track vertex (JetFitter)

Figure 8.16: Results of the *b*-tagging efficiency measurements for the MVb algorithm corresponding to an operating point of 70% efficiency as a function of the angular separation between the vertex direction and the jet axis $\Delta R(\text{vertex}, \text{jet})$. The measurements are performed separately for jets. having a vertex reconstructed with the iterative vertex finder (a-b) and the JetFitter algorithm (c-f), where the vertex candidates based on the JetFitter are subdivided into single- and multi-track topologies. The *b*-tagging efficiencies (left column) are shown for the predictions by the simulation (as a red line) and the measurements in data by the tag and probe (T&P) method (as black dots). The total uncertainties of these measurements are displayed as well (by the green filled area). The uncertainties on the predicted tagging efficiencies are based only on the the Monte Carlo statistics. The corresponding data-to-simulation scale factors are presented in addition (right column). As these measurements take only jets into account that have an appropriate type of secondary vertex reconstructed, the definition of the presented *b*-tagging efficiencies is not inclusive as in the measurements corresponding to the jet p_{T}, η or ΔR^{min} [9].

p_T[GeV]	25-30	30-60	60-90	90-140	140-200	200-300	300-500
ε_c	±1.5	±0.9	±0.7	±0.8	±0.8	±0.9	±0.5
ε_{light}	±1.2	±0.4	±0.3	±0.2	±0.2	±0.2	±0.8
ε_{fake}	±0.6	±0.2	±0.2	±0.1	±0.0	±0.0	±0.1
QCD normalisation	±0.9	±0.6	±0.5	±0.4	±0.3	±0.0	±0.1
$t\bar{t}$ normalisation	±0.8	±0.6	±0.5	±0.5	±0.4	±0.3	±0.2
Z+jets normalisation	±0.4	±0.3	±0.2	±0.2	±0.1	±0.2	±0.0
Single-top normalisation	±0.3	±0.3	±0.2	±0.2	±0.3	±0.2	±0.6
Luminosity	±0.3	±0.2	±0.1	±0.1	±0.1	±0.1	±0.0
Jet energy scale	±6.2	±2.1	±0.8	±0.4	±0.4	±0.2	±1.9
ISR/FSR	±5.7	±4.8	±4.1	±3.7	±3.8	±2.7	±1.8
Top-quark mass	±0.8	±0.4	±0.0	±0.4	±0.2	±0.5	±1.5
Top-quark p_T reweighting	±0.2	±0.0	±0.1	±0.6	±1.5	±2.7	±2.4
Jet energy resolution	±8.6	±4.1	±2.5	±2.3	±1.6	±2.5	±1.5
$t\bar{t}$ generator	±5.9	±4.2	±3.6	±4.0	±4.7	±5.5	±6.9
Fragmentation	±2.1	±2.2	±1.0	±1.0	±1.1	±2.9	±2.0
Trips in Tile	±0.7	±0.1	±0.3	±0.2	±0.2	±0.4	±2.5
Stat.	±2.9	±0.8	±0.8	±0.9	±1.8	±3.5	±10.6
Total Syst	±13.8	±8.3	±6.2	±6.1	±6.6	±7.8	±8.7
Total	±14.1	±8.3	±6.3	±6.2	±6.9	±8.5	±13.7
Scale factor	0.98 ± 0.14	1.01 ± 0.08	1.01 ± 0.06	0.99 ± 0.06	1.00 ± 0.07	0.95 ± 0.08	0.98 ± 0.13

(a) Systematic uncertainties in each p_T bin

η	0.0-0.5	0.5-1.0	1.0-1.5	1.5-2.0	2.0-2.5
ε_c	±0.8	±0.8	±0.9	±0.8	±0.8
ε_{light}	±0.3	±0.3	±0.3	±0.4	±0.8
ε_{fake}	±0.1	±0.1	±0.2	±0.2	±0.2
QCD normalisation	±0.5	±0.5	±0.6	±0.7	±1.0
$t\bar{t}$ normalisation	±0.5	±0.5	±0.6	±0.7	±0.8
Z+jets normalisation	±0.2	±0.2	±0.3	±0.4	±0.3
Single-top normalisation	±0.3	±0.2	±0.3	±0.3	±0.2
Luminosity	±0.2	±0.2	±0.2	±0.2	±0.3
Jet energy scale	±0.5	±1.0	±0.9	±0.4	±0.7
ISR/FSR	±4.1	±4.2	±4.6	±5.2	±5.6
Top-quark mass	±0.3	±0.2	±0.5	±0.3	±1.3
Top-quark p_T reweighting	±0.5	±0.4	±0.5	±0.4	±0.3
Jet energy resolution	±2.9	±2.2	±3.8	±3.5	±6.0
$t\bar{t}$ generator	±4.3	±4.6	±4.4	±3.3	±3.2
Fragmentation	±1.5	±1.4	±1.6	±2.3	±1.9
Trips in Tile	±0.3	±0.3	±0.1	±0.1	±0.6
Stat.	±0.8	±0.9	±1.0	±1.5	±2.3
Total Syst	±6.9	±6.9	±7.8	±7.6	±9.3
Total	±7.0	±6.9	±7.8	±7.8	±9.6
SF	1.01 ± 0.07	1.00 ± 0.07	0.99 ± 0.08	1.01 ± 0.08	0.98 ± 0.09

(b) Systematic uncertainties in each $|\eta|$ bin

Table 8.4: Systematic uncertainties (in %) on the measured data-to-simulation scale factor of the MVb algorithm in the various jet p_T (a) and $|\eta|$ (b) regions. The results are presented for a representative operating point that corresponds to an overall b-tagging efficiency of 70%.

$\Delta R^{\min}$	0.4-0.6	0.6-0.8	0.8-1.0	1.0-1.3	1.3-1.6	1.6-2.0
ε_{c}	±1.0	±0.9	±0.9	±0.8	±0.8	±0.7
$\varepsilon_{\mathrm{light}}$	±0.6	±0.4	±0.3	±0.3	±0.3	±0.3
$\varepsilon_{\mathrm{fake}}$	±0.2	±0.2	±0.1	±0.2	±0.1	±0.1
QCD normalisation	±0.8	±0.7	±0.5	±0.4	±0.4	±0.5
$t\bar{t}$ normalisation	±0.7	±0.7	±0.5	±0.4	±0.4	±0.5
Z+jets normalisation	±0.3	±0.3	±0.3	±0.2	±0.3	±0.3
Single-top normalisation	±0.3	±0.3	±0.2	±0.3	±0.2	±0.2
Luminosity	±0.2	±0.2	±0.2	±0.1	±0.1	±0.2
Jet energy scale	±1.1	±1.5	±0.5	±0.6	±0.5	±0.7
ISR/FSR	±6.0	±4.6	±4.1	±4.2	±3.6	±4.4
Top-quark mass	±0.1	±0.1	±0.3	±0.3	±0.7	±0.7
Top-quark p_{T} reweighting	±2.0	±1.4	±1.0	±0.5	±0.1	±0.2
Jet energy resolution	±3.0	±2.3	±2.5	±3.7	±2.9	±3.2
$t\bar{t}$ generator	±5.3	±5.1	±4.5	±4.6	±3.9	±3.1
Fragmentation	±2.2	±1.8	±2.3	±1.6	±1.6	±1.1
Trips in Tile	±0.3	±0.1	±0.1	±0.1	±0.3	±0.0
Stat.	±1.8	±1.3	±1.2	±1.0	±1.1	±1.2
Total Syst	±9.3	±7.9	±7.2	±7.5	±6.5	±6.5
Total	±9.4	±8.0	±7.3	±7.6	±6.6	±6.7
SF	1.01 ± 0.10	1.00 ± 0.08	1.01 ± 0.07	0.99 ± 0.08	1.02 ± 0.07	1.00 ± 0.07

(a) Systematic uncertainties in each $\Delta R^{\min}$ bin

ΔR(vertex, jet)	0.00-0.025	0.025-0.050	0.050-0.075	0.075-0.100	0.100-0.150	0.150-0.250
ε_{c}	±0.2	±0.2	±0.2	±0.3	±0.4	±0.7
$\varepsilon_{\mathrm{light}}$	±0.1	±0.1	±0.1	±0.2	±0.5	±0.8
$\varepsilon_{\mathrm{fake}}$	±0.0	±0.0	±0.0	±0.3	±0.1	±0.1
Light-flavour jet normalisation	±0.3	±0.5	±0.8	±1.1	±2.0	±4.3
QCD normalisation	±0.0	±0.0	±0.0	±0.1	±0.1	±0.0
$t\bar{t}$ normalisation	±0.0	±0.0	±0.0	±0.0	±0.1	±0.1
Z+jets normalisation	±0.0	±0.0	±0.0	±0.0	±0.0	±0.0
Single-top normalisation	±0.0	±0.0	±0.0	±0.0	±0.0	±0.0
Luminosity	±0.0	±0.0	±0.0	±0.0	±0.0	±0.0
Jet energy scale	±0.0	±0.1	±0.0	±0.3	±0.2	±0.2
ISR/FSR	±0.3	±0.2	±0.4	±0.6	±0.7	±1.1
Top-quark mass	±0.0	±0.0	±0.0	±0.0	±0.1	±0.1
Top-quark p_{T} reweighting	±0.0	±0.0	±0.0	±0.0	±0.0	±0.1
Jet energy resolution	±0.2	±0.1	±0.0	±0.8	±0.3	±0.4
$t\bar{t}$ generator	±0.2	±0.3	±0.3	±0.2	±0.7	±1.1
Fragmentation	±0.0	±0.1	±0.1	±0.2	±0.2	±0.5
Trips in Tile	±0.0	±0.0	±0.0	±0.0	±0.3	±0.2
Stat.	±0.5	±0.4	±0.6	±1.0	±1.3	±2.3
Total Syst	±0.6	±0.7	±1.0	±1.6	±2.4	±4.7
Total	±0.7	±0.8	±1.2	±1.8	±2.7	±5.2
SF	1.01 ± 0.01	1.01 ± 0.01	1.00 ± 0.01	1.01 ± 0.02	1.00 ± 0.03	0.95 ± 0.05

(b) Systematic uncertainties in each ΔR(vertex, jet) bin

Table 8.5: Systematic uncertainties (in %) on the measured data-to-simulation scale factor of the MVb algorithm in the various jet $\Delta R^{\min}$ (a) and ΔR(vertex, jet) regions. The considered vertices are reconstructed with the iterative vertex finder (using the SV1 setup). The results are presented for a representative operating point that corresponds to an overall b-tagging efficiency of 70%.

ΔR(vertex, jet)	0.00-0.025	0.025-0.050	0.050-0.075	0.075-0.100	0.100-0.150	0.150-0.250
ε_{c}	±0.2	±0.3	±0.3	±0.4	±0.5	±0.6
$\varepsilon_{\mathrm{light}}$	±0.1	±0.1	±0.2	±0.3	±0.6	±1.6
$\varepsilon_{\mathrm{fake}}$	±0.1	±0.1	±0.1	±0.1	±0.1	±0.7
Light-flavour jet normalisation	±0.7	±0.9	±1.5	±2.8	±4.3	±6.0
QCD normalisation	±0.0	±0.0	±0.1	±0.1	±0.1	±0.0
$t\bar{t}$ normalisation	±0.0	±0.0	±0.1	±0.1	±0.1	±0.1
Z+jets normalisation	±0.0	±0.0	±0.0	±0.1	±0.1	±0.0
Single-top normalisation	±0.0	±0.0	±0.0	±0.0	±0.0	±0.1
Luminosity	±0.0	±0.0	±0.0	±0.0	±0.0	±0.0
Jet energy scale	±0.1	±0.1	±0.2	±0.1	±0.4	±0.3
ISR/FSR	±0.3	±0.4	±0.6	±0.9	±0.8	±0.8
Top-quark mass	±0.0	±0.0	±0.0	±0.1	±0.0	±0.0
Top-quark p_{T} reweighting	±0.0	±0.0	±0.0	±0.0	±0.0	±0.1
Jet energy resolution	±0.3	±0.4	±0.3	±0.5	±0.4	±0.7
$t\bar{t}$ generator	±0.3	±0.3	±0.4	±1.1	±0.7	±1.0
Fragmentation	±0.1	±0.0	±0.3	±0.4	±0.0	±0.1
Trips in Tile	±0.0	±0.0	±0.0	±0.0	±0.1	±0.1
Stat.	±0.5	±0.4	±0.6	±1.1	±1.5	±3.2
Total Syst	±0.9	±1.2	±1.8	±3.2	±4.6	±6.5
Total	±1.0	±1.2	±1.9	±3.4	±4.8	±7.2
SF	1.00 ± 0.01	1.00 ± 0.01	0.98 ± 0.02	0.99 ± 0.03	0.98 ± 0.05	0.95 ± 0.07

(a) Systematic uncertainties in each ΔR(vertex, jet) bin

ΔR(vertex, jet)	0.00-0.025	0.025-0.050	0.050-0.075	0.075-0.100	0.100-0.150	0.150-0.250
ε_{c}	±2.6	±2.3	±2.0	±1.6	±2.1	±1.3
$\varepsilon_{\mathrm{light}}$	±1.2	±0.9	±1.7	±1.4	±3.0	±4.4
$\varepsilon_{\mathrm{fake}}$	±0.4	±0.5	±0.2	±2.0	±0.7	±1.4
Light-flavour jet normalisation	±15.2	±16.8	±17.9	±21.2	±23.1	±23.4
QCD normalisation	±0.5	±0.5	±0.7	±0.8	±0.7	±0.7
$t\bar{t}$ normalisation	±0.5	±0.5	±0.5	±0.6	±0.7	±0.8
Z+jets normalisation	±0.3	±0.3	±0.2	±0.3	±0.3	±0.4
Single-top normalisation	±0.2	±0.3	±0.3	±0.2	±0.3	±0.3
Luminosity	±0.2	±0.2	±0.2	±0.2	±0.2	±0.3
Jet energy scale	±0.3	±1.3	±1.5	±2.1	±4.1	±3.8
ISR/FSR	±4.0	±3.9	±4.0	±5.5	±4.7	±5.2
Top-quark mass	±0.0	±0.2	±0.2	±0.7	±0.4	±1.5
Top-quark p_{T} reweighting	±0.2	±0.3	±0.2	±0.2	±0.3	±0.6
Jet energy resolution	±3.0	±0.3	±2.0	±0.9	±1.7	±0.1
$t\bar{t}$ generator	±3.1	±5.6	±2.4	±4.2	±6.5	±7.8
Fragmentation	±5.0	±4.0	±6.0	±5.1	±3.5	±4.0
Trips in Tile	±0.6	±0.5	±1.2	±1.8	±1.0	±1.2
Stat.	±4.8	±5.4	±6.8	±9.2	±8.8	±12.9
Total Syst	±17.4	±18.8	±19.8	±23.2	±25.4	±26.4
Total	±18.0	±19.6	±20.9	±25.0	±26.9	±29.4
SF	1.06 ± 0.19	1.09 ± 0.21	1.02 ± 0.21	0.98 ± 0.25	0.87 ± 0.23	0.94 ± 0.28

(b) Systematic uncertainties in each ΔR(vertex, jet) bin

Table 8.6: Systematic uncertainties (in %) on the measured data-to-simulation scale factors of the MVb algorithm in the various ΔR(vertex, jet) regions for multi- (a) and single-track (b) vertices reconstructed with the JetFitter algorithm. The results are presented for a representative operating point that corresponds to an overall b-tagging efficiency of 70%.

Further cross checks corresponding to the calibration results of the MVb algorithm evaluated at an operating point that matches an overall b-tagging efficiency of 70% are presented in Figures 8.17 (a) and (b).

Figure 8.17 (a) shows four sets of b-tagging efficiency scale factors and their combined systematic and statistical uncertainties, which are measured in different jet samples as a function of the jet p_{T}. These measurements are performed for an inclusive event sample, in which all events are taken into account that contain at least four jets, and also for an exclusive event sample, in which all events are taken into account that contain exactly four jets. In addition, this scale factor measurement is repeated for the case that the tag requirement is changed (i.e. the tag requirement is applied to the b-jet candidate on the hadronic side of the selected events, while the b-jet candidate on the leptonic side of the event is used as the probe jet).

In general, the four sets of scale factors are compatible with each other within their combined systematic and statistical uncertainties. The measurement in the exclusive (exactly four jets) sample, provides a significantly smaller total systematic uncertainty due to a higher b-jet purity, while the statistical uncertainty is substantially increased with respect to the inclusive measurement. As a consequence, the combined systematic and statistical uncertainties of the scale factors corresponding to the exactly four jets sample are significantly smaller with respect to the scale factors obtained in the inclusive event sample. Exceptions are the first and the last jet p_{T} bin, in which the statistical component gives a relative large contribution to the total uncertainty. For jets with a p_{T} between 60 GeV and 300 GeV, the total uncertainties on the scale factors range between 2.4% to 4.6% (for the measurements in the exclusive sample of the probe jets from the leptonic side of the selected events), between 3.6% to 5.3% (for the measurements in the inclusive sample of the probe jets from the leptonic side) and between 4.6% to 8.1% (for the measurements in the exclusive sample of the probe jets from the hadronic side). The combined systematic and statistical uncertainties obtained using the exclusive event sample and the b-jet candidates from the leptonic side of the selected events are even competitive to the results provided by measurements in $t\bar{t}$ dilepton events.

Similar comparisons are shown in Figure 8.17 (b), in which also four sets of different b-tagging efficiency scale factors and their combined systematic and statistical uncertainties are presented. These scale factors are measured as a function of the angular separation of the selected probe jets to their nearest neighbouring jet in four disjoint jet samples. For this purpose the inclusive event sample is split into a subsample including events that contain exactly four jets and into another subsample that contains events with five and more jets. Also this measurement is not only performed on the probe jet sample corresponding to the b-jet candidates on the hadronic side of the selected and reconstructed $t\bar{t}$ candidate events, but also on a second probe jet sample that corresponds to the b-jet candidates on the leptonic side. All four sets of the calibration scale factors are compatible with each other within their combined statistical and systematic uncertainties. The compatibility of these results implies that the measured scale factors do not have a significant underlying dependency on additional topology effects as e.g. the jet multiplicity.

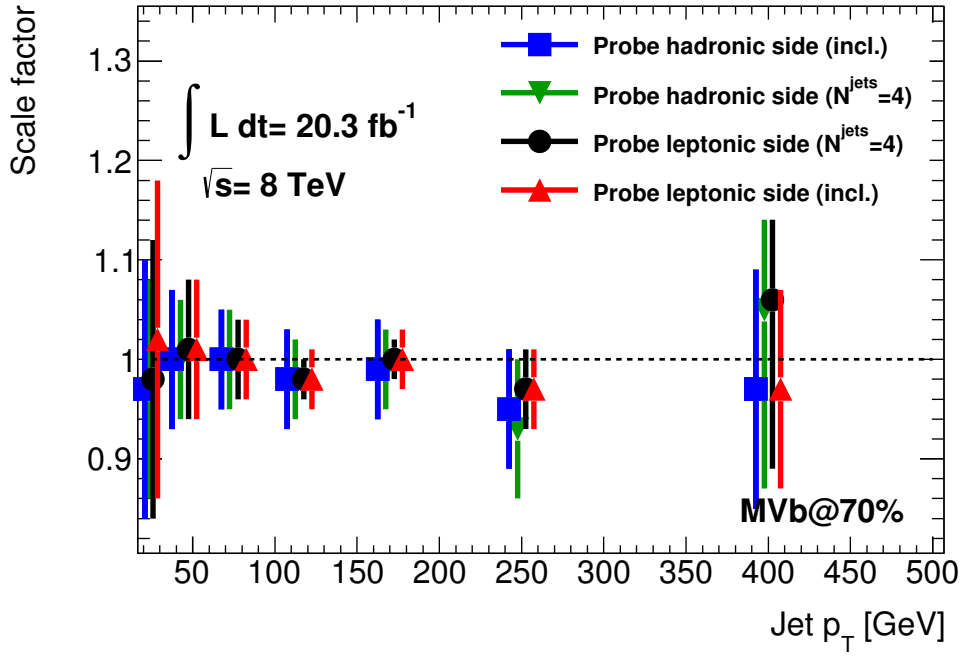

(a)

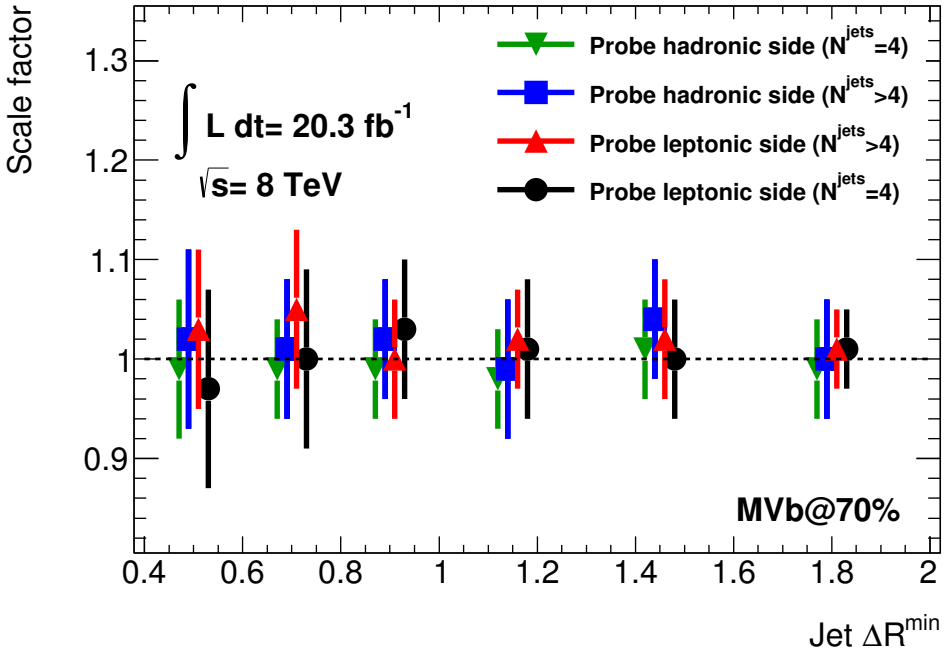

(b)

Figure 8.17: Comparison of several sets of b-tagging efficiency scale factors for the MVb algorithm corresponding to an operating point of an overall efficiency of 70% measured as a function of the probe jet p_{T} (a) and the probe jet ΔR^{min} (b). The measurements are repeated in order to probe individually the b-tagging performance of the b-jet candidate stemming from the leptonic and the hadronic top-quark decay. Additionally, the calibration results are also compared for the case that the jet multiplicity requirement of the selected candidate events is varied.

8.3.2 Calibration results of the MV1 algorithm

The calibration results corresponding to the MV1 algorithm measured for an operating point that matches an overall b-tagging efficiency of 70% are presented graphically in Figures 8.18 and 8.19 for the combined e + jets and μ + jets channel. This operating point is defined by considering all jets as b-tagged that have an MV1 weight exceeding a value of 0.7892.

Both the b-tagging efficiency and the corresponding scale factors are measured (as for the MVb algorithm) as a function of the jet p_{T} (Figures 8.18 (a) and (b)), the jet $|\eta|$ (Figures 8.18 (c) and (d)), the ΔR between the probe jet and its nearest neighbouring jet 8.18 (e) and (f)), and the angular separation between the vertex direction and the axis of the probe jet $\Delta R(\mathrm{vertex}, \mathrm{jet})$ (Figures 8.19 (a) to (f)). The resulting scale factors corresponding to the MV1 algorithm are very similar with respect to those obtained for the MVb algorithm. A detailed break-down of all the relevant systematic uncertainties on the measured scale factors corresponding to the MV1 algorithm at the 70% operating point is given in Tables 8.7 (a-b), 8.8 (a-b) and 8.9 (a-b) for the various p_{T}, $|\eta|$, ΔR^{min} and $\Delta R(\mathrm{vertex}, \mathrm{jet})$ bins. Both the magnitude and the relative importance of the individual systematic uncertainties are very similar to what is obtained for the MVb algorithm.

The scale factors that are obtained by the application of the tag and probe method to a sample of $t\bar{t}$ candidate events containing a single charged lepton (SL), at least four jets and missing transverse momentum in the final state are compared in Figure 8.20 to the b-tagging calibration results provided by the combinatorial likelihood method (PDF) [110] applied to $t\bar{t}$ dilepton events containing exactly two or three jets.

The results of the tag and probe method are provided for the case that the b-jet candidates on the hadronic side of the selected events are used as the probe jets, but also in case that the b-jet candidates on the leptonic side are used. In general, the three sets of scale factors are compatible within their combined statistical and systematic uncertainties. The application of the tag and probe method is beneficial, in particular for high-p_{T} jets as the corresponding combined uncertainties are smaller than those obtained from measurements in the dilepton $t\bar{t}$ events using the PDF calibration approach. In case that the b-jets from the hadronic (leptonic) side of the $t\bar{t}$ events are used to obtain the probe jet sample, the corresponding uncertainties on the scale factor are smaller than those of the dilepton PDF method for jets with a p_{T} above 200 GeV (140 GeV). In addition, the tag and probe method is the first $t\bar{t}$ based b-tagging calibration technique that also provides a scale factor measurement for b-jets with a p_{T} between 300 GeV and 500 GeV.

Again, it is shown that the scale factors from the leptonic side are more precise than the scale factors from the hadronic side. However, they tend to stem from a less busy environment with fewer nearby jets. A summary of the uncertainties related to the scale factors that are measured in the jet sample that is obtained from the leptonic top quark decays is presented in Table 8.10.

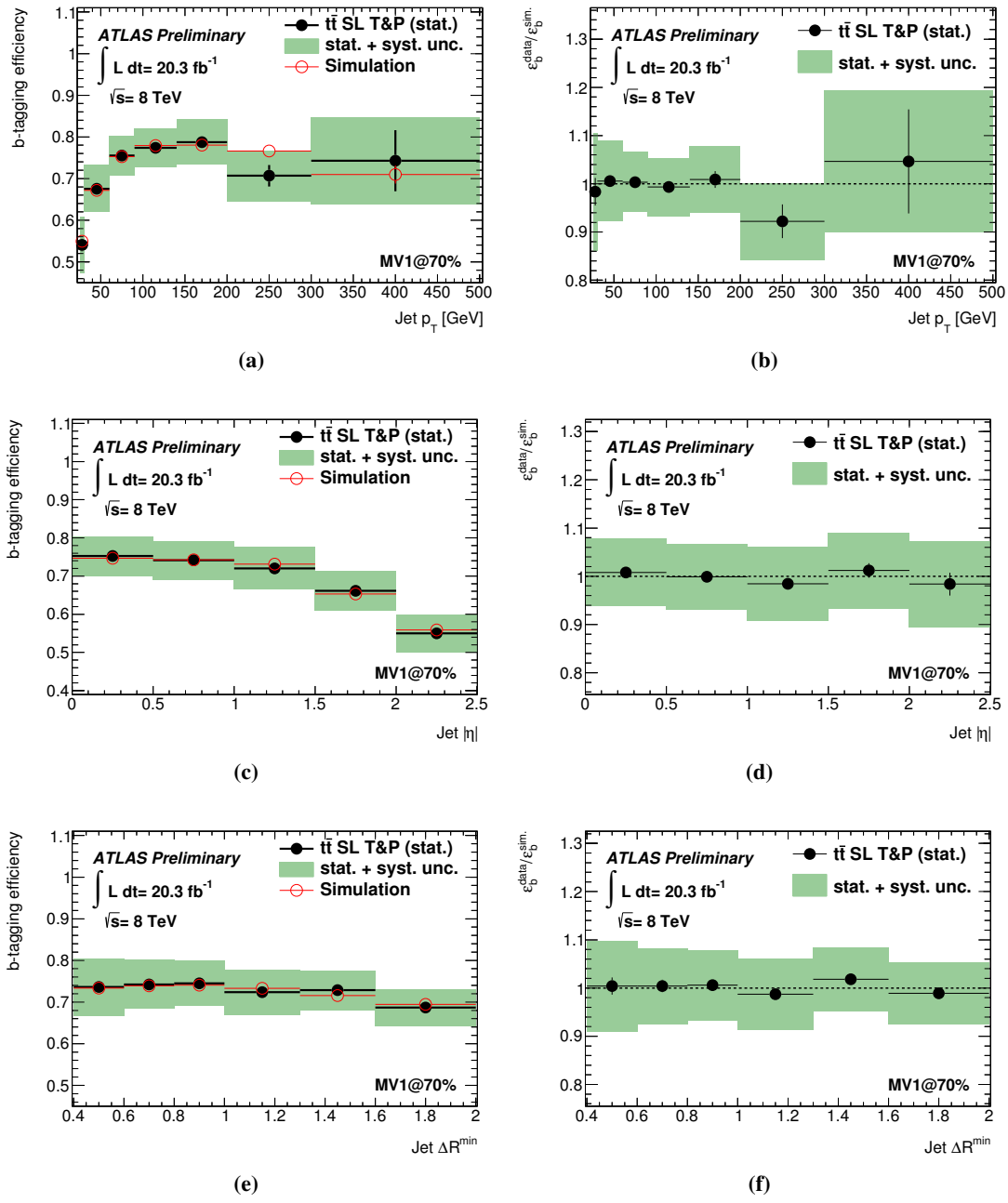

Figure 8.18: The *b*-tagging efficiencies for the MV1 algorithm corresponding to an operating point of an overall efficiency of 70% as a function of the transverse momentum (a), the absolute pseudorapidity (c) and the ΔR^{min} (e) of the jets contained in the sample of $t\bar{t}$ single lepton (SL) candidate events. The *b*-tagging efficiencies are shown for the predictions by the simulation (as a red line) and the measurements in data by the tag and probe (T&P) method (as black dots). The total uncertainties of these measurements are displayed as well (by the green filled area). The uncertainties on the predicted tagging efficiencies are based only on the the Monte Carlo statistics. The corresponding data-to-simulation scale factors are presented in addition also as a function of the jet p_{T} (b), $|\eta|$ (d) and ΔR^{min} (f) [9].

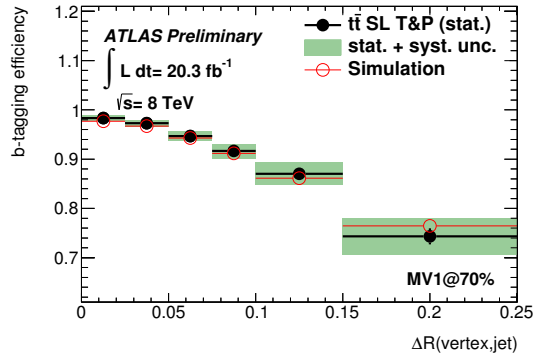

(a) multi-track vertex (SV1)

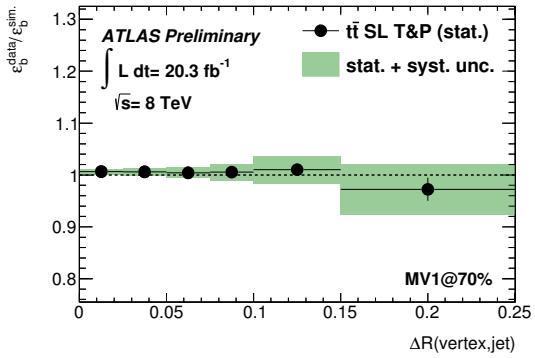

(b) multi-track vertex (SV1)

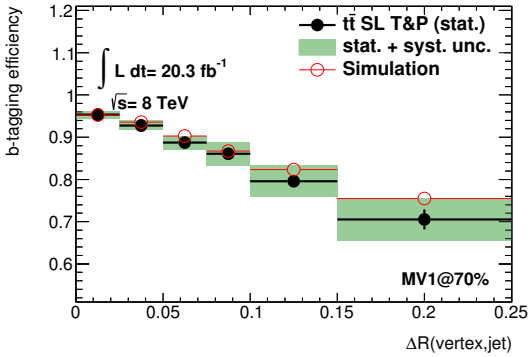

(c) multi-track vertex (JetFitter)

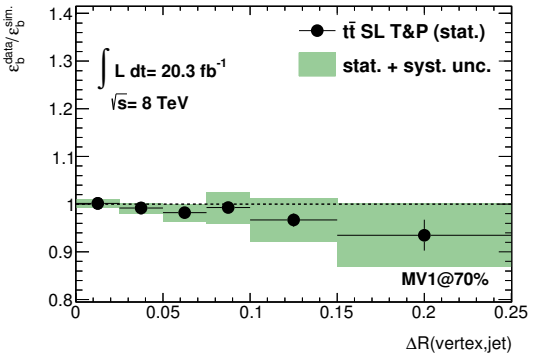

(d) multi-track vertex (JetFitter)

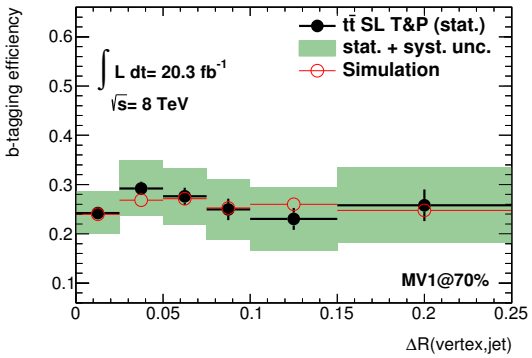

(e) single-track vertex (JetFitter)

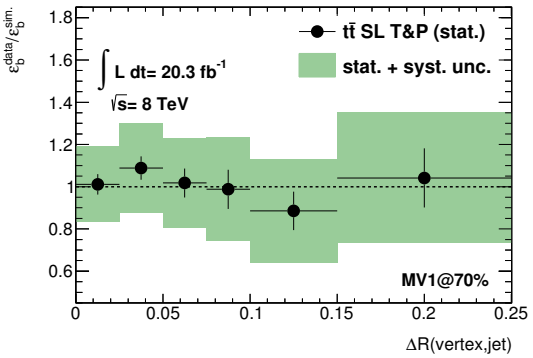

(f) single-track vertex (JetFitter)

Figure 8.19: Results of the *b*-tagging efficiency measurements for the MV1 algorithm corresponding to an operating point of 70% efficiency as a function of the angular separation between the vertex direction and the jet axis $\Delta R(\text{vertex}, \text{jet})$. The measurement is performed separately for jets having a vertex reconstructed with the iterative vertex finder (a-b) and the JetFitter algorithm (c-f), where the vertex candidates based on the JetFitter are subdivided into single- and multi-track vertices. The *b*-tagging efficiencies (left column) are shown for the predictions by the simulation (as a red line) and the measurements in data by the tag and probe (T&P) method (as black dots). The total uncertainties of these measurements are displayed as well (by the green filled area). The uncertainties on the predicted tagging efficiencies are based only on the the Monte Carlo statistics. The corresponding data-to-simulation scale factors are presented in addition (right column). As these measurements take only jets into account that have an appropriate type of secondary vertex reconstructed, the definition of the presented *b*-tagging efficiencies is not inclusive as in the measurements corresponding to the jet p_{T}, η or ΔR^{min} [9].

p_T[GeV]	25-30	30-60	60-90	90-140	140-200	200-300	300-500
ε_c	±0.7	±0.3	±0.2	±0.2	±0.4	±0.4	±0.2
ε_{light}	±0.8	±0.2	±0.1	±0.1	±0.1	±0.1	±0.2
ε_{fake}	±0.6	±0.2	±0.2	±0.1	±0.0	±0.0	±0.1
QCD normalisation	±0.9	±0.6	±0.5	±0.4	±0.3	±0.0	±0.1
$t\bar{t}$ normalisation	±0.8	±0.6	±0.5	±0.5	±0.4	±0.3	±0.2
Z+jets normalisation	±0.4	±0.3	±0.2	±0.2	±0.1	±0.2	±0.0
Single-top normalisation	±0.3	±0.3	±0.2	±0.2	±0.3	±0.2	±0.7
Luminosity	±0.3	±0.2	±0.1	±0.1	±0.1	±0.1	±0.0
Jet energy scale	±6.0	±2.1	±0.8	±0.4	±0.5	±0.1	±1.2
ISR/FSR	±5.7	±4.8	±4.1	±3.7	±3.8	±2.7	±1.8
Top-quark mass	±0.8	±0.4	±0.0	±0.4	±0.3	±0.5	±1.6
Top-quark p_T reweighting	±0.2	±0.0	±0.1	±0.6	±1.5	±2.7	±2.5
Jet energy resolution	±5.8	±4.1	±2.6	±2.1	±1.5	±2.9	±2.8
$t\bar{t}$ generator	±5.9	±4.2	±3.5	±3.9	±4.7	±5.5	±7.0
Fragmentation	±2.1	±2.2	±1.0	±1.0	±1.1	±2.9	±1.8
Trips in Tile	±0.7	±0.1	±0.3	±0.2	±0.2	±0.4	±2.7
Stat.	±2.9	±0.8	±0.8	±0.9	±1.7	±3.5	±10.8
Total Syst	±12.1	±8.3	±6.2	±6.0	±6.6	±7.9	±9.1
Total	±12.4	±8.3	±6.2	±6.0	±6.8	±8.6	±14.1
SF	0.98 ± 0.12	1.01 ± 0.08	1.00 ± 0.06	0.99 ± 0.06	1.01 ± 0.07	0.92 ± 0.08	1.05 ± 0.15

(a) Systematic uncertainties in each p_T bin

η	0.0-0.5	0.5-1.0	1.0-1.5	1.5-2.0	2.0-2.5
ε_c	±0.3	±0.3	±0.3	±0.2	±0.2
ε_{light}	±0.1	±0.1	±0.2	±0.2	±0.4
ε_{fake}	±0.1	±0.1	±0.2	±0.2	±0.2
QCD normalisation	±0.5	±0.5	±0.6	±0.7	±1.0
$t\bar{t}$ normalisation	±0.5	±0.5	±0.6	±0.7	±0.8
Z+jets normalisation	±0.2	±0.2	±0.3	±0.4	±0.3
Single-top normalisation	±0.3	±0.2	±0.3	±0.3	±0.2
Luminosity	±0.2	±0.2	±0.2	±0.2	±0.3
Jet energy scale	±0.5	±0.9	±0.9	±0.2	±0.8
ISR/FSR	±4.1	±4.2	±4.6	±5.2	±5.6
Top-quark mass	±0.3	±0.2	±0.5	±0.3	±1.3
Top-quark p_T reweighting	±0.5	±0.4	±0.5	±0.4	±0.3
Jet energy resolution	±2.9	±1.9	±3.7	±3.5	±5.2
$t\bar{t}$ generator	±4.3	±4.6	±4.4	±3.3	±3.2
Fragmentation	±1.5	±1.4	±1.6	±2.3	±1.9
Trips in Tile	±0.3	±0.3	±0.1	±0.1	±0.6
Stat.	±0.8	±0.8	±1.0	±1.5	±2.4
Total Syst	±6.8	±6.7	±7.7	±7.6	±8.8
Total	±6.9	±6.8	±7.7	±7.7	±9.1
SF	1.01 ± 0.07	1.00 ± 0.07	0.98 ± 0.08	1.01 ± 0.08	0.98 ± 0.09

(b) Systematic uncertainties in each $|\eta|$ bin

Table 8.7: Systematic uncertainties (in %) on the measured data-to-simulation scale factor of the MV1 algorithm in the various jet p_T (a) and $|\eta|$ (b) regions. The results are presented for a representative operating point that corresponds to an overall b-tagging efficiency of 70%.

ΔR^{min}	0.4-0.6	0.6-0.8	0.8-1.0	1.0-1.3	1.3-1.6	1.6-2.0
ε_{c}	±0.3	±0.3	±0.3	±0.2	±0.2	±0.2
$\varepsilon_{\text{light}}$	±0.2	±0.2	±0.2	±0.1	±0.1	±0.1
$\varepsilon_{\text{fake}}$	±0.2	±0.2	±0.1	±0.2	±0.1	±0.1
QCD normalisation	±0.8	±0.7	±0.5	±0.4	±0.4	±0.5
$t\bar{t}$ normalisation	±0.7	±0.7	±0.5	±0.4	±0.4	±0.5
Z+jets normalisation	±0.3	±0.3	±0.3	±0.2	±0.3	±0.3
Single-top normalisation	±0.3	±0.3	±0.2	±0.3	±0.2	±0.2
Luminosity	±0.2	±0.2	±0.2	±0.1	±0.1	±0.2
Jet energy scale	±1.0	±1.4	±0.4	±0.6	±0.5	±0.7
ISR/FSR	±6.1	±4.6	±4.1	±4.2	±3.6	±4.4
Top-quark mass	±0.1	±0.1	±0.3	±0.3	±0.7	±0.7
Top-quark p_{T} reweighting	±2.0	±1.4	±1.0	±0.5	±0.1	±0.2
Jet energy resolution	±2.8	±1.9	±2.6	±3.6	±2.8	±2.9
$t\bar{t}$ generator	±5.3	±5.1	±4.5	±4.6	±3.9	±3.1
Fragmentation	±2.2	±1.8	±2.3	±1.6	±1.5	±1.1
Trips in Tile	±0.3	±0.1	±0.1	±0.1	±0.3	±0.0
Stat.	±1.8	±1.3	±1.2	±1.0	±1.1	±1.2
Total Syst	±9.2	±7.7	±7.1	±7.4	±6.4	±6.4
Total	±9.3	±7.8	±7.2	±7.5	±6.5	±6.5
SF	1.00 ± 0.09	1.00 ± 0.08	1.01 ± 0.07	0.99 ± 0.07	1.02 ± 0.07	0.99 ± 0.06

(a) Systematic uncertainties in each ΔR^{min} bin

ΔR(vertex, jet)	0.00-0.025	0.025-0.050	0.050-0.075	0.075-0.100	0.100-0.150	0.150-0.250
ε_{c}	±0.1	±0.1	±0.1	±0.1	±0.2	±0.3
$\varepsilon_{\text{light}}$	±0.0	±0.1	±0.1	±0.1	±0.2	±0.4
$\varepsilon_{\text{fake}}$	±0.0	±0.0	±0.0	±0.3	±0.1	±0.1
Light-flavour jet normalisation	±0.3	±0.4	±0.7	±0.9	±2.0	±4.2
QCD normalisation	±0.0	±0.0	±0.0	±0.1	±0.1	±0.0
$t\bar{t}$ normalisation	±0.0	±0.0	±0.0	±0.0	±0.1	±0.1
Z+jets normalisation	±0.0	±0.0	±0.0	±0.0	±0.0	±0.0
Single-top normalisation	±0.0	±0.0	±0.0	±0.0	±0.0	±0.0
Luminosity	±0.0	±0.0	±0.0	±0.0	±0.0	±0.1
Jet energy scale	±0.0	±0.0	±0.0	±0.2	±0.5	±0.1
ISR/FSR	±0.2	±0.2	±0.3	±0.5	±0.7	±1.2
Top-quark mass	±0.0	±0.0	±0.0	±0.0	±0.1	±0.1
Top-quark p_{T} reweighting	±0.0	±0.0	±0.0	±0.0	±0.0	±0.1
JJet energy resolution	±0.1	±0.1	±0.0	±0.6	±0.3	±0.2
$t\bar{t}$ generator	±0.1	±0.2	±0.2	±0.2	±0.7	±1.0
Fragmentation	±0.0	±0.1	±0.1	±0.1	±0.2	±0.5
Trips in Tile	±0.0	±0.0	±0.0	±0.0	±0.3	±0.2
Stat.	±0.4	±0.4	±0.6	±0.9	±1.2	±2.2
Total Syst	±0.4	±0.6	±0.8	±1.3	±2.4	±4.5
Total	±0.6	±0.7	±1.0	±1.6	±2.7	±5.0
SF	1.01 ± 0.01	1.01 ± 0.01	1.00 ± 0.01	1.01 ± 0.02	1.01 ± 0.03	0.97 ± 0.05

(b) Systematic uncertainties in each ΔR(vertex, jet) bin

Table 8.8: Systematic uncertainties (in %) on the measured data-to-simulation scale factor of the MV1 algorithm in the various jet ΔR^{min} (a) and ΔR(vertex, jet) regions. The considered vertices are reconstructed with the iterative vertex finder (using the SV1 setup). The results are presented for a representative operating point that corresponds to an overall b-tagging efficiency of 70%.

ΔR(vertex, jet)	0.00-0.025	0.025-0.050	0.050-0.075	0.075-0.100	0.100-0.150	0.150-0.250
ε_{c}	±0.1	±0.1	±0.1	±0.2	±0.2	±0.2
$\varepsilon_{\mathrm{light}}$	±0.0	±0.1	±0.1	±0.2	±0.3	±0.9
$\varepsilon_{\mathrm{fake}}$	±0.1	±0.1	±0.1	±0.1	±0.1	±0.7
Light-flavour jet normalisation	±0.7	±0.9	±1.5	±2.7	±4.2	±5.9
QCD normalisation	±0.0	±0.0	±0.1	±0.1	±0.1	±0.0
$t\bar{t}$ normalisation	±0.0	±0.0	±0.1	±0.1	±0.1	±0.1
Z+jets normalisation	±0.0	±0.0	±0.0	±0.1	±0.1	±0.0
Single-top normalisation	±0.0	±0.0	±0.0	±0.0	±0.0	±0.1
Luminosity	±0.0	±0.0	±0.0	±0.0	±0.0	±0.0
Jet energy scale	±0.1	±0.1	±0.2	±0.2	±0.5	±0.6
ISR/FSR	±0.3	±0.4	±0.6	±0.8	±0.8	±0.9
Top-quark mass	±0.0	±0.0	±0.0	±0.1	±0.0	±0.0
Top-quark p_{T} reweighting	±0.0	±0.0	±0.0	±0.0	±0.0	±0.1
Jet energy resolution	±0.1	±0.3	±0.3	±0.2	±0.9	±1.2
$t\bar{t}$ generator	±0.3	±0.3	±0.4	±1.1	±0.6	±1.1
Fragmentation	±0.1	±0.0	±0.3	±0.4	±0.0	±0.1
Trips in Tile	±0.0	±0.0	±0.0	±0.0	±0.1	±0.0
Stat.	±0.4	±0.4	±0.6	±1.1	±1.4	±3.2
Total Syst	±0.8	±1.1	±1.7	±3.1	±4.5	±6.3
Total	±0.9	±1.2	±1.8	±3.3	±4.7	±7.1
SF	1.00 ± 0.01	0.99 ± 0.01	0.98 ± 0.02	0.99 ± 0.03	0.97 ± 0.05	0.94 ± 0.07

(a) Systematic uncertainties in each ΔR(vertex, jet) bin

ΔR(vertex, jet)	0.00-0.025	0.025-0.050	0.050-0.075	0.075-0.100	0.100-0.150	0.150-0.250
ε_{c}	±0.9	±0.8	±0.6	±0.4	±0.8	±0.4
$\varepsilon_{\mathrm{light}}$	±0.5	±0.5	±0.9	±0.6	±0.9	±1.9
$\varepsilon_{\mathrm{fake}}$	±0.5	±0.5	±0.2	±2.0	±0.7	±1.3
Light-flavour jet normalisation	±15.4	±16.7	±17.9	±20.9	±24.1	±23.6
QCD normalisation	±0.5	±0.5	±0.7	±0.8	±0.7	±0.8
$t\bar{t}$ normalisation	±0.5	±0.5	±0.5	±0.6	±0.7	±0.8
Z+jets normalisation	±0.3	±0.3	±0.2	±0.3	±0.3	±0.4
Single-top normalisation	±0.2	±0.3	±0.3	±0.2	±0.3	±0.3
Luminosity	±0.2	±0.2	±0.2	±0.2	±0.2	±0.3
Jet energy scale	±0.3	±0.3	±0.6	±2.9	±5.0	±3.5
ISR/FSR	±4.0	±3.9	±4.0	±5.5	±4.7	±5.2
Top-quark mass	±0.0	±0.2	±0.2	±0.7	±0.4	±1.5
Top-quark p_{T} reweighting	±0.2	±0.3	±0.2	±0.2	±0.3	±0.6
Jet energy resolution	±1.5	±0.5	±0.4	±0.5	±0.1	±1.5
$t\bar{t}$ generator	±3.1	±5.5	±2.4	±4.3	±6.5	±7.8
Fragmentation	±4.9	±3.9	±6.0	±5.1	±3.5	±4.0
Trips in Tile	±0.5	±0.5	±1.2	±1.8	±1.0	±1.3
Stat.	±4.9	±5.5	±6.9	±9.3	±9.1	±14.0
Total Syst	±17.1	±18.5	±19.6	±23.0	±26.2	±26.2
Total	±17.8	±19.4	±20.8	±24.8	±27.7	±29.7
SF	1.01 ± 0.18	1.09 ± 0.21	1.02 ± 0.21	0.99 ± 0.25	0.89 ± 0.25	1.04 ± 0.31

(b) Systematic uncertainties in each ΔR(vertex, jet) bin

Table 8.9: Systematic uncertainties (in %) on the measured data-to-simulation scale factors of the MV1 algorithm in the various ΔR(vertex, jet) regions for multi- (a) and single-track (b) vertices reconstructed with the JetFitter algorithm. The results are presented for a representative operating point that corresponds to an overall b-tagging efficiency of 70%.

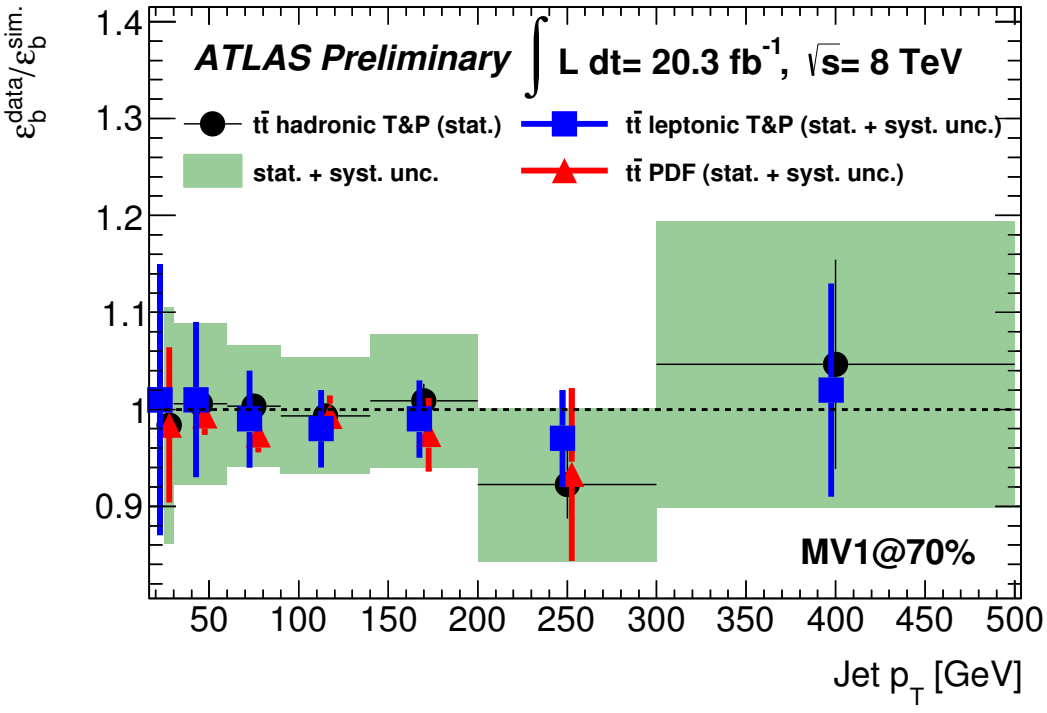

Figure 8.20: Data-to-simulation scale factors for the MV1 algorithm evaluated at an operating point that matches an overall b-tagging efficiency of 70%. The results of the tag and probe method (T&P) applied to $t\bar{t}$ candidate decays into a final state of a single lepton (SL), at least four jets and missing transverse momentum are compared to the scale factors that are obtained with the combinatorial likelihood (PDF) method applied to $t\bar{t}$ dilepton events containing exactly two or three jets (presented as red triangles). The results of the tag and probe method (T&P) are displayed for the case that the b-jet candidates on the hadronic side of the selected events are used as the probe jets (shown as black dots) and also for the case that the b-jet candidates on the leptonic side are used (blue squares) [9].

p_T[GeV]	25-30	30-60	60-90	90-140	140-200	200-300	300-500
Statistical	±2.6	±0.8	±0.8	±0.8	±1.4	±2.9	±10.1
Total Systematic	±13.7	±8.0	±4.9	±3.8	±3.3	±4.4	±3.1
Total	±14.0	±8.0	±4.9	±3.9	±3.5	±5.3	±10.5
SF	1.01 ± 0.14	1.01 ± 0.08	0.99 ± 0.05	0.98 ± 0.04	0.99 ± 0.04	0.97 ± 0.05	1.02 ± 0.11

Table 8.10: Summary of combined systematic and statistical uncertainties (in %) on the measured data-to-simulation scale factor of the MV1 algorithm in the various jet p_T regions. These scale factors are calculated using a b-jet sample obtained from leptonic top quark decays.

Chapter 9

Search for $t\bar{t}$ resonances

The search for new heavy particles decaying into top-quark pairs was already performed at the Tevatron, where the CDF and D0 collaborations excluded leptophobic topcolour Z' with masses below 915 GeV using a data set corresponding to an integrated luminosity of approximately 9.5 fb^{-1} obtained from $p\bar{p}$ collisions at a centre-of-mass energy of $\sqrt{s}$ = 1.96 TeV [147]. At the LHC this search for $t\bar{t}$ resonances was continued by both the ATLAS and CMS collaborations at 7 TeV and 8 TeV using data sets corresponding to integrated luminosities of 2.1 fb^{-1} [148], 4.7 fb^{-1} [77], 14.3 fb^{-1} [149] and 20.3 fb^{-1} [36] respectively. Meanwhile, the exclusion limits for the leptophobic Z' model are extended up to 2 TeV using both the boosted and resolved event reconstruction techniques that are described in Section 5.2. Also further benchmark models such as warped extra dimensions are now taken into account.

The current strategy in ATLAS to search for new heavy particles decaying into top-quark pairs is based on probing the invariant mass spectrum of the reconstructed $t\bar{t}$ candidate events for local excesses or deficits. As neither a significant local excess nor a significant local deficit was found in the data measured by the ATLAS detector during the 2012 run of the LHC [36], limits are set on $\sigma \times BR$, the product of the production cross-section and the branching ratio, of new particles decaying into top-quark pairs. To interpret this measurement various samples of hypothetical processes are simulated according to the predictions of the BSM models described in Section 2.2.2. The corresponding $\sigma \times BR$ limits are then translated into bounds on the minimum mass allowed for such new particles.

This chapter describes how a connection between the topology of the reconstructed $t\bar{t}$ candidate decays and the b-tagged jets contained in the particular events can be exploited to improve the sensitivity to search for new heavy particles decaying into top-quark pairs. This analysis is performed using the current default b-tagging algorithm MV1, but also with the previously described new b-taggers, MVb and MVbCharm in order to compare the resulting exclusion limits and draw conclusions to what extent the application of this new b-tagging algorithm can improve the sensitivity in the search for new heavy particles.

9.1 Event sample composition

The search for $t\bar{t}$ resonances is currently performed using candidate events that are selected and reconstructed by the techniques described in Sections 5.1 and 5.2. Depending on which of these two different selection and reconstruction approaches are used to identify a top-quark pair candidate, the corresponding event is either associated to the so-called boosted decay channel or to the so-called resolved decay channel.

Top-quark pair candidate events passing the resolved selection requirements are reconstructed using the χ^2 minimisation procedure that is described in Section 5.2. In order to reduce the number of possible permutations within this method, the b-tagged jets contained in

the studied events are exclusively used as the b-jet candidates on the leptonic or hadronic side of the particular events[1]. For the purpose of b-tagging, the MV1 algorithm is applied using an operating point corresponding to an overall b-tagging efficiency of 70%.

However the two samples obtained after applying independently the boosted and resolved selection requirements are not disjoint, as an event passing all the requirements of the boosted decay channel can also pass the requirements of the resolved channel (and vice versa). In order to avoid statistical correlations between the two resulting samples, first the entire selection and reconstruction requirements corresponding to the boosted decay channel are applied to the candidate events. Only events that fail any of these requirements are considered for the resolved decay channel. Thus an overlap between these two channels is avoided.

In the following studies, the so-called electroweak correction scale factors are applied to the simulated SM $t\bar{t}$ events in order to take gauge and Higgs boson contribution via loop-diagrams into account, which become relevant at larger energy scales $E >> m_{W,Z}$. The calculation of the corresponding scale factors is based on an extended version of HATHOR (HATHOR 2.1-alpha [34]), which contains theoretical predictions by J. Kühn, A. Scharf, P. Uwer [150–152]. The simulated $t\bar{t}$ events are reweighted using event specific scale factors $w = 1+F^{\text{weak}}$, where an uncertainty of 10% is assigned to the weak corrections F^{weak} (following the recommendations of the authors). A detailed description of the expected effects on top-quark physics due to this weak corrections can be found in Reference [150]. However, a re-weighting of the top-quark p_{T} spectrum (as it was done in the studies presented in Section 8 in order to correct for a mismodelling of the jet p_{T} distribution) is not appropriate in the search for $t\bar{t}$ resonances, as a possible signal might be canceled that way.

Table 9.1 (a) presents the final yields of the events passing the full boosted selection requirements separately for the two different lepton plus jets channels. The event numbers of the various background processes are shown as they are obtained either via the predictions by the simulation or via the data-driven estimations of the charge-asymmetry (for the W+jets production) or the matrix method (for the non-prompt and fake lepton backgrounds). The yields of the observed candidate events in data are shown additionally. In total, 4559 (3928) events, from the data set collected during the 2012 run of the LHC, pass the requirements of the boosted e + jets (μ + jets) decay channels, while 5100 ± 780 (4440 ± 660) events are expected. According to the predictions by the simulation approximately 85% (88%) of the selected candidate events are due to the production of top-quark pairs, while the main non-$t\bar{t}$ contributions arise from the associated production of a W-boson and jets but also due to single top-quarks. The Z+jets or diboson production as well as the fake and non-prompt lepton backgrounds are less significant. Comparing the observed events in data and the total expectations, a deficit in data that is of the order of 11% (12%) is seen for the e + jets (μ + jets) channel. However, when taking the total uncertainties into account, this deficit is roughly covered. After the full event selection and reconstruction requirements corresponding to the resolved decay channel are applied to the 2012 data set, exactly 118910 (111949) events are observed in the e + jets and μ + jets channels respectively, while 115500 ± 12900 (105900 ± 13100) events are predicted. Taking the total systematic uncertainties on the selection acceptance for all considered processes into account, the predictions of the simulation and the data collected by the ATLAS detector are compatible. As for the boosted μ + jets channel, the main contribution of non-$t\bar{t}$ events passing the resolved selection requirements are due to the associated production of a W-boson and jets, followed by the production of single top-quarks. In the resolved e + jets channel, the backgrounds corresponding to non-prompt and fake leptons give the main non-$t\bar{t}$ contributions. Further significant

[1] In contrast to the approach used in Section 8, in which all jets were tested as the two b-jet candidates.

background processes arise from the associated production of a W-boson and jets as well as from single top-quarks. A detailed summary of the event sample composition obtained after applying the full selection and reconstruction requirements of the resolved decay channel are presented in Table 9.1 (b).

Source	$N_{e\text{+jets}}$	$N_{\mu\text{+jets}}$
$t\bar{t}$	4310 ± 760	3850 ± 640
$t\bar{t}+V$	41 ± 7	38 ± 6
W + jets	420 ± 170	360 ± 140
Z + jets	59 ± 35	23 ± 15
Diboson	15 ± 8	14 ± 7
Single top	151 ± 30	150 ± 25
Fake and non-prompt lepton background	100 ± 23	3 ± 1
Total predictions	5100 ± 780	4440 ± 660
Observed	4559	3928

(a) Boosted decay channel

Source	$N_{e\text{+jets}}$	$N_{\mu\text{+jets}}$
$t\bar{t}$	92100 ± 12600	90700 ± 13000
$t\bar{t}+V$	270 ± 40	260 ± 40
W + jets	7600 ± 1500	8400 ± 1700
Z + jets	1570 ± 890	740 ± 410
Diboson	210 ± 80	190 ± 80
Single top	3800 ± 500	3700 ± 500
Fake and non-prompt lepton background	9900 ± 2200	1890 ± 420
Total predictions	115500 ± 12900	105900 ± 13100
Observed	118910	111949

(b) Resolved decay channel

Table 9.1: Numbers of events passing the full event selection and reconstruction procedures of the boosted (a) and resolved (b) decay channels. The event yields are shown separately for the predicted signal and background processes and the observations in data. The uncertainties correspond to the expected total systematics relevant for this analysis.

Figures (a-d) display data-to-simulation comparisons of the invariant $t\bar{t}$ mass spectra separately for the boosted and the resolved decay channels as well as for e+jets and μ+jets final states. A comparison between the data collected by the ATLAS detector during the 2012 run of the LHC and the predictions provided by the simulation are presented in these figures, where the non-prompt and fake lepton backgrounds, diboson and single top-quark events as well as the associated production of a Z-boson and jets is summarised as one single component (referred to as "others"). The contribution that is denoted by $t\bar{t}$ contains both the top-quark pair production and the associated production of top-quark pairs and a vector boson. In addition, also the corresponding data-to-simulation ratios are shown.

The data-to-simulation comparisons in the boosted decay channel show a significant deficit in data, which is in the order of approximately 10% for $m_{t\bar{t}}$ masses below 1.4 TeV for both the e+jets and μ+jets channels and up to 30% for larger $m_{t\bar{t}}$ values. The corresponding ratio curves are situated for most $m_{t\bar{t}}$ bins at the edge of the uncertainty band.

However, the comparisons in the resolved $t\bar{t}$ decay channels show a consistency between the predictions by the simulation and the measured data taking the combined statistical and systematic uncertainties into account. The two different lepton plus jets final states show relative similar data-to-simulation ratios over the full range of $m_{t\bar{t}}$ values in both, the boosted and the resolved decay channels.

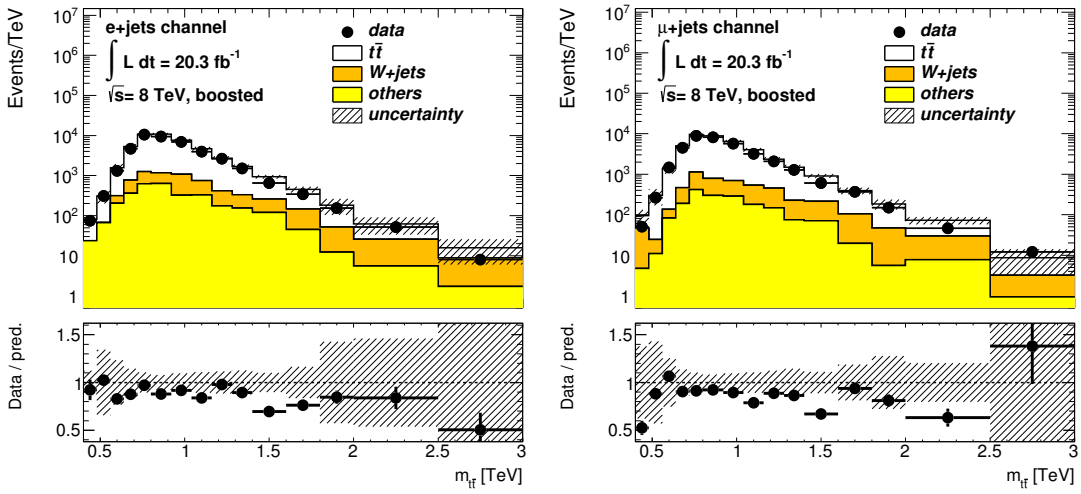

(a) Boosted e+jets channel

(b) Boosted μ+jets channel

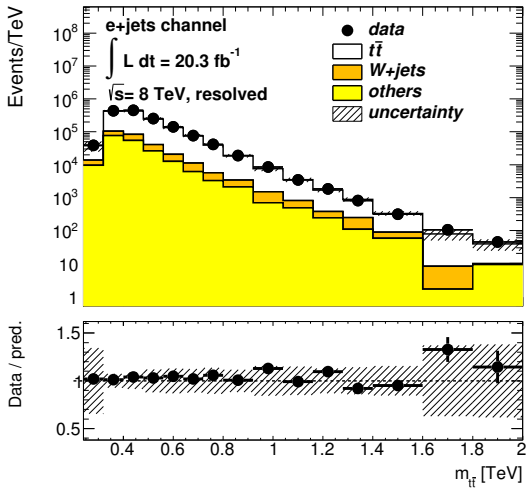

(c) Resolved e+jets channel

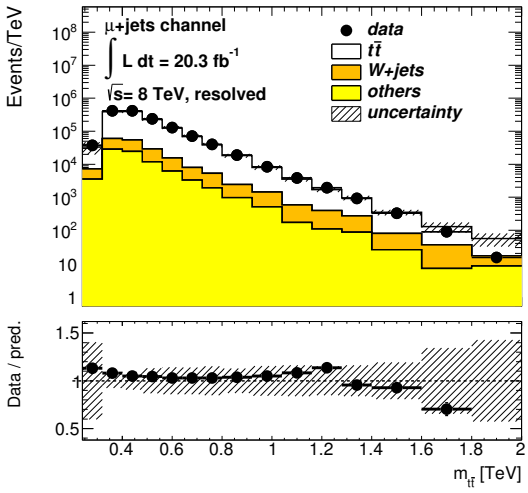

(d) Resolved μ+jets channel

Figure 9.1: Distribution of the invariant $t\bar{t}$ mass as reconstructed within the boosted (top row) and the resolved (bottom row) decay channels. Separate mass spectra are displayed for the e+jets (left column) and μ+jets (right column) final states. The data collected by the ATLAS detector during the 2012 run of the LHC (solid black points) is compared to the predictions by the simulation (filled histograms). The simulated Monte Carlo samples are normalised according to their predicted cross-sections to an integrated luminosity of 20.3 fb^{-1}. In addition, data-to-simulation ratios are displayed at the bottom of each plot.

9.2 Categorisation of $t\bar{t}$ candidate events using b-tagging in the event reconstruction

Previous studies showed that the sensitivity to search for heavy resonances decaying into top-quark pairs is significantly enlarged, if the selected event sample is split according to the multiplicity of b-tagged jets contained in the studied events [153, 154]. The main advantage of such an event categorisation is a possible profiling of certain systematic uncertainties during the calculation of the exclusion limits, a better signal-to-background ratio in some of these categories and a reduction of the combinatorial background (events in which the $t\bar{t}$ decay is reconstructed incorrectly), as these events have a worse mass resolution with respect to the correctly reconstructed events.

The following studies describe how these exclusion limits can be even further improved using a more sophisticated classification scheme, which exploits additionally the information whether the b-tagged jets contained in the candidate events are associated to any of the objects used in the reconstruction of the invariant $t\bar{t}$ mass or not. For the purpose of b-tagging, the MV1 algorithm is applied to the anti-k_t $R = 0.4$ jets contained in the candidate events using an operating point that matches an overall b-tagging efficiency of 70% (i.e. the jet weight of the MV1 algorithm is required to be larger than 0.7892).

9.2.1 Boosted decay channel

Boosted $t\bar{t}$ candidate events can be classified into four different categories depending on the number of contained b-tagged jets and whether these jets are associated to any object that is used in the reconstruction procedure of the invariant $t\bar{t}$ mass. For this purpose only events containing at least one b-tagged anti-k_t $R = 0.4$ jet are considered. An event is classified into the category "BtagCat1", if both the b-jet candidate on the leptonic side and one of the jets associated to the hadronic side are b-tagged. The jets on the hadronic side have to be ΔR matched to the large-radius jet in order to be taken into account, where an anti-k_t $R = 0.4$ jet is considered as successfully matched if the axis of both jet objects have an angular separation below 1.0. In the case that an event has a b-tagged jet that is either ΔR matched to the large-radius jet or equal to the b-jet candidate on the leptonic side of the top-quark decay, the event is classified into the categories "BtagCat2" and "BtagCat3" respectively. Events that contain a b-tagged jet, which is neither identical to the b-jet candidate on the leptonic side of the event nor ΔR matched to the large-radius jet, are classified into the category "BtagCat4". This class contains almost exclusively events that are reconstructed assigning the wrong $R = 0.4$ jet to the leptonic top-quark decay or events, in which the particle shower corresponding to the b-quark from the $t \to bW \to bq\bar{q}$ decay) is not included in the large-radius jet. A short summary of these categories is given in Table 9.2.

Category	Definition
"BtagCat1"	b-tagged jet on both the leptonic and hadronic side of the event.
"BtagCat2"	b-tagged jet on the hadronic side of the event.
"BtagCat3"	b-tagged jet on the leptonic side of the event.
"BtagCat4"	b-tagged jet not assigned to either of these two sides.

Table 9.2: Definition of the various b-tagging categories.

Figure 9.2 displays the distribution of the boosted $t\bar{t}$ candidate events into these various b-tagging categories separately for the e+jets (a) and μ+jets (b) channels. A comparison between the data collected by the ATLAS detector during the 2012 run of the LHC and the predictions provided by the simulation are presented in these figures, where the non-prompt and fake lepton backgrounds, diboson and single top-quark events as well as the associated production of a Z-boson and jets is summarised as one single component ("others"). The contribution that is denoted by $t\bar{t}$ contains both the top-quark pair production and the associated production of top-quark pairs and a vector boson. In addition, also the corresponding data-to-predictions ratios are shown. An overall disagreement of the order of 10% to 20% can be seen between the observations in data and the predictions of the simulation for these various categories.

From all the candidate events in data that pass the full selection requirements of the e+jets (μ+jets) channel, 35% (36%) are contained in the category "BtagCat1", 33% (32%) are contained in "BtagCat2", 23% (23%) in "BtagCat3" and 9% (9%) in "BtagCat4". The contamination of non-top-quark pair events within these four regions is predicted to be approximately 2%, 22%, 13% and 34% respectively for the e+jets channel and 3%, 21%, 13% and 29% for the μ+jets channel. In both, the e+jets and μ+jets channel it is shown that the category "BtagCat2" contains substantially more $t\bar{t}$ candidate events than the category "BtagCat3". This effect is mainly related to the problem that the highest-p_{T} jet on the leptonic side is in a significant fraction of the selected $t\bar{t}$ candidate events not a b-jet. In addition, the fact that roughly $1/2$ of the hadronic top-quark decays contain not only a b- but also a c-jet contribute to this difference, as the mis-tagging efficiency for c-jets is relative large.

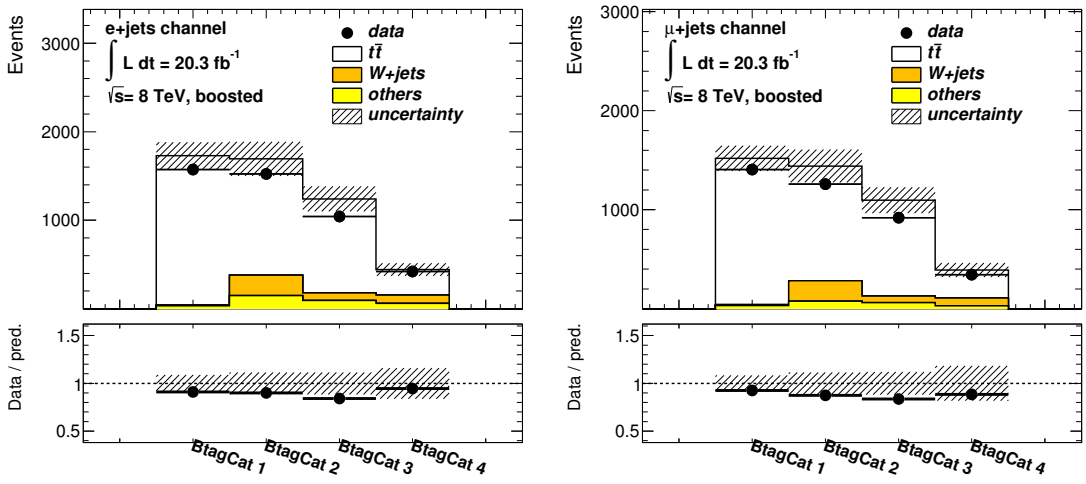

(a) b-tagging categories in e+jets channel

(b) b-tagging categories in μ+jets channel

Figure 9.2: Distribution of the boosted $t\bar{t}$ candidate events into the various b-tagging categories shown separately for the e+jets (a) and μ+jets (b) channels. The data measured by the ATLAS detector during 2012 (solid black points) is compared to the predictions of the simulation (filled histograms). The simulated Monte Carlo samples are normalised according to their predicted cross-sections to an integrated luminosity of 20.3 fb^{-1}. In addition, data-to-simulation ratios are displayed at the bottom of each plot.

The mass resolution of the reconstructed $t\bar{t}$ candidates calculated with respect to the invariant mass of the top-quark pairs at generator level is presented in Figure 9.3 separately for the various b-tagging categories. These comparisons are based on a sample of $t\bar{t}$ decays that are simulated with the POWHEG and PYTHIA generators according to the predictions of the SM. It is obvious that the reconstructed mass of the $t\bar{t}$ candidate has the best agreement to the true mass value (as obtained from the four-vector sum of the generator level particles) if the corresponding events have both the b-jet candidate on the leptonic side b-tagged and at least one of the $R = 0.4$ jets ΔR matched to the large-radius jet. The worst mass resolution of all investigated categories can be seen for events classified into "BtagCat4", as their $m_{t\bar{t}} - m_{t\bar{t}}^{\text{truth}}$ distribution is much broader than that of the other categories. However, the categories "BtagCat2" and "BtagCat3", which have both either a jet on the hadronic side or on the leptonic side b-tagged, show as well broad tails extending to relative large and positive $m_{t\bar{t}} - m_{t\bar{t}}^{\text{truth}}$ values (i.e. a large fraction of events contained in these categories has a reconstructed m_{tt} that is much larger than their true m_{tt} value). This indicates that a relative large fraction of the events that are contained in these two categories is reconstructed incorrectly. Furthermore, events that do not have a b-tagged jet on the hadronic side tend to have a slightly worse mass resolution than events that have no b-tagged jet on the leptonic side, which could be related to the problem that the large-radius jet does not contain all the decay products of the hadronic top-quark decay for a certain fraction of these events.

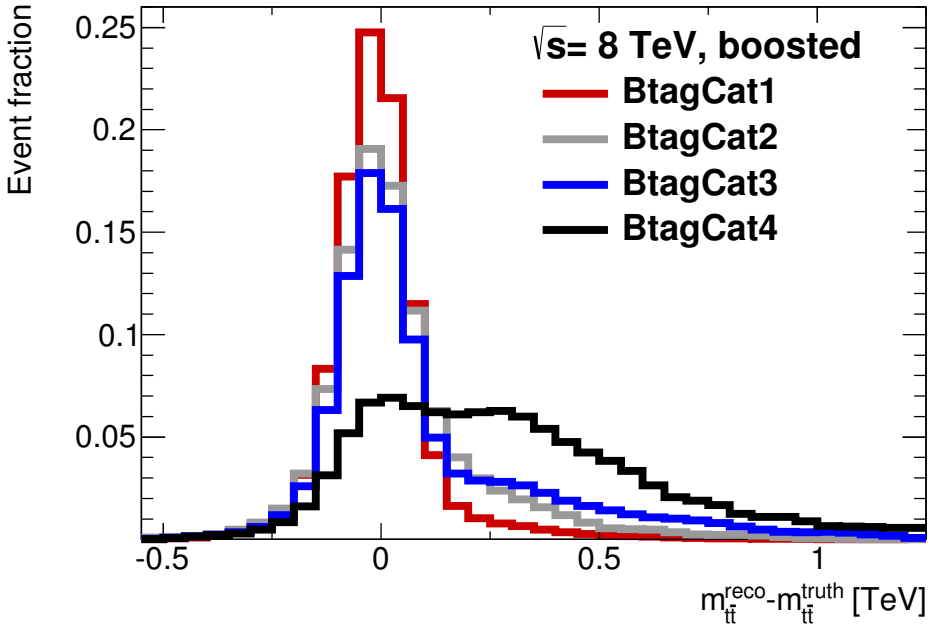

Figure 9.3: Resolution of the reconstructed invariant mass $m_{t\bar{t}}$ determined with respect to $m_{t\bar{t}}^{\text{truth}}$, the invariant mass of the $t\bar{t}$ system evaluated at generator level after the emission of final state radiation. A sample of $t\bar{t}$ events that is simulated by the POWHEG and PYTHIA generators according to the SM predictions is used to calculate the mass resolution separately for the various b-tagging categories. Only events passing the entire selection and reconstruction requirements of the boosted decay channel are considered.

9.2.2 Resolved decay channel

The classification procedure applied to the resolved decay channel is similar to that used in the boosted decay channel (see Table 9.2). This means that events are included in the category "BtagCat1" if the b-jet candidates on both the hadronic and leptonic side are b-tagged, while events are classified into the categories "BtagCat2" or "BtagCat3" if only one of these jets is tagged.

However, as the default settings of the χ^2 minimisation procedure, used to reconstruct the resolved $t\bar{t}$ candidate events, assigns automatically any b-tagged jet contained in the event to either the b-jet candidate on the hadronic or the leptonic side, the resolved decay channel provides only three disjoint event classes instead of four.

The distribution of the selected $t\bar{t}$ candidate events corresponding to the resolved decay channel into the three different b-tagging categories is presented separately in Figures 9.4 (a) and (b) for the e+jets and μ+jets channels. Again, the distribution of the non-prompt and fake lepton backgrounds, the Z+jets and diboson production and single top-quark events are summed up in order to form one single component ("others"). Data-to-predictions ratios are shown as well. From all the candidate events in data that pass the full selection and reconstruction requirements of the resolved e+jets (μ+jets) channel, 40% (41%) are contained in the category "BtagCat1", while 33% (32%) and 27% (27%) are contained in the categories "BtagCat2" and "BtagCat3". The predicted contamination of non-top-quark pair events within these three classes is approximately 7%, 29% and 27% for the e+jets channel as well as 5%, 21% and 19% for the μ+jets channel. As in the boosted decay channel, both the e+jets and μ+jets channel show that the category "BtagCat2" contains significantly more $t\bar{t}$ candidate events than the category "BtagCat3". However, in the resolved decay channel this effect is mainly caused by the χ^2 minimisation procedure and the corresponding $\log_{10}(\chi^2_{\text{total}})$ selection requirement. The main reason is that by construction events that have a b-tagged b-jet candidate on their hadronic side, tend to pass more often the cut on the $\log_{10}(\chi^2_{\text{total}})$ than events in which the b-jet corresponding to the hadronic top-quark decay is not b-tagged.

The resolution of the invariant mass of the $t\bar{t}$ system obtained using the resolved selection and reconstruction procedures is presented in Figure 9.4 (c) separately for the three possible b-tagging categories. As for the boosted decay channel, the category "BtagCat1" provides a better mass resolution compared to the other classes. However, the relative difference between the mass resolution obtained in the various categories is significantly smaller for the resolved decay channel than for the boosted channel. This is mainly due to the fact that only events with $\log_{10}(\chi^2_{\text{total}}) < 0.9$ are considered in the resolved channel, which leads already to a discarding of a large fraction of the less well reconstructed $t\bar{t}$ decays.

9.3 Upper production cross-section limits on $t\bar{t}$ resonances

A common procedure for the calculation of the exclusion limits on a certain signal model is based on a frequentist significance test that uses a likelihood ratio formalism [155]. With this approach the production cross-section times branching ratio of the assumed signal model is determined taking the so-called nuisance parameters θ of the signal and the background processes into account. These parameters account for a change in the shape of the probed mass spectrum of the reconstructed $t\bar{t}$ candidate due to the systematic uncertainties assigned to the mass measurement. The introduction of the nuisance parameters, whose values are obtained during the fit of the data, lead to an increased flexibility that is required to handle systematic effects but also to a loss of sensitivity. The binned likelihood function used in the fitting procedure is defined for

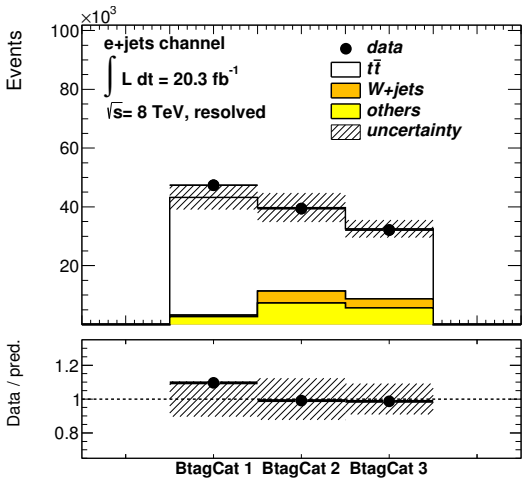

(a) b-tagging categories in e+jets channel

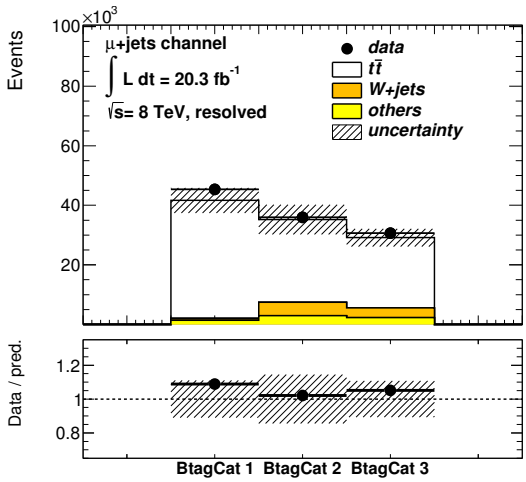

(b) b-tagging categories in μ+jets channel

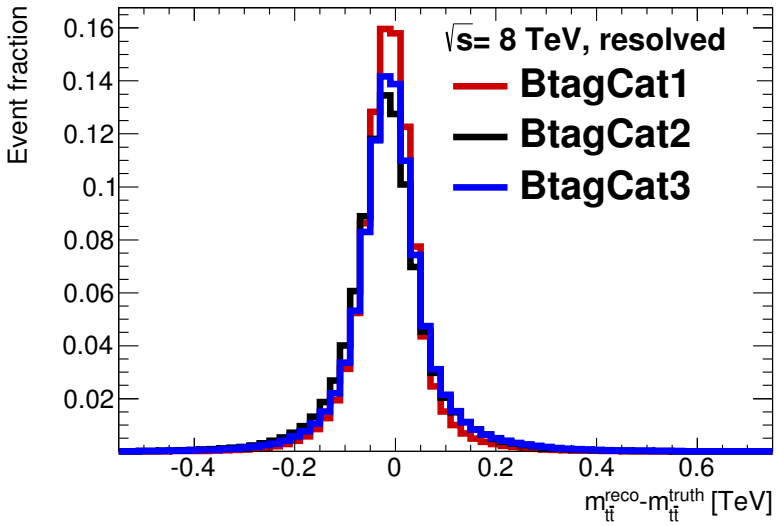

(c) $m_{t\bar{t}}^{\text{truth}} - m_{t\bar{t}}$ distribution

Figure 9.4: Distribution of the resolved $t\bar{t}$ candidate events into the various b-tagging categories shown separately for the e+jets (a) and μ+jets (b) channels. The data collected by the ATLAS detector during 2012 (solid black points) is compared to the predictions of the simulation (filled histograms). The simulated Monte Carlo samples are individually normalised according to their predicted cross-sections to an integrated luminosity of 20.3 fb^{-1}. In addition, data-to-simulation ratios are displayed at the bottom of each plot. Also the distribution of the $m_{t\bar{t}}$–$m_{t\bar{t}}^{\text{truth}}$ is presented for each of the three categories. This distribution corresponds to the reconstructed invariant mass $m_{t\bar{t}}$ determined with respect to $m_{t\bar{t}}^{\text{truth}}$, the invariant mass of the $t\bar{t}$ system evaluated at generator level after the emission of final state radiation. A sample of $t\bar{t}$ events that is simulated by the POWHEG and PYTHIA generators according to the SM predictions is used to calculate the mass resolution separately for the various b-tagging categories. Only events passing the entire selection and reconstruction requirements of the boosted decay channel are considered.

a particular resonance mass m as the product of Poisson distributions of event counts contained in the various mass bins:

$$L(\mu, \theta) = \prod_{j \in N} \frac{(\mu s_j + b_j)^{n_j}}{n_j!} \cdot e^{-(\mu s_j + b_j)} \prod_{k \in S} G(\theta_k^0 - \theta_k) \, . \tag{9.1}$$

Here s_j, b_j and n_j are the number of predicted signal and background events contained in the j-th mass bin as well as the counted events in data within this bin. The parameter μ represents the signal strength. While for $\mu = 0$ the background-only hypothesis is tested, for $\mu = 1$ the signal expectation is equal to the nominal value predicted by the model under consideration. Systematic uncertainties are accounted for by the Gaussians G and the nuisance parameter θ, where θ^0 is the central value around which θ can be varied when maximising the likelihood function and is typically set to zero. The index j runs over all bins of the $m_{t\bar{t}}$ spectrum, which ranges from 0.4 TeV to 3.6 TeV in the boosted channel and from 0.24 TeV to 2 TeV in the resolved channel, while S is the full list of systematic uncertainties considered in the analysis.

Equation 9.1 corresponds to the use of an inclusive event sample, but indeed the events considered here are split into several classes depending on the flavour of the selected lepton, the fact whether the event passes the boosted or resolved selection requirements or on the various b-tagging related categories. To comply with this conditions, Equation 9.1 is extended by introducing a further product sum over all the various signal regions.

The various signal strength hypothesis are tested using a profile likelihood ratio formalism, which leads to a test statistic that is defined by

$$q_\mu = -2 \ln \left(\frac{L(\mu, \hat{\hat{\theta}})}{L(\hat{\mu}, \hat{\theta})} \right) . \tag{9.2}$$

The parameter $\hat{\hat{\theta}}$ denotes the value of θ that maximises the likelihood function L for a tested signal strength, while $\hat{\mu}$ and $\hat{\theta}$ are the values of μ and θ that maximise the denominator.

The parameter q_μ can be interpreted as a measure of the compatibility between the observations in data and the presence of a signal, where larger values of q_μ indicate a disagreement between the measured data and the signal hypothesis. The extent of this disagreement is quantified by the so-called p-value, which is defined according to

$$p_\mu = \int_{q_{\mu,\mathrm{obs}}}^{\infty} f(t_\mu | \mu) dt_\mu \, , \tag{9.3}$$

where $q_{\mu,\mathrm{obs}}$ and $f(q_\mu|\mu)$ denote the value of the test statistic q_μ that is observed in the data and its probability density function evaluated for a given signal strength μ, respectively. This probability density function can be determined either via the generation of pseudo-experiments according to a certain input model or via asymptotic approximations [156].

9.3.1 Improvement of the exclusion limits due to the categorisation of the selected candidate events using *b*-tagging

The b-tagging related event classification scheme described in Section 9.2 is used in the following studies in order to quantify how their usage can improve the sensitivity to search for $t\bar{t}$ resonances. In the boosted $t\bar{t}$ decay channel, the exclusion limits on the production cross section times branching ratio corresponding to a certain benchmark model are calculated with

the binned likelihood ratio formalism for the cases that all four categories (referred to as "BtagCat1234") are taken into account in the limit setting procedure, that the first three categories are taken into account (referred to as "BtagCat123") and also for the case that the first three categories are taken into account but the categories "BtagCat2" and "BtagCat3" are combined into one single component (referred to as "BtagCat1comb23"). The corresponding limits are compared to each other and in particular to the exclusion limits that are obtained from the inclusive event sample and for the case that the selected events are classified according to their multiplicity of b-tagged jets ("Btag12"), where the latter categorisation scheme distinguishes between events having one and two ore more b-tagged jets. In the resolved $t\bar{t}$ decay channel, the exclusion limits corresponding to the inclusive event sample are compared to the case that the selected events are categorised according to their multiplicity of b-tagged jets ("Btag12") as well as to the limits that correspond to a splitting of the selected event sample into three different b-tagging related categories (referred to as "BtagCat123").

These optimisation studies are performed on the so-called Asimov data set, which is the sum of the various background processes obtained from the simulation and the data-driven background estimations. Due to the relative large difference in terms of mass resolution and signal-to-background ratio observed for the selected events from the boosted and the resolved decay channels, the improvements on the expected exclusion limits obtained after applying such an event classification procedure is studied for both these channels independently. The chosen benchmark model on which these comparisons are based, correspond to a topcolor assist technicolor predicting the existence of a leptophobic Z'-boson, while results based on further benchmark models are presented in Appendix C.

Boosted decay channel

Figure 9.5 (a) displays the expected limits on the production cross-section times branching ratio as a function of the leptophobic Z' mass at the 95% confidence level as well as the predicted cross sections corresponding to this particular Z' model [134]. The limits are presented separately for the inclusive event sample and also for two different b-tagging categorisation schemes. The existence of a Z' resonance is excluded at the 95% confidence level in the mass range from 600 GeV to 2 TeV according to the results obtained from the inclusive event sample. However, with the event classification scheme denoted as "BtagCat1234", the excluded mass region is extended by approximately 100 GeV with respect to the exclusion limits that are obtained using the inclusive event sample, while also a leptophobic Z' with a mass below 600 GeV can be successfully excluded. In addition, the relative improvements of the exclusion limits obtained using the various combinations of the different event categories with respect to the inclusive event sample are shown as well as a function of the leptophobic Z' mass in Figure 9.5 (b). The best results are provided by the setup that uses all four b-tagging categories (referred to as "BtagCat1234"), but is closely followed by the setup that includes only the events that have a b-tagged jet associated to any object used in the mass reconstruction of the $t\bar{t}$ candidate events ("BtagCat123"). Indeed, the improvements due to the use of events classified into the fourth category are relative small for most Z' mass points.

The setup "BtagCat1234" provides improvements on the expected production cross-section times branching ratio limits that are of the order of 10% to 30% for Z' masses between 0.75 TeV and 3 TeV and even up to 65% for Z' masses below 0.75 TeV. Using simply the number of b-tagged jets contained in the event as a classification characteristic ("Btag12"), gives improvements at the order of 2% to 10% for Z' masses in the range between 0.75 TeV and 3 TeV and about 35% to 40% for the two lowest Z' mass points. The setup "BtagCat1comb23", which

corresponds to the case that the categories 2 and 3 are merged into one single category, gives exclusion limits that are of similar size to that corresponding to the setup "Btag12" for Z' masses below 1.25 TeV, while the exclusion limits for resonance masses above 1.25 TeV are similar to those of the setup "BtagCat123".

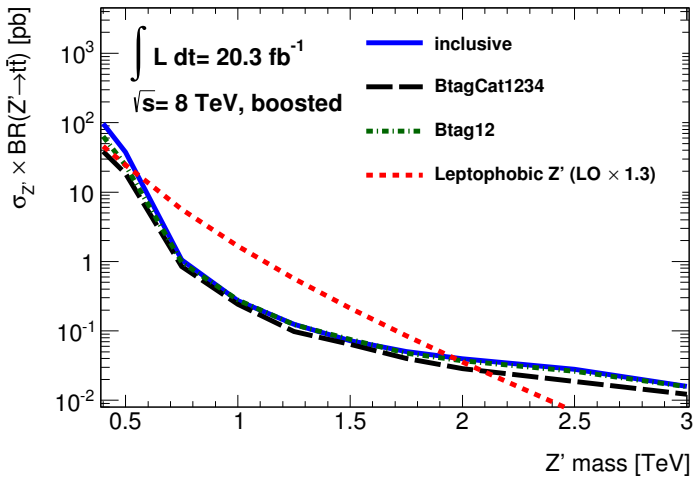

(a) Expected exclusion limits

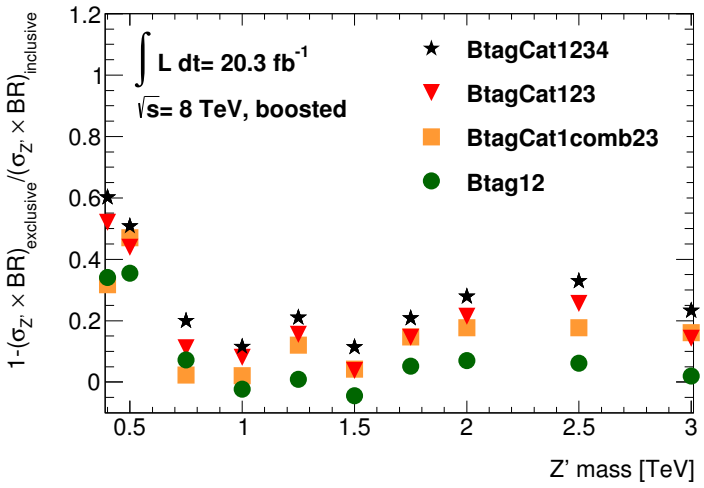

(b) Ratios

Figure 9.5: Expected exclusion limits on the production cross-section times branching ratio as a function of the leptophobic Z' mass at the 95% confidence level obtained from events that are reconstructed in the boosted event channel (a). The limits are presented for the inclusive event sample (blue solid line), but also for the case that the selected candidate events are categorised according to their multiplicity of b-tagged jets (green dashed line) or according to the classification scheme referred to as "BtagCat1234" (black dashed line). The predicted production cross section times branching ratio for a leptophobic Z' is displayed as well as a function of the resonance mass (dashed red line). In addition, also the relative improvements with respect to the inclusive event sample are shown for various event classification schemes (b).

The distribution of the various nuisance parameters obtained after applying the profile likelihood formalism to the various background processes and an exemplary signal corresponding to a Z' with the mass of 2 TeV are displayed in Figure 9.6. The parameters are presented separately for the fit results of the inclusive and the exclusive event samples. For this comparison, the events are split according to the classification scheme referred to as "BtagCat123". It is shown that some of the considered systematic uncertainties are constrained more strongly during the fit, if the event sample is split into various categories. The largest constraint is observed for the systematic uncertainty that corresponds to the eight eigenvalue of the b-tagging scale factors. Thus the improvements on the expected exclusion limits on the production cross-section times branching ratio are not only related to a better resolution of the reconstructed mass or a lower contamination of non-$t\bar{t}$ events in the various categories, but also due to a profiling of some of the systematic uncertainties.

Resolved decay channel

The expected exclusion limits on the production cross-section times branching ratio corresponding to the resolved decay channel are displayed at a 95% confidence level in Figure 9.7 (a) as a function of the leptophobic Z' mass. Again, the exclusion limits are presented separately for the inclusive event sample and the case that the event sample is split into disjoint categories ("BtagCat123" and "Btag12").

The exclusion limits obtained from the resolved $t\bar{t}$ decay channel are significantly stronger for resonance masses below 750 GeV with respect to those of the boosted $t\bar{t}$ decay channel. However, the corresponding exclusion limits obtained from the boosted decay channel dominate for Z' masses above 750 GeV. Also the total differences between the inclusive and the two exclusive event samples obtained for the resolved decay channel are less significant compared to the boosted decay channel. Nevertheless, with all three approaches, leptophobic Z' masses below approximately 1.2 TeV are successfully excluded at the 95% confidence level. The relative improvements of the exclusion limits calculated with respect to the inclusive event sample are shown for these two categorisation schemes in Figure 9.7 (b). The improvements on the expected production cross-section times branching ratio limits corresponding to the setup "BtagCat123" range between 5% and 20% for resonance masses of 0.75 TeV or larger, while the improvements for the event classification according to the multiplicity of b-tagged jets ("Btag12") is slightly lower for most Z' mass points.

The distribution of the nuisance parameters obtained during the application of the profile likelihood fit to the mass spectra obtained from the resolved $t\bar{t}$ decay channel is shown in Figure 9.8 separately for the inclusive and the exclusive event sample (i.e. the sample that corresponds to the classification scheme "BtagCat123") using an exemplary Z' signal with a mass of 2 TeV. As in the boosted $t\bar{t}$ decay channel, several systematic uncertainties are constrained more strongly in the fits corresponding to the categorised event sample. In particular, the systematic uncertainty corresponding to the eight eigenvalue of the b-tagging scale factors (referred to as "b-tag EV8") is constraint the most with respect to the results of the inclusive event sample.

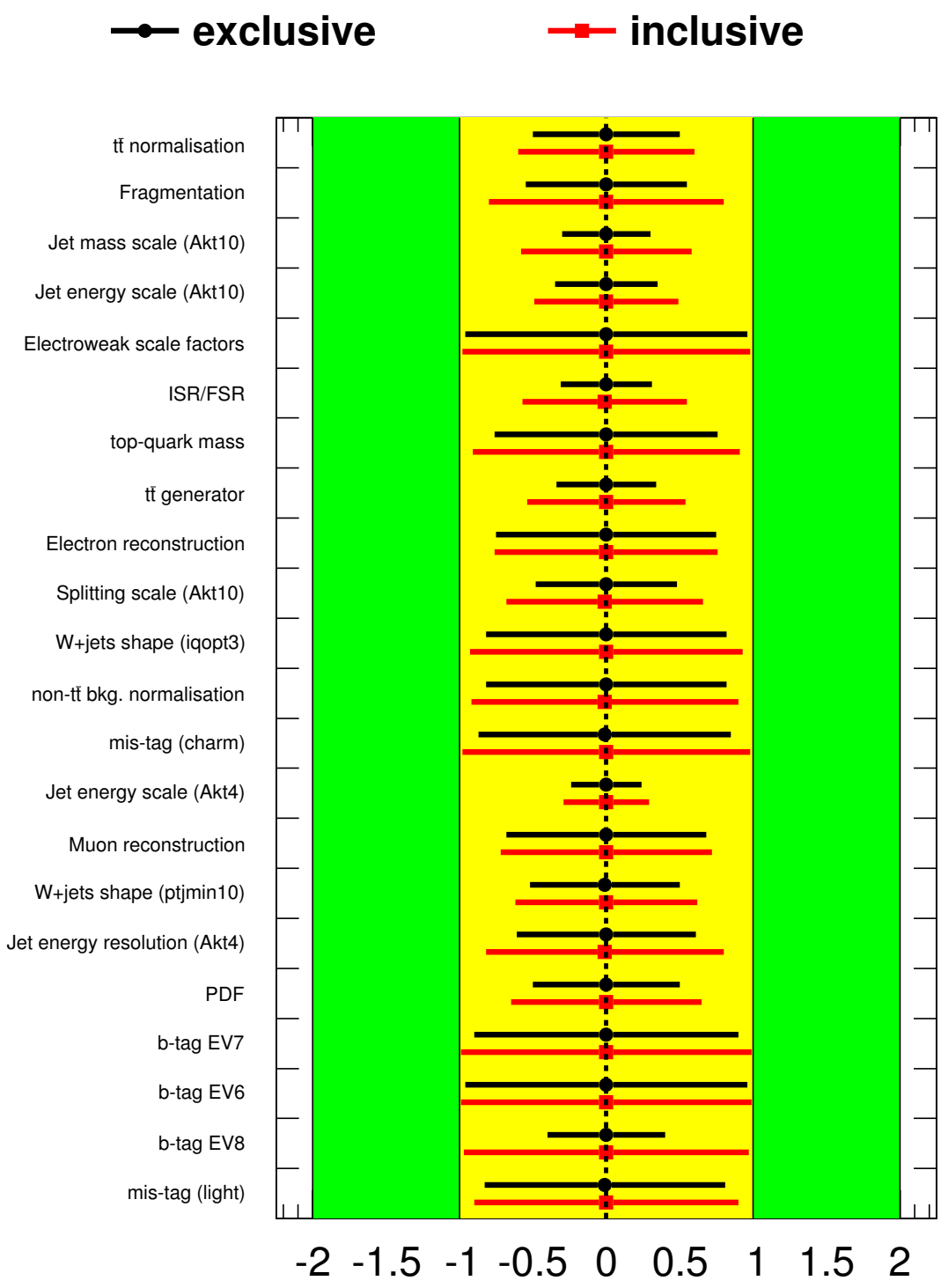

Figure 9.6: Distribution of the nuisance parameters obtained from the profile likelihood fit of the Asimov data set in the boosted decay channel for an exemplary Z' mass point of 2 TeV. The nuisance parameters obtained after fitting the inclusive event sample (red markers) are compared to the nuisance parameters (black markers) that result after performing the fit in an event sample that is split according to the classification scheme "BtagCat123".

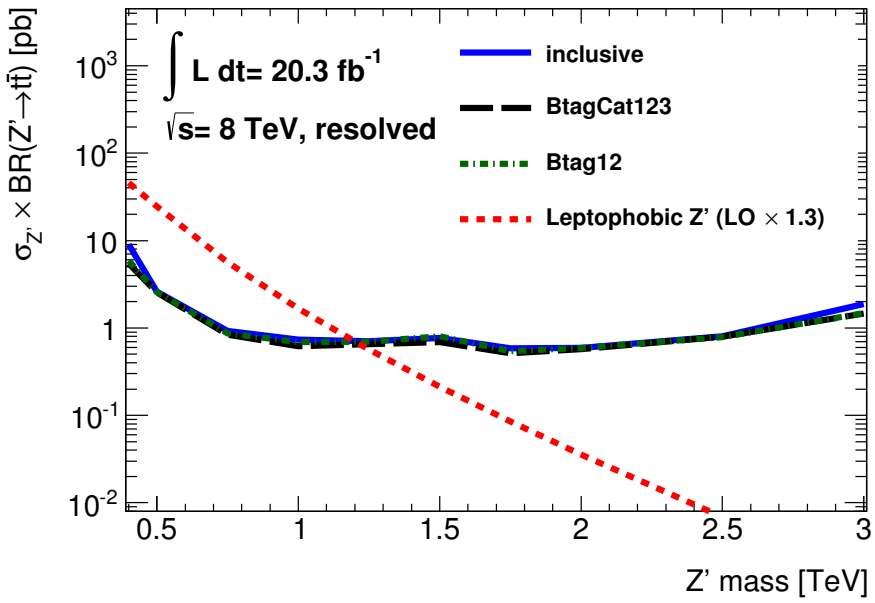

(a) Expected exclusion limits

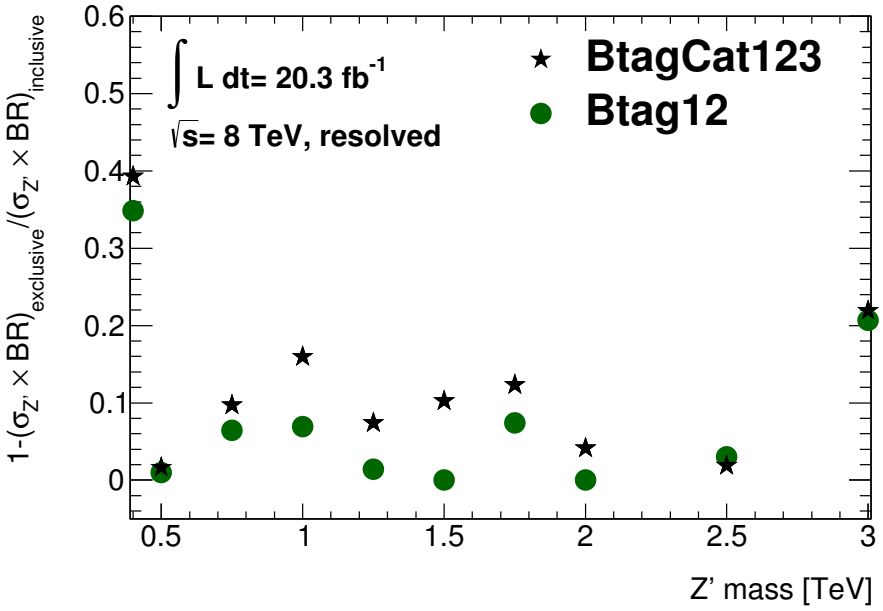

(b) Ratios

Figure 9.7: Expected exclusion limits on the production cross-section times branching ratio as a function of the leptophobic Z' mass at the 95% confidence level obtained from events that are reconstructed in the resolved event channel (a). The limits are presented for the inclusive event sample (blue solid line), but also for two different exclusive event samples (black and green dashed lines). The predicted production cross section times branching ratio for a leptophobic Z' is displayed as well. In addition, also the relative improvements with respect to the inclusive event sample are shown (b).

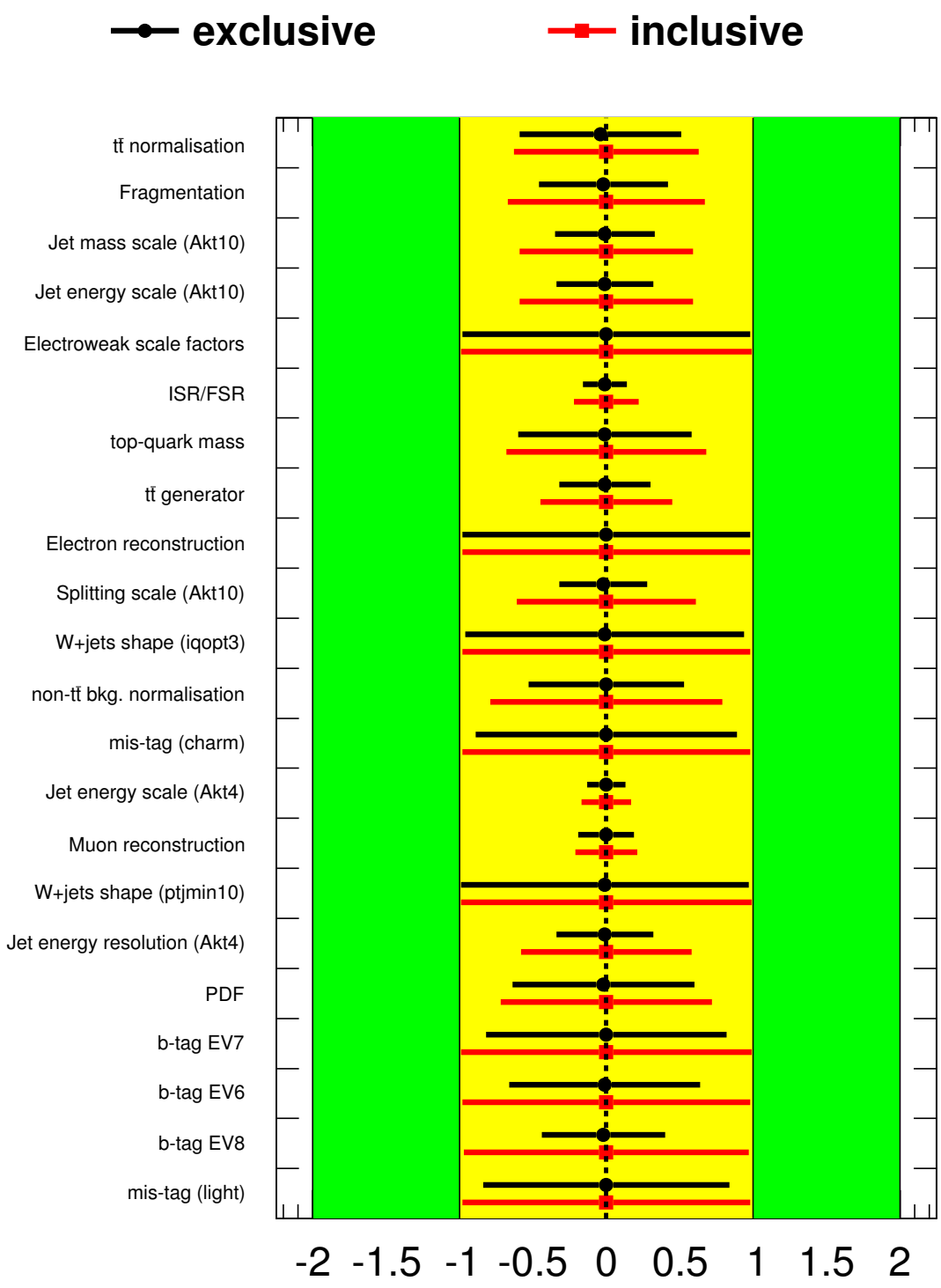

Figure 9.8: Distribution of the nuisance parameters obtained from the profile likelihood fit of the Asimov data set in the resolved decay channel for an exemplary Z' mass point of 2 TeV. The nuisance parameters obtained after fitting the inclusive event sample (red markers) are compared to the nuisance parameters (black markers) that result after performing the fit in an event sample that is split according to the classification scheme "BtagCat123".

9.3.2 Application of the MVb and MVbCharm algorithms to the search for $t\bar{t}$ resonances

In the following section, a study is presented that quantifies to what extent the expected exclusion limits on the production cross-section times branching ratio for the leptophobic Z'-boson can be improved using the combination of the MVb and MVbCharm algorithms, the MVbComb tagger, instead of MV1 in the boosted event selection. The chosen operation point of the MVbComb tagger matches an overall b-tagging efficiency of 70% (see again Section 6.4.4).

Table 9.3 lists the expected exclusion limits on the production cross-section times branching ratio for a leptophobic Z'-boson at the 95% confidence level based only on the statistical uncertainties. Limits are shown for both the case that MV1 is used in the event selection but also in case MVbComb is used. In addition, the relative improvements obtained after replacing MV1 with MVbComb are listed as well. These comparisons are performed for several Z' masses, which range from 1.75 TeV to 3.00 TeV. In this interval, the relative improvements obtained after replacing the MV1 tagger by MVbComb vary between 0.5% (for the lowest mass point) to 4.1% (for the mass point corresponding to 3.00 TeV). In case the full list of systematic uncertainties are taken into account, the improvements are further reduced and become negligible.

Z' mass point	1.75 TeV	2.00 TeV	2.50 TeV	3.00 TeV
Expected exclusion limits (MV1)	0.0369	0.0279	0.0198	0.0147
Expected exclusion limits (MVbComb)	0.0367	0.0272	0.0193	0.0141
Relative improvements [%]	0.5	2.5	2.5	4.1

Table 9.3: Expected exclusion limits on the production cross-section times branching ratio for a leptophobic Z'-boson at the 95% confidence level obtained after taking only the statistical uncertainties into account. The limit setting procedure is applied to the inclusive event sample of the boosted candidate events. Results for mass points between 1.75 TeV and 3.00 TeV are shown. The limits are listed for the case that the MV1 algorithm is used in the analysis but also for the case that the MVbComb tagger is used. The relative improvements obtained after replacing MV1 with MVbComb are also contained.

In order to obtain a better understanding why the expected exclusion limits are only slightly improved using MVbComb instead of MV1, the selection efficiencies corresponding to the b-tagging requirement in the boosted decay channel are studied as a function of the reconstructed invariant mass of the $t\bar{t}$ candidates separately for events from the sum of the various $Z' \rightarrow t\bar{t}$ samples, for events from the SM $t\bar{t}$ production and also for the various non-$t\bar{t}$ background events (i.e. the sum of the W+jets, Z+jets, single top-quark, diboson and the non-prompt and fake lepton backgrounds). Here, the selection efficiency is defined by the number of events passing the selection and reconstruction requirements of the boosted decay channel including the b-tagging requirement divided by the number of events obtained before applying the b-tagging requirement. These comparisons are displayed in Figure 9.9 (a) for the case that the MV1 algorithm is used in the event selection, and in Figure 9.9 (b) in case that MVbComb is used instead. It can be seen that the selection efficiencies for both $Z' \rightarrow t\bar{t}$ events as well as for the SM $t\bar{t}$ production are increased significantly if the MVbComb tagger is used instead of MV1. In this case, the selection efficiencies of the sum of the various $Z' \rightarrow t\bar{t}$ samples are increased by a factor of 1.04 for invariant masses between 1.2 TeV and 1.4 TeV and up to a factor of 1.25 for the highest invariant mass bin. However, the relative improvements of the selection efficiencies of the SM $t\bar{t}$ production are very similar, while the non-$t\bar{t}$ background is also increased in this mass

regions by a factor of up to 1.1. The fact that the improvements on the selection efficiencies for both $Z' \rightarrow t\bar{t}$ and SM $t\bar{t}$ events are equally strong is the main reason for the relative small improvements on the expected exclusion limits that are seen in case the MVbComb tagger is used instead of MV1.

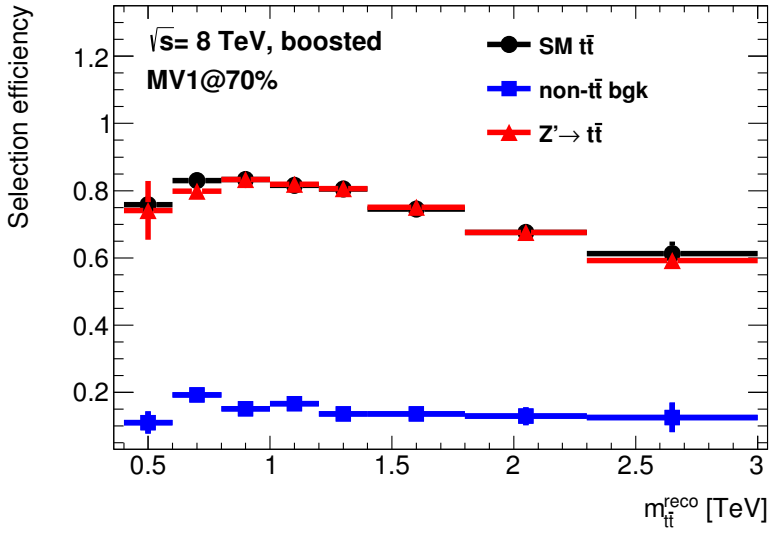

(a) Selection efficiencies based on MV1

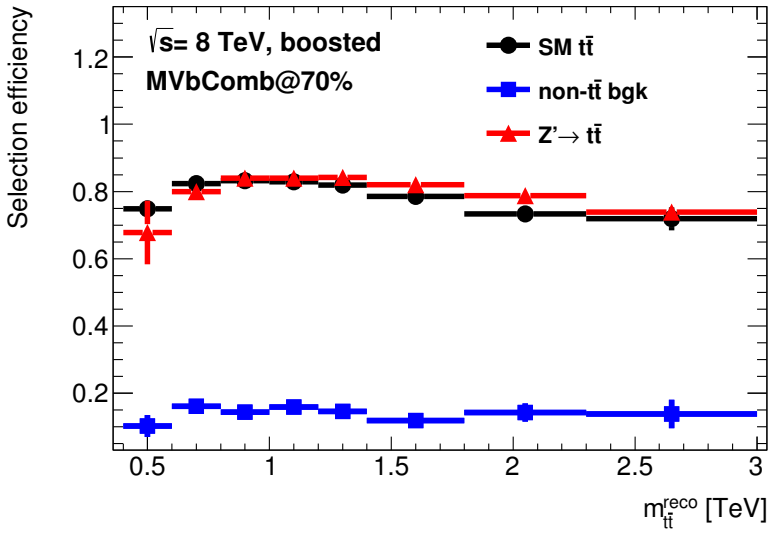

(b) Selection efficiencies based on MVb

Figure 9.9: Selection efficiencies corresponding to the b-tagging requirement as a function of the reconstructed invariant mass of the $t\bar{t}$ candidate in case the MV1 algorithm is used (a) and also in case the MVbComb algorithm is used (b). The chosen operation point for both taggers matches an overall b-tagging efficiency of 70%. The efficiencies are presented separately for events from the sum of the various $Z' \rightarrow t\bar{t}$ samples with Z' masses in a range between 0.4 TeV and 3 TeV (red line), for events from the SM $t\bar{t}$ production (black line) and also for the non-$t\bar{t}$ background events (blue line).

Chapter 10

Summary and outlook

The performance of the main ATLAS b-tagging algorithms were studied in the context of boosted $t \to bW \to bqq$ decays. It was shown that their performance is strongly degraded for such conditions, which is mainly due to an increased misalignment between the jet axis and the flight direction of the corresponding b-hadron or a contamination with additional tracks stemming from nearby light-flavour decays. The shift of the jet axis leads mainly to a loss of tracks in the track-to-jet association procedure. Thus several tracks from the b-hadron decay will not be used by the various b-tagging algorithms.

Furthermore, information at the generator level is used to identify particle jets reconstructed with the anti-k_t algorithm with a radius parameter of 0.4 containing b-quarks and at least one of the decay products of the W-boson. The properties of these jets are compared to the properties of jets having no significant overlap in order to understand which of the b-tagging related quantities are sensitive to such an overlap and which are stable. To avoid these problems, two new b-tagging algorithms, called MVb and MVbCharm, have been developed. These taggers are dedicated to boosted topologies as they compensate for the loss of separation power of several variables used in the training of the BDT. The new input quantities of the MVb and MVbCharm algorithms (e.g. the number of tracks having a d_0 significance above 1.8 or the jet width) play particularly an important role for b-tagging in boosted topologies.

The performance of these new tools are compared to that of the current ATLAS default b-tagger, for b-, c, and light-flavour jets that are obtained from either simulated dijet or $t\bar{t}$ events or also from decays of a hypothetical Kaluza-Klein gluon into top-quark pairs. It was found that the MVb tagger performs similarly well in resolved topologies and shows improvements for boosted top quark decays between 50% and 160% in terms of light-flavour rejection rate at a constant b-tagging efficiency.

Both, the MVb and MVbCharm algorithms are retrained for track jet collections that are clustered with three different distance parameters R. The small radius jets show a significantly improved performance in boosted hadronic top-quark decays, while the standard-sized jets provide a better performance in the low-p_{T} regime.

In addition, b-tagging calibration results for MVb and the current ATLAS default tagger, MV1, have been presented in the form of data-to-simulation scale factors. These scale factors are measured not only as a function of the jet p_{T} and η, but also for the first time as a function of the angular separation between the reconstructed vertex and the jet axis, $\Delta R(\mathrm{vertex}, \mathrm{jet})$, and the angular separation between the probe jet and its nearest neighbour jet ΔR^{min}, which are both quantities that are expected to be sensitive to close-by jet activity. For this purpose, a new b-tagging calibration method was developed. The measurements of the b-tagging efficiencies are based on counting the number of b-tagged jets contained in a certain phase space region in data and correcting for the expected number of b-tagged c- and light-flavour jets using information provided by simulation. These measurements are performed on a b-jet enriched jet sample, which is extracted from reconstructed top-quark pair candidates that decay into a final state of

exactly one charged lepton, missing transverse momentum and at least four jets. It was found that the resulting data-to-simulation scale factors measured as a function of the jet p_{T}, η, ΔR^{min} and $\Delta R(\mathrm{vertex}, \mathrm{jet})$ are compatible with unity considering the combined systematic and statistical uncertainties for the relevant phase space regions. For this purpose, exemplary operating points of the MVb and the MV1 algorithms were investigated that match an overall b-tagging efficiency of 70%. The combined statistical and systematic uncertainties on the scale factors that are measured with this new approach are significantly smaller (by a factor of around 2) relative to those of the current default b-tagging calibration technique (the dilepton combinatorial likelihood method) for jets with a p_{T} above 200 GeV. In addition, the p_{T} range up to which the calibration of b-jets is accessible, was extended up to 500 GeV by this method.

Another part of this thesis was dedicated to improve the sensitivity to search for heavy particles decaying into top-quark pairs. This was approached by connecting the topology of the reconstructed $t\bar{t}$ candidate events in both the boosted and the resolved decay channel and the b-tagged jets contained in the particular events. These studies suggest an event classification scheme that categorises the selected $t\bar{t}$ candidates depending on whether a b-tagged jet is associated to the reconstructed leptonic or (and) hadronic top-quark decays or not. The main advantages of such an event categorisation are due to a profiling of e.g. the b-tagging uncertainties during the calculation of the exclusion limits, a better signal-to-background ratio in some of these categories and a reduction of incorrectly reconstructed $t\bar{t}$ decays and thus an improved mass resolution in certain categories. Using this event classification scheme, the expected exclusion limits on the production cross section times branching ratio for a leptophobic Z are improved by 10% to 65% (5% to 25%) for Z' masses in a range between 0.4 TeV to 3 TeV using events reconstructed in the boosted (resolved) decay channel.

The application of the new developed MVb and MVbCharm algorithms led only to relative small improvements (which vary between 0.5% and 4.1% in the high mass region) on the expected exclusion limits, as the relative increase of the selection efficiencies for signal events and the SM $t\bar{t}$ production, the main background, are in the same order of magnitude, while also a small increase of the selected number of W+jets background events is predicted.

However, the use of the MVb and MVbCharm algorithms could still be beneficial for $t\bar{t}$ resonance searches, in case that the b-tagging related information are linked to more sophisticated top-tagging procedures, in order to further suppress non-$t\bar{t}$ based backgrounds, like W+jets, which become particularly important in the high-$m_{t\bar{t}}$ region.

Further improvements in the reconstruction of boosted $t\bar{t}$ candidate events might be achieved in case that the b-jet candidate, corresponding to the leptonic top-quark decay, is defined as the jet with the largest MVb (or MV1) output weight, instead of the jet with the largest p_{T}. In order to apply such a procedure to the data, a continuous calibration of b-tagging algorithms has to be available, which will probably be the case for Run II analysis. The main problems for b-tagging in the dense environments of a boosted hadronic top-quark decay are caused by a merging of two or more partons into one single jet and the fact that this jet does not sufficiently describe the flight direction of the b-hadrons. Thus it might be more appropriate to use jets with small-R parameters for the purpose of b-tagging in high-p_{T} top-quark decays, as these jets are better suited to resolve the partonic structure of the corresponding event topologies and as they provide a better alignment to the initial b-hadrons. However, the performance of these small-R jets is strongly degraded for low- and even medium-p_{T} jets. A promising approach to overcome this conflict is based on the use of jets, which are clustered with a variable, p_{T} dependent, distance parameter R [157]. The general idea for variable-R jets was introduced for the first time in Reference [158].

Bibliography

[1] L. Evans et al., *LHC Machine*, *JINST* **3** (2008) S08001.

[2] C. T. Hill , *Topcolor assisted technicolor*, *Phys. Lett.* **B345** (1995) 483–489, [arXiv:hep-ph/9411426].

[3] L. Randall et al., *A Large mass hierarchy from a small extra dimension*, *Phys. Rev. Lett.* **83** (1999) 3370–3373, [arXiv:hep-ph/9905221].

[4] W. Beenakker, et al., *Stop production at hadron colliders*, *Nucl. Phys.* **B515** (1998) 3–14, [arXiv:hep-ph/9710451].

[5] W. Beenakker, et al., *Supersymmetric top and bottom squark production at hadron colliders*, *JHEP* **1008** (2010) 098, [arXiv:1006.4771].

[6] G.C. Branco, et al., *Theory and phenomenology of two-Higgs-doublet models*, *Phys. Rept.* **516** (2012) 1–102, [arXiv:1106.0034].

[7] ATLAS Collaboration, *b-tagging in dense environments*, *ATL-PHYS-PUB-2014-013,* https://cds.cern.ch/record/1750682.

[8] ATLAS Collaboration, *Flavor Tagging with Track Jets in Boosted Topologies with the ATLAS Detector*, *ATL-PHYS-PUB-2014-013,* https://cds.cern.ch/record/1750681.

[9] ATLAS Collaboration, *Calibration of ATLAS b-tagging algorithms in dense jet environments*, *ATLAS-CONF-2016-001,* https://cds.cern.ch/record/2127958.

[10] A. Zee, *Quantum Field Theory in a Nutshell*. Princeton University Press, Princeton, 2010.

[11] G. Bernardi et al., *Higgs bosons: theory and searches* , *Reviews of Particle Data Group: Hypothetical particles and Concepts,* http://pdg.lbl.gov/2008/reviews/higgs_s055.pdf (2007).

[12] Particle Data Group, *Review of Particle Physics (RPP)*, *Phys. Rev.* **D86** (2012) 010001.

[13] ATLAS Collaboration, CDF Collaboration, CMS Collaboration and D0 Collaboration, *First combination of Tevatron and LHC measurements of the top-quark mass*, .

[14] D. J. Gross, *Twenty Five Years of Asymptotic Freedom*, *Nuclear Physics B - Proceedings Supplements 74* (1998) [arXiv:hep-th/9809060].

[15] N. Cabibbo, *Unitary Symmetry and Leptonic Decays*, *Phys. Rev. Lett.* **10** (Jun, 1963) 531–533.

[16] M. Kobayashi et al., *CP-Violation in the Renormalizable Theory of Weak Interaction*, *Progress of Theoretical Physics* **49** (1973) 652–657.

[17] Particle Data Group, *Review of Particles Physics: The CKM Quark-Mixing Matrix*, *Phys. Rev.* **D80** (2012) 010001.

[18] K2K Collaboration, *Measurement of Neutrino Oscillation by the K2K Experiment*, *Phys.Rev.* **D74** (2006) 072003, [hep-ex/0606032].

[19] A. Salam et al., *On a gauge theory of elementary interactions*, *Nuovo Cim.* **19** (1961) 165–170.

[20] S. E. Collaboration, *Precision measurement of the weak mixing angle in Moller scattering*, *Phys.Rev.Lett.* **95** (2005) 081601, [hep-ex/0504049].

[21] ATLAS Collaboration, *Observation of a new particle in the search for the Standard Model Higgs boson with the ATLAS detector at the LHC*, *Phys.Lett.* **B716** (2012) 1–29, [arXiv:1207.7214].

[22] CMS Collaboration, *Observation of a new boson at a mass of 125 GeV with the CMS experiment at the LHC*, *Phys.Lett.* **B716** (2012) 30–61, [arXiv:1207.7235].

[23] CDF Collaboration, *The CDF-II detector: Technical design report*, .

[24] D0 Collaboration, *The D0 Detector*, *Nucl.Instrum.Meth.* **A338** (1994) 185–253.

[25] C. Campagnari et al., *The Discovery of the top quark*, *Rev.Mod.Phys.* **69** (1997) 137–212, [hep-ex/9608003].

[26] ATLAS Collaboration, *Measurement of the top-quark mass in the fully hadronic decay channel from ATLAS data at* $\sqrt{s} = 7$ *TeV*, [arXiv:1409.0832].

[27] ATLAS Collaboration, *Measurement of the top quark charge in pp collisions at* $\sqrt{s} = 7$ *TeV with the ATLAS detector*, *JHEP* **1311** (2013) 031, [arXiv:1307.4568].

[28] ATLAS Collaboration, *Measurement of the* $t\bar{t}$ *production cross-section using* $e\mu$ *events with b-tagged jets in pp collisions at* $\sqrt{s} = 7$ *and 8 TeV with the ATLAS detector*, *Eur. Phys. J.* **C74** (2014) 3109, [arXiv:1406.5375].

[29] ATLAS Collaboration, *Measurement of Top Quark Polarization in Top-Antitop Events from Proton-Proton Collisions at* $\sqrt{s} = 7$*TeV using the ATLAS Detector*, *Phys.Rev.Lett.* **111** (2013) 232002, [arXiv:1307.6511].

[30] ATLAS Collaboration, *Measurements of spin correlation in top-antitop quark events from proton-proton collisions at* $\sqrt{s} = 7$ *TeV using the ATLAS detector*, [arXiv:1407.4314].

[31] F.P. Schilling, *Top Quark Physics at the LHC: A Review of the First Two Years*, *Int.J.Mod.Phys.* **A27** (2012) 1230016, [arXiv:1206.4484].

[32] W. Wagner, *Top quark physics in hadron collisions*, *Rept.Prog.Phys.* **68** (2005) 2409–2494, [arXiv:hep-ph/0507207].

[33] H. L. Lai et al., *New parton distributions for collider physics*, *Phys. Rev.* **D82** (2010) 074024, [arXiv:1007.2241].

[34] H. Lacker et al., *HATHOR: HAdronic Top and Heavy quarks crOss section calculatoR*, *Comput.Phys.Commun.* **182** (2011) 1034–1046, [arXiv:1007.1327].

[35] M. Beneke et al., *Hadronic top-quark pair production with NNLL threshold resummation*, *Nucl.Phys.* **B855** (2012) 695–741, [arXiv:1109.1536].

[36] ATLAS collaboration, *A search for $t\bar{t}$ resonances using lepton plus jets events in proton-proton collisions at $\sqrt{s}$ = 8 TeV with the ATLAS detector*, *JHEP* **08** (2015) 148, [arXiv:1505.0701].

[37] C. T. Hill, *Topcolor: Top quark condensation in a gauge extension of the standard model*, *Phys.Lett.* **B266** (1991) 419–424.

[38] R. Harris, et al., *Cross Section for Topcolor Z' decaying to top-antitop*, [hep-ph/9911288].

[39] M. Gogberashvili, *Four dimensionality in noncompact Kaluza-Klein model*, *Mod.Phys.Lett.* **A14** (1999) 2025–2032, [hep-ph/9904383].

[40] K. Agashe et al., *Warped Gravitons at the LHC and Beyond*, *Phys.Rev.* **D76** (2007) 036006, [hep-ph/0701186].

[41] A. D. Sakharov, *Violation of CP Invariance, c Asymmetry, and Baryon Asymmetry of the Universe*, *Pisma Zh.Eksp.Teor.Fiz.* **5** (1967) 32–35.

[42] ATLAS Collaboration, *The ATLAS Experiment at the CERN Large Hadron Collider*, *JINST* **3** (2008) S08003.

[43] ATLAS Collaboration, *Evidence for the spin-0 nature of the Higgs boson using ATLAS data*, *Phys.Lett.* **B726** (2013) 120–144, [arXiv:1307.1432].

[44] ATLAS Collaboration, *Expected Performance of the ATLAS Experiment - Detector, Trigger and Physics*, [arXiv:0901.0512].

[45] CMS Collaboration, *The CMS experiment at the CERN LHC*, *JINST* **3** (2008) S08004.

[46] LHCb Collaboration, *The LHCb Detector at the LHC*, *JINST* **3** (2008) S08005.

[47] ALICE Collaboration, *The ALICE experiment at the CERN LHC*, *JINST* **3** (2008) S08002.

[48] J. Montano, et al., *Design upgrade of the ISOLDE target unit for HIE-ISOLDE*, *Nucl.Instrum.Meth.* **B317** (2013) 430–433.

[49] C. Lefvre, *The CERN accelerator complex. Complexe des acclrateurs du CERN*, http://cds.cern.ch/record/1260465.

[50] J. Pinfold, *The MoEDAL Experiment at the LHC*, *EPJ Web Conf.* **71** (2014) 00111.

[51] TOTEM Collaboration, *The TOTEM experiment at the CERN Large Hadron Collider*, *JINST* **3** (2008) S08007.

[52] LHCf Collaboration, *Technical design report of the LHCf experiment: Measurement of photons and neutral pions in the very forward region of LHC*, .

[53] M. Bajko et al., *Report of the Task Force on the Incident of 19th September 2008 at the LHC*, tech. rep.

[54] ATLAS Collaboration, *Improved luminosity determination in pp collisions at $\sqrt{s}$ = 7 TeV using the ATLAS detector at the LHC*, *Eur. Phys. J.* **C73** (2013) 2518, [arXiv:1302.4393].

[55] CERN Photolab, "Computer generated image of the whole ATLAS detector." http://cdsweb.cern.ch/record/1095924, 2010.

[56] ATLAS Collaboration, *Alignment of the ATLAS Inner Detector Tracking System with 2010 LHC proton-proton collisions at $\sqrt{s}$ = 7 TeV*, *ATLAS-CONF-2011-012,* http://cds.cern.ch/record/1334582.

[57] ATLAS Collaboration, *Monitoring and data quality assessment of the ATLAS liquid argon calorimeter*, *JINST* **9** (2014) P07024, [arXiv:1405.3768].

[58] C. Oleari, *The POWHEG-BOX*, *Nucl.Phys.Proc.Suppl.* **205-206** (2010) 36–41, [arXiv:1007.3893].

[59] S. Frixione et al., *The MC@NLO 4.0 Event Generator*, [arXiv:1010.0819].

[60] M. L. Mangano et al., *ALPGEN, a generator for hard multiparton processes in hadronic collisions*, *JHEP* **0307** (2003) 001, [hep-ph/0206293].

[61] J. Alwall et al., *MadGraph 5 : Going Beyond*, *JHEP* **1106** (2011) 128, [arXiv:1106.0522].

[62] T. Sjöstrand et al., *PYTHIA 6.4 Physics and Manual*, *JHEP* **0605** (2006) 026, [arXiv:hep-ph/0603175].

[63] T. Sjöstrand et al., *A Brief Introduction to PYTHIA 8.1*, *Comput. Phys. Commun.* **178** (2008) 852–867, [arXiv:0710.3820].

[64] G. Corcella et al., *HERWIG 6.5 release note*, [arXiv:hep-ph/0210213].

[65] T. Gleisberg et al., *Event generation with SHERPA 1.1*, *JHEP* **0902** (2009) 007, [arXiv:0811.4622].

[66] B. Andersson et al., *Parton Fragmentation and String Dynamics*, *Phys.Rept.* **97** (1983) 31–145.

[67] J. C. Winter et al., *A Modified cluster hadronization model*, *Eur. Phys. J.* **C36** (2004) 381–395, [hep-ph/0311085].

[68] ATLAS Collaboration, *The ATLAS Simulation Infrastructure*, *Eur. Phys. J.* **C70** (2010) 823–874, [arXiv:1005.4568].

[69] GEANT4 Collaboration, *GEANT4: A Simulation toolkit*, *Nucl. Instrum. Meth.* **A506** (2003) 250–303.

[70] ATLAS Collaboration, *The simulation principle and performance of the ATLAS fast calorimeter simulation FastCaloSim*, *ATL-PHYS-PUB-2010-013,* http://inspirehep.net/record/1194623 (Oct, 2010).

[71] T. Cornelissen, et al., *Concepts, Design and Implementation of the ATLAS New Tracking (NEWT)*, *ATL-SOFT-PUB-2007-007,* http://cds.cern.ch/record/1020106.

[72] R. Frühwirth et al., *Data Analysis Techniques for High-Energy Physics*. Cambridge Monographs on Particle Physics, Nuclear Physics and Cosmology, 2000.

[73] ATLAS Collaboration, *Performance of primary vertex reconstruction in proton-proton collisions at $\sqrt{s}$ =7 TeV in the ATLAS experiment*, *ATLAS-CONF-2010-069,* https://cds.cern.ch/record/1281344.

[74] ATLAS Collaboration, *Characterization of Interaction-Point Beam Parameters Using the pp Event-Vertex Distribution Reconstructed in the ATLAS Detector at the LHC*, *ATLAS-CONF-2010-027,* https://cds.cern.ch/record/1277659.

[75] R. Frühwirth et al., *Adaptive Vertex Fitting*, *CMS-NOTE-2007-008,* https://cdsweb.cern.ch/record/1027031.

[76] W. Lampl et al., *Calorimeter Clustering Algorithms: Description and Performance*, *ATL-LARG-PUB-2008-002,* http://cds.cern.ch/record/1099735.

[77] ATLAS Collaboration, *Search for $t\bar{t}$ resonances in the lepton plus jets final state with ATLAS using 4.7 fb^{-1} of pp collisions at $\sqrt{s}$ = 7 TeV*, *Phys. Rev.* **D88** (2013) 012004, [arXiv:1305.2756].

[78] ATLAS Collaboration, *Electron reconstruction and identification efficiency measurements with the ATLAS detector using the 2011 LHC proton-proton collision data*, *Eur. Phys. J.* **C74** (2014) 2941, [arXiv:1404.2240].

[79] ATLAS Collaboration, *Electron efficiency measurements with the ATLAS detector using the 2012 LHC proton-proton collision data*, *ATLAS-CONF-2014-032,* https://cds.cern.ch/record/1706245.

[80] D. Adams et al., *Track reconstruction in the ATLAS Muon Spectrometer with MOORE 007*, *ATL-SOFT-2003-007,* http://cds.cern.ch/record/685500.

[81] ATLAS Collaboration, *ATLAS muon spectrometer: Technical design report*, *CERN-LHCC-97-22, ATLAS-TDR-10,* http://cds.cern.ch/record/331068.

[82] ATLAS Collaboration, *Measurement of the muon reconstruction performance of the ATLAS detector using 2011 and 2012 LHC proton-proton collision data*, *Eur. Phys. J.* **C74** (2014) 3130, [arXiv:1407.3935].

[83] D0 Collaboration, *Cone Algorithm for Jet Finding*, *D0-0904* (1989).

[84] G. C. Blazey et al., *Run II jet physics*, [hep-ex/0005012].

[85] J. Tseng et al., *Sequential recombination algorithm for jet clustering and background subtraction*, *Phys.Rev.* **D88** (2013) 014044, [arXiv:1304.1025].

[86] S. D. Ellis, et al., *Successive combination jet algorithm for hadron collisions*, *Phys.Rev.* **D48** (1993) 3160–3166, [arXiv:hep-ph/9305266].

[87] Y. L. Dokshitzer et al., *Better jet clustering algorithms*, *JHEP* **9708** (1997) 001, [arXiv:hep-ph/9707323].

[88] G. S. Salam et al., *The Anti-k_t jet clustering algorithm*, *JHEP* **0804** (2008) 063, [arXiv:0802.1189].

[89] G. P. Salam et al., *FastJet User Manual*, *Eur. Phys. J.* **C72** (2012) 1896, [arXiv:1111.6097].

[90] ATLAS Collaboration, *Jet energy measurement with the ATLAS detector in proton-proton collisions at* $\sqrt{s}$ = 7 *TeV*, *Eur. Phys. J.* **C73** (2013) 2304, [arXiv:1112.6426].

[91] ATLAS Collaboration, *Performance of large-R jets and jet substructure reconstruction with the ATLAS detector*, *ATLAS-CONF-2012-065,* https://cds.cern.ch/record/1459530.

[92] ATLAS Collaboration, *Pile-up subtraction and suppression for jets in ATLAS*, *ATLAS-CONF-2013-083,* https://cds.cern.ch/record/1570994.

[93] ATLAS Collaboration, *Jet energy scale and its systematic uncertainty in proton-proton collisions at* $\sqrt{(}s)$ = 7 *TeV with ATLAS 2011 data*, *ATLAS-CONF-2013-004,* https://cds.cern.ch/record/1509552.

[94] ATLAS Collaboration, *Jet energy measurement and its systematic uncertainty in proton-proton collisions at* $\sqrt{s}$ = 7 *TeV with the ATLAS detector*, *Eur. Phys. J.* **C75** (2015) 17, [arXiv:1406.0076].

[95] ATLAS Collaboration, *Jet energy resolution and selection efficiency relative to track jets from in-situ techniques with the ATLAS Detector Using Proton-Proton Collisions at a Center of Mass Energy* $\sqrt{s}$ = 7 *TeV*, *ATLAS-CONF-2010-054,* https://cdsweb.cern.ch/record/1281311.

[96] ATLAS Collaboration, *ATLAS measurements of the properties of jets for boosted particle searches*, *Phys. Rev. D* **86** (Oct, 2012) 072006.

[97] ATLAS Collaboration, *Jet mass and substructure of inclusive jets in* $\sqrt{s}$ = 7 *TeV pp collisions with the ATLAS experiment*, *JHEP* **1205** (2012) 128, [arXiv:1203.4606].

[98] T. Plehn et al., *Top Tagging*, *J.Phys.* **G39** (2012) 083001, [arXiv:1112.4441].

[99] S. Schaetzel et al., *Tagging highly boosted top quarks*, *Phys.Rev.* **D89** (2014) 014007, [arXiv:1308.0540].

[100] S. D. Ellis, et al., *Techniques for improved heavy particle searches with jet substructure*, *Phys.Rev.* **D80** (2009) 051501, [arXiv:0903.5081].

[101] D. Krohn et al., *Jet Trimming*, *JHEP* **1002** (2010) 084, [arXiv:0912.1342].

[102] ATLAS Collaboration, *Performance of Impact Parameter-Based b-tagging Algorithms with the ATLAS Detector using Proton-Proton Collisions at* $\sqrt{s}$ = 7 *TeV*, *ATLAS-CONF-2010-091,* https://cds.cern.ch/record/1277681.

[103] ATLAS Collaboration, *Performance of the ATLAS Secondary Vertex b-tagging Algorithm in 7 TeV Collision Data*, *ATLAS-CONF-2010-042,* https://cds.cern.ch/record/1277682.

[104] ATLAS Collaboration, *Commissioning of the ATLAS high-performance b-tagging algorithms in the* 7 TeV *collision data*, *ATLAS-CONF-2011-102,* https://cds.cern.ch/record/1369219.

[105] ATLAS Collaboration, *Calibration of the performance of b-tagging for c- and light-flavour jets in the 2012 ATLAS data*, *ATLAS-CONF-2014-046,* https://cds.cern.ch/record/1741020.

[106] G. Piacquadio and C. Weiser, *A new inclusive secondary vertex algorithm for b-jet tagging in ATLAS*, *J. Phys. Conf. Ser.* **119** (2008) 032032.

[107] ATLAS Collaboration, *Performance of b-Jet Identification in the ATLAS Experiment*, *JINST* **11** (2016), no. 04 P04008, [arXiv:1512.0109].

[108] ATLAS Collaboration, *Measurement of the Mistag Rate with 5 fb^{-1} of Data Collected by the ATLAS Detector*, *ATLAS-CONF-2012-040,* https://cds.cern.ch/record/1435194.

[109] ATLAS Collaboration, *Measurement of the b-tag Efficiency in a Sample of Jets Containing Muons with 5 fb^{-1} of Data from the ATLAS Detector*, *ATLAS-CONF-2012-043,* https://cds.cern.ch/record/1435197.

[110] ATLAS Collaboration, *Calibration of b-tagging using dileptonic top pair events in a combinatorial likelihood approach with the ATLAS experiment*, *ATLAS-CONF-2014-004,* https://cds.cern.ch/record/1664335.

[111] T. Chwalek, *Measurement of W-boson helicity fractions in top quark decays with the CDF II experiment and prospects for an early ttbar cross-section measurement with the CMS experiment*. PhD thesis, Karlsruhe U., Karlsruhe, 2010. Presented 12 Feb 2010.

[112] S. Frixione et al., *Matching NLO QCD computations with Parton Shower simulations: the POWHEG method*, *JHEP* **0711** (2007) 070, [arXiv:0709.2092].

[113] P. Zeiler et al., *Tuning Monte Carlo Generators: The Perugia Tunes*, *Phys. Rev.* **D82** (2010) 074018, [arXiv:1005.3457].

[114] J.H. Butterworth et al., *Multiparton interactions in photoproduction at HERA*, *Z. Phys.* **C72** (1996) 637–646, [arXiv:hep-ph/9601371].

[115] B. P. Kersevan et al., *The Monte Carlo event generator AcerMC versions 2.0 to 3.8 with interfaces to PYTHIA 6.4, HERWIG 6.5 and ARIADNE 4.1*, *Comput. Phys. Commun.* **184** (2013) 919–985, [hep-ph/0405247].

[116] ATLAS Collaboration, *Measurement of $t\bar{t}$ production with a veto on additional central jet activity in pp collisions at $\sqrt{s}$ = 7 TeV using the ATLAS detector*, *Eur. Phys. J.* **C72** (2012) 2043, [arXiv:1203.5015].

[117] ATLAS Collaboration, *Monte Carlo generator comparisons to ATLAS measurements constraining QCD radiation in top anti-top final states*, *ATL-PHYS-PUB-2013-005,* https://cds.cern.ch/record/1532067.

[118] J. Pumplin et al., *New generation of parton distributions with uncertainties from global QCD analysis*, *JHEP* **0207** (2002) 012, [hep-ph/0201195].

[119] J. M. Campbell et al., *$t\bar{t}W^{\pm}$ production and decay at NLO*, *JHEP* **1207** (2012) 052, [arXiv:1204.5678].

[120] M. V. Garzelli, *$t\bar{t}\,W^{\pm}$ and $t\bar{t}\,Z$ Hadroproduction at NLO accuracy in QCD with Parton Shower and Hadronization effects*, *JHEP* **1211** (2012) 056, [arXiv:1208.2665].

[121] S. Frixione et a., *Single-top production in MC@NLO*, *JHEP* **03** (2006) 092, [hep-ph/0512250].

[122] N. Kidonakis, *Differential and total cross sections for top pair and single top production*, [arXiv:1205.3453].

[123] M. Czakon et al., *Top++: A Program for the Calculation of the Top-Pair Cross-Section at Hadron Colliders*, *Comput.Phys.Commun.* **185** (2011) 2930, [arXiv:1112.5675].

[124] M. Czakon et al., *Top-pair production at hadron colliders with next-to-next-to-leading logarithmic soft-gluon resummation*, *Phys. Lett.* **B710** (2012) 612–622, [arXiv:1111.5869].

[125] M. Czakon et al., *The total top quark pair production cross-section at hadron colliders through $O(\alpha_S^4)$*, *Phys. Rev. Lett.* **110** (2013) 252004, [arXiv:1303.6254].

[126] M. Czakon et al., *NNLO corrections to top pair production at hadron colliders: the quark-gluon reaction*, *JHEP* **1301** (2013) 080, [arXiv:1210.6832].

[127] J. Alwall et al., *Comparative study of various algorithms for the merging of parton showers and matrix elements in hadronic collisions*, *Eur. Phys. J.* **C53** (2008) 473–500, [arXiv:0706.2569].

[128] ATLAS Collaboration, *Study of heavy-flavor quarks produced in association with top-quark pairs at $\sqrt{s} = 7$TeV using the ATLAS detector*, *Phys. Rev.* **D89** (2014) 072012, [arXiv:1304.6386].

[129] ATLAS Collaboration, *Measurement of the top quark-pair production cross section in pp collisions at $\sqrt{s} = 7$ TeV*, *Eur. Phy. J.* **C71** (2011) 1577.

[130] R. Gavin et al., *W Physics at the LHC with FEWZ 2.1*, *Comput. Phys. Commun.* **184** (2013) 208–214, [arXiv:1201.5896].

[131] ATLAS Collaboration, *Summary of ATLAS Pythia 8 tunes*, *ATL-PHYS-PUB-2012-003,* http://cds.cern.ch/record/1474107.

[132] R. M. Harris, et al., *Cross Sections for Leptophobic Topcolor Z' Decaying to Top-Antitop*, *Eur. Phys. J.* **C72** (2012) 2072, [arXiv:1112.4928].

[133] A. D. Martin et al., *Parton distributions for the LHC*, *Eur. Phys. J.* **C63** (2009) 189–285, [arXiv:0901.0002].

[134] J. Gao et al., *Next-to-leading order QCD corrections to the heavy resonance production and decay into top quark pair at the LHC*, *Phys.Rev.* **D82** (2010) 014020, [arXiv:1004.0876].

[135] B. Lillie et al., *The Bulk RS KK-gluon at the LHC*, *JHEP* **0709** (2007) 074, [hep-ph/0701166].

[136] D. Dicus et al., *Higgs decay to top quarks at hadron colliders*, *Phys. Lett.* **B333** (1994) 126–131, [hep-ph/9404359].

[137] J. Alwall et al., *The automated computation of tree-level and next-to-leading order differential cross sections, and their matching to parton shower simulations*, *JHEP* **07** (2014) 079, [arXiv:1405.0301].

[138] M. Botje et al., *The PDF4LHC Working Group Interim Recommendations*, [arXiv:1101.0538].

[139] R. D. Ball et al., *Parton distributions with LHC data*, *Nucl.Phys.* **B867** (2013) 244–289, [arXiv:1207.1303].

[140] ATLAS Collaboration, *Estimation of non-prompt and fake lepton backgrounds in final states with top quarks produced in proton-proton collisions at* $\sqrt{s} = 8$ *TeV with the ATLAS detector*, *ATLAS-CONF-2014-058,* http://cds.cern.ch/record/1951336 .

[141] V. A. Khoze, et al., *Proceedings, Conference on High-Energy Physics, Tbilisi 1976*, *Phys. Rev. D17* (1978) 171.

[142] Y. Freund et al., *Proceedings, Conference on High-Energy Physics, Tbilisi 1976*, *Proc COLT, 209-217, ACM Press, New York* (1996).

[143] A. Hoecker, et al., *TMVA - Toolkit for Multivariate Data Analysis*, *PoS* **ACAT** (2007) 040, [arXiv:physics/0703039].

[144] J. Friedman, et al., *Classification and Regression Trees*. Chapman & Hall, New York, 1984.

[145] ATLAS Collaboration, *Measuring the b-tag efficiency in a top-pair sample with 4.7* fb^{-1} *of data from the ATLAS detector*, *ATLAS-CONF-2012-097,* https://cds.cern.ch/record/1460443.

[146] ATLAS Collaboration, *Differential top-antitop cross-section measurements as a function of observables constructed from final-state particles using pp collisions at* $\sqrt{s} = 7$ *TeV in the ATLAS detector*, *JHEP* **06** (2015) 100, [arXiv:1502.0592].

[147] CDF Collaboration, *Search for Resonant Top-Antitop Production in the Lepton Plus Jets Decay Mode Using the Full CDF Data Set*, *Phys.Rev.Lett.* **110** (2013) 121802, [arXiv:1211.5363].

[148] ATLAS Collaboration, *A search for* $t\bar{t}$ *resonances in lepton+jets events with highly boosted top quarks collected in* pp *collisions at* $\sqrt{s} = 7$ *TeV with the ATLAS detector*, *JHEP* **1209** (2012) 041, [arXiv:1207.2409].

[149] ATLAS Collaboration, *A search for* $t\bar{t}$ *resonances in the lepton plus jets final state with ATLAS using 14* fb^1 *of pp collisions at* $\sqrt{s} = 8$ *TeV*, *ATLAS-CONF-2013-052,* http://cds.cern.ch/record/1547568.

[150] J. H. Kühn et al., *Weak Interactions in Top-Quark Pair Production at Hadron Colliders: An Update*, [arXiv:1305.5773].

[151] J. H. Kühn et al., *Electroweak corrections to top-quark pair production in quark-antiquark annihilation*, *Eur. Phys. J.* **C45** (2006) 139–150, [hep-ph/0508092].

[152] J. H. Kühn et al., *Electroweak effects in top-quark pair production at hadron colliders*, *Eur. Phys. J.* **C51** (2007) 37–53, [hep-ph/0610335].

[153] A. Horoshilov, *A search for $t\bar{t}$ resonances in the lepton plus jets final state at ATLAS using exclusive systematic study for events with different number of b-tagged jets*. PhD thesis, Bergische Universitaet Wuppertal, Wuppertal, 2015. To be published.

[154] CMS Collaboration, *Search for ttbar resonances in semileptonic final state*, *CMS-PAS-B2G-12-006,*https://cds.cern.ch/record/1543467.

[155] M. Baak et al., *HistFitter software framework for statistical data analysis*, arXiv:1410.1280.

[156] G. Cowan, *Asymptotic formulae for likelihood-based tests of new physics*, *Eur. Phys. J.* **C71** (2011) 1554, [arXiv:1007.1727].

[157] J. K. Behr, *Search for New Heavy Resonances in Final States with Boosted Top-Quarks and Studies to Improve the Identification of Boosted Top-Quarks, b-Quarks and Higgs-Bosons using Variable-R jets*. PhD thesis, University of Oxford, Oxford, 2015. To be published.

[158] David Krohn et al., *Jets with Variable R*, *JHEP* **0906** (2009) 059, [arXiv:0903.0392].

Acknowledgements

First of all I would like to thank Peter Mättig for giving me the opportunity to work on a very interesting research topic and for his constant support and encouragement. I thank Frank Filthaut for agreeing to be the second referee of my PhD thesis and for supporting me during his convenership in the ATLAS flavour tagging group. Furthermore, I thank Tobias Golling for being the third referee of my PhD thesis. I thank Sebastian Fleischmann for being a brilliant supervisor (during my first three years here in Wuppertal), as he spend a lot of his time to teach me various things needed for a physics analysis.

I would like to express my gratitude to the current and some of the former flavour-tagging convenors of the ATLAS collaboration Giacinto Piacquadio, Tim Scanlon, Fabrizio Parodi and Sara Strandberg for their great support leading to awesome opportunities like presenting a poster at the PLHC conference in Vancouver or giving talks at the BOOST14 conference in London as well as at workshops in Nijmegen, Stockholm and CERN and also during an ATLAS week.

I would like to thank Dominic Hirschbühl, Simon Köhlmann, Gunar Ernis, Julia Fischer and in particular Arwa Bannoura for proofreading parts of my manuscript.

In addition, I would like to thank my current and former "roommates", who shared an office and thus a large fraction of my time here in Wupertal with me. Namely: Thorsten Boek, Markus Mechtel, Jan Küchler, Daniela Börner, Daniel Rosenbaum and Christina Czaikowski. It was really cool to work with you (and next to you).

A big thank to the whole working groups of Peter Mättig, Wolfgang Wagner and Christian Zeitnitz for a very pleasant working environment and in particular for giving me the opportunity to assimilate so quickly after my joining. I really enjoyed our daily lunch and coffee breaks as well as all kind of meetings (especially those that have involved cake, cookies or other sweets).

Last but not least I want to thank my family and friends for always supporting me in all kind of ways.

Appendix A

List of Monte Carlo samples

The Monte Carlo samples that were used for the studies presented in Chapters 8 and 9 are listed in the following section. Table A.1 presents the various Monte Carlo samples that are used to describe the number of expected $t\bar{t}$ events, their kinematic distribution and the corresponding systematical uncertainties. Lists of the various Monte Carlo samples that are used to estimate the contribution due to the associated production of a top-quark pair and a vector boson as well as the production of single top-quarks via the *s*-, *t*- or *Wt*-channels are given by Tables A.2 (a) and (b). The samples that are used to describe the production of diboson or *W*/*Z*-boson events in association with jets are listed in Tables A.3, A.4 and A.5, respectively. In addition, all tables present the according production cross sections of these processes and the *k*-factors that are used to scale these cross sections to the predictions of the next highest order.
Several of these background sources are subdivided according to the number of additional partons (NP) produced in association with the particular process. The various Monte Carlo samples that correspond to the simulated decay of a BSM particle into a top-quark pair are listed in Tables A.6, A.7 and A.8, in which also particle properties as the particular resonance mass, their width and the predicted production cross section times branching ratio are listed.

Process	Cross section [pb]	*k*-factor	MC Generators	Features
$t\bar{t}$ (leptonic)	114.49	1.1994	POWHEG + PYTHIA	hdamp= ∞
$t\bar{t}$ (hadronic)	96.346	1.1995	POWHEG + PYTHIA	hdamp= ∞
$t\bar{t}$ (leptonic)	112.94	1.2158	MC@NLO * HERWIG	
$t\bar{t}$ (leptonic)	115.56	1.1883	POWHEG + HERWIG	
$t\bar{t}$ (leptonic)	114.47	1.1996	POWHEG + PYTHIA	hdamp= m_{top}
$t\bar{t}$ (leptonic)	123.27	1.1998	POWHEG + PYTHIA	hdamp= ∞, m_{top} = 170 GeV
$t\bar{t}$ (leptonic)	106.46	1.1988	POWHEG + PYTHIA	hdamp= ∞, m_{top} = 170 GeV
$t\bar{t}$ (leptonic)	59.624	2.3031	ACERMC+PYTHIA	
$t\bar{t}$ (leptonic)	59.622	2.3032	ACERMC+PYTHIA	
$t\bar{t}$ (leptonic)	0.61653	1.1995	POWHEG + PYTHIA	hdamp= m_{top}, 1.1 TeV < $m_{t\bar{t}} \leq$ 1.3 TeV
$t\bar{t}$ (leptonic)	0.21613	1.1995	POWHEG + PYTHIA	hdamp= m_{top}, 1.3 TeV < $m_{t\bar{t}} \leq$ 1.5 TeV
$t\bar{t}$ (leptonic)	0.081813	1.1995	POWHEG + PYTHIA	hdamp= m_{top}, 1.5 TeV < $m_{t\bar{t}} \leq$ 1.7 TeV
$t\bar{t}$ (leptonic)	0.041373	1.1995	POWHEG + PYTHIA	hdamp= m_{top}, 1.7 TeV < $m_{t\bar{t}} \leq$ 2.0 TeV
$t\bar{t}$ (leptonic)	0.016888	1.1995	POWHEG + PYTHIA	hdamp= m_{top}, $m_{t\bar{t}} >$ 2.0 TeV

Table A.1: List of the various $t\bar{t}$ event samples, that were used in the studies presented in Chapters 8 and 9. In addition, information corresponding the predicted production cross section, the NNLO *k*-factor and the according MC generator are given.

Process	Cross section [pb]	k-factor
$t\bar{t}$ + W + Np0 (excl.)	0.10410	1.1700
$t\bar{t}$ + W + Np1 (incl.)	0.093317	1.1700
$t\bar{t}$ + Z + Np0 (excl.)	0.067690	1.3500
$t\bar{t}$ + Z + Np1 (incl.)	0.087339	1.3500

(a) $t\bar{t} + V$

Process	Cross section [pb]	k-factor
t-channel (lept.) (top)	17.520	1.0500
t-channel (lept.) (antitop)	9.3932	1.0616
s-channel (lept.)	1.6424	1.1067
Wt-channel (incl.)	20.461	1.0933

(b) Single top-quark production

Table A.2: List of the Monte Carlo samples used to estimate the contribution due to the associated production of a top-quark pair and a vector boson (a) and single top-quarks (b), including also the production cross sections and the according k-factors. MadGraph is used to modell $t\bar{t} + V$ events, while the single top-quark production is simulated with POWHEG and PYTHIA.

Process	Cross section [pb]	k-factor
$WW \to e\nu qq$ with up to Np3	7.2790	1.0600
$WW \to \mu\nu qq$ with up to Np3	7.2776	1.0600
$WW \to \tau\nu qq$ with up to Np3	7.2756	1.0600
$ZZ \to eeqq$ with up to Np3	0.24854	1.0000
$ZZ \to \mu\mu qq$ with up to Np3	0.24747	1.0000
$ZZ \to \tau\tau qq$ with up to Np3	0.24167	1.0000
$WZ \to e\nu qq$ with up to Np3	1.9022	1.0500
$WZ \to \mu\nu qq$ with up to Np3	1.9076	1.0500
$WZ \to \tau\nu qq$ with up to Np3	1.9086	1.0500
$ZW \to eeqq$ with up to Np3	1.4622	1.0500
$ZW \to \mu\mu qq$ with up to Np3	1.4624	1.0500
$ZW \to \tau\tau qq$ with up to Np3	1.4523	1.0500

Table A.3: List of the various Monte Carlo samples used to describe the associated production of dibosons and jets. The production cross section is shown separately for each of the individual subprocesses together with the according k-factors. All these samples are generated with SHERPA.

Process	Cross section [pb]	k-factor
$W \to e\nu$ + Np0	8136.8	1.1330
$W \to e\nu$ + Np1	1791.5	1.1330
$W \to e\nu$ + Np2	541.60	1.1330
$W \to e\nu$ + Np3	146.65	1.1330
$W \to e\nu$ + Np4	37.334	1.1330
$W \to e\nu$ + Np5 (incl.)	11.355	1.1330
$W \to \mu\nu$ + Np0	8133.4	1.1330
$W \to \mu\nu$ + Np1	1792.7	1.1330
$W \to \mu\nu$ + Np2	541.27	1.1330
$W \to \mu\nu$ + Np3	146.49	1.1330
$W \to \mu\nu$ + Np4	37.341	1.1330
$W \to \mu\nu$ + Np5 (incl.)	11.364	1.1330
$W \to \tau\nu$ + Np0	8135.7	1.1330
$W \to \tau\nu$ + Np1	1793.7	1.1330
$W \to \tau\nu$ + Np2	541.24	1.1330
$W \to \tau\nu$ + Np3	146.48	1.1330
$W \to \tau\nu$ + Np4	37.344	1.1330
$W \to \tau\nu$ + Np5 (incl.)	11.477	1.1330
$W + cc$ + Np0	149.39	1.1330
$W + cc$ + Np1	143.90	1.1330
$W + cc$ + Np2	84.227	1.1330
$W + cc$ + Np3 (incl.)	44.277	1.1330
$W + c$ + Np0	758.93	1.5200
$W + c$ + Np1	274.47	1.5200
$W + c$ + Np2	71.643	1.5200
$W + c$ + Np3	16.482	1.5200
$W + c$ + Np4 (incl.)	4.7824	1.5200
$W + bb$ + Np0	52.237	1.1330
$W + bb$ + Np1	45.628	1.1330
$W + bb$ + Np2	23.955	1.1330
$W + bb$ + Np3 (incl.)	13.633	1.1330

Table A.4: List of the various Monte Carlo samples used to describe the associated production of a W-boson and jets. The production cross section is shown separately for each of the individual subprocesses together with the according k-factors. All these samples are generated with ALPGEN interfaced to PYTHIA.

Process	Cross section [pb]	k-factor
$Z \to ee$ + Np0	718.97	1.1800
$Z \to ee$ + Np1	175.70	1.1800
$Z \to ee$ + Np2	58.875	1.1800
$Z \to ee$ + Np3	15.636	1.1800
$Z \to ee$ + Np4	4.0116	1.1800
$Z \to ee$ + Np5 (incl.)	1.2592	1.1800
$Z \to \mu\mu$ + Np0	719.16	1.1800
$Z \to \mu\mu$ + Np1	175.74	1.1800
$Z \to \mu\mu$ + Np2	58.882	1.1800
$Z \to \mu\mu$ + Np3	15.673	1.1800
$Z \to \mu\mu$ + Np4	4.0057	1.1800
$Z \to \mu\mu$ + Np5 (incl.)	1.2544	1.1800
$Z \to \tau\tau$ + Np0	718.87	1.1800
$Z \to \tau\tau$ + Np1	175.76	1.1800
$Z \to \tau\tau$ + Np2	58.856	1.1800
$Z \to \tau\tau$ + Np3	15.667	1.1800
$Z \to \tau\tau$ + Np4	4.0121	1.1800
$Z \to \tau\tau$ + Np5 (incl.)	1.2560	1.1800
$Z \to ee$ + cc + Np0	11.763	1.1800
$Z \to ee$ + cc + Np1	7.1249	1.1800
$Z \to ee$ + cc + Np2	3.3656	1.1800
$Z \to ee$ + cc + Np3 (incl.)	1.7010	1.1800
$Z \to \mu\mu$ + cc + Np0	11.795	1.1800
$Z \to \mu\mu$ + cc + Np1	7.1254	1.1800
$Z \to \mu\mu$ + cc + Np2	3.3694	1.1800
$Z \to \mu\mu$ + cc + Np3 (incl.)	1.7003	1.1800
$Z \to \tau\tau$ + cc + Np0	11.760	1.1800
$Z \to \tau\tau$ + cc + Np1	7.1410	1.1800
$Z \to \tau\tau$ + cc + Np2	3.3582	1.1800
$Z \to \tau\tau$ + cc + Np3 (incl.)	1.7046	1.1800
$Z \to ee + bb$ + Np0	6.5083	1.1800
$Z \to ee + bb$ + Np1	3.2948	1.1800
$Z \to ee + bb$ + Np2	1.2546	1.1800
$Z \to ee + bb$ + Np3 (incl.)	0.61800	1.1800
$Z \to \mu\mu + bb$ + Np0	6.5056	1.1800
$Z \to \mu\mu + bb$ + Np1	3.2909	1.1800
$Z \to \mu\mu + bb$ + Np2	1.2585	1.1800
$Z \to \mu\mu + bb$ + Np3 (incl.)	0.61808	1.1800
$Z \to \tau\tau + bb$ + Np0	6.5062	1.1800
$Z \to \tau\tau + bb$ + Np1	3.2935	1.1800
$Z \to \tau\tau + bb$ + Np2	1.2485	1.1800
$Z \to \tau\tau + bb$ + Np3 (incl.)	0.61363	1.1800

Table A.5: List of the various Monte Carlo samples used to describe the associated production of a Z-boson and jets. The production cross section is shown separately for each of the individual subprocesses together with the according k-factors. All these samples are generated with ALPGEN interfaced to PYTHIA.

Resonance mass [GeV]	Width [%]	Predicted cross section times branching ratio [pb]
400	2.86	45.66
500	2.94	24.63
750	3.05	5.65
1000	3.10	1.66
1250	3.12	0.566
1500	3.14	0.213
1750	3.15	0.0853
2000	3.16	0.0357
2500	3.17	0.00687
3000	3.17	0.00147

Table A.6: List of the various Monte Carlo samples used to describe the decay of a hypothetical leptophobic Z'-boson into a top-quark pair. Each sample corresponds to a different resonance mass. The predicted production cross section times branching ratio and the width of the resonance are presented additionally. All these samples are generated using PYTHIA8.

Resonance mass [GeV]	Width [%]	Predicted cross section times branching ratio [pb]
400	2.810	1.943
500	3.674	1.342
600	4.337	0.622
700	4.799	0.2859
800	5.125	0.1368
900	5.361	0.06838
1000	5.535	0.03569
1200	5.769	0.01077
1400	5.915	0.003578
1600	6.011	0.001288
1800	6.078	0.0004936
2000	6.125	0.0001978
2500	6.199	0.00002345

Table A.7: List of the various Monte Carlo samples used to describe the decay of a hypothetical RS-graviton into a top-quark pair. Each sample corresponds to a different resonance mass. The predicted production cross section times branching ratio and the width of the resonance are presented additionally. All these samples are generated using MadGraph interfaced to PYTHIA8.

Resonance mass [GeV]	Width [%]	Predicted cross section times branching ratio [pb]
400	15.3	112.2
500	15.3	81.9
600	15.3	45.0
700	15.3	25.2
800	15.3	14.6
900	15.3	8.81
1000	10.0	3.61
	15.0	5.37
	15.3	5.47
	20.0	7.08
	25.0	8.72
	30.0	10.3
	35.0	11.7
	40.0	13.1
1150	15.3	2.82
1300	15.3	1.52
1600	15.3	0.500
1800	15.3	0.255
2000	10.0	0.080
	15.0	0.133
	15.3	0.137
	20.0	0.193
	25.0	0.257
	30.0	0.324
	35.0	0.393
	40.0	0.461
2250	15.3	0.0670
2500	15.3	0.0351
2750	15.3	0.0196
3000	10.0	0.0057
	15.0	0.0113
	15.3	0.0120
	20.0	0.0184
	25.0	0.0268
	30.0	0.0361
	35.0	0.0462
	40.0	0.0568

Table A.8: List of the various Monte Carlo samples used to describe the decay of a hypothetical KK-gluon into a top-quark pair. Each sample corresponds to a different resonance mass. The predicted production cross section times branching ratio and the width of the resonance are presented additionally. All these samples are generated using MadGraph interfaced to PYTHIA8.

Appendix B

Additional calibration results corresponding to the MVb, MVbCharm and the MVbComb taggers

The calibration results corresponding to the MVbCharm and MVbComb algorithms measured for an operation point with a b-tagging efficiency of 70% are presented in Figures B.1, B.2, B.3 and B.4 for the combined e + jets and μ + jets channel. The b-tagging efficiencies and the corresponding scale factors are measured again as a function of the jet p_{T}, the jet $|\eta|$, the ΔR between the probe jet and its nearest neighbouring jet and the angular separation between the vertex direction and the axis of the probe jet $\Delta R(\text{vertex, jet})$. For the latter case results are shown that correspond to jets including vertices reconstructed either with the iterative vertex finder or the JetFitter algorithm studying both single- and multi-track topologies. The scale factors are obtained using the same method described in Section 8 (and also in Reference [9]) and they are compatible with unity within their combined statistical and systematic uncertainties.

A summary of all the relevant systematic uncertainties on the measured scale factors corresponding to the MVbCharm and MVbComb taggers at the 70% operating point is given in Tables B.1 and B.2 separately the various p_{T}, $|\eta|$, ΔR^{min} and $\Delta R(\text{vertex, jet})$ bins. Both the magnitude and the relative importance of the individual systematic uncertainties are very similar to the results for the MVb and MV1 algorithm.

Additional measurements of b-tagging efficiencies for the MVb tagger and the corresponding calibration scale factors are presented in Figures B.5, B.6 and B.7. These results correspond to operating points with efficiencies of 60%, 80% and 85%. Figure B.5 shows these results measured as a function of the jet p_{T}, while Figure B.6 and B.7 shows these measurements as a function of the jet $|\eta|$ and the ΔR between the probe jet and its nearest neighbouring jet, respectively. Summaries on the uncertainties corresponding to these measurements are presented in the Tables B.3 and B.4.

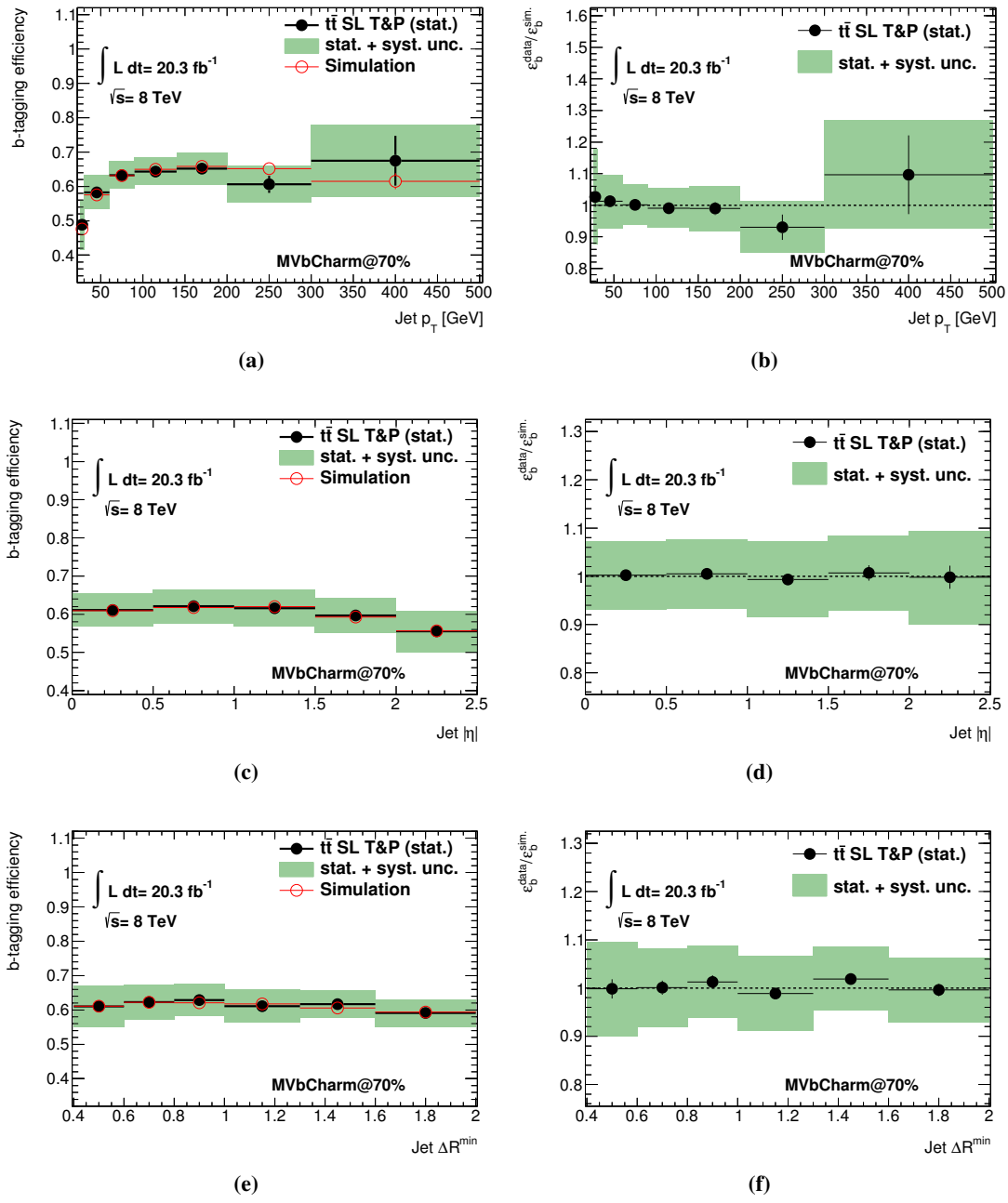

Figure B.1: The *b*-tagging efficiencies for the MVbCharm algorithm corresponding to an operating point of an overall efficiency of 70% as a function of the transverse momentum (a), the absolute pseudorapidity (c) and the ΔR^{min} (e) of the jets contained in the sample of $t\bar{t}$ single lepton (SL) candidate events. The *b*-tagging efficiencies are shown for the predictions by the simulation (as a red line) and the measurements in data by the tag and probe (T&P) method (as black dots). The total uncertainties of these measurements are displayed as well (by the green filled area). The uncertainties on the predicted tagging efficiencies are based only on the the Monte Carlo statistics. The corresponding data-to-simulation scale factors are presented in addition also as a function of the jet p_{T} (b), $|\eta|$ (d) and ΔR^{min} (f).

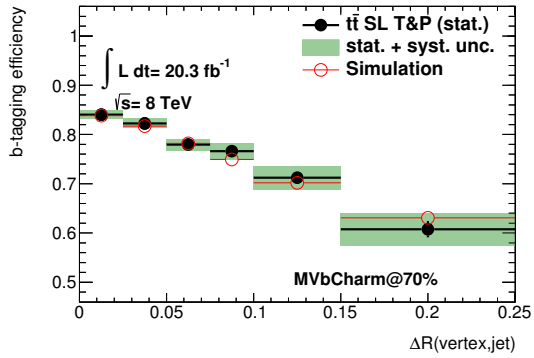

(a) multi-track vertex (SV1)

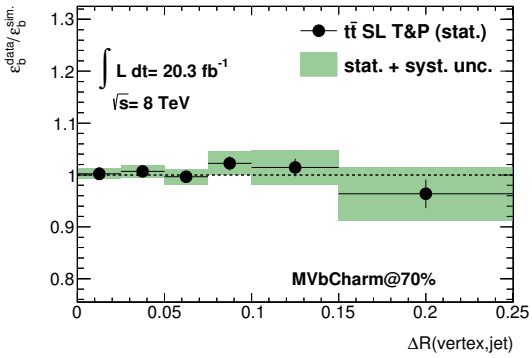

(b) multi-track vertex (SV1)

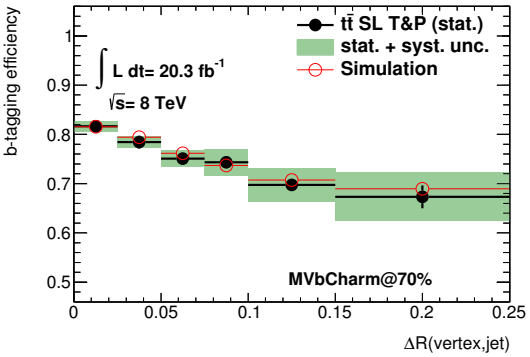

(c) multi-track vertex (JetFitter)

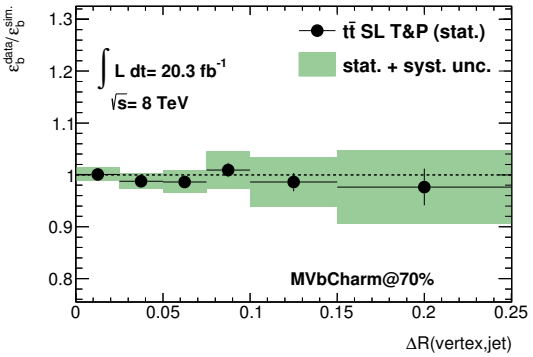

(d) multi-track vertex (JetFitter)

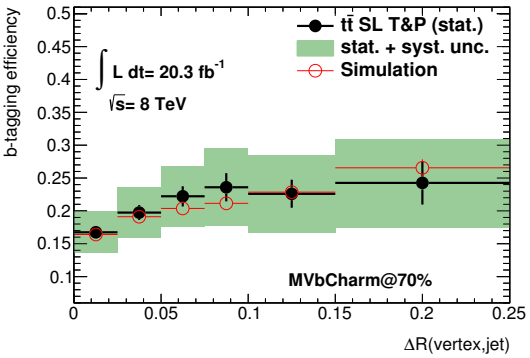

(e) single-track vertex (JetFitter)

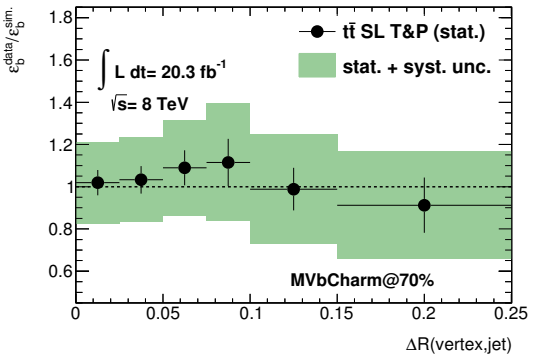

(f) single-track vertex (JetFitter)

Figure B.2: Results of the *b*-tagging efficiency measurements for the MVbCharm algorithm corresponding to an operating point of 70% efficiency as a function of the angular separation between the vertex direction and the jet axis $\Delta R(\text{vertex}, \text{jet})$. The measurements are performed separately for jets. having a vertex reconstructed with the iterative vertex finder (a-b) and the JetFitter algorithm (c-f), where the vertex candidates based on the JetFitter are subdivided into single- and multi-track topologies. The *b*-tagging efficiencies (left column) are shown for the predictions by the simulation (as a red line) and the measurements in data by the tag and probe (T&P) method (as black dots). The total uncertainties of these measurements are displayed as well (by the green filled area). The uncertainties on the predicted tagging efficiencies are based only on the the Monte Carlo statistics. The corresponding data-to-simulation scale factors are presented in addition (right column). As these measurements take only jets into account that have an appropriate type of secondary vertex reconstructed, the definition of the presented *b*-tagging efficiencies is not inclusive as in the measurements corresponding to the jet p_{T}, η or ΔR^{min}.

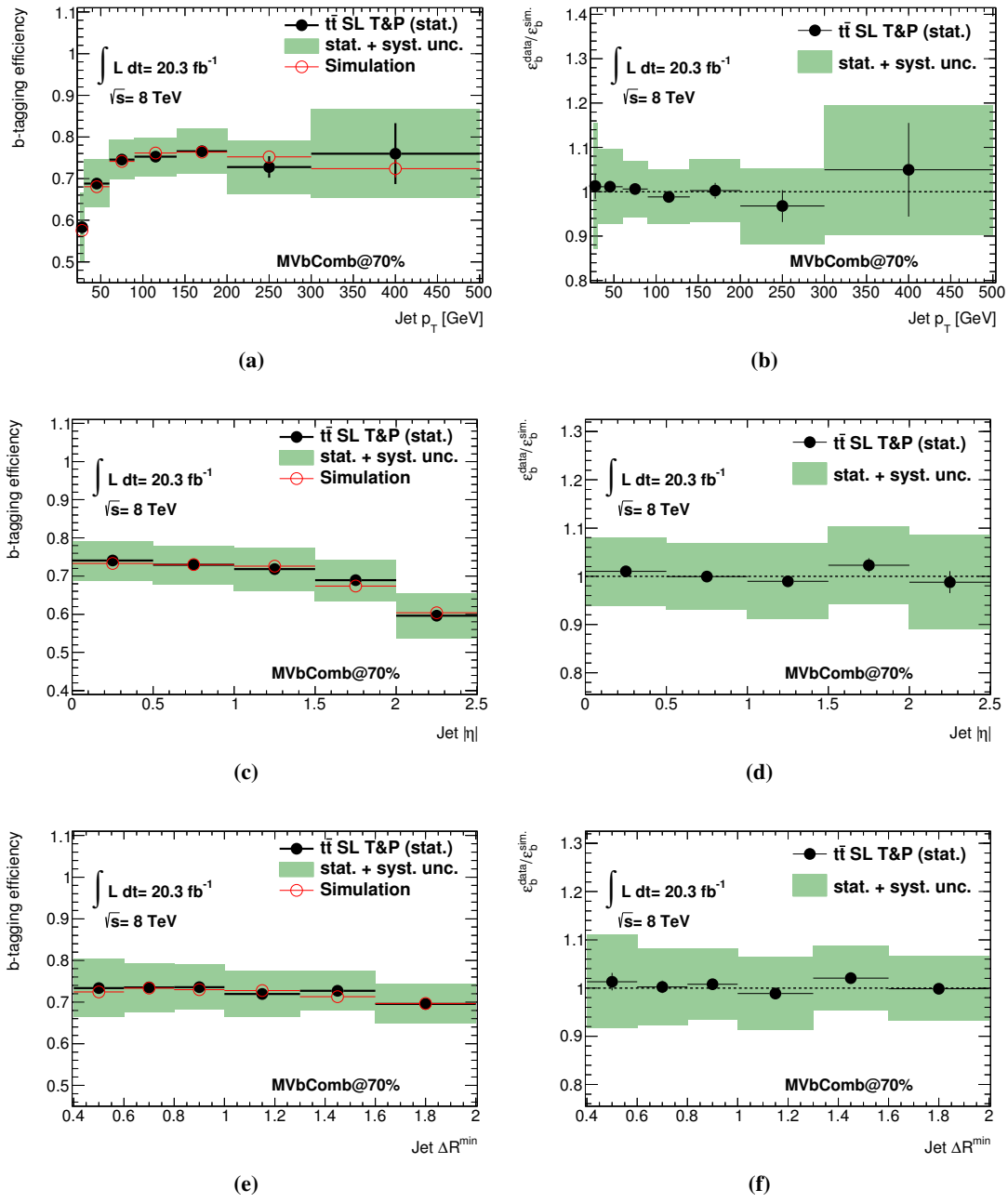

Figure B.3: The *b*-tagging efficiencies for the MVbComb algorithm corresponding to an operating point of an overall efficiency of 70% as a function of the transverse momentum (a), the absolute pseudorapidity (c) and the ΔR^{min} (e) of the jets contained in the sample of $t\bar{t}$ single lepton (SL) candidate events. The *b*-tagging efficiencies are shown for the predictions by the simulation (as a red line) and the measurements in data by the tag and probe (T&P) method (as black dots). The total uncertainties of these measurements are displayed as well (by the green filled area). The uncertainties on the predicted tagging efficiencies are based only on the the Monte Carlo statistics. The corresponding data-to-simulation scale factors are presented in addition also as a function of the jet p_{T} (b), $|\eta|$ (d) and ΔR^{min} (f).

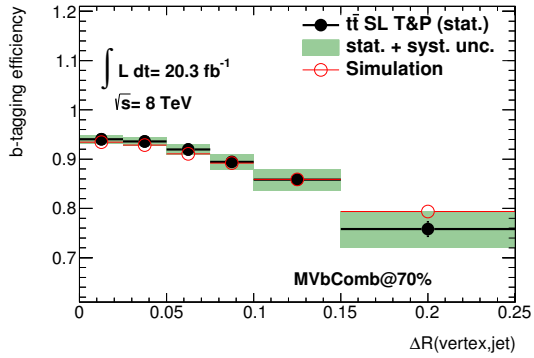

(a) multi-track vertex (SV1)

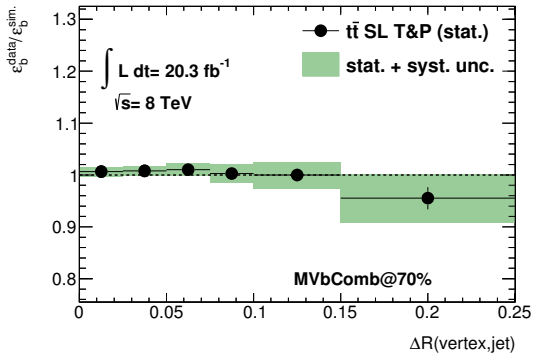

(b) multi-track vertex (SV1)

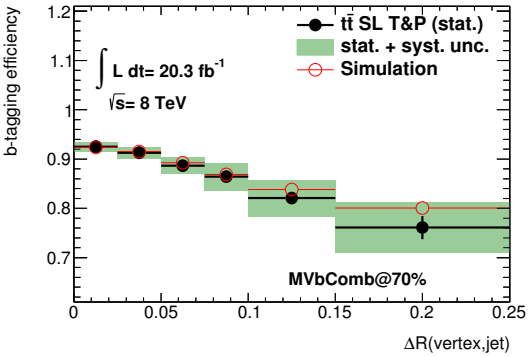

(c) multi-track vertex (JetFitter)

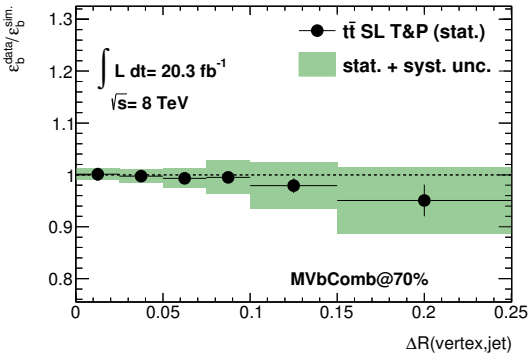

(d) multi-track vertex (JetFitter)

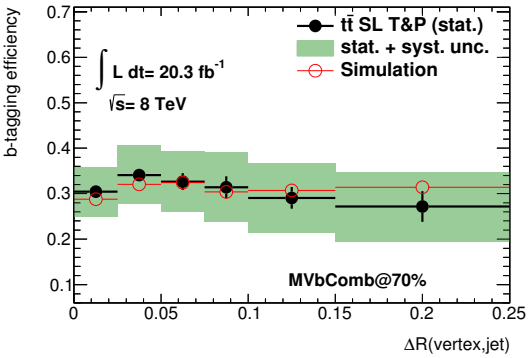

(e) single-track vertex (JetFitter)

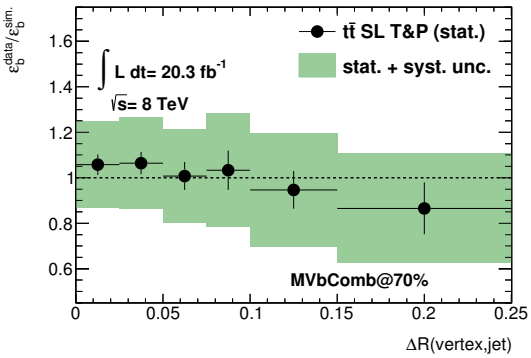

(f) single-track vertex (JetFitter)

Figure B.4: Results of the *b*-tagging efficiency measurements for the MVbComb algorithm corresponding to an operating point of 70% efficiency as a function of the angular separation between the vertex direction and the jet axis $\Delta R(\text{vertex}, \text{jet})$. The measurements are performed separately for jets. having a vertex reconstructed with the iterative vertex finder (a-b) and the JetFitter algorithm (c-f), where the vertex candidates based on the JetFitter are subdivided into single- and multi-track topologies. The *b*-tagging efficiencies (left column) are shown for the predictions by the simulation (as a red line) and the measurements in data by the tag and probe (T&P) method (as black dots). The total uncertainties of these measurements are displayed as well (by the green filled area). The uncertainties on the predicted tagging efficiencies are based only on the the Monte Carlo statistics. The corresponding data-to-simulation scale factors are presented in addition (right column). As these measurements take only jets into account that have an appropriate type of secondary vertex reconstructed, the definition of the presented *b*-tagging efficiencies is not inclusive as in the measurements corresponding to the jet p_{T}, η or ΔR^{min}.

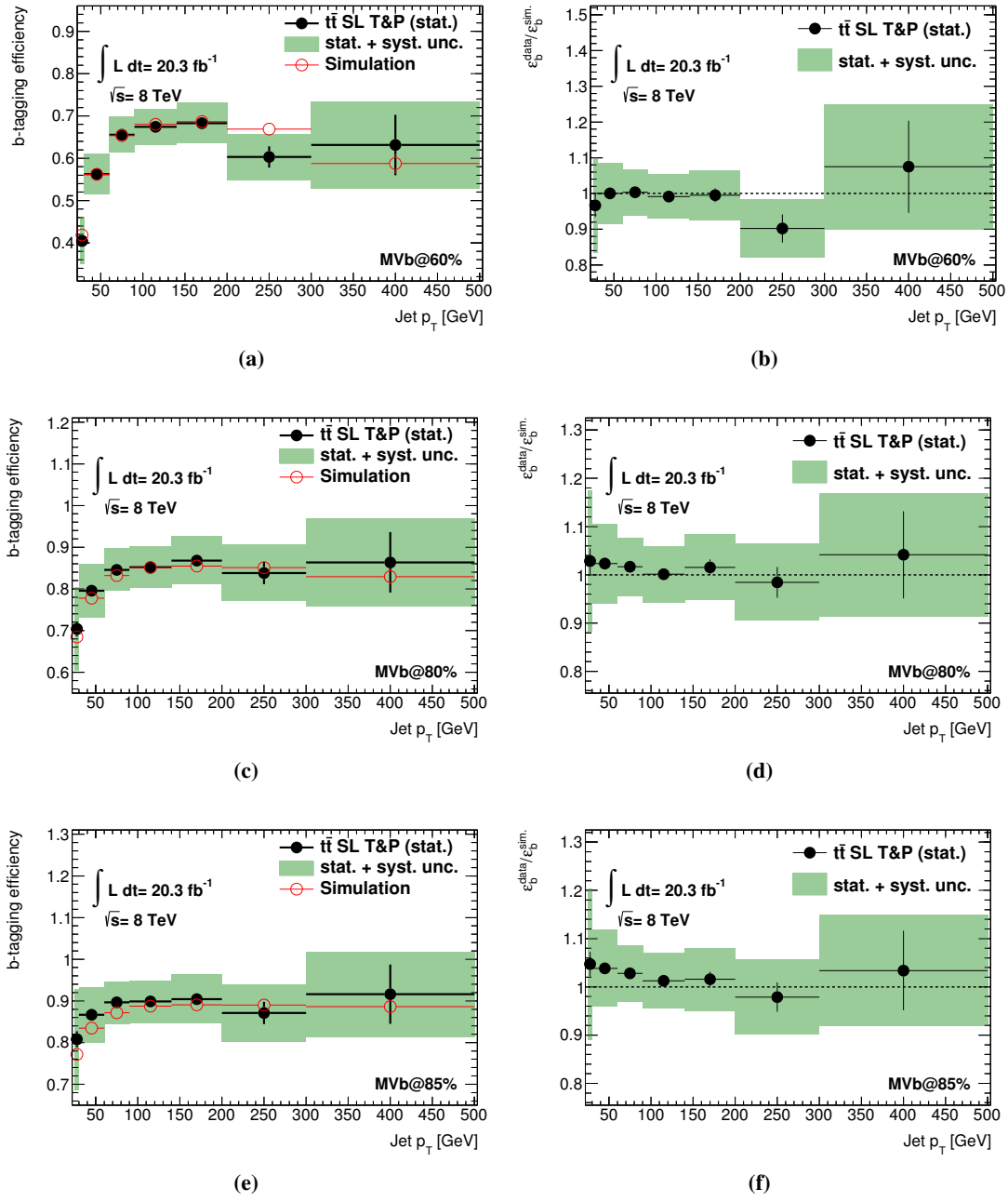

Figure B.5: The *b*-tagging efficiencies for the MVb algorithm corresponding to operating points of overall efficiencies of 60%, 80% and 85% as a function of the transverse momentum of the jets contained in the sample of $t\bar{t}$ single lepton (SL) candidate events. The *b*-tagging efficiencies are shown for the predictions by the simulation (as a red line) and the measurements in data by the tag and probe (T&P) method (as black dots). The total uncertainties of these measurements are displayed as well (by the green filled area). The uncertainties on the predicted tagging efficiencies are based only on the the Monte Carlo statistics. The corresponding data-to-simulation scale factors are presented in addition also as a function of the jet p_{T}.

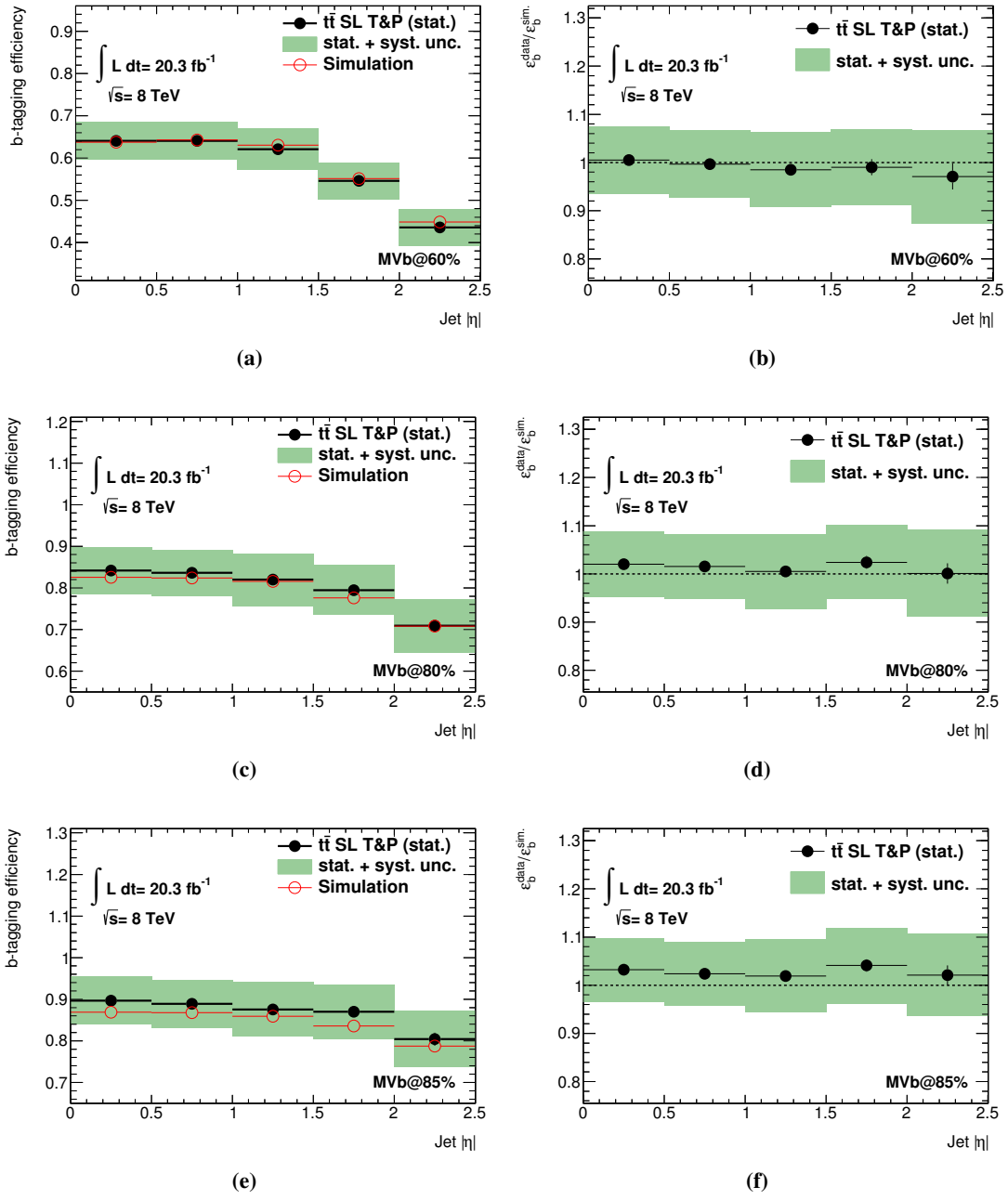

Figure B.6: The *b*-tagging efficiencies for the MVb algorithm corresponding to operating points of overall efficiencies of 60%, 80% and 85% as a function of the absolute pseudorapidity of the jets contained in the sample of $t\bar{t}$ single lepton (SL) candidate events. The *b*-tagging efficiencies are shown for the predictions by the simulation (as a red line) and the measurements in data by the tag and probe (T&P) method (as black dots). The total uncertainties of these measurements are displayed as well (by the green filled area). The uncertainties on the predicted tagging efficiencies are based only on the the Monte Carlo statistics. The corresponding data-to-simulation scale factors are presented in addition also as a function of the jet $|\eta|$.

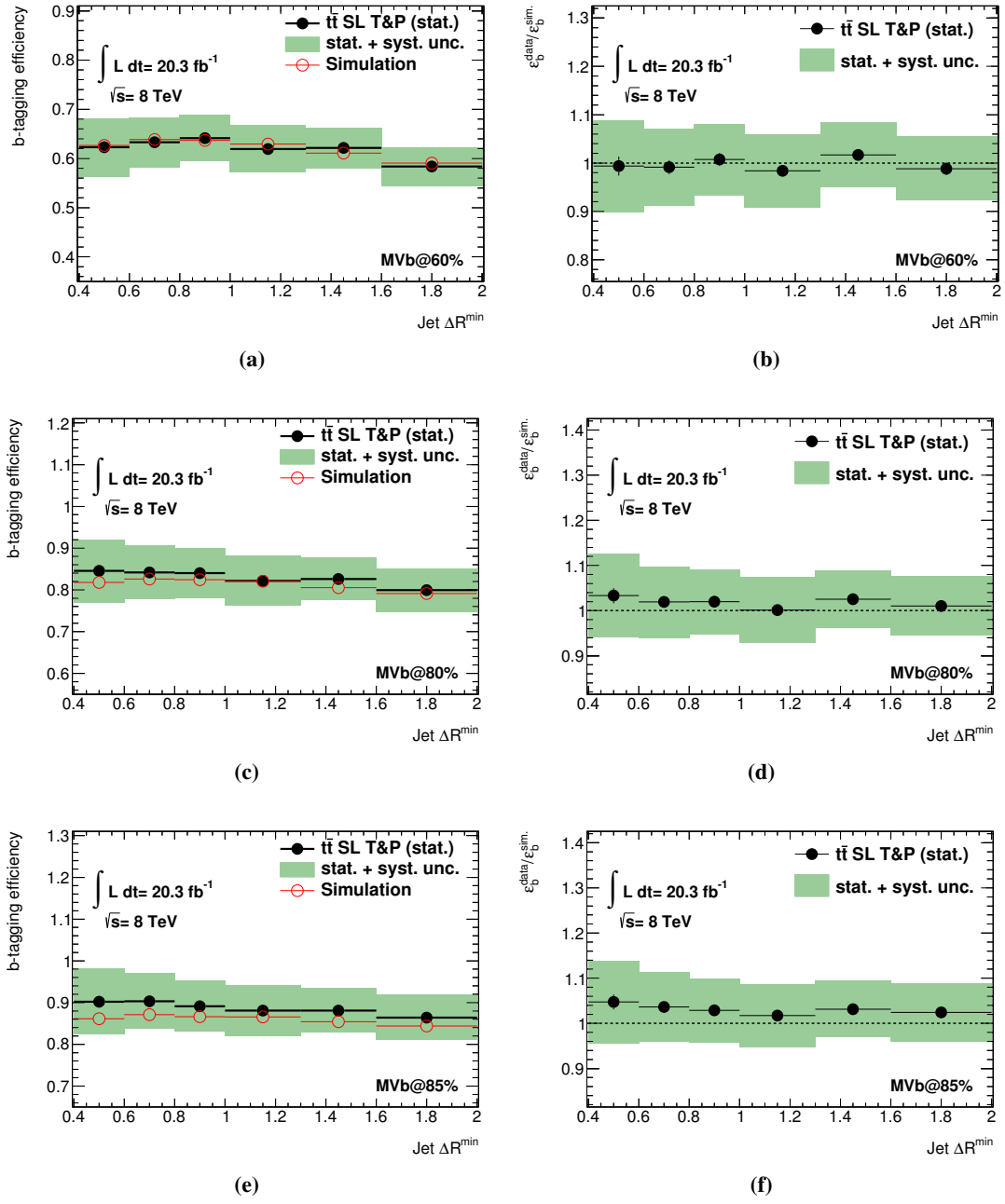

Figure B.7: The *b*-tagging efficiencies for the MVb algorithm corresponding to operating points of overall efficiencies of 60%, 80% and 85% as a function of the ΔR^{min} of the jets contained in the sample of $t\bar{t}$ single lepton (SL) candidate events. The *b*-tagging efficiencies are shown for the predictions by the simulation (as a red line) and the measurements in data by the tag and probe (T&P) method (as black dots). The total uncertainties of these measurements are displayed as well (by the green filled area). The uncertainties on the predicted tagging efficiencies are based only on the the Monte Carlo statistics. The corresponding data-to-simulation scale factors are presented in addition also as a function of the jet ΔR^{min}.

p_T[GeV]	25-30	30-60	60-90	90-140	140-200	200-300	300-500
Stat.	±3.2	±0.9	±0.9	±1.0	±2.0	±4.0	±12.5
Total Syst	±14.4	±8.3	±6.3	±6.2	±6.9	±7.8	±9.4
Total	±14.8	±8.4	±6.4	±6.3	±7.2	±8.8	±15.6
SF	1.03 ± 0.15	1.01 ± 0.08	1.00 ± 0.06	0.99 ± 0.06	0.99 ± 0.07	0.93 ± 0.08	1.10 ± 0.17

(a) Systematic uncertainties in each p_T bin

η	0.0-0.5	0.5-1.0	1.0-1.5	1.5-2.0	2.0-2.5
Stat.	±0.9	±1.0	±1.1	±1.6	±2.4
Total Syst	±7.0	±7.0	±7.8	±7.6	±9.4
Total	±7.1	±7.1	±7.9	±7.7	±9.7
SF	1.00 ± 0.07	1.01 ± 0.07	0.99 ± 0.08	1.01 ± 0.08	1.00 ± 0.10

(b) Systematic uncertainties in each $|\eta|$ bin

ΔR^{min}	0.4-0.6	0.6-0.8	0.8-1.0	1.0-1.3	1.3-1.6	1.6-2.0
Stat.	±2.0	±1.4	±1.4	±1.1	±1.2	±1.3
Total Syst	±9.6	±8.0	±7.3	±7.7	±6.4	±6.6
Total	±9.8	±8.1	±7.4	±7.8	±6.5	±6.7
SF	1.00 ± 0.10	1.00 ± 0.08	1.01 ± 0.07	0.99 ± 0.08	1.02 ± 0.07	1.00 ± 0.07

(c) Systematic uncertainties in each ΔR^{min} bin

ΔR(vertex, jet)	0.000-0.025	0.025-0.050	0.050-0.075	0.075-0.100	0.100-0.150	0.150-0.250
Stat.	±0.7	±0.6	±0.9	±1.3	±1.7	±2.8
Total Syst	±0.8	±1.0	±1.2	±1.7	±2.8	±4.6
Total	±1.0	±1.2	±1.5	±2.2	±3.3	±5.4
SF	1.00 ± 0.01	1.01 ± 0.01	1.00 ± 0.01	1.02 ± 0.02	1.01 ± 0.03	0.96 ± 0.05

(d) Systematic uncertainties in each ΔR(vertex, jet) bin for multi-track vertices reconstructed with the iterative vertex finder

ΔR(vertex, jet)	0.000-0.025	0.025-0.050	0.050-0.075	0.075-0.100	0.100-0.150	0.150-0.250
Stat.	±0.6	±0.6	±0.9	±1.4	±1.8	±3.5
Total Syst	±1.1	±1.4	±2.0	±3.4	±4.5	±6.3
Total	±1.3	±1.5	±2.2	±3.6	±4.8	±7.2
SF	1.00 ± 0.01	0.99 ± 0.02	0.99 ± 0.02	1.01 ± 0.04	0.99 ± 0.05	0.98 ± 0.07

(e) [Systematic uncertainties in each ΔR(vertex, jet) bin for multi-track vertices reconstructed with the JetFitter algorithm

ΔR(vertex, jet)	0.000-0.025	0.025-0.050	0.050-0.075	0.075-0.100	0.100-0.150	0.150-0.250
Stat.	±6.0	±6.5	±8.3	±11.1	±10.1	±13.1
Total Syst	±17.9	±18.3	±19.0	±22.4	±24.1	±24.7
Total	±18.9	±19.4	±20.7	±25.0	±26.1	±27.9
SF	1.02 ± 0.19	1.03 ± 0.20	1.09 ± 0.23	1.11 ± 0.28	0.99 ± 0.26	0.91 ± 0.25

(f) [Systematic uncertainties in each ΔR(vertex, jet) bin for single-track vertices reconstructed with the JetFitter algorithm

Table B.1: Summary of the combined systematic and statistical uncertainties (in %) on the measured data-to-simulation scale factors of the MVbCharm algorithm in the various jet p_T (a), $|\eta|$ (b), ΔR^{min} (c) and ΔR(vertex, jet) (d-f) regions. These values correspond to an operation point that provides a b-tagging efficiency of 70%.

p_T[GeV]	25-30	30-60	60-90	90-140	140-200	200-300	300-500
Stat.	±2.8	±0.8	±0.8	±0.9	±1.8	±3.6	±10.6
Total Syst	±13.8	±8.3	±6.2	±6.1	±6.8	±8.1	±9.2
Total	±14.1	±8.3	±6.3	±6.2	±7.0	±8.8	±14.0
SF	1.01 ± 0.14	1.01 ± 0.08	1.01 ± 0.06	0.99 ± 0.06	1.00 ± 0.07	0.97 ± 0.09	1.05 ± 0.15

(a) Systematic uncertainties in each p_T bin

η	0.0-0.5	0.5-1.0	1.0-1.5	1.5-2.0	2.0-2.5
Stat.	±0.8	±0.9	±1.0	±1.5	±2.3
Total Syst	±7.0	±6.9	±7.8	±7.7	±9.6
Total	±7.0	±6.9	±7.9	±7.8	±9.9
SF	1.01 ± 0.07	1.00 ± 0.07	0.99 ± 0.08	1.02 ± 0.08	0.99 ± 0.10

(b) Systematic uncertainties in each $|\eta|$ bin

ΔR^{min}	0.4-0.6	0.6-0.8	0.8-1.0	1.0-1.3	1.3-1.6	1.6-2.0
Stat.	±1.8	±1.3	±1.2	±1.0	±1.1	±1.2
Total Syst	±9.4	±7.9	±7.2	±7.6	±6.5	±6.6
Total	±9.5	±8.0	±7.3	±7.7	±6.5	±6.7
SF	1.01 ± 0.10	1.00 ± 0.08	1.01 ± 0.07	0.99 ± 0.08	1.02 ± 0.07	1.00 ± 0.07

(c) Systematic uncertainties in each ΔR^{min} bin

ΔR(vertex, jet)	0.000-0.025	0.025-0.050	0.050-0.075	0.075-0.100	0.100-0.150	0.150-0.250
Stat.	±0.5	±0.5	±0.7	±1.0	±1.2	±2.1
Total Syst	±0.7	±0.8	±1.0	±1.4	±2.2	±4.5
Total	±0.9	±0.9	±1.2	±1.7	±2.6	±5.0
SF	1.01 ± 0.01	1.01 ± 0.01	1.01 ± 0.01	1.00 ± 0.02	1.00 ± 0.03	0.96 ± 0.05

(d) Systematic uncertainties in each ΔR(vertex, jet) bin for multi-track vertices reconstructed with the iterative vertex finder

ΔR(vertex, jet)	0.000-0.025	0.025-0.050	0.050-0.075	0.075-0.100	0.100-0.150	0.150-0.250
Stat.	±0.5	±0.5	±0.6	±1.1	±1.4	±3.0
Total Syst	±1.0	±1.2	±1.8	±3.1	±4.4	±6.0
Total	±1.1	±1.3	±1.9	±3.2	±4.6	±6.7
SF	1.00 ± 0.01	1.00 ± 0.01	0.99 ± 0.02	1.00 ± 0.03	0.98 ± 0.04	0.95 ± 0.06

(e) [Systematic uncertainties in each ΔR(vertex, jet) bin for multi-track vertices reconstructed with the JetFitter algorithm

ΔR(vertex, jet)	0.000-0.025	0.025-0.050	0.050-0.075	0.075-0.100	0.100-0.150	0.150-0.250
Stat.	±4.5	±4.9	±6.2	±8.6	±8.3	±11.4
Total Syst	±17.5	±18.3	±19.5	±22.6	±25.0	±25.5
Total	±18.1	±18.9	±20.5	±24.2	±26.4	±27.9
SF	1.06 ± 0.19	1.06 ± 0.20	1.01 ± 0.21	1.03 ± 0.25	0.95 ± 0.25	0.87 ± 0.24

(f) [Systematic uncertainties in each ΔR(vertex, jet) bin for single-track vertices reconstructed with the JetFitter algorithm

Table B.2: Summary of the combined systematic and statistical uncertainties (in %) on the measured data-to-simulation scale factors of the MVbComb algorithm in the various jet p_T (a), $|\eta|$ (b), ΔR^{min} (c) and ΔR(vertex, jet) (d-f) regions. These values correspond to an operation point that provides a b-tagging efficiency of 70%.

p_T[GeV]	25-30	30-60	60-90	90-140	140-200	200-300	300-500
Stat.	±3.3	±0.9	±0.9	±1.0	±1.9	±3.9	±12.9
Total Syst	±13.4	±8.4	±6.3	±6.2	±6.7	±8.1	±9.9
Total	±13.8	±8.5	±6.4	±6.2	±7.0	±9.0	±16.3
SF	0.97 ± 0.13	1.00 ± 0.08	1.00 ± 0.06	0.99 ± 0.06	0.99 ± 0.07	0.90 ± 0.08	1.07 ± 0.17

(a) Systematic uncertainties in each p_T bin 60%

p_T[GeV]	25-30	30-60	60-90	90-140	140-200	200-300	300-500
Stat.	±2.6	±0.8	±0.7	±0.8	±1.6	±3.2	±9.0
Total Syst	±14.0	±8.0	±5.9	±5.8	±6.5	±7.4	±8.3
Total	±14.2	±8.0	±6.0	±5.8	±6.7	±8.1	±12.3
SF	1.03 ± 0.15	1.02 ± 0.08	1.02 ± 0.06	1.00 ± 0.06	1.02 ± 0.07	0.98 ± 0.08	1.04 ± 0.13

(b) Systematic uncertainties in each p_T bin 80%

p_T[GeV]	25-30	30-60	60-90	90-140	140-200	200-300	300-500
Stat.	±2.6	±0.7	±0.7	±0.8	±1.5	±3.1	±8.2
Total Syst	±14.7	±7.6	±5.6	±5.6	±6.3	±7.3	±7.6
Total	±14.9	±7.7	±5.7	±5.7	±6.4	±7.9	±11.2
SF	1.05 ± 0.16	1.04 ± 0.08	1.03 ± 0.06	1.01 ± 0.06	1.02 ± 0.07	0.98 ± 0.08	1.03 ± 0.12

(c) Systematic uncertainties in each p_T bin 85%

η	0.0-0.5	0.5-1.0	1.0-1.5	1.5-2.0	2.0-2.5
Stat.	±0.9	±0.9	±1.1	±1.7	±2.7
Total Syst	±6.9	±7.0	±7.7	±7.7	±9.6
Total	±7.0	±7.0	±7.8	±7.9	±10.0
SF	1.01 ± 0.07	1.00 ± 0.07	0.98 ± 0.08	0.99 ± 0.08	0.97 ± 0.10

(d) Systematic uncertainties in each η bin 60%

η	0.0-0.5	0.5-1.0	1.0-1.5	1.5-2.0	2.0-2.5
Stat.	±0.7	±0.8	±0.9	±1.3	±2.1
Total Syst	±6.6	±6.6	±7.7	±7.3	±8.8
Total	±6.7	±6.6	±7.7	±7.5	±9.0
SF	1.02 ± 0.07	1.02 ± 0.07	1.01 ± 0.08	1.02 ± 0.08	1.00 ± 0.09

(e) Systematic uncertainties in each η bin 80%

η	0.0-0.5	0.5-1.0	1.0-1.5	1.5-2.0	2.0-2.5
Stat.	±0.7	±0.7	±0.9	±1.3	±2.0
Total Syst	±6.4	±6.4	±7.3	±7.4	±8.1
Total	±6.4	±6.4	±7.4	±7.5	±8.4
SF	1.03 ± 0.07	1.02 ± 0.07	1.02 ± 0.08	1.04 ± 0.08	1.02 ± 0.09

(f) Systematic uncertainties in each η bin 85%

Table B.3: Summary of the combined systematic and statistical uncertainties (in %) on the measured data-to-simulation scale factors of the MVb algorithm in the various jet p_T (a-c) and $|\eta|$ (d-f), regions. These values correspond to operation points that provide b-tagging efficiencies of 60%, 80% and 85%.

$\Delta R^{\min}$	0.4-0.6	0.6-0.8	0.8-1.0	1.0-1.3	1.3-1.6	1.6-2.0
Stat.	±2.0	±1.4	±1.4	±1.1	±1.2	±1.3
Total Syst	±9.3	±7.9	±7.2	±7.6	±6.5	±6.5
Total	±9.5	±8.1	±7.3	±7.7	±6.6	±6.7
SF	0.99 ± 0.09	0.99 ± 0.08	1.01 ± 0.07	0.98 ± 0.08	1.02 ± 0.07	0.99 ± 0.07

(a) Systematic uncertainties in each $\Delta R^{\min}$ bin 60%

$\Delta R^{\min}$	0.4-0.6	0.6-0.8	0.8-1.0	1.0-1.3	1.3-1.6	1.6-2.0
Stat.	±1.7	±1.2	±1.1	±0.9	±1.0	±1.1
Total Syst	±8.8	±7.6	±7.0	±7.2	±6.1	±6.4
Total	±8.9	±7.7	±7.1	±7.2	±6.2	±6.5
SF	1.03 ± 0.09	1.02 ± 0.08	1.02 ± 0.07	1.00 ± 0.07	1.03 ± 0.06	1.01 ± 0.07

(b) Systematic uncertainties in each $\Delta R^{\min}$ bin 80%

$\Delta R^{\min}$	0.4-0.6	0.6-0.8	0.8-1.0	1.0-1.3	1.3-1.6	1.6-2.0
Stat.	±1.6	±1.2	±1.1	±0.8	±0.9	±1.0
Total Syst	±8.5	±7.3	±6.8	±6.8	±6.0	±6.2
Total	±8.7	±7.4	±6.8	±6.8	±6.0	±6.3
SF	1.05 ± 0.09	1.04 ± 0.08	1.03 ± 0.07	1.02 ± 0.07	1.03 ± 0.06	1.02 ± 0.06

(c) Systematic uncertainties in each $\Delta R^{\min}$ bin 85%

Table B.4: Summary of the combined systematic and statistical uncertainties (in %) on the measured data-to-simulation scale factors of the MVb algorithm in the various jet $\Delta R^{\min}$ regions. These values correspond to operation points that provide b-tagging efficiencies of 60%, 80% and 85%.

Appendix C

Upper cross-section times branching ratio limits on the production of RS gravitons and KK gluons

This section presents exclusion limits on the upper cross-section times branching ratio for the production of hypothetical RS gravitons G_{RS} and KK gluons g_{KK} (based on resonance decays into a top-quark pair). Results are obtained for the various event classification schemes analogously to what is shown in Section 9.3.1.

Figure C.1 displays the exclusion limits on the production of RS gravitons as a function of the resonance mass, while Figure C.2 presents limits on the production of KK gluons as a function of the gluon width for a fixed resonance mass of $m_{g_{KK}} = 2.0$ TeV. Both sets of limits are presented separately for the inclusive event sample and also for two different b-tagging categorisation schemes.

Figure C.1 (a) shows that the available statistics of the 8 TeV run of the LHC is not sufficient in order to exclude the production of RS gravitons in the studied mass range. However, with the event classification scheme denoted as"BtagCat1234", significantly stronger upper limits on the production cross-section times branching ratio can be set than with the inclusive event sample. The Improvements, as shown in Figure C.1 (b), are around 60% for graviton masses up-to 0.6 TeV and between 10% and 30% for resonance masses between 0.6 TeV and 2.5 TeV.

Figure C.2 (a) shows that the production of KK gluons is excluded for all the studied resonance widths at a gluon mass of $m_{g_{KK}} = 2.0$ TeV. Again the event classification scheme denoted as"BtagCat1234" provides much better results than the inclusive event sample or any other event classification scheme. The corresponding improvements, as shown in Figure C.2 (b), vary between 25% and 30%. The relative improvements with respect to the inclusive event sample increase slightly for increasing resonance width values.

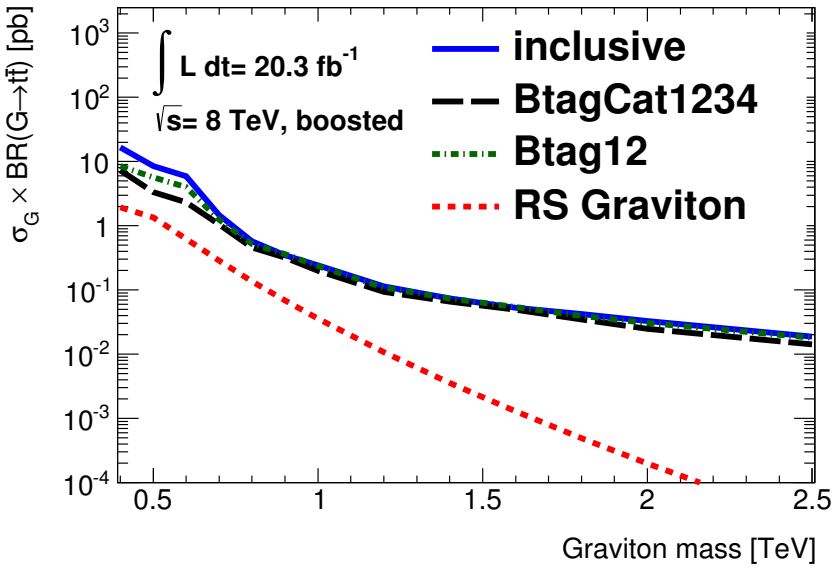

(a) Expected exclusion limits

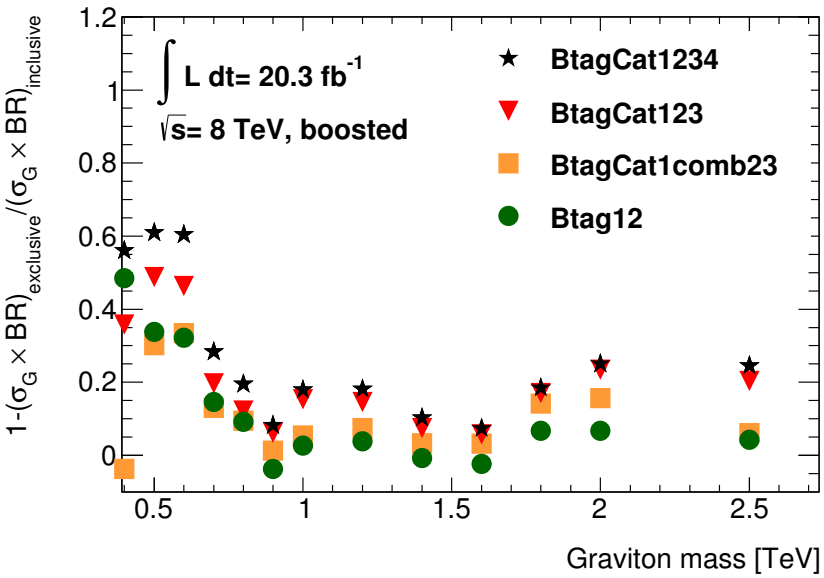

(b) Ratios

Figure C.1: Expected exclusion limits on the production cross-section times branching ratio as a function of the RS graviton mass at the 95% confidence level obtained from events that are reconstructed in the boosted event channel (a). The limits are presented for the inclusive event sample (blue solid line), but also for the case that the selected candidate events are categorised according to their multiplicity of *b*-tagged jets (green dashed line) or according to the classification scheme referred to as "BtagCat1234" (black dashed line). The predicted production cross section times branching ratio for the RS graviton is displayed as well as a function of the resonance mass (dashed red line). In addition, also the relative improvements with respect to the inclusive event sample are shown for various event classification schemes (b).

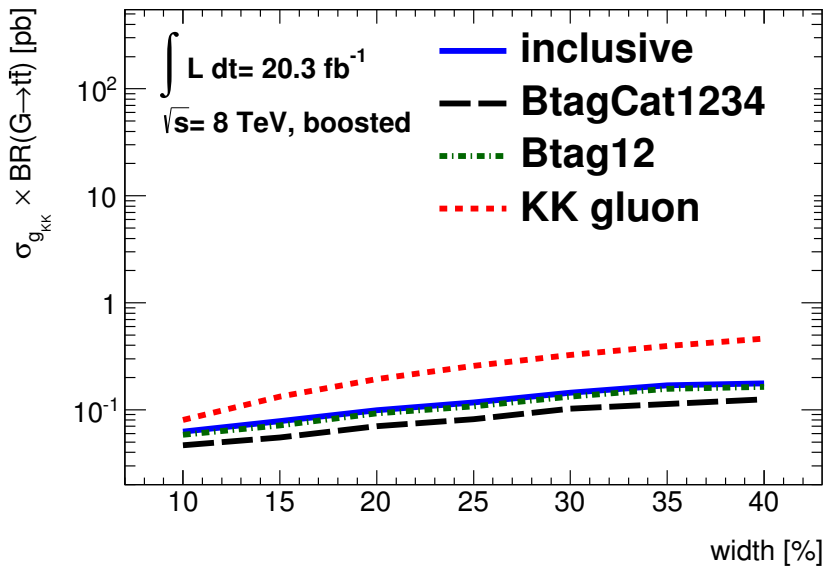

(a) Expected exclusion limits

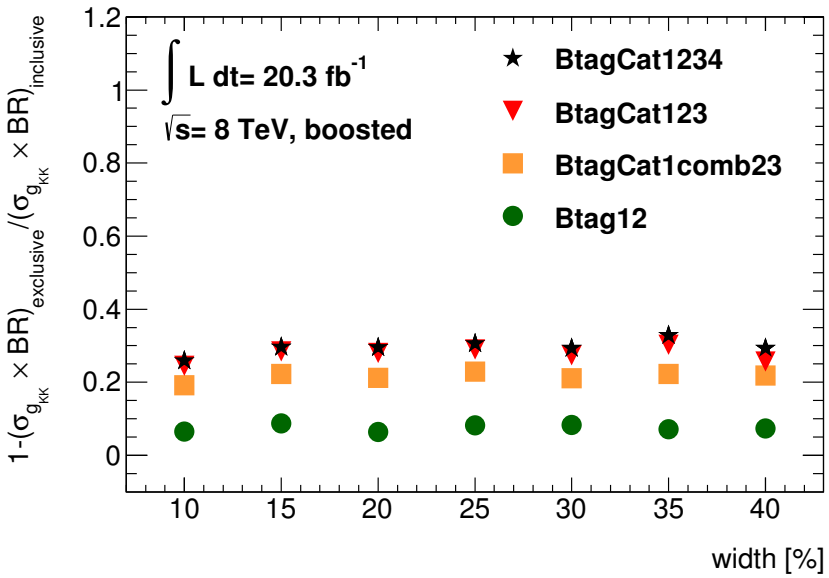

(b) Ratios

Figure C.2: Expected exclusion limits on the production cross-section times branching ratio as a function of the width of a KK gluon of the mass $m_{g_{KK}} = 2.0$ TeV at the 95% confidence level obtained from events that are reconstructed in the boosted event channel (a). The limits are presented for the inclusive event sample (blue solid line), but also for the case that the selected candidate events are categorised according to their multiplicity of b-tagged jets (green dashed line) or according to the classification scheme referred to as "BtagCat1234" (black dashed line). The predicted production cross section times branching ratio for the KK gluon is displayed as well as a function of the resonance width (dashed red line). In addition, also the relative improvements with respect to the inclusive event sample are shown for various event classification schemes (b).